Shock Properties of Homogeneous Anisotropic Dielectrics

Gareth Richard Tear

Imperial College London, Department of Physics

Supervised by Dr. William G Proud

Submitted in partial fulfilment of the degrees of

Doctor of Philosophy

Diploma of Imperial College London

Abstract

Anisotropy, the directional dependence of a physical quantity, is present in numerous physical processes involved in the shock compression of solid materials. The effect that a particular property's anisotropy has on the propagation of a shock wave is obscured by other effects such as those from strain rate and material heterogeneity. Recent studies have focussed on single- and bi-crystal metals to understand the effect of crystal anisotropy on the mechanics of shock wave propagation. This thesis extends this work to optically transparent non-metallic dielectric single crystals by developing an optical model for anisotropic dielectrics and performing experimental measurements to test the validity of that optical model.

Current optical models for shock compressed materials use an isotropic Gladstone-Dale model or isotropic modifications of the Gladstone-Dale model. This thesis extends the isotropic Gladstone-Dale model to an anisotropic photoelastic model for the optical behaviour of linear anisotropic materials under shock compression in the elastic regime. The model uses static photoelastic tensor values available in the literature to predict material response under uniaxial strain in an arbitrary crystal orientation. The effect of varying photoelastic tensor values is studied using Monte Carlo techniques, and confidence intervals on dynamic predictions are presented.

Polarimetry is applied to experimentally measure birefringence under shock compression delivered using plate impact on a single stage light gas gun. This method is used to validate the linear photoelastic model developed in this thesis. Experiments were performed on $\langle 1\,0\,\bar{1}\,0\rangle$ (a-cut) sapphire up to 15 GPa longitudinal stress and $\langle 1\,0\,\bar{1}\,0\rangle$ (a-cut) calcite up to 2 GPa longitudinal stress. It was found that the birefringence of a-cut sapphire under shock compression behaved in agreement with the model in the elastic regime for a 5% error on the photoelastic tensor. Furthermore it was found that birefringence predictions for a-cut calcite as given by the same model did not agree with experimentally measured results. The discrepancy was 0.3% at 1.2 GPa, in excess of 5

standard deviations. Possible reasons for the discrepancy are put forward.

Copyright

The copyright of this thesis rests with the author and is made available under a Creative Commons Attribution Non-Commercial No Derivatives licence. Researchers are free to copy, distribute or transmit the thesis on the condition that they attribute it, that they do not use it for commercial purposes and that they do not alter, transform or build upon it. For any reuse or redistribution, researchers must make clear to others the licence terms of this work.

Declaration of Originality

The content of this thesis is my own work, except where explicitly stated and referenced in the text.

Collaborations

During the course of the thesis some collaborative work was carried out and results from that work forms part of this thesis. The optical samples used in this work were produced by Crystran, Knight Optical and SP3 Plus. The large bore gas gun at Imperial College London is run by Dr David Chapman, who has built and maintains the Photonic Doppler Velocimetry (PDV) equipment. The Institute of Shock Physics (ISP) technical support team, Mr Steve Johnson and Mr David Pitman, clean prepare and fire the gas gun as well as machine sabots and target components.

Acknowledgements

Firstly I would like to thank my supervisor Dr. William G Proud for giving me the opportunity to conduct this research. I am also grateful to Dr. David J Chapman whose dedication to scientific rigour has taught me much about shock physics and to Dr. William Neal for guiding me in the early stages of this research. From the technical staff, I am particularly appreciative of the hard work of Mr. Steven Johnson and Mr. David Pitman, who carefully machined components for each experiment, only to see them destroyed.

Several individuals outside of Imperial have also been supportive, and I would like to thank Dr. Dennis E Grady, Dr. John B Aidun and Scott Grant for their helpful and useful discussions at conferences and over email.

I would also like to thank my parents for their love and support, encouraging my scientific interests from a young age, and especially for reading this thesis with the improvements they have suggested.

Finally I could not have completed this without the endless love and encouragement of Rebecca Pearson.

Contents

1 Introduction **18**

1.1 Background 19

1.1.1 Anisotropic Shock Experiments 20

1.1.2 Numerical Models 22

1.1.3 Concluding Comments about Anisotropic Materials 25

1.2 Optical Measurements 25

1.2.1 Optical Velocimetry via Interferometry 26

1.2.2 Polarimetry 28

1.2.3 Optical Anisotropy 30

1.3 Mechanical Properties of Homogeneous Anisotropic Dielectrics 31

1.3.1 Sapphire 31

1.3.2 Calcite 34

1.3.3 Other Materials 37

1.4 Optical properties of Homogeneous Anisotropic Dielectrics 38

1.4.1 Sapphire 38

1.4.2 Calcite 38

1.4.3 Other Materials 39

1.5 Context of This Work 39

1.5.1 Research Objectives 40

2 Prerequisites for Shock-Wave Studies of Anisotropic Materials **41**

2.1 Treatment of Steady Shock Waves using the Jump Equations 42
2.1.1 The Jump Equations 42
2.1.2 Impact of Two Materials 44
2.1.3 Off-Hugoniot States 45
2.2 Notation for Anisotropic Systems 46
2.3 Anisotropic Elastodynamics 47
2.4 Mathematical Representation of Anisotropic Optics 49
2.4.1 Photoelasticity 50
2.5 Photoelasticity in Shock Compression 51
2.5.1 Shocks along the a-axis 51
2.6 Experimentally Measurable Quantities 53
2.6.1 Birefringence 53
2.6.2 Polarimetry 56
2.6.3 Direct Refractive Index Measurement 59
2.7 Chapter Conclusions 62

3 Computing the Birefringence of Shocked Sapphire and Calcite 63
3.1 Error on Photoelastic Prediction 66
3.1.1 Estimating Tensor Errors 67
3.1.2 Estimating Directional Errors 68
3.1.3 Propagation of Errors 69
3.2 Simulating Experimental Data 71
3.2.1 Choice of Algorithms 71
3.2.2 Optical Algorithm 72
3.3 Estimating Impact Tilt 73
3.4 Results 74
3.4.1 Crystallographic tilt 75
3.4.2 Impact Tilt 78

3.5 Chapter Conclusions 78

4 Measuring Calcite Birefringence with the 12.7 mm Bore Light Gas Gun 80

4.1 Facility Description 81

4.1.1 Breech Design 82

4.1.2 Light Gates 83

4.1.3 Test Targets 84

4.2 Calcite Experiment One 85

4.2.1 Experimental Setup 85

4.2.2 Results 88

4.2.3 Summary 91

4.3 Second Calcite Experiment 92

4.3.1 Experimental Method 92

4.3.2 Results 93

4.3.3 Summary 93

4.4 Third Calcite Experiment 98

4.4.1 Experimental Method 98

4.4.2 Results 98

4.4.3 Summary 101

4.5 Discussion 101

4.6 Conclusions and Further Work 101

5 Final Configuration of High Speed Polarimeter for Shock Physics Applications 103

5.1 Experimental Configuration 105

5.2 Calibration 107

5.2.1 Calibrating the Polarimeter 109

5.3 Analysis of Sample Birefringence and Optical Axis 112

5.3.1 Birefringence 113

5.3.2 Optical Axis . . . 113
5.4 Sources of Error . . . 115
5.5 Chapter Conclusions . . . 116

6 Experimental Methods for Large Gas Gun Experiments 117
6.1 Description of 100 mm Bore Gas Gun . . . 119
6.1.1 Shot Characterisation . . . 121
6.1.2 Timing and Triggering . . . 123
6.2 Photonic Doppler Velocimetry (PDV) . . . 126
6.2.1 Experimental Configuration . . . 127
6.2.2 Analysis of PDV for Impact and Rear Surface Velocimetery . . . 131
6.2.3 Sources of Error . . . 139
6.3 Chapter Conclusions . . . 139

7 Large Gas Gun Results 141
7.1 Experimental Setup . . . 142
7.2 Sapphire . . . 149
7.2.1 PDV Analysis . . . 150
7.2.2 Polarimetry . . . 154
7.2.3 Window correction for PDV and Direct PDV Birefringence Measurement . . . 155
7.3 Calcite . . . 157
7.3.1 PDV Results . . . 157
7.3.2 Polarimeter Results . . . 161
7.3.3 Window correction for PDV and Direct PDV Birefringence Measurement . . . 163
7.4 Measurements of Optical Axis . . . 163
7.5 Chapter Conclusions . . . 164

8 Discussion **167**

8.1 Improvements in the Polarimetry System 167

8.1.1 Further Developments 168

8.2 Sapphire 169

8.2.1 Hugoniot Literature Comparison 169

8.2.2 Birefringence Prediction Comparison 170

8.2.3 Further Investigations 171

8.3 Calcite 172

8.3.1 Hugoniot and Sound speed Comparison 172

8.3.2 Birefringence Prediction Comparison 172

8.3.3 Further Investigations 177

9 Conclusions **178**

9.1 Previous Work 179

9.2 This Work 179

9.2.1 Linear Photoelastic Predictions 180

9.2.2 Develop and Verify Birefringence Technique 180

9.2.3 Experimental Work 181

9.3 Further Work 182

A Equations **192**

B Extended Results **194**

B.1 Preliminary Calcite Experiments 194

B.2 Calcite Large Bore Gas Gun Experiments 197

B.3 Sapphire Large Bore Gas Gun Results 200

C Material Model Constants **203**

C.1 Copper 203

C.2 Magnesium AZ31B 204

C.3 PMMA 204
C.4 Aluminium 6061 205
C.5 Sapphire Reintjes 206
C.6 Sapphire Waxler 207
C.7 Sapphire Jones 208
C.8 Calcite ¡10-10¿ 209

D List of Symbols **210**

E Acronyms **214**

F Glossary **216**

List of Figures

1.1 Example Yield Surface 24
1.2 Crystal Structures of Sapphire, Rutile and Calcite 32
1.3 Ahrens calcite hugoniot 36

2.1 Single steady shock illustration 43
2.2 Flyer material Hugoniots 44
2.3 Impedance Match Example 45
2.4 Illustration of the effect of birefringence on polarised light 54
2.5 Shock birefringence illustration 55
2.6 Shock refractive index illustration 60

3.1 Predicted photoelastic behaviour for calcite, sapphire and rutile 64
3.2 Various literature values for the photoelastic tensor of sapphire 64
3.3 Variation in sapphire photoelastic prediction using Monte Carlo methods 66
3.4 Calcite elastic wave surface 70
3.5 Error on birefringence prediction for sapphire 71
3.6 Biaxial refraction illustration 74
3.7 Tilt simulation illustration 75
3.8 Illustration of crystallographic tilt simulation 76
3.9 Variation in birefringence with optical axis for calcite 76
3.10 Variation in birefringence with optical axis for sapphire 77

4.1 Reverse firing breech illustration 82

4.2 Wrap around breech illustration 83
4.3 Small bore gas gun experimental setup 86
4.4 Impedance matched Hugoniots for preliminary experiments 87
4.5 Polarimeter optical setup for experiment P1 89
4.6 PDV data for experiment P1 90
4.7 PDV breadboard optical setup 93
4.8 Polarimeter optical setup for experiment P2 94
4.9 Polarimetry data for experiment P2 95
4.10 PDV data for experiment P2 96
4.11 Free surface velocity for experiment P2 97
4.12 Polarimeter optical setup for experiment P3 99
4.13 PDV data for experiment P3 100

5.1 Polarimeter static setup for large gas gun experiments 106
5.2 Polarimeter dynamic setup for large gas gun experiments 108
5.3 Detector linearity and gain measurement 110
5.4 Polarimeter calibration measurement using rotating linear input 111
5.5 Polarimeter Fast Fourier Transform (FFT) peak fitting 114

6.1 Impedance matched impact predictions for sapphire and calcite 118
6.2 Large 100 mm bore gas gun photo 120
6.3 Large gas gun breech design 121
6.4 Large gas gun timing diagram 124
6.5 Large gas gun oscilloscope triggering diagram 125
6.6 Circuit diagram for shorting pins 126
6.7 Generation zero PDV diagram 128
6.8 PDV bank B 129
6.9 Generation one PDV diagram 130
6.10 Projectile velocity PDV channel 130

6.11 Generation three PDV diagram 131
6.12 Generation three PDV diagram 132
6.13 Bare fibre oscilloscope signal with fitted sinusoid 134
6.14 Tilt calculation for calcite experiment C1 135
6.15 PDV peak fitting 138

7.1 Large gas gun experimental setup 143
7.2 Drawing of target back plate 145
7.3 Drawing of target side 146
7.4 Drawing of target front 147
7.5 Isometric projections of target 148
7.6 Large gas gun target photo 148
7.7 Short window PDV for sapphire experiment S2 151
7.8 Long window PDV for sapphire experiment S2 152
7.9 Corrected velocities from PDV spectrogram 153
7.10 Sapphire Hugoniot comparison 154
7.11 Sapphire experiment S1 polarimetry data 155
7.12 Shock birefringence measurement for sapphire 156
7.13 Sapphire polarimetry vs. PDV birefringence measurement 157
7.14 Short window PDV for calcite experiment C2 158
7.15 Long window PDV for calcite experiment C2 159
7.16 Velocities extracted from PDV data 159
7.17 Calcite Hugoniot comparison 160
7.18 Calcite elastic Hugoniot measurement 161
7.19 Polarimetry data for calcite experiment C1 162
7.20 Birefringence measurement for calcite 163
7.21 Calcite PDV vs. polarimetry birefringence measurement 164
7.22 Shocked optical axis measurements 165

8.1 Sapphire measured birefringence and comparison with prediction 170
8.2 Calcite measured birefringence and comparison with prediction 173
8.3 PDV data for calcite experiment C3 174

B.1 PDV data for experiment P1 195
B.2 Polarimetry data for experiment P1 195
B.3 PDV data for experiment P2 195
B.4 Polarimetry data for experiment P2 196
B.5 PDV data for experiment P3 196
B.6 PDV data for experiment C1 197
B.7 Polarimetry data for experiment C1 197
B.8 PDV data for experiment C2 198
B.9 Polarimetry data for experiment C2 198
B.10 PDV data for experiment C3 198
B.11 Polarimetry data for experiment C3 199
B.12 PDV data for experiment S1 200
B.13 Polarimetry data for experiment S1 200
B.14 PDV data for experiment S2 201
B.15 Polarimetry data for experiment S2 201
B.16 PDV data for experiment S3 201
B.17 Polarimetry data for experiment S3 202
B.18 PDV data for experiment S4 202
B.19 Polarimetry data for experiment S4 202

List of Tables

1.1 Sapphire literature yield values 33

1.2 Calcite literature Hugoniot inflections 36

4.1 Summary of preliminary experiments 81

4.2 Summary of preliminary experimental results 81

4.3 Dimensions of preliminary targets 85

4.4 Preliminary results summary 102

5.1 Polarimeter angular calibration values 110

6.1 Planned large gas gun experimental impact scenarios 118

7.1 Summary of 100 mm bore gas gun experiments 142

7.2 Summary of 100 mm bore gas gun experimental results 142

7.3 Geometry of samples used on the large gas gun 146

7.4 Summary of sapphire large gas gun experiments 150

7.5 Sapphire Hugoniot data 153

7.6 Summary of calcite large gas gun experiments 157

7.7 Calcite Hugoniot data 160

7.8 Optical axis measurements 165

Outputs

During the course of this thesis, work was presented at several conferences and three peer reviewed publications were produced. Posters were presented at Shock Compression of Condensed Matter (SCCM) 2013 and SCCM 2015, both leading to peer reviewed conference proceedings [1, 3]. At SCCM 2015 an oral presentation was also given, leading to the peer reviewed conference proceeding [2]. In addition, oral presentations at the Pressure Energy Temperature and Extreme Rates (PETER) 2014 and PETER 2015 conference were given, as well as an invited presentation at the University of Cambridge.

Publications

[1] G R Tear, D E Eakins, D J Chapman, W G Proud. *Technique to measure birefringence under shock compression.* In *Shock Compression Condens. Matter* 2014. Journal of Physics: Conference Series, **500**, 19 pg 2020.

[2] G R Tear, D J Chapman, D E Eakins, W G Proud. *Birefringence Measurements in Single Crystal Sapphire and Calcite Shocked Along the* a *Axis.* In *Shock Compression Condens. Matter* 2015. (accepted)

[3] G R Tear, W G Proud. *Predicting the Optical Behaviour of Shock Compressed Dielectrics.* In *Shock Compression Condens. Matter* 2015. (accepted)

Chapter 1

Introduction

Anisotropic homogeneous dielectrics are materials which have uniform anisotropic mechanical and optical properties. The uniformity requires that they be single crystals. They are electrically insulating with a negligible isotropic magnetic susceptibility. Materials such as sapphire, calcite and rutile are excellent examples and many are important geological minerals as well as significant materials in modern optics. The static material properties of these materials are well understood, with measurements of material properties from room temperature and pressure up to tens of GPa and temperature up to hundreds of Celsius in a Diamond High Pressure Cell (DHPC) common for many materials. A mathematical framework for describing quasi-static behaviour has existed for decades as outlined in chapter 2. Dynamic measurements of calcite, sapphire, and rutile exist, however there are few predictive models which compare static anisotropic literature with dynamic experimental results.

This thesis will therefore develop analytic methods for predicting the behaviour of linear anisotropic dielectric materials undergoing shock compression in chapter 2 and chapter 3. An important body of work presented in this thesis, in chapter 3, is the development of a Monte Carlo method for comparing errors in static literature with dynamic experiments. This is crucial if meaningful comparisons between static anisotropic and dynamic anisotropic experiments are to be made.

Optical anisotropy can been observed in the form of birefringence, and this technique has been employed successfully in a wide range of fields such as mineral identification and stress field analysis. In chapter 4 an experimental method measuring the birefringence of anisotropic dielectrics under shock compression is developed. Using the analysis developed and described in chapters 2 and 5 the static predictions and dynamic results can be compared. These developments extend current literature for shock compressed birefringence measurements by quantifying shocked birefringence of calcite for the first time, and gaining an order of magnitude precision in the measurement of sapphire shocked birefringence. This work has lead to the publication of several papers [1, 2, 3].

Finally a series of experiments was undertaken on sapphire and calcite, the results of which are presented in chapter 7. Comparison of these results with static literature predictions developed earlier in the thesis are made and discussed in chapter 8.

1.1 Background

The dynamic behaviour of materials is an extensive field, with the rate of deformation, or strain rate, an important aspect of the material response. At the high strain rate limit is the shock wave. This non-linear phenomena occurs when a material is compressed rapidly enough to cause a discontinuity in the material. Rather than a smooth increase in state variables, there exists a sharp shock wave which propagates through the material causing the transition from one thermodynamic state to another, across a boundary of the order of nanometres in thickness [4].

Using techniques such as those in Courant and Friedrichs [4] it is possible to relate the state variables on one side of a shock wave to those on the other using conservation of mass, momentum and energy. However the measurement of the response of a specific material at high strain rate is required to give predictable and repeatable results for that material. Given a known impact velocity and material response, the shocked state variables can be accurately and reproducibly predicted with the range of previously measured

values.

However, at present there are very few materials for which the material state post-shock can be predicted *without previous measurement*. Predicting the shock state of a material, purely from static measurements, has only been achieved in a handful of cases for very simple materials. The effect of dislocations, phase changes, non linear interactions, grain boundaries, crystallographic texture, temperature and anisotropy have all been identified as processes which contribute to the shock response and hence need to be understood in order to form predictive models.

1.1.1 Anisotropic Shock Experiments

This is not a simple topic as anisotropy simply means a directional dependence to some physical property. The nature of anisotropy is varied, and often closely associated with other physical processes. For example, anisotropy can be caused by anisotropic crystal lattices, however in a polycrystalline sample the orientation of crystal grains may be random and in this case no bulk anisotropy is expected. Typically crystal grain orientation is not random and there is crystallographic texture from machining processes, so there is a residual bulk anisotropy. This bulk anisotropy is related to the underlying crystal symmetry and some function of the degree of crystallographic texture. As a shock wave propagates through such a polycrystalline material (for example magnesium or titanium), the shock front will pass through a crystal in one orientation, then through another in a different orientation.

How does the anisotropy of a material such as that above affect the process of shock propagation? As well as the crystal anisotropy, there are wave reflections at boundaries to consider and the wave reflections will propagate in shocked material so material deformation must be considered. Separating these physical processes is technically challenging, and whilst numerous studies of anisotropy in shock compression have been made, only in the past ten years have studies of single crystal and bi-crystal metal samples started to shed light on this convoluted problem. Anisotropy has become a major direction of

current research in the field of shock compression and as metals are the predominant material of choice due to their direct engineering applications, studies of single crystal metals have been conducted.

Single Crystal Metals

The recent development of both single crystal metal growing techniques and laser shock compression have allowed a range of single crystal metals to be studied at high strain rate. Single crystal metal samples such as tantalum [5], copper [6], and copper-aluminium alloy [7] have been investigated. Tantalum is Body Centred Cubic (BCC) at ambient pressures and temperatures, whilst copper is Face Centred Cubic (FCC). Both are cubic and so their elastic symmetry is identical, however FCC has many more cross slip directions, so is significantly more ductile. In the shock regime, copper is therefore expected to be more isotropic, and indeed the solid Hugoniot differs with orientation by an amount lower than the experimental error. However the melt point of shock compressed copper was observed by Budzevich *et al.* [8] to vary by up to 20% in longitudinal stress with orientation. For BCC tantalum there is a strong directional dependence on plasticity modes, with recovered samples showing twinning in the [1 2 3] orientation, whilst not at all in [0 0 1] [9].

Single crystal metal shock compression experiments have both been studied at millimetre scale with laser shocks [5, 6] and centimetre scale with gas gun shocks [10]. The investigation into single crystal metals has been continued by studying a shock propagating across the boundary of two crystals by Cao *et al.* [6]. This work begins to address the problem of how variation in a metal's microstructure gives rise to observed variations in dynamic mechanical properties. The experimental work is combined with elastic wave mechanics to understand the role of grain boundaries on the reflection and refraction of elastic shock fronts by Loomis [11] and Cao *et al.* [6]. Elastic wave models have been developed and compared to more traditional finite element models [11]. It would be desirable to investigate the behaviour of a grain boundary directly, given that *in situ*

methods for opaque materials are limited, optically transparent non-metallic materials offer an opportunity to investigate this.

Single Crystal Non-Metals

Naturally occurring materials (both geological and biological) often show a high degree of anisotropy, with material properties such as elastic wave speed varying by up to 50% with orientation [12]. However, the extension of single crystal shock compression experiments into non-metals is limited, in part due to the dominance of porosity in the behaviour of rocks and other geological materials. Whilst much research has been carried out into geological materials under shock compression, driven by the mineral extraction industry as well as a research desire to understand planetary impact phenomena, few single crystal samples have been studied in the recent literature. Early research on single crystal dielectrics is somewhat more extensive, but has not been updated with modern diagnostics.

In calcite the variation in the Hugoniot has been measured by Ahrens and Gregson [13] for x, y, z, and cleavage cut single crystals. The complex phase structure of calcite and highly anisotropic single crystals showed an anisotropic shock velocity particle velocity Hugoniot, but little difference in the Hugoniot inflections indicating phase transformation stresses are isotropic. At low final pressure states, below 10 GPa, the difference in wave velocities is around 2 km s^{-1} however at a high final state around 25 GPa there was no discernible difference.

1.1.2 Numerical Models

Numerical modelling of material deformation is a significant aspect of shock physics. It is important to have material models that can be used to predict the behaviour of a material under large strain and high strain rates. The hydrodynamic approximation is an effective approximation that assumes a strengthless isotropic fluid. For materials such as copper that are FCC the high ductility and isotropic yield are well approximated by a

fluid. Broadly their are two, closely related, forms of anisotropy to consider in numerical modelling: The material's elasticity, and the material's strength or yield surface. In a similar scenario to that described at the beginning of section 1.1, separating the effects of elasticity and yield in a dynamic experiment is technically challenging.

Strength

The introduction of material strength to the hydrodynamic model has been highly successful in the case of ductile materials which can be assumed to be elastic perfectly plastic, leading to accurate predictable behaviour in many metals by simply measuring their static yield stress. The effect of strain rate and strain hardening in materials which are not perfectly plastic has been included in models such as the Johnson-Cook strength model [14]. The Johnson-Cook model is empirical however, requiring the measurement of a material at high strain rate, and offers no predictive extrapolation. Zerilli and Armstrong [15] attempted to rectify this problem and developed a crystal structure dependant strength model, allowing the prediction of plasticity and hardening based on the materials crystal structure. The model does however still require some material dependant constants to be measured at higher strain rates.

The strength models discussed have been isotropic, and build on the isotropic hydrodynamic approximation. The extension of strength models into anisotropic materials has been attempted, however they tend to have a hydrodynamic shock approximation underneath. Recent dislocation dynamics models by Shehadeh *et al.* [16] make use of the material's anisotropic elasticity to predict anisotropic plasticity. Because of this, anisotropic elasticity is key to understanding the plastic response.

Elasticity and Yield

Plastic flow or yield occurs when a material can no longer support a shear stress. The critical shear stress τ_c required to cause yield can be plotted as a function of the stress tensor's principle stresses σ_1, σ_2, and σ_3 with the highest shear stress being $\sigma_1 - \sigma_3$. This

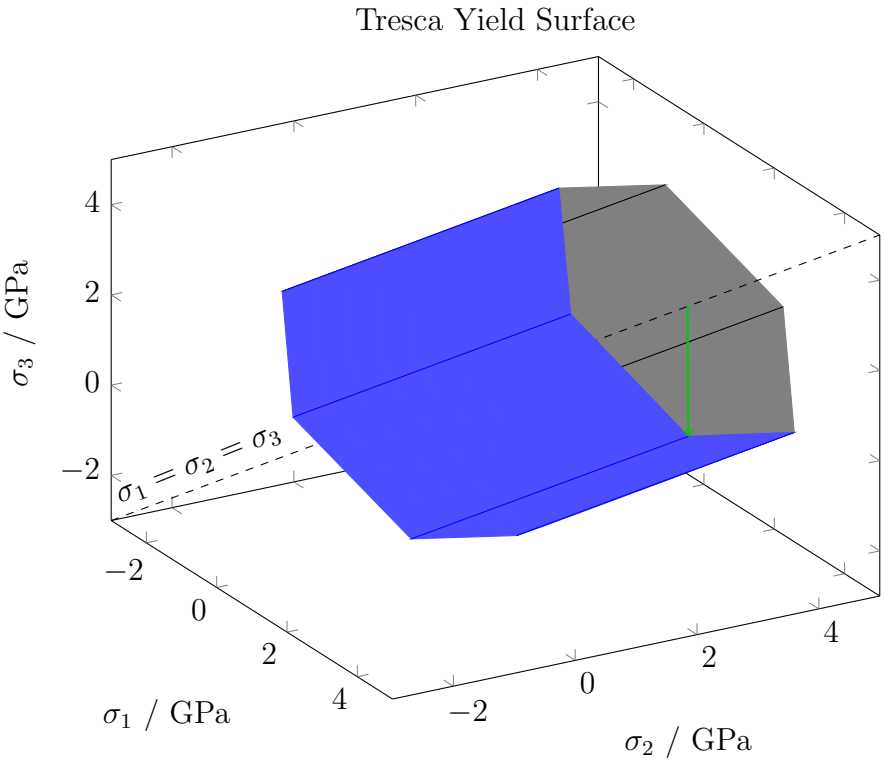


Figure 1.1: An example yield surface using a condition of maximum shear (Tresca) plotted on the principle stress components of the stress tensor. Under hydrostatic compression the load follows the hydrostat ($\sigma_1 = \sigma_2 = \sigma_3$), any shear stress is represented by a departure from this line (for example the green arrow). If the total shear or deviatoric stress exceeds a given critical value (represented by the surface) the material will yield.

surface is plotted in figure 1.1.

Given the close relationship of elasticity with the yield surface it seems important to develop anisotropic elasticity models for shock compression. The experimental work on single crystals in section 1.1.1 has been complemented by recent developments that include the non-linear component of elasticity, and recently Clayton [17] have developed an anisotropic Finite Element Method (FEM) model and applied it to aluminium [18]. Clayton [19] also applied this model to single crystal sapphire, quartz and diamond to compare to literature data, finding good agreement at the 1% level.

Polycrystalline samples with anisotropic crystals, and how the crystallographic microstructure affects macroscopic material behaviour is also of interest. Anisotropic wave propagation at a crystal boundary has been studied by Loomis [11] and this work is closely related to studies of non-uniformity in the shock front by Furnish *et al.* [20].

Case and Horie [21] have implemented a numerical model demonstrating that shock front heterogeneity occurs from polycrystalline samples. The anisotropy in the single crystals gives rise to a distribution of particle velocities at the shock front.

1.1.3 Concluding Comments about Anisotropic Materials

In general there is a lack of a consistent description of anisotropy in shock physics. There are many physical processes taking place in a propagating shock wave, and most of them can have a degree of anisotropy. Identifying the key anisotropic processes is an active challenge, and this challenge has recently become more achievable with single crystal and bi-crystal metal shock experiments. It would be beneficial to directly measure a bi-crystal boundary so that anisotropic models being developed to include anisotropy at a crystalline length scale can be validated effectively for application to polycrystalline samples. This measurement has been achieved with isotropic studies using an optical window [22, 23].

The advantages of using optically transparent materials is offset by the lack of specific validation of optical models with respect to arbitrarily orientated anisotropic single crystal dielectrics. Optical models for shocked dielectrics available in the literature are a fit to an isotropic model for a specific direction of an anisotropic material [22, 24, 25]. With good optical models for anisotropic dielectrics, verification of assumptions such as zero slip across a grain boundary can be studied. A discussion of optical models available in the literature is presented in section 1.2.

1.2 Optical Measurements

Optical measurements are extremely important in shock physics as they allow measurements to be made on the nanosecond timescale. Events, such as elastic precursor decay, occur over tens of nanoseconds so in order to study these processes, it is necessary to use optical techniques. The most common use of optical measurements in shock physics is to

measure the velocity of a surface. Usually this optical velocimetery is performed at the rear surface of the target. This means the material is fully released to ambient pressure on measurement. To make a velocimetery measurement at pressure an optical window is placed on the back of the sample to confine the material, maintaining a shock state at the sample – window interface that is above ambient pressure. Optical measurements at the sample – window interface must pass through the optical window, requiring an understanding of the window's optical properties under shock loading.

There are several optical techniques other than velocimetery. Polarimetry measures the polarisation state of light. This can be used in ellipsometry to measure the dielectric properties of shocked materials. Pyrometry and reflectometry can measure the temperature of a shocked surface.

1.2.1 Optical Velocimetry via Interferometry

Optical velocimetry measurements rely on an interferometer to measure velocity. This can be a Michelson interferometer with one arm as the target and a reference arm, however numerous problems with such a system have lead to the development of Photonic Doppler Velocimetry (PDV) by Strand *et al.* [26] and the Velocity Interferometry System for Any Reflector (VISAR) by Barker and Hollenbach [27].

Velocity Interferometry System for Any Reflector

The VISAR has been a standard velocimetery technique since 1972 [27]. Light collected from the target surface enters a Mach-Zenner interferometer with an optical etalon in one path, delaying the light in one path by several nanoseconds. If the path length to the target is changing with time, then the phase of light in one arm of the Mach-Zenner is different to the other, and interference fringes move. The degree of fringe movement is proportional to the velocity of the target, making this interferometer a direct velocimeter.

Photonic Doppler Velocimetry

With the development of fibre optic based telecommunications in the 1990s there has been mass production of stable high power fibre optic lasers operating at 1550 nm as well as high bandwidth detectors and digitizers of 10 GHz and higher allowing sub-nanosecond resolution. This technology has been used by Strand *et al.* [26] to create a fibre based Michelson interferometer which is sensitive to velocities up to 10 km $s^{-1}$and stable over path length changes of kilometres. This velocimeter actually directly measures displacement of the target surface, however it is usually analysed to find velocity.

Window Attributes

In order to conduct such experiments effectively the optical properties of the window must be measured and accounted for to avoid systematic errors in any results. Barker and Hollenbach [22] measured the refractive index of sapphire, PMMA and fused silica. They found that a Gladstone-Dale relationship described the refractive index of PMMA and fused silica well and presented a modified Gladstone-Dale for sapphire. The Gladstone-Dale relationship in equation 1.1 is a linear isotropic relationship between density ρ and refractive index n using a density constant D and refractive index constant n_0.

$$n = \rho D + n_0 \tag{1.1}$$

All interferometry systems rely on the phase difference between the reference and target paths, and anything which changes this (not necessarily the target) will be detected. An optical window will affect the path length and so the apparent velocity measured by the interferometer will be different to the actual velocity. The work by Barker and Hollenbach [22] measured the shock refractive index of PMMA, fused silica and sapphire to calculate this velocity correction for these materials. Recently some of these results have been repeated for PDV which operates at different optical wavelengths.

Window corrections for VISAR are numerous and are provided between 514.5 nm and

633 nm depending on the wavelength of the laser used in the VISAR system. Sapphire, fused silica and PMMA were measured at 633 nm by Barker and Hollenbach [22] and a Gladstone-Dale model was fitted to PMMA effectively. A modified Gladstone-Dale model was used for *c*-cut sapphire. Barker and Hollenbach [22] also showed mathematically that if the window's refractive index density relation was linear, as is the case for a Gladstone-Dale model, then for an arbitrary volumetric compression of the material, no velocity correction was needed. More recently *a*-cut sapphire has been measured at 514.5 nm by Jones *et al.* [24] and some photoelastic tensor components were fitted and compared to static literature. Jones *et al.* [28] also measured *c*-cut sapphire in tension as well as compression at 532 nm, finding a different Gladstone-Dale relation for tensile strain compared to compressive strain. *z*-cut quartz has been measured at 514.5 nm by Jones and Gupta [25] and LiF [1 0 0] has been measured by LaLone *et al.* [29] at 532 nm under re-shock and ramp loading conditions, finding also that a Gladstone-Dale model was sufficient.

Window correction measurements for PDV have been performed for the same materials as for VISAR. PDV operates at 1550 nm and due to this wavelength difference, dispersion can be a substantial effect when comparing VISAR and PDV window correction measurements. PDV window corrections for LiF, *z*-cut quartz and *c*-cut sapphire at 1550 nm have been measured by Jensen *et al.* [30] along with VISAR at 532 nm for comparison. PMMA has been measured by Chapman *et al.* [31], and the Gladstone-Dale model was found to be sufficient again. Whilst the constants in the correction factors change with wavelength, the change is small for *c*-cut sapphire, and in all cases the linear isotropic form of the optical model remained the same.

1.2.2 Polarimetry

The measurement of polarisation under shock compression has largely been limited to ellipsometry. Ellipsometers have been developed for shock physics applications such as detecting phase changes [32] or measuring the complex dielectric constant of a metal under

pressure. Birefringence is a material property which causes a change in the polarisation of a light wave propagating through the material, however few direct measurements of birefringence under shock compression have been made. Birefringence measurements on *a*-cut sapphire by Jones *et al.* [24] are due to a polarised VISAR, and a dedicated polarimetry measurement was not performed.

Ellipsometry

The ratio of reflected polarisations from a dielectric boundary is related to the complex dielectric constant in the two materials at the boundary. Measurements of this under shock compression have made use of polarimetry to make ellipsometry measurements. Ellipsometry has been carried out extensively for laser shocks [33] and also on gas gun driven experiments [34]. Ellipsometry requires an oblique incidence measurement at a confined interface, requiring an optical window and given that even an isotropic window material will become birefringent in the shock direction when it is compressed, this has lead to measurements of shock induced birefringence in LiF by Nguyen and Holmes [35].

Birefringence

Few measurements of birefringence under shock compression have been made. A value can be obtained from Jones *et al.* [24] for *a*-cut sapphire, however most birefringence observations have been used to look at the shape of stress fields. This approach uses birefringence to identify lines of constant stress, highlighting the shape and wave positions rather than the actual quantitative stress measurement. Field *et al.* [36] provide a review of these methods, however the experimental technique is focused on imaging, and so is not as relevant to this thesis.

Whilst Nguyen and Holmes [35] have quantitatively measured birefringence in shock compressed LiF this is the birefringence induced in the direction of shock propagation. LiF is not anisotropic at ambient conditions, and so an anisotropic photoelastic model is not required to describe its optical behaviour. Anisotropic materials which are birefrin-

gent prior to impact have not been studied in a systematic way.

1.2.3 Optical Anisotropy

As c-cut sapphire has been extensively used as a window material its optical properties under compression along the c-axis are well measured. The c-axis is its optical axis so sapphire is not birefringent in this direction, making isotropic optical models suitable. The standard relation is the modified Gladstone-Dale relationship by Barker and Hollenbach [22]. For small compressions of sapphire the apparent behaviour is a negative refractive index density relation which is unusual, as the electron density is likely to be increasing with density which usually increases the refractive index of the material.

The difference in the velocity correction for a-cut sapphire measured by Jones *et al.* [24] (1.896 ± 0.005) compared to c-cut sapphire measured by Setchell [37] (1.786 ± 0.005) is the first indication of the effect of photoelastic anisotropy. Both papers fit linear models to each direction, however a general anisotropic material can be described by a photoelastic tensor, which is an anisotropic generalisation of the Gladstone-Dale relationship. The photoelastic tensor can have negative components so long as it is overall positive definite [38], allowing a negative density refractive index response in particular directions, whilst overall increasing the electron density.

Combining optical anisotropy with mechanical anisotropy would allow a consistent anisotropic model for optical window materials in shock physics. This would support current research into single crystal metal samples discussed in section 1.1.1, both directly by extending into non-metal single crystal samples, and by opening the possibility of an optical window bi-crystal experiment. Using anisotropic optical windows would allow direct velocimetry measurement of a bi-crystal interface in a similar experiment to those already standard in isotropic materials, discussed in section 1.2.1.

An in-depth review of anisotropic dielectrics will follow, and suitable materials will be identified for this thesis.

1.3 Mechanical Properties of Homogeneous Anisotropic Dielectrics

We now turn to optically transparent dielectrics which are both mechanically and optically anisotropic, and are single crystals so that the anisotropy is homogeneous throughout the material. Materials that are ionically bonded have large band gaps giving rise to transmission in all optical frequencies, satisfying the optical transparency criteria. More complex crystal structures, often with covalently bonded ions, give strongly anisotropic materials and these can be found naturally in many minerals. Single crystals of these minerals can either be grown synthetically or mined from a deposit.

Single crystal minerals often have impurities which lead to specific absorption bands and their value as gem stones. Sapphire and ruby are two examples of α-corundum or Al_2O_3 with different lattice inclusions or dopants (Chromium in the case of ruby) giving rise to a deep blue or red colour respectively. In synthetic sapphire (which this work will be interested in) there are lower levels of impurity and as such the sapphire is colourless. Calcite is a compound of calcium Ca^{2+} and a carbonate $CO_3{}^{2-}$ ion. As the carbonate ion has three fold planer symmetry the crystal has a lower symmetry than might be expected. Rutile is a titanium dioxide allotrope with slightly higher symmetry than calcite or sapphire. These mineral crystal structures are shown in figure 1.2.

1.3.1 Sapphire

The homogeneous anisotropic dielectric that has been most extensively studied under shock compression is sapphire. This is largely due to its suitability as an optical window material having a large Hugoniot Elastic Limit (HEL) and high shock impedance [22]. Whilst sapphire belongs to the trigonal group $\overline{3}\frac{2}{m}$ it is not strongly anisotropic. The variation in its elastic waves speeds is no more than 10% between different orientations, observed in shock compression by Kanel *et al.* [39] and statically by several authors but most notably Tarumi *et al.* [40]. Furthermore sapphire is also well studied under static

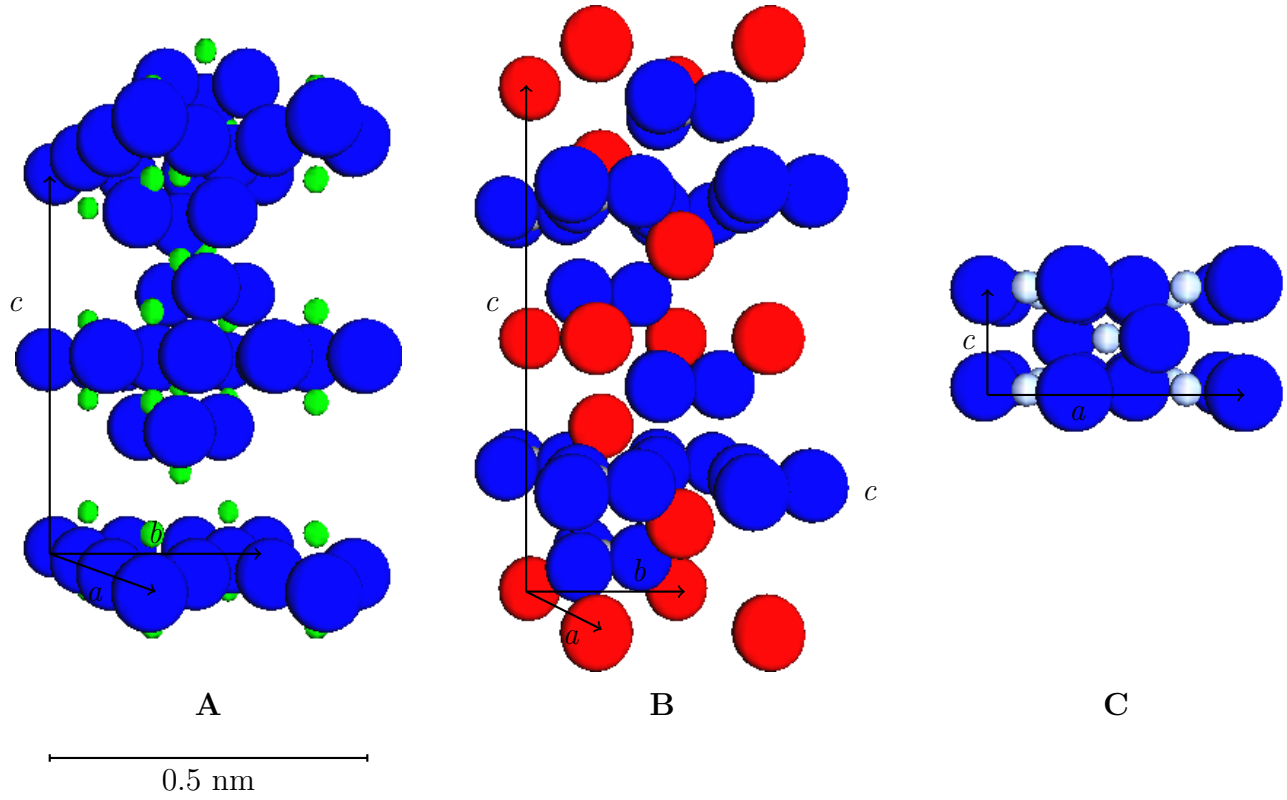


Figure 1.2: To scale crystal structure of **A** Sapphire, trigonal symmetry space group $\overline{3}\frac{2}{m}$, **B** Calcite, trigonal symmetry space group $\overline{3}\frac{2}{m}$ and **C** Rutile, tetragonal symmetry space group $\frac{P4_2}{mnm}$. The blue spheres are oxygen ions, red are calcium ions, green are aluminium ions and grey are titanium ions.

Reference	Orientation	Longitudinal Yield Stress Min / GPa	Max / GPa	l / mm
Graham and Brooks [42]	$\langle 0\,0\,0\,1\rangle$	14	21	6 - 13
	$\langle 1\,0\,\bar{1}\,0\rangle$	13.5	18	6 - 13
	$\langle 1\,1\,\bar{2}\,3\rangle$	12	16.5	6 - 13
Kanel *et al.* [39]	$\langle 0\,0\,0\,1\rangle$	16	24.2	5
	$\langle 1\,0\,\bar{1}\,0\rangle$	15.1	22.3	5
	$\langle 1\,1\,\bar{2}\,3\rangle$	12.4	14.1	5
	$\langle 1\,0\,\bar{1}\,1\rangle$	13.6	20.9	5
Mashimo *et al.* [44]	$\langle 1\,\bar{2}\,1\,0\rangle$	14.4	17.3	2.8 - 4.028
	$\langle 0\,0\,0\,1\rangle$	14.6		3.007

Table 1.1: Literature values for sapphire yield stresses. Measured using rear surface velocimetry data collected with a VISAR. Thinner sample thicknesses have a higher HEL due to elastic precursor decay. Errors on values are to the last significant figure.

and quasi-static conditions. The elastic matrix has been measured by Tarumi *et al.* [40], Gladden *et al.* [41] using elastic wave speeds in different crystal orientations.

The mechanical behaviour has been studied above the HEL extensively by Kanel *et al.* [39], Graham and Brooks [42] and in the elastic regime by Jones *et al.* [28]. There is some disagreement over the HEL, due to variation in sample size. As the shock wave propagates the HEL reduces, observed as the decay of peak elastic stress in the elastic precursor with time. This phenomena is known as precursor decay and was extensively studied by Gupta *et al.* [43] in $\langle 1\,0\,0\rangle$ LiF. Because of precursor decay the variation in HEL observed in different crystallographic orientations is no greater than differences observed for the same orientation. For example the HEL is typically quoted at 12 GPa for c-cut sapphire, though some measurements as high as 19 GPa have been observed by Graham and Brooks [42] in thinner samples. Kanel *et al.* [39] observed a scatter in the HEL at intermediate strains of 12 GPa to 19 GPa which is also consistent with Graham and Brooks [42]. HEL values of 18 GPa have been stated for a-cut sapphire [28] however Kanel *et al.* [39] have found values as low as 11 GPa for a-cut. The summary of HEL data for sapphire from several sources is presented in table 1.1.

The general phenomenon of reducing HEL with sample thickness is known as precursor decay and is not a property related to sapphire's anisotropy. This highlights the difficulties

isolating anisotropic behaviour in dynamic material response, first discussed in section 1.1.

1.3.2 Calcite

Calcite has been studied extensively, but not to the same degree as sapphire in recent years. It has a complex phase structure with two distorted metastable phases of calcite and a high pressure aragonite phase. Bridgman [45] found that under static compression the trigonal calcite distorts to a monoclinic [46] calcite-II phase, and under further compression becomes a monoclinic [47] calcite-III phase. With heating, both calcite-II and calcite-III phases will transform to the stable orthorhombic aragonite phase, indicating a kinetic barrier to forming aragonite.

The calcite – calcite-II transition occurs at a mean stress of around 1.3 GPa in a DHPC first measured by Bridgman [45]. The calcite-II phase is a monoclinic distortion of the calcite lattice, and the calcite-II crystal structure was indexed by Merrill and Bassett [46]. Measurements of the rarefaction shock produced by release through a phase transition by Grady [48] found an anomalous unloading before the rarefaction shock, which was unexplained in the paper. A reanalysis of Grady [48] by Stapleton [49] attributed a wave at 2 GPa to elastic reflection from the calcite – calcite-II transition second wave. This brought Grady [48] into line with both Stapleton [49], Ahrens and Gregson [13] for c-cut calcite. Other orientations of calcite have not been studied under shock compression since Ahrens and Gregson [13].

There is great interest in carbonate based materials from the extraction community due to the presence of oil in carbonate layers. However in the shock regime by far the dominant aspect of these materials is their inhomogeneity and porosity. The anisotropy of the individual grains in a polycrystalline porous rock does not play an important role in their shock behaviour when compared with porosity. Because of the insignificance of anisotropy in rock samples compared with porosity, recent studies focus much more heavily on polycrystalline samples with a move away from the behaviour of individual single crystals [50].

Whilst the calcite shock impedance is much lower than sapphire with a density around half of sapphire at 2.71 g cm^{-3} and a sound speed around two thirds at 7.4 km s^{-1}, it is of the same symmetry group, $\overline{3}\frac{2}{m}$. As such the symmetry of its mechanical and optical properties are identical. This makes it a natural extension of any work focused on anisotropic dielectrics that started with sapphire. The variation of mechanical properties with direction is much greater in calcite than for sapphire. The longitudinal sound speed varies from 7.4 km s^{-1} along the *a*-axis to 5.2 km s^{-1} along the *c*-axis. It has been well studied under static and quasi-static regimes with its elastic tensor components measured by Dandekar [12], Peselnick and Robie [51], Kaga [52] and calcite's photoelastic components measured by Nelson *et al.* [53].

However calcite has not been studied to the same degree under shock compression as sapphire. Early inclined mirror measurements by Ahrens and Gregson [13] gave Hugoniot data for single crystal calcite in *a*-cut (shown in figure 1.3), *c*-cut and cleavage cut orientations as well as polycrystalline samples. They observed a Hugoniot inflection visible in figure 1.3 at 1.4 GPa mean stress, which they attributed to the HEL. The most recent single crystal measurements by Grady [48], Stapleton [49] only performed experiments on *c*-cut calcite, and attributed the first inflection to the calcite – calcite-II phase transformation. The mean stress of the calcite – calcite-II transformation does not appear to change with orientation based on the work of Ahrens and Gregson [13]. Optical measurements of calcite have not been performed under shock compression in any orientation. A summary of single crystal work is given in table 1.2.

The results from shock compression have been compared to static high pressure results by all authors. Ahrens and Gregson [13] compared sound speeds with the ultrasound measurements of Peselnick and Robie [51] and found discrepancies of up to 5.5%. This discrepancy increases with more recent ultrasound measurements by Dandekar [12]. Aidun [50] used pressure-shear experiments to measure strength in shock compressed Carrara marble, and compared results with static high pressure strength measurements by Wang [54]. Stapleton [49] concluded that the calcite – calcite-II transition occurred at a density

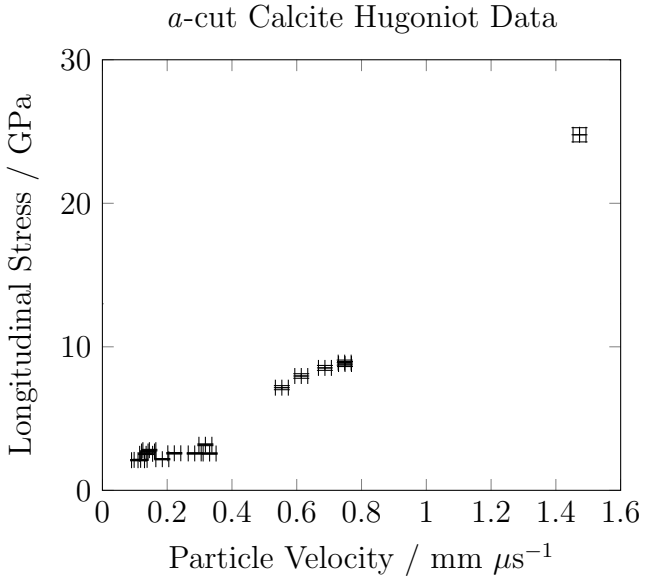


Figure 1.3: Hugoniot for a-cut calcite taken from Ahrens and Gregson [13] plotted in the stress particle velocity plane. There are three inflections, two very close at longitudinal stresses of 1.7 GPa and 1.9 GPa, and a third at 7 GPa, 600 m s^{-1}. These inflection points in a Hugoniot usually indicate either an elastic-plastic transition or a phase change.

		Mean Stress		
Reference	**Orientation**	**HEL / GPa**	**Peak / GPa**	l_0 **/ mm**
Stapleton [49]	$\langle 0\,0\,0\,1 \rangle$	1.38 ± 0.04		6 - 12
Grady [48]	$\langle 0\,0\,0\,1 \rangle$	1.5 ± 0.2	11.5 ± 0.5	5.08
Grady [48]		1.5 ± 0.2	17.9 ± 0.5	3.02, 5.05, 8.03
Grady [48]		Not Observed	26.4 ± 0.5	2.07, 6.10
Ahrens and Gregson [13]	$\langle 0\,0\,0\,1 \rangle$	1.4 ± 0.1	10	
Ahrens and Gregson [13]	$\langle 1\,0\,\bar{1}\,0 \rangle$	1.4 ± 0.1	10	

Table 1.2: Previous literature values for the first Hugoniot inflection of calcite single crystals. There was no observable variation in the mean stress of the inflection with different sample thicknesses in [48, 49].

compression of 2.1%, in order to explain the transition pressure discrepancy of 0.15 GPa between hydrostatic and shock compression results.

Despite there being no single crystal calcite shock experiments reported since 1990, there has been continued interest in single crystal calcium carbonate in the static high pressure community. Calcium carbonate decomposes into lime and carbon dioxide under pressure, and this process is of interest to planetary and climate scientists interested in studying the role of carbon dioxide in planetary processes. The behaviour of calcite under pressure is therefore a key research direction. Biellmann *et al.* [55] successfully quenched calcite-II to room temperature. Using electron diffraction, the monoclinic crystal structure of calcite-II proposed by Merrill and Bassett [46] was confirmed. Van Valkenburg [56] observed phase transition boundaries propagating through calcite rhombs in a DHPC, observing at least two transformation directions for calcite – calcite-II. Van Valkenburg [56] also attributed the calcite-II – calcite-III transition to a nucleation and growth mechanism where domains of calcite-III spontaneously nucleate and grow into the surrounding calcite-II crystal, however the original calcite single crystal was obtained after unloading.

Below a density compression of 2.1% it is expected that the calcite will remain as calcite-I and be entirely elastic. The photoelastic behaviour measured by Nelson *et al.* [53] should therefore be linear up to this level of compression. Given that calcite-II and calcite-III are optically transparent, any phase transformation may leave the crystal transparent, or may occur in a way which scatters light, leading to opacity. Either way, calcite above 2.1% density compression is likely to be optically non-linear, so experiments should be kept below this level of compression.

1.3.3 Other Materials

Other anisotropic dielectrics which are well studied statically include rutile and quartz. Rutile is of a slightly higher symmetry group than sapphire, rutile being tetragonal $\frac{P4_2}{mnm}$. Quartz is also anisotropic but is similar to sapphire in having only slight variations in its material properties with orientation.

1.4 Optical properties of Homogeneous Anisotropic Dielectrics

The photoelastic tensor is the anisotropic generalisation of the galdstone dale optical model defined in equation 1.2. For many anisotropic dielectrics this tensor has been numerically measured at room temperature and pressure.

$$\eta_{ij} = p_{ijkl}\varepsilon_{kl} + \eta_{0\ mn} \tag{1.2}$$

1.4.1 Sapphire

The photoelastic properties are also statically measured by Chistyi *et al.* [57], Balzaretti *et al.* [58], Davis and Vedam [59]. Whilst no direct prediction of shocked optical properties from static optical properties has been put forward, extensive experimental measurements, both dynamic and static, with a variety of experimental techniques make it a material of choice against which to benchmark any new diagnostic techniques.

Early optical measurements in c-cut sapphire under shock compression were made by Barker and Hollenbach [22], Setchell [60], measuring the shock refractive index at 513 nm. More recent optical measurements have measured the shock refractive index in the a-cut direction [24], r-cut direction [61], in tension [28] and at 532 nm by Hayes *et al.* [62].

1.4.2 Calcite

Whilst there are several studies of calcite's quasi-static optical properties, there are no shock compression studies. Measurements of refractive indices in DHPC have given their pressure dependence up to 0.7 GPa [63]. Furthermore calcite's photoelastic tensor has been measured using Brillion scattering by Nelson *et al.* [53] and both results are in close agreement, well within error.

1.4.3 Other Materials

Quartz however also shows circular birefringence, making optical modelling and measurement more difficult as a photoelastic tensor is insufficient to fully describe its behaviour. Availability of single crystal rutile is limited, and both these materials have been excluded from the experimental part of this study.

1.5 Context of This Work

There has been no in-depth study of the validity of a quasi-static photoelastic model when applied to anisotropic dielectrics undergoing shock compression. In order to carry this out it is necessary to build a prediction for the behaviour of optically anisotropic dielectrics under uniaxial strain, and this will be carried out in chapter 2. Experimental validation will be presented in chapter 7. Due to the number of variables needed to describe anisotropic materials, and the experimental error in measuring each variable, a numerical approach is applied to the error analysis. This will be discussed in chapter 3.

This thesis expands an area of dynamic mechanical behaviour into optically transparent, highly anisotropic materials. Recent investigations into single crystal metals discussed in section 1.1.1 would be complemented by optical window measurements to investigate anisotropy at a crystal boundary under pressure. However optical window models, similar to those of Barker and Hollenbach [22] for velocimetry, have not been developed for anisotropic materials in a way which is consistent with anisotropic elasticity models currently in development, discussed in section 1.1.2. By investigating the optical properties of homogeneous anisotropic dielectrics and how the optical properties change under compression, further investigations can be undertaken into studying more complex systems. For example transparent bi-crystals can be used to study grain boundary conditions to give insight into dynamic behaviour or optically anisotropic windows can be used for ellipsometry measurements similar to those of Nguyen and Holmes [35].

1.5.1 Research Objectives

1. Extended the isotropic Gladstone-Dale optical model for shock compressed optical windows to include anisotropic homogeneous dielectrics using a photoelastic model. Furthermore use this model to predict birefringence of single crystal anisotropic dielectrics under high strain rate elastic compression.

2. Develop a method of measuring birefringence in a shock compressed sample, and validate this method against literature measurements.

3. undertake a series of experiments to verify the birefringence predictions of item 1 by measuring the birefringence of various single crystal dielectrics using the method developed for item 2.

Chapter 2

Prerequisites for Shock-Wave Studies of Anisotropic Materials

Development of mathematical expressions relating physical quantities such as strain, refractive index and shock velocity is required in order to test the validity of theoretical relationships between them. These derived relationships will then be tested experimentally in chapter 7. For anisotropic dielectric materials, their material properties can be represented by tensors to include directional dependence.

This chapter will describe the mathematical representation of anisotropic dielectrics, both their optical and mechanical behaviour. As there is no literature available on the combination of static mechanical and photoelastic tensors with dynamic one dimensional strain, this chapter will also develop relationships between measurable quantities under dynamic compression, such as birefringence Δn, particle velocity u_p and shock velocity U_s, with the mechanical and optical tensors. This is significant as there are numerous static measurements of the mechanical and optical tensors for many anisotropic dielectrics, so the development of a theoretical relationship between the tensor quantities and dynamic measurements will allow the comparison of dynamic and static photoelastic data for anisotropic dielectrics. The relationships developed in section 2.6.1 will form the basis of the analysis performed in chapters 3 and 6.

2.1 Treatment of Steady Shock Waves using the Jump Equations

2.1.1 The Jump Equations

The standard jump equations for a steady one dimensional shock travelling into stationary material at zero pressure are given in equations 2.1-2.3. These equations are derived from the conservation of mass, momentum and energy in Courant and Friedrichs [4]. The key variables in the shocked region are pressure P and density ρ. The jump equations relate these quantities to the shock velocity U_s, particle velocity u_p and the original density ρ_0. The change in internal energy ΔE is calculated by considering the work done by the shock wave.

$$P = \rho_0 U_s u_p \tag{2.1}$$

$$\rho_0 U_s = \rho(U_s - u_p) \tag{2.2}$$

$$P u_p = \rho_0 U_s (\frac{1}{2} {u_p}^2 + \Delta E) \tag{2.3}$$

Whilst equations 2.1-2.3 are derived without material dependence, it is necessary to have a fourth material dependant equation relating two of the variables. This is called a material's Hugoniot and is usually expressed in terms of shock velocity and particle velocity. In an impact the pressure and particle velocity must be continuous across the boundary, so it is necessary to solve the two materials' Hugoniot equations for the pressure particle velocity point for a given impact velocity.

For materials with strength, elastic shocks travel at the longitudinal wave speed found in equation 2.10. This gives the shock velocity for the jump equations. At yield, the material behaves plastically, and assuming a perfectly plastic response (no hardening) then using Davison and Shahinpoor [64] an elastic plastic Hugoniot is found. For Copper, Magnesium, Aluminium and PMMA using Marsh [65] the material Hugoniots are plotted

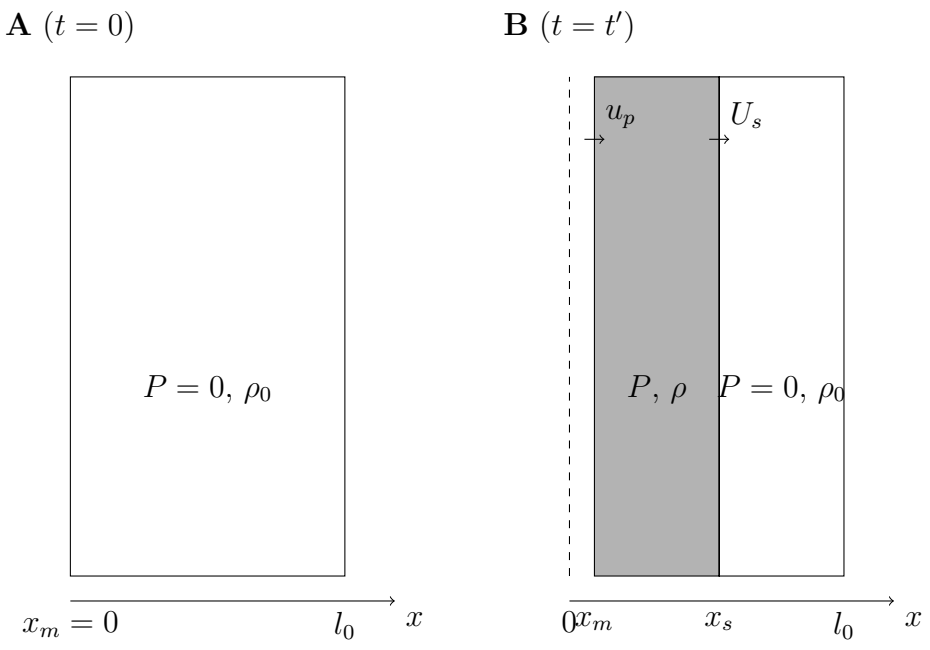


Figure 2.1: A single steady shock wave. **A** represents the pre-shock state where the material is at zero pressure and its original density ρ_0. An impact from the left hand side starts the material moving and at some time t' the material is represented by **B**. The material in the shaded region is moving at a velocity u_p and the region is expanding into the unshocked (unshaded) region at a velocity U_s. The material has been compressed, so the original position of the left hand side of the sample at $x = 0$ when $t = 0$ is now at x_m.

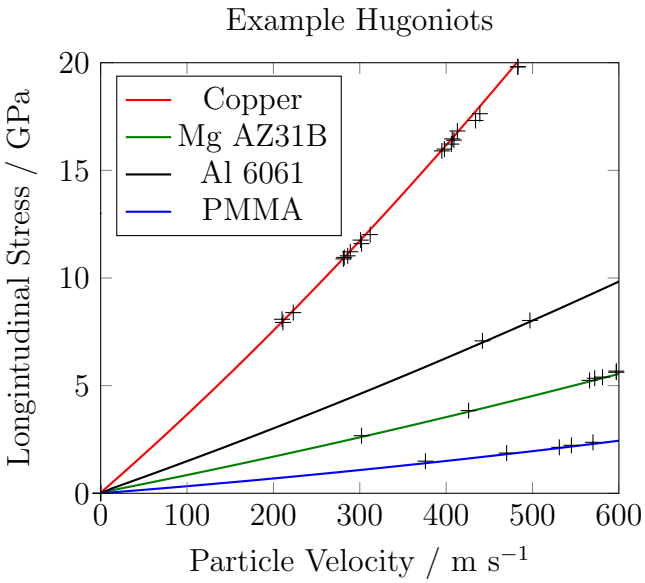


Figure 2.2: Hugoniots for several materials commonly used as flyers because an elastic perfectly plastic Hugoniot fits their behaviour well. The lines are fits provided by Marsh [65, Page 5] and these fits are to experimental results listed in Marsh [65] and plotted as black crosses above. Strength has been added to all models based on a Tresca yield surface with the yield strength taken from standard engineering textbooks.

in figure 2.2. The thermodynamic state in one of these materials after a shock must lie on the respective materials Hugoniot line. By choosing different flyer materials, different areas in pressure velocity space can be reached. The varying density and sounds speed in each material leads to different Hugoniot gradients. This value of the gradient $\rho_0 U_s$, known as the shock impedance, is a measure of the materials inertia and is important in calculations of states resulting from impact.

2.1.2 Impact of Two Materials

Using figure 2.2 predictions of shock states resulting from an impact can be made. It is known that the shock state must be on the material's Hugoniot line, and that as stress and particle velocity are continuous across a boundary, the particle velocity and longitudinal stress must be identical in both the material impacted and the material impactor. In the laboratory frame the impactor travelling at impact velocity v into a stationary target results in an in-material particle velocity u_p and longitudinal stress σ_l shown in figure 2.3.

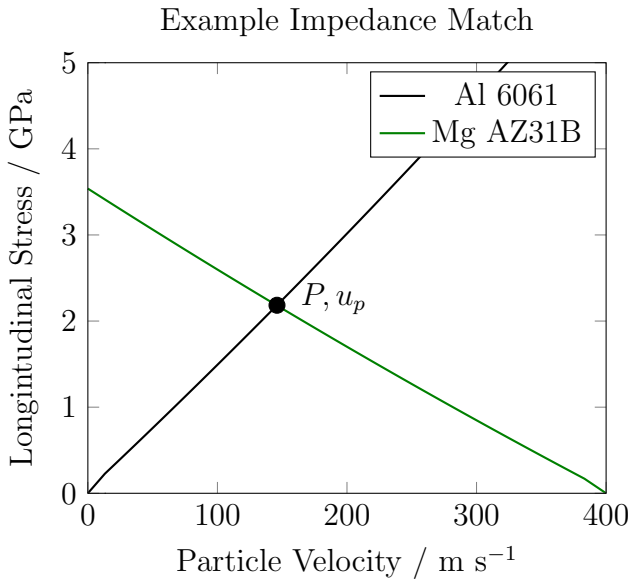


Figure 2.3: The magnesium AZ31B flyer impacts the stationary aluminium 6061 target at 400.0 m s^{-1}. As the resulting shock state must be on both material's Hugoniot lines, the only consistent shock state is where the two lines intersect. In this case 2.18 GPa, 146 m s^{-1}.

2.1.3 Off-Hugoniot States

The Hugoniot of a material is the locus of all points obtained through a single shock and is only valid at a specific initial pressure and density. For waves travelling into already shocked material, it is necessary to recalculate the Hugoniot using an Equation of State (EoS). For many materials a Mei-Gruneisen EoS is used, which introduces the Gruneisen parameter which can be used to calculate off-Hugoniot states. As no reshocks are studied during this work, only the principle Hugoniot is needed. The Hugoniot approximates the release curve well at low compressions (strain less than 10%) because the first non-zero entropy term is third order along the Hugoniot [4]. Release is an isentropic process, and so follows the isentrope, which is close to the Hugoniot at compressions less than 10%. Because no reshocks are studied and because all compressions are elastic and well below 10%, the is no need to calculate any off Hugoniot states, so a full EoS and Gruneisen parameter is unnecessary.

As the shock is one dimensional and inertially confined, a shocked region is in a state

of one dimensional strain. The strain is the ratio of the shock velocity to the particle velocity as in equation 2.4.

$$\varepsilon = \frac{u_p}{U_s} \tag{2.4}$$

2.2 Notation for Anisotropic Systems

Due to the complexity of describing anisotropic materials a strict notation will be laid out. Firstly, it is important to distinguish the way in which mathematically the theory is described and experimentally the way in which it is measured. Mathematically it is useful to construct the theory in the form of tensors and not to fix a basis. However experimentally the basis is not only fixed, it has an associated error. It is useful therefore to have a distinction between the mathematical concepts and the experimental measurements. The theoretical quantities will be expressed as tensors (e.g. Cauchy tensor) and the Einstein summation convention will be used. For experimental results the values will be expressed as column vectors and matrices (Voigt notation). For example strain ε can be expressed in the Cauchy tensor form as

$$\varepsilon_{ij} = \begin{pmatrix} \varepsilon_{11} & \varepsilon_{12} & \varepsilon_{13} \\ \varepsilon_{12} & \varepsilon_{22} & \varepsilon_{23} \\ \varepsilon_{13} & \varepsilon_{23} & \varepsilon_{33} \end{pmatrix}, \tag{2.5}$$

and in the Voigt column vector form as

$$\underline{\varepsilon_i} = \begin{pmatrix} \varepsilon_{11} \\ \varepsilon_{22} \\ \varepsilon_{33} \\ 2\varepsilon_{23} \\ 2\varepsilon_{13} \\ 2\varepsilon_{12} \end{pmatrix}. \tag{2.6}$$

Any quantity expressed in a basis independent manner such as in its tensor form will be in plain notation with its indices, as in equation 2.5. This includes any standard vectors such as electric field vectors. Any basis dependant quantity (matrix or Voigt vector) will be expressed as in 2.6 with an underline. In some circumstances vector equations will be expressed with vector quantities in bold (no underline) and matrix quantities in bold with an underline. However the presence of an underline still indicates a basis dependant expression.

2.3 Anisotropic Elastodynamics

At low-pressure states (linear elastic behaviour) anisotropic elastic materials can be represented with an elastic tensor C_{ijkl} . A few key results are presented here. A full description of the derivations can be found in a number of textbooks such as Ting [38]. The Voigt notation, where the elastic tensor can be reduced to a 6 by 6 elastic matrix $\underline{\mathbf{C}}$ in the principle frame of the crystal axes, is shown in equation 2.7 for a trigonal crystal such as calcite or sapphire. Experimentally the components are found by measuring

ultrasound velocities in the crystal in different orientations and polarisations [12, 40, 66].

$$\underline{\mathbf{C}}= \begin{pmatrix} C_{11} & C_{12} & C_{13} & C_{14} & 0 & 0 \\ C_{12} & C_{11} & C_{13} & -C_{14} & 0 & 0 \\ C_{13} & C_{13} & C_{33} & 0 & 0 & 0 \\ C_{14} & -C_{14} & 0 & C_{44} & 0 & 0 \\ 0 & 0 & 0 & 0 & C_{44} & C_{14} \\ 0 & 0 & 0 & 0 & C_{14} & \frac{C_{11}-C_{12}}{2} \end{pmatrix} \tag{2.7}$$

The relation between the components of the elastic tensor and the elastic matrix are given in Ting [38], which also derives equation 2.8. Equation 2.8 gives the accoustic tensor Q_{ij} which contains information about elastic waves in the direction of propagation x_i. Q_{ij} is a symmetric tensor so can be diagonalised using a rotation matrix $\underline{\mathbf{\Lambda}}$. When diagonalised in equation 2.9 the eigenvectors are the polarisation modes and the eigenvalues are proportional to the wave velocities U_i, found in equation 2.10.

$$Q_{ik} = C_{ijkl} x_j x_l \tag{2.8}$$

$$Q_{ik} = \underline{\mathbf{\Lambda}}\ \underline{\mathbf{Q}}\ \underline{\mathbf{\Lambda}}^{-1} \tag{2.9}$$

$$\underline{\mathbf{Q}} = \rho_0 \begin{pmatrix} U_1 & & \\ & U_2 & \\ & & U_3 \end{pmatrix}^2 \tag{2.10}$$

These equations hold for small perturbations of linearly elastic materials. Higher order elastic tensors have been measured for many anisotropic dielectrics, for example calcite by Kaga [52], and have been used in shock compression experiments by Stapleton [49], Aidun [50]. The strains studied by Stapleton [49], Aidun [50] were 2% – 10% which is high, above calcite's elastic limit. In the scope of this work it was extremely challenging to incorporate

non-linear anisotropy in a consistent manner into an optical model because the method of finding the photoelastic tensor involves knowledge of the elastic tensor, and assumes no non-linear corrections. For small compressions (strain less than 1%) non-linear terms are usually negligible, for calcite the third order terms are of order 100 GPa, with a strain of 0.01 the contribution of the third order terms is 0.0001. Therefore the third order term for calcite contributes 0.01 GPa at 1% strain, compared to the first order terms (around 100 GPa) which contribute 1 GPa at 1% strain. At 1% strain the contribution of second order terms is about 100 times lower, which is the typical experimental error on the first order components. This limits the validity of the model to be laid out in section 2.6.1 to strains of around 1%.

2.4 Mathematical Representation of Anisotropic Optics

Using the results in Yariv and Yeh [67, chapter 2], optical behaviour of anisotropic dielectric materials can be expressed with a dielectric constant in tensor form ϵ_{ij} from which refractive indices can be calculated using the wave surface. In a generalised material the dielectric constant is symmetric so can always be diagonalised giving the principle frame. The principle refractive indices n_i can be calculated from the diagonalised tensor, however for a general direction in the material it is not straightforward to solve for the refractive indices as the refractive indices are not a tensor and do not transform between coordinates. Because of this the optical impermeability η_{ij} is used which is related to the refractive indices through equation 2.11. The optical impermeability has the advantage that it is a tensor and so is basis independent (unlike the refractive indices).

$$\eta_{ij} = \begin{pmatrix} n_1 & 0 & 0 \\ 0 & n_2 & 0 \\ 0 & 0 & n_3 \end{pmatrix}^{-2} \tag{2.11}$$

For a trigonal material, $n_1 = n_2$ and so the refractive indices are expressed as an ordinary refractive index $n_o = n_1 = n_2$ and an extraordinary refractive index $n_e = n_3$.

In order to make use of this and calculate the phase of an optical wave travelling through a material in an arbitrary direction, the full wave equation in terms of the electric field must be considered. For wave solutions with wave vector k and angular frequency ω, equation 2.12 can be used where the permeability μ can be absorbed into the optical impermeability by $\eta = \mu\epsilon$. If the dielectric tensor is in the principle coordinates, then equation 2.12 expands out to equation 2.13.

$$\mathbf{k} \times (\mathbf{k} \times \mathbf{E}) + \omega^2 \mu \epsilon \mathbf{E} = 0 \tag{2.12}$$

$$\begin{pmatrix} \omega^2\mu\epsilon_x - {k_y}^2 - {k_z}^2 & k_x k_y & k_x k_z \\ k_y k_x & \omega^2\mu\epsilon_y - {k_x}^2 - {k_z}^2 & k_y k_z \\ k_z k_x & k_z k_y & \omega^2\mu\epsilon_z - {k_x}^2 - {k_y}^2 \end{pmatrix} \begin{pmatrix} E_x \\ E_y \\ E_z \end{pmatrix} = 0 \tag{2.13}$$

2.4.1 Photoelasticity

Using Yariv and Yeh [67, chapter 6], a linear anisotropic relationship between strain and refractive index can be expressed as equation 2.14 where the photoelastic tensor p_{ijkl} replaces a scaler Gladstone-Dale constant. The photoelastic tensor shown in equation 2.14 can be expressed as a 6×6 matrix, in the same method as for the elastic tensor in section 2.3. This gives the photoelastic matrix $\underline{\mathbf{p}}$, which does not have to be symmetric (unlike the elastic matrix). Equation 2.15 shows the photoelastic matrix form for trigonal materials of the symmetry group $\overline{3}\frac{2}{m}$ such as calcite and sapphire.

$$\eta_{ij} = p_{ijkl}\varepsilon_{kl} + \eta_{0\ mn} \tag{2.14}$$

$$\underline{\mathbf{p}} = \begin{pmatrix} p_{11} & p_{12} & p_{13} & p_{14} & 0 & 0 \\ p_{12} & p_{11} & p_{13} & -p_{14} & 0 & 0 \\ p_{31} & p_{31} & p_{33} & 0 & 0 & 0 \\ p_{41} & -p_{41} & 0 & p_{44} & 0 & 0 \\ 0 & 0 & 0 & 0 & p_{44} & p_{14} \\ 0 & 0 & 0 & 0 & p_{41} & \frac{p_{11}-p_{12}}{2} \end{pmatrix} \tag{2.15}$$

2.5 Photoelasticity in Shock Compression

Using the anisotropic elastic results in section 2.3 and the photoelastic model in section 2.4.1 an analytical prediction will be developed for shock compressed dielectrics. The condition of one dimensional strain imposed by shock compression, combined with the directional dependence of the models, gives a variation in optical behaviour as the shock direction changes.

2.5.1 Shocks along the *a*-axis

This direction is convenient as the Voigt notation can be used effectively. As the strain is one dimensional and along a principle axis of the crystal, the full matrix representation is reduced to a single strain component and four photoelastic components. The uniaxial strain condition along the a-axis restricts the strain vector to

$$\underline{\varepsilon} = \begin{pmatrix} \varepsilon_1 \\ 0 \\ 0 \\ 0 \\ 0 \\ 0 \end{pmatrix} \tag{2.16}$$

where from the definition of a shock in section 2.1.1

$$\varepsilon_1 = \frac{u_p}{U_s} \tag{2.17}$$

and the shock velocity U_s can be taken as the fastest wave solution U_1 to the accoustic tensor in the a-axis direction $x_i = (1,\ 0,\ 0)$. From equation 2.14,

$$\underline{\eta}' = \begin{pmatrix} p_{11} \\ p_{21} \\ p_{31} \\ p_{41} \\ 0 \\ 0 \end{pmatrix} \frac{u_p}{U_s} + \underline{\eta}_0 \tag{2.18}$$

where the original optical impermeability at room temperature and pressure is $\underline{\eta}_0$ defined as

$$\underline{\eta}_0 = \begin{pmatrix} {n_o}^{-2} \\ {n_o}^{-2} \\ {n_e}^{-2} \\ 0 \\ 0 \\ 0 \end{pmatrix}. \tag{2.19}$$

Converting the Voigt notation to Cauchy tensor tensor notation, the optical impermeability can be diagonalised

$$\underline{\mathbf{\Lambda}}\ \eta_{ij}\ \underline{\mathbf{\Lambda}}^{-1} = \eta'_{kl} \tag{2.20}$$

where

$$\eta_{ij} = \begin{cases} \eta_i & \text{if } i = j = [1,2,3] \\ 0 & \text{if } i \neq j \end{cases} \tag{2.21}$$

Given that η_{51} and η_{61} are both zero, the transformation matrix $\underline{\mathbf{\Lambda}}$ will not rotate the η tensor around the y or z axes, however the angle of the optical axis in the shocked material is expected to rotate around the direction of shock propagation x.

2.6 Experimentally Measurable Quantities

Using the result of section 2.5 is necessary to derive predictions for experimentally measurable quantities. The experimental quantities need to be measurable in a plate impact experiment to a precision which allows a meaningful test of the theoretical result of section 2.5. Birefringence is an established experimental technique and a relationship between a birefringence measurement and the shocked optical impermeability will be derived in section 2.6.1.

2.6.1 Birefringence

From section 2.5 the optical axes only rotate around the x axis during compression along the x axis, and so the birefringence along x (a-axis, and shock direction), in the shock compressed region, can be calculated as

$$\Delta n = \frac{1}{\sqrt{\eta_2}} - \frac{1}{\sqrt{\eta_3}} = n_2 - n_3 \ . \tag{2.22}$$

The optical impermeability η is not to be confused with non-linear optical refractive indices. It is related to the first order refractive indices through equation 2.11 (the Eigan values represent linear refractive indices in different directions) and the Eigan values are labelled according to equation 2.21.

This quantity is experimentally measurable through normal incidence polarimetry and as such is a differential measurement between η_2 and η_3 . This is ideal for investigating anisotropic materials as the presence of birefringence indicts that the refractive index is different in one direction compared to another, an inherent example of anisotropy. It is not observed in isotropic materials and this quantity is measurable in a relatively

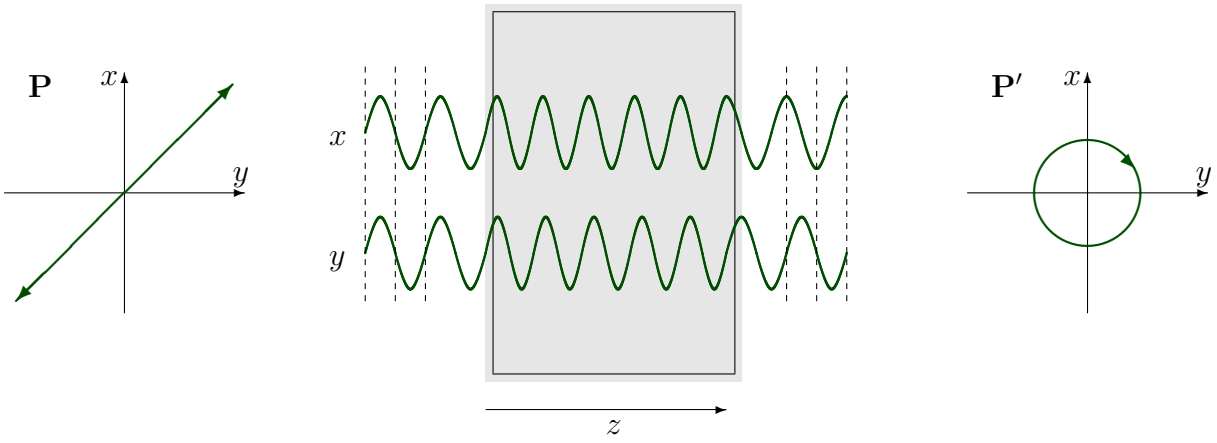


Figure 2.4: An optical wave propagating in the z direction is linearly polarised at 45° to the x and y axes in polarisation state **P**. The wave propagates through a dielectric material with its optical axis in the y direction, leading to the x and y components having different optical path lengths in the material. When the optical wave emerges its polarisation state $\mathbf{P}'$ is found by combining the x and y components again. However the x component now leads the y component by $\pi/2$. The electric field therefore rotates with time, rather than oscillating in a linear fashion. This is called circular polarisation.

accurate (0.1% error) and straightforward manner through polarimetry. As a birefringent material has two different phase velocities for orthogonal polarisations, the polarisation state changes as the wave passes through the material. By knowing the size of the sample, the difference in the two refractive indices can be measured with far greater precision than measuring each individually and subtracting.

Polarimetry is the measurement of the polarisation of light used to probe a system or experiment. In birefringent systems there are two refractive indices for a light ray depending on its polarisation. This causes a phase slip or offset between the two polarisations that will move in and out of phase depending on the distance propagated through the birefringent medium, and the difference in the two refractive indices. This is illustrated in figure 2.4.

The optical path difference is the difference in apparent distance travelled by two light rays. This takes into account the difference in refractive index that the two rays have experienced over a distance l, and has units of length. This is converted to an

optical phase difference $\Delta\phi$ by multiplying by $\frac{2\pi}{\lambda}$ which gives a value in radians. For a birefringent material the optical phase difference between two orthogonal polarisations after travelling a distance l in the material is

$$\Delta\phi = l\frac{2\pi}{\lambda}\Delta n \ . \tag{2.23}$$

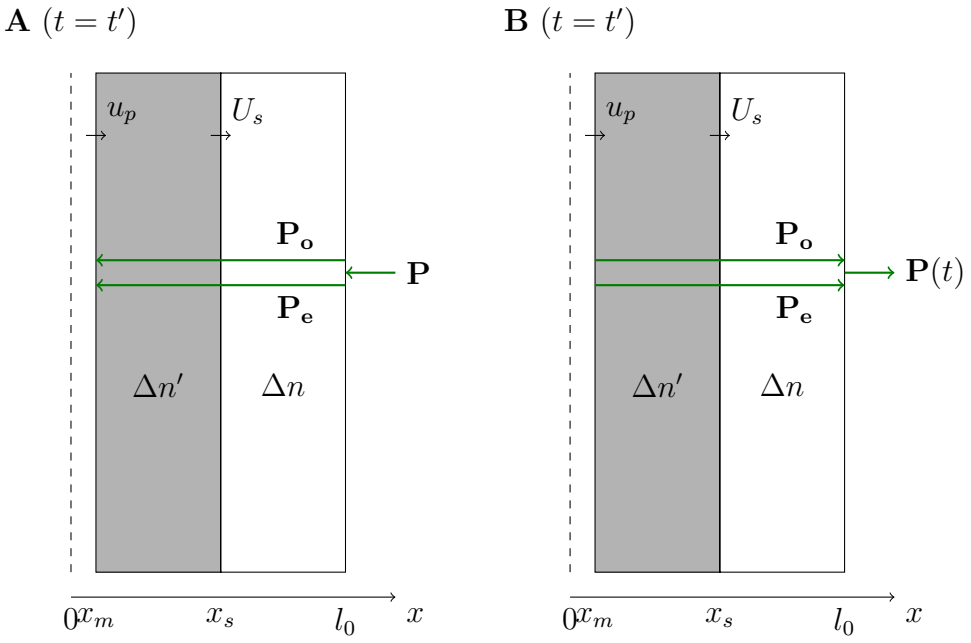


Figure 2.5: Illustration of shock propagation model, used to derive equation 2.25. An input polarisation state $\mathbf{P}$ propagates as two orthogonal polarisations $\mathbf{P_o}$ and $\mathbf{P_e}$ in the birefringent material. The emerging polarisation state $\mathbf{P(t)}$ is a function of the phase difference between $\mathbf{P_o}$ and $\mathbf{P_e}$, which is in turn dependant on the shocked birefringence $\Delta n'$ and the positions of the interfaces given by $U_s t$ and $U_p t$ where time is t. $\mathbf{P(t)}$ can be measured with a polarimeter.

Consider a one wave structure travelling with a shock velocity and a particle velocity as shown in figure 2.5. Remembering that the light passes through the material twice the path difference between each polarisation state is

$$\Delta\phi = \frac{2\pi}{\lambda}2l\Delta n + 2l'\Delta n'$$
$$\Delta\phi = \frac{2\pi}{\lambda}2(l_0 - U_s t)\Delta n + 2(U_s - U_p)t\Delta n'$$

$$\Delta\phi = 2\pi(2\frac{l_0 - U_s t}{\lambda}\Delta n + 2\frac{U_s - U_p}{\lambda}t\Delta n') \ . \tag{2.24}$$

The detected optical intensity at the polarimeter is equal to the amplitude squared. If we assume the optical phase has the form $\Delta\phi = \omega t + \delta$ as so

$$I \propto \sin^2(\Delta\phi)$$
$$I \propto \sin^2(\omega t + \delta) \ .$$

Then substituting in equation 2.24 and solving for $\Delta n'$ leads us to equation 2.25 where f is the frequency detected by the polarimeter.

$$\begin{aligned}\delta &= 4\pi\frac{l_0}{\lambda}\Delta n \\ \omega t &= 2\frac{2\pi}{\lambda}((U_s - U_p)\Delta n' - U_s\Delta n)t \\ f\lambda &= -2U_s\Delta n + 2(U_s - U_p)\Delta n'\end{aligned}$$

$$\Delta n' = \frac{f\lambda + 2U_s\Delta n}{2(U_s - U_p)} \ . \tag{2.25}$$

Hence to make this measurement experimentally, a method for measuring f, u_p and U_s simultaneously needs to be found.

2.6.2 Polarimetry

Measuring the polarisation of an optical wave is achieved using a polarimeter. There are several ways to express a polarisation state, however a Stokes vector is the most natural representation for an experimental measurement. The vector is defined in equation 2.26 in terms of the electric field components in linear x and y, linear at 45° to x and y, and

left and right handed circular components (difference in real $\Re$ and imaginary $\Im$ phase).

$$\underline{S} = \begin{pmatrix} I \\ L \\ D \\ C \end{pmatrix} = \begin{pmatrix} |E_x|^2 + |E_y|^2 \\ |E_x|^2 - |{E_y}^2|^2 \\ 2\Re(E_x {E_y}^*) \\ -2\Im(E_x {E_y}^*) \end{pmatrix} \tag{2.26}$$

In a polarimeter each detector is setup to measure one electric field component. Ideally two orthogonal components are measured simultaneously such as $|E_x|^2$ and $|E_y|^2$. In some setups a Beam Intensity Monitor (BIM) is used giving a direct measurement of I, and an indication of the degree of non-polarised light in the system. For light propagating in birefringent media, the polarisation state will oscillate between C and some linear plane which is a function of L and D. The linear plane is determined by the orientation of the media, and will always be at 45° to the optical axis of the material. To see why this is, consider a phase difference introduced to the x component with respect to the y component. Initially the components are in phase

$$E_x = E_y = \frac{1}{\sqrt{2}} E_0 e^{i\delta}$$

and the initial stokes vector stokes vector is

$$\begin{pmatrix} {E_0}^2 \\ 0 \\ {E_0}^2 \\ 0 \end{pmatrix}.$$

After propagating through a birefringent material with its optical axis aligned to the x

axis however, a phase difference is introduced

$$E_y = \frac{1}{\sqrt{2}} E_0 e^{i\phi}$$
$$E_x = \frac{1}{\sqrt{2}} E_0 e^{i\phi'}.$$

It is clear that the value of the intensity $|E_x|^2 + |E_y|^2$ and the linear component of the stokes vector $|E_x|^2 - |E_y|^2$ have not changed. For the other components

$$E_x {E_y}^* = \frac{1}{2} {E_0}^2 e^{i(\phi - \phi')} \ .$$

For a birefringent material of thickness l and refractive index difference Δn, equation 2.25 relates the optical phase difference $\phi - \phi'$ to l and Δn. This has been substituted into the above equation to get

$$E_x {E_y}^* = \frac{1}{2} {E_0}^2 e^{i\frac{l}{\lambda}\Delta n}$$

Taking the stokes vector components D and C gives us

$$\begin{aligned} D &= 2\Re(E_x {E_y}^*) \\ &= \Re {E_0}^2 e^{i\frac{l}{\lambda}\Delta n} \\ C &= -2\Im(E_x {E_y}^*) \\ &= -\Im {E_0}^2 e^{i\frac{l}{\lambda}\Delta n} \end{aligned}$$

for a final stokes vector of

$$\begin{pmatrix} {E_0}^2 \\ 0 \\ {E_0}^2 \cos(\frac{l}{\lambda}\Delta n) \\ {E_0}^2 \sin(\frac{l}{\lambda}\Delta n) \end{pmatrix} .$$

If the optical axis is not aligned perfectly with the $\pm 45^o$ components on the polarimeter, then an angular rotation of the final result in the linear plane will be expected.

Applying the rotation matrix for an optical axis orientation with respect to the $\pm 45^{o}$ frame gives

$$\begin{pmatrix} {E_0}^2 \\ \sin^4(\zeta){E_0}^2 \cos\left(\frac{l}{\lambda}\Delta n\right) \\ \cos^4(\zeta){E_0}^2 \cos\left(\frac{l}{\lambda}\Delta n\right) \\ {E_0}^2 \sin\left(\frac{l}{\lambda}\Delta n\right) \end{pmatrix}.$$

2.6.3 Direct Refractive Index Measurement

This method directly measures the refractive indices by considering a window correction to the optical path length of a velocimeter. This can be done for multiple refractive indices with PDV, or a single refractive index with VISAR. A VISAR measurement has been done for a birefringent sample (a-cut sapphire) by Jones *et al.* [24]. Due to the polarised light in the VISAR, a beat frequency was observed as the two path lengths interfered.

As discussed in section 1.2, window corrections are a standard optical measurement in shock physics. The shock refractive index has been measured for LiF [68, 29], c-cut sapphire [22, 37], PMMA [31] and Quartz [25]. The measurement is usually achieved by assuming a single shock wave in the material, and the material state is known by using a symmetric impact technique. This setup is shown in figure 2.6 and derived below based on Barker and Hollenbach [22], Goosman [69].

The optical phase of the light reflected by the second window surface is

$$\phi = \int_L n(x,t)\, dx$$

and we can treat $n(x,t)$ using the Heaviside step function $H(x)$ giving the form

$$n(x,t) = n_0 + n' H(x_s - x). \tag{2.27}$$

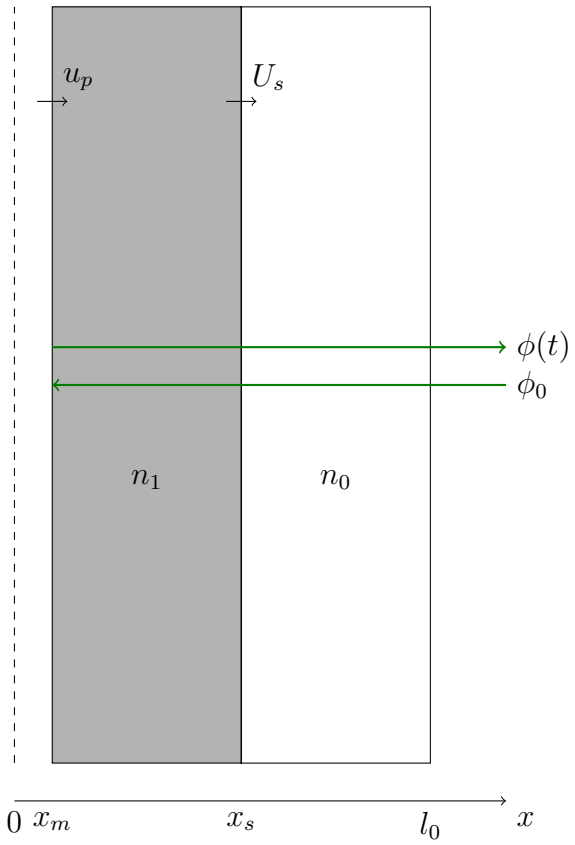


Figure 2.6: Illustration of step wave shock model used for refractive index calculation. The initial refractive index n_0 and the shocked refractive index n_1 are related by $n_1 = n' + n_0$ in the text. The location of the reflective surface x_m is moving at u_p and the shock front location x_s is moving at U_s.

The location of the step function is given be the location of the shock x_s and the integral limits are given by

$$x_s = U_s t$$

$$x_m = u_p t$$

and combining this with equation 2.27 above (remembering that the light makes two passes in this geometry) the complete integral is

$$\phi = 2 \int_{u_p t}^{l_0} n_0 + n' H(U_s t - x)\ dx. \tag{2.28}$$

Solving this integral and cancelling the original phase gives

$$\begin{aligned} \phi &= 2[n_0 x - (U_s t - x) n' H(U_s t - x)]_{u_p t}^{l_0} \\ &= 2t(n_0 u_p + (u_p - U_s) n' H((U_s - u_p)t)) \end{aligned}$$

and given that

$$H((U_s - u_p)t) = 1 \quad \text{for } t > 0$$

the solution is

$$\phi(t) = 2t(n_0 u_p + (u_p - U_s) n'). \tag{2.29}$$

At the detector the optical intensity of the interference pattern between the optical phase of the light propagated through the window and the reference ϕ_0 is

$$\begin{aligned} I &\propto \sin^2(\phi) \\ I &\propto \sin^2(\omega t) \\ \omega &= 2(n_0 u_p + (u_p - U_s) n'). \end{aligned}$$

This can be used to find the refractive index of the shocked region as

$$n' = \frac{\frac{1}{2}\omega - n_0 u_p}{u_p - U_s} \ . \tag{2.30}$$

In PDV multiple frequencies can be detected and measured. As birefringent dielectrics have two refractive indices, there will be two window corrections causing two close but distinct frequencies for light not propagating along an optical axis. Multiple refractive indices can be measured in this way, and the difference used to find the birefringence.

2.7 Chapter Conclusions

The analytic prediction for a-cut trigonal dielectrics in section 2.5 is a novel combination of standard mathematical methods to describe anisotropic elastic behaviour and anisotropic optical behaviour. The method uses static literature measurements of elastic and photoelastic constants to predict the optical impermeability of a crystal in uniaxial compression along an arbitrary axis. For uniaxial strain along the a-axis of a trigonal crystal the prediction is on-axis birefringence, an experimentally measurable quantity. Predictions for sapphire, calcite and rutile will be put forward in chapter 3 using these equations.

Experimental methods in chapter 5 will make use of the polarimetry results in section 2.6.2 to measure the birefringence and compare with predictions made using static literature data and section 2.5. The birefringence method will be a new measurement for anisotropic dielectrics under shock compression, and will be a difference measurement, directly measuring the optical anisotropy in the shocked region. The method described in section 2.6.1 can be applied to the data in Jones *et al.* [24], allowing a source of data for a literature comparison of the measurement.

The development in section 2.6.1 furthers current literature on birefringence under shock compression and has been published in Tear *et al.* [2].

Chapter 3

Computing the Birefringence of Shocked Sapphire and Calcite

It has been shown that anisotropic material properties can be represented with tensors in chapter 2. Using the method laid out in section 2.5, the expected birefringence particle velocity relationship was calculated for different materials. Figure 3.1 shows the expected behaviour for the common anisotropic minerals calcite, sapphire and rutile based on the literature values of Dandekar [12], Nelson *et al.* [53] for calcite, Tarumi *et al.* [40], Reintjes and Schulz [70] for sapphire and Manghnani [71], Reintjes and Schulz [70] for rutile. There are several literature values for the photoelastic tensor of sapphire by Reintjes and Schulz [70], Waxler and Farabaugh [72], Jones *et al.* [24] and these are plotted in figure 3.2, from which it is clear that some caution must be applied. The differences in photoelastic values in the literature have led to quite different predictions.

Each literature value of the photoelastic tensor for sapphire used in figure 3.2 is experimentally obtained, and each has a stated error value for each tensor component. However, the errors on each tensor component are correlated, as a change in one tensor component implies a change in others in order to remain consistent with the experimental measurements. A method of estimating tensor errors was needed to assess whether the differences presented in figure 3.2 are within experimental error. Further to estimating

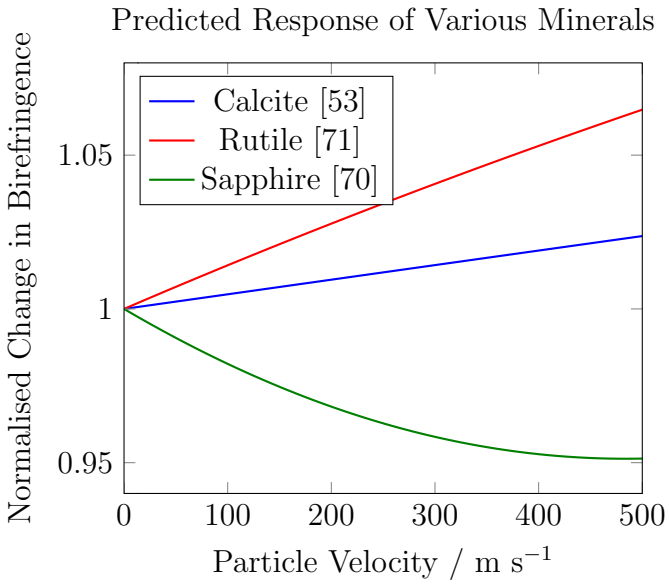


Figure 3.1: An analytical fit using literature photoelastic tensors (in references [53, 12, 40, 70, 71]) and equations in section 2.5 for the birefringence behaviour under shock compression for calcite, sapphire and rutile. The birefringence has been normalised to the birefringence at static room temperature and pressure conditions, showing a general summary of the range of behaviour of different available materials.

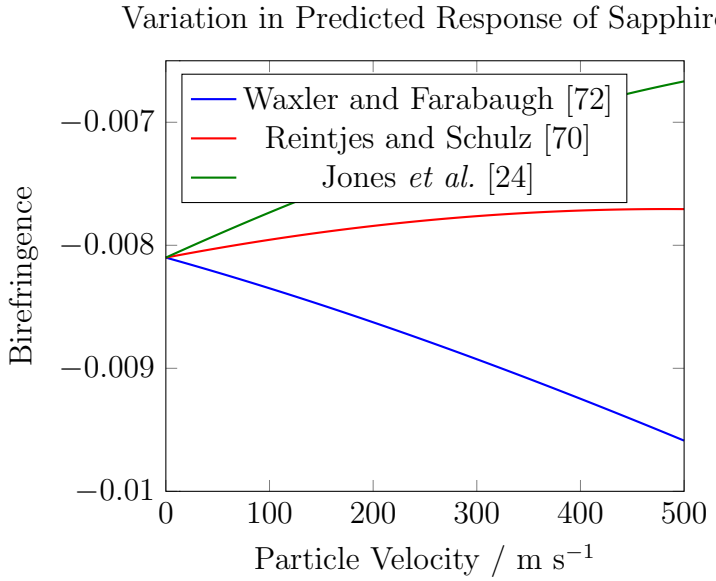


Figure 3.2: There are three literature values for the photoelastic tensor of sapphire, and the analytical fit for each one is plotted above. This gives an idea of the error range of these predictions, as there is clear disagreement in the literature.

tensor errors, propagating tensor errors is not straightforward because the acoustic tensor and impermeability tensor need to be diagonalised. This is summed up in Stewart [73, chap. 4]:

> 'Of all the problems in matrix perturbation theory the perturbation of the eigenvalues of a matrix presents the most varied technical difficulties. The problem itself is simply stated. Given a matrix A and a perturbation E of A, how are the spectra $\mathcal{L}(A)$ and $\mathcal{L}(A + E)$ related? But this simplicity is elusive...'

In order to tackle this challenge, computational methods have been developed to perform the error analysis. There are several error sources to model:

A. The measurement error on the photoelastic tensor from the literature. Typically the error is given as a per component value of the order of 5%.

B. The measurement error on the elastic tensor from the literature. Typically the error is again given as a per component value of the order of 1%.

C. The error on the crystallographic alignment of the sample with the desired shock direction. This is usually around 2^{o}.

D. The impact tilt, and its effect on the shock direction, compounded with crystallographic tilt error. Impact tilt of 1 milliradian can be achieved on typical gas gun facilities.

To estimate items A and B, a Monte Carlo approach was used and is described in section 3.1. A similar Monte Carlo approach was used for item C in the prediction. For item D a ray tracing model will be outlined to predict data in section 3.2.

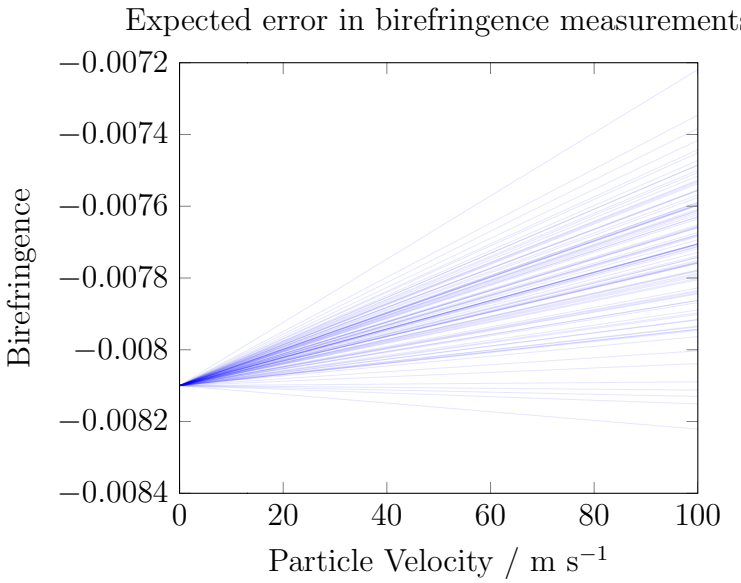


Figure 3.3: In order to estimate an error of sapphire $\langle 1\,0\,\bar{1}\,0\rangle$ the photoelastic tensor from Reintjes and Schulz [70] was randomly pertubated and used in the analytical prediction. The result of 100 of these Monte Carlo simulations are plotted above. This gives a more accurate estimate of the error than figure 3.2. The error on the elastic matrix was 1% and on the photoelastic matrix 5%. The density of lines conform well to a Gaussian distribution, indicating substructure is due to random noise.

3.1 Error on Photoelastic Prediction

Given the variation in sapphire literature values shown in figure 3.2 it is necessary to propagate the literature experimental errors in the elastic tensor and photoelastic tensor. These tensors can be represented by a matrix and the prediction is found by diagonalising the matrix as described in section 2.5, hence the problem becomes one of quantifying the error on the eigenvalues, given the error on the original matrix.

A Monte Carlo method was developed that simulated random Gaussian variation in literature values, discussed in more depth in section 3.1.1. Each random result was propagated through the photoelastic model, and a final prediction calculated. The output of 100 perturbations is shown in figure 3.3, and from this the variance in predicted values was calculated.

3.1.1 Estimating Tensor Errors

To estimate the error on a tensor quantity, it is necessary to consider how it is measured. A series of measurements are taken (wave speeds for a given direction and polarisation) and then a maximum likelihood estimator is found for the tensor, which is the quoted literature tensor. This method is described in detail in Tarumi *et al.* [40]. Typically error values are quoted on a particular component of a tensor, but this is not particularly useful as the variance between different tensor components is related because of the experimental method used to measure these values. If a particular value of the tensor is changed, the maximum likelihood values of other components change in order to remain consistent with experimental results. One method to handle this is to use Principle Coordinate Analysis (PCA), where the tensor is diagonalised and the principle eigenvalues perturbed by an error, and then reform the original tensor. This can be done for rank 4 elasticity tensors by perturbing their matrix form.

For example to perturb the elastic matrix for a trigonal material, the elastic tensor is diagonalised in equation 3.1 and the eigenvalues λ_i are varied using a Gaussian distribution with standard deviation of $\pm 1\%$.

$$\begin{pmatrix} C_{11} & C_{12} & C_{13} & C_{14} & 0 & 0 \\ C_{12} & C_{11} & C_{13} & -C_{14} & 0 & 0 \\ C_{13} & C_{13} & C_{33} & 0 & 0 & 0 \\ C_{14} & -C_{14} & 0 & C_{44} & 0 & 0 \\ 0 & 0 & 0 & 0 & C_{44} & C_{14} \\ 0 & 0 & 0 & 0 & C_{14} & \frac{C_{11}-C_{12}}{2} \end{pmatrix} = \underline{\Lambda} \begin{pmatrix} \lambda_1 & & & & & \\ & \lambda_2 & & & & \\ & & \lambda_3 & & & \\ & & & \lambda_4 & & \\ & & & & \lambda_5 & \\ & & & & & \lambda_6 \end{pmatrix} \underline{\Lambda}^{-1} \quad (3.1)$$

Perturbing each eigenvalue of a tensor by the same fractional error relies on the experimental literature values having been taken 'evenly', i.e. that the directions and polarisations of wave speeds that have been measured such that the tensor component errors are correlated by the same fractional value. This ensures an even distribution of

perturbed tensors and that the fractional error on each Eigen value is identical. Given that methods described in the literature use sets of orthogonal directions for propagation and polarisation directions, it is reasonable to assume that the measurements are 'even'. The transformation $\underline{\Lambda}$ is dependant on the crystal symmetry and so is fixed, regardless of the elastic component values.

The validity of this method for generating suitable perturbations of the elastic and photoelastic matrices was verified by comparing the distribution of perturbed tensor components to the quoted errors in the literature. It was confirmed that the individual tensor component distributions are closely Gaussian and are in agreement with the literature component errors taken directly from maximum likelihood techniques.

3.1.2 Estimating Directional Errors

Crystallographic tilt is quoted at $\pm$ 2^o from manufacturing tolerances. It is difficult to measure the crystallographic surface normal with greater precision than this. Electron Back-Scatter Diffraction (EBSD) may offer some possibility of greater precision, however as this was unavailable the error in crystallographic orientation is taken as $\pm$ 2^o, an angular error that is Gaussian in $\delta\theta$ and $\delta\phi$.

The effect of a crystallographic misalignment is two fold. Firstly the wave speed in an anisotropic crystal varies with direction and so the predicted shock velocity has an additional uncertainty caused by the unknown crystallographic alignment. This is discussed in this section. Secondly the refractive indices change with orientation and so the change in polarisation has an additional uncertainty. Including the effect of misalignment on refractive index requires a more involved treatment in section 3.2, because the measurement of birefringence in a shock compression experiment is affected by both shock velocity and the refractive indices simultaneously.

The shock velocity in the elastic regime is the quasi-longitudinal wave velocity. The quasi-longitudinal wave velocity for different propagation directions in calcite is shown in figure 3.4. Depending on the orientation of the crystal, the effect of an error in alignment

on wave velocity varies. The curvature of the wave surface defines the nature of the error, if the direction has a local maxima in the wave velocity surface, then any variation in direction reduces the velocity. This gives a distribution similar to an exponential distribution. If the direction is a local minima then the distribution is also exponential, but inverted. If the region is a saddle point, then the distribution resembles a Lorentz distribution. For most other points on the surface (if it is relatively flat), then the distribution is approximated well by a Gaussian.

3.1.3 Propagation of Errors

Once error estimates have been made for the elastic tensor, photoelastic tensor and crystallographic orientation, it is necessary to combine them into the prediction. Using Monte Carlo methods to perturb each source of error, the result is propagated through, and the process is repeated, until an expectation and a variance are found. How many Monte Carlo simulations need to be run is determined by estimating the χ^2 parameter of the result. The final distribution is closely approximated by a Gaussian so when enough simulations are run, the χ^2 value converges to the expected value for the given Degrees of Freedom (DoF). The final distribution in birefringence expectations approximated a Gaussian well with a chi square within the 95% confidence level ($\chi^2 = 440$ for 27000 DoF).

The distribution of birefringence particle velocity results can then be used to give 68% (1σ), 95% (2σ), and 99.3% (3σ) confidence intervals, such as in figure 3.5. This can be done for each of the sapphire literature predictions in figure 3.2 and all agree at the 3σ level. This is a fairly significant deviation, however not enough to suggest that the variation of photoelastic behaviour of sapphire is dependent on manufacturing processes.

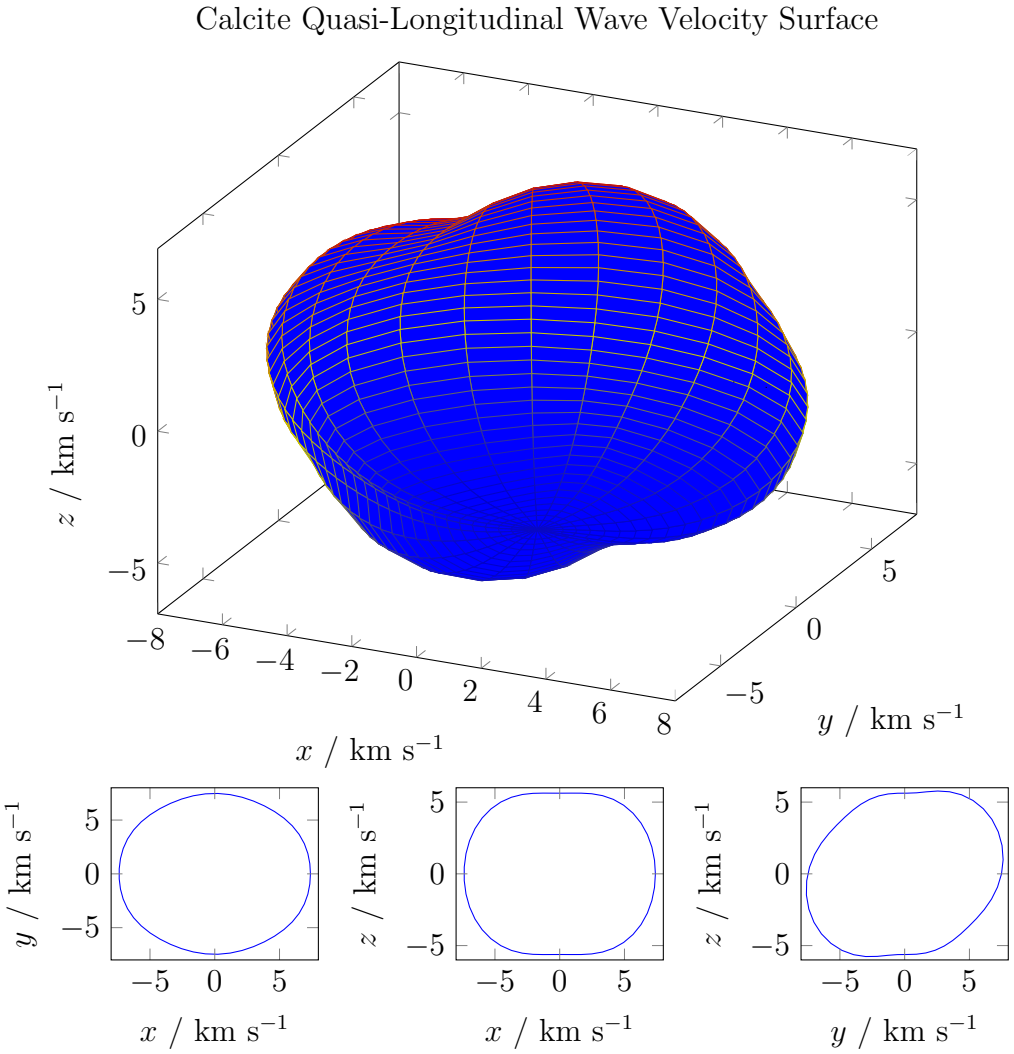


Figure 3.4: The Quasi-longitudinal wave surface for calcite showing the wave velocity in km s^{-1} as a function of direction using the elastic tensor measured by Dandekar [12]. The axis x corresponds to $\langle 1\,0\,\bar{1}\,0\rangle$ or the a-axis, y corresponds to $\langle \bar{1}\,1\,2\,0\rangle$, and z corresponds to $\langle 0\,0\,0\,1\rangle$ or the c-axis. The projections along the x, y and z planes show the variation in wave velocity with small deviations in orientation can be quite high, depending on the desired direction of propagation. The wave velocity varies by up to 50% with orientation, indicating a highly anisotropic material in which small errors in propagation direction can cause large uncertainties in propagation velocity.

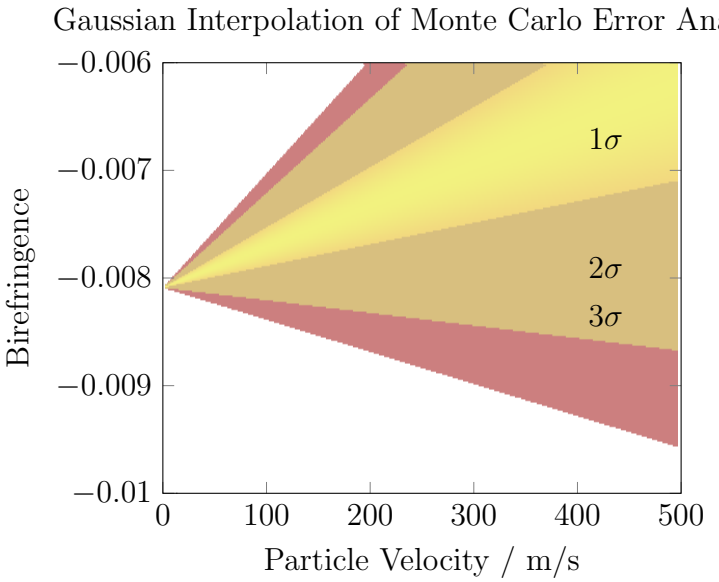


Figure 3.5: Gaussian error profiles fitted to Monte Carlo outputs for sapphire in figure 3.3 with 68% (1σ) 95% (2σ), and 99.3% (3σ) confidence intervals. This represents the uncertainty in the prediction of birefringence under shock compression, when using statically measured elastic and photoelastic tensor values.

3.2 Simulating Experimental Data

In order to investigate the effect of impact tilt and crystallographic tilt on the expected birefringence measurement in a dynamic plate impact experiment, a numerical model was developed. This model was developed by the author directly for, and as part of this thesis. The numerical model combined the variation of shock velocity with crystallographic orientation with an optical model to predict optical propagation in arbitrarily aligned shock compressed biaxial media.

3.2.1 Choice of Algorithms

Typical hydrocodes use the Finite Element Method (FEM) to solve the differential equations describing material deformation. The finite element mesh could be converted to an optical mesh for an optical FEM computer code to solve the optical behaviour. However such methods are usually computationally intense. A full three dimensional code is needed as despite the one dimensional strain being simulated, the materials anisotropy

means stresses in 3 dimensions must be considered. Secondly the optical FEM package would need to be run at a time resolution that was impractical. For PDV data a temporal resolution of 30 ps was needed. This is calculated from the Nyquist condition for a 16 GHz PDV signal, the typical bandwidth of the detectors used in the Institute of Shock Physics (ISP). For an experiment lasting 1 μs this requires of the order of 10^5 FEM calculations to converge per experiment to model.

In view of this a characteristics model was developed to simulate expected material behaviour. As all experiments would be performed in the elastic regime, only the elastic part of the material model needed to be anisotropic. The strain state behind the shock front was then used to calculate the expected optical behaviour.

For optical modelling in shock compressed dielectrics, the transfer matrix method is common. The transfer matrix method uses a matrix to describe the optical transmission and reflection of a multi-layered dielectric material. It takes into account Fresnel reflections and interference, and allows analytical solutions for systems in which the materials crystal symmetry axes line up with the layer symmetry axes. However for systems of arbitrary orientation and non-parallel layers the method is no longer suitable.

Optical ray tracing was used to directly calculate the transmission of the shocked materials and to calculate the emerging polarisation state. This allowed a simulation of expected behaviour should the material's crystallographic axes be misaligned and it also allowed simulation of non-planer impacts. As the geometry of the experiment is relatively simple with a single step wave shock, using a characteristics and ray tracing model is computationally efficient.

3.2.2 Optical Algorithm

The biaxial refraction routine is based on McClain *et al.* [74], Yariv and Yeh [67]. This algorithm solves the dielectric tensor at a biaxial – biaxial interface, formalised in equation 2.12, as an infinite half space problem. The vectors are shown in figure 3.6 and the equation to solve is equation 3.2. All quantities in equation 3.2 are expressed in the plane

of incidence basis with

$$k = \begin{pmatrix} k_1 \\ k_2 \\ 0 \end{pmatrix}$$

where k_1 is conserved at the dielectric boundary.

$$A{k_2}^4 + B{k_2}^3 + C{k_2}^2 + Dk_2 + E = 0 \tag{3.2}$$

$$\begin{aligned}
A &= -\omega^2\mu_0\epsilon_{11} \\
B &= -2\omega^2\mu_0\epsilon_{12}k_1 \\
C &= \omega^4{\mu_0}^2(\epsilon_{11}\epsilon_{22} + \epsilon_{11}\epsilon_{33} - {\epsilon_{13}}^2 - {\epsilon_{12}}^2) - \omega^2\mu_0(\epsilon_{11} + \epsilon_{22}){k_1}^2 \\
D &= 2\omega^4{\mu_0}^2(\epsilon_{12}\epsilon_{33} - \epsilon_{13}\epsilon_{23})k_1 - 2\omega^2\mu_0\epsilon_{12}{k_1}^3 \\
E &= -\omega^2\mu_0\epsilon_{11}{k_1}^4 + \omega^4{\mu_0}^2(\epsilon_{22}\epsilon_{11} + \epsilon_{22}\epsilon_{33} - \epsilon_{12}^2 - \epsilon_{23}^2){k_1}^2 \\
&\quad + \omega^6{\mu_0}^3(\epsilon_{12}^2\epsilon_{33} + \epsilon_{13}^2\epsilon_{22} + \epsilon_{11}\epsilon_{23}^2 - \epsilon_{11}\epsilon_{22}\epsilon_{33} - 2\epsilon_{12}\epsilon_{23}\epsilon_{13})
\end{aligned}$$

There are four solutions to equation 3.2 and if real the solutions are $\pm k_n$ and $\pm k_m$. Ignoring negative solutions for refracted rays and positive solutions for reflected rays, the four vectors in figure 3.6 can be calculated. If a solution is imaginary then the ray does not propagate, and complex solutions are impossible for real valued dielectrics.

3.3 Estimating Impact Tilt

A series of simulations were performed varying the angle of the shock wave and the impact surface interface. An illustration of the simulation is shown in figure 3.7. The impact tilt is set and the shock front tilt is defined by equation 3.3. From section 3.1.2 it is known that the variation of shock speed with direction is small for small angles, so the change

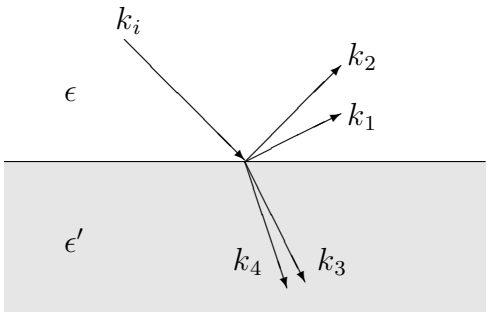


Figure 3.6: Illustration of the optical wave vectors involved at a biaxial – biaxial material interface. The angle of incidence does not equal the angle of reflection as the refractive index of the reflected waves is different to the incident wave. For arbitrarily aligned materials it is necessary to convert all values (dielectric tensors, wave vectors) into the plane of incidence basis. This is the interface normal, and the interface tangents, with one tangent aligned along the projection of the incident wave vector onto the surface. These are also known as S and P polarisations.

in shock velocity is negligible.

$$\theta_s = \theta_i \frac{U_s}{u_p} \tag{3.3}$$

The model proceeds by calculating the elastic wave speed in the given crystallographic direction the shock is propagating in. This is then the wave speed of the shock interface (angle θ_s). The particle velocity is a given parameter, and determines the velocity of the mirror interface (angle θ_i). The effect a given parameter has on the model outcome can then be investigated, the key points to investigate are:

- The effect of crystallographic rotation, without impact or shock tilt.
- The effect of impact and shock tilt, with and without crystallographic tilt

3.4 Results

Simulations were performed which varied crystallographic orientation and impact tilt. As the optical path length changes, the measured polarisation oscillates, and this oscillation frequency is predicted.

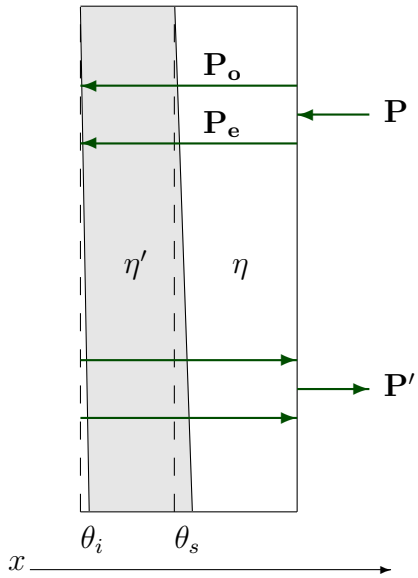


Figure 3.7: An illustration of the tilt simulation setup. The interfaces propagate in the x direction. The reflection and refraction of $\underline{\mathbf{P_o}}$ and $\underline{\mathbf{P_e}}$ (not shown), will result in a change in $\underline{\mathbf{P}'}$.

3.4.1 Crystallographic tilt

The expected results for different crystallographic cuts of calcite were simulated in 10° increments. The effect of a 2° tilt around the a-cut direction was also simulated in 0.2°. For 2° tilt the change in measured polarisation oscillation frequency is 1 MHz, and this was taken as the error due to crystallographic tilt on birefringence for experimental work.

There exists an angle in calcite at which the biaxial phase behind the shock front perfectly cancels the birefringence of the unshocked region. This is visible in the figure 3.9. Sapphire does not show this as the shocked biaxial region is of the opposite sign to calcite (sapphire's refractive indices decrease under shock compression). This shows an anomalous increase near this region in figure 3.10.

a-axis $\langle 1\,0\,\bar{1}\,0\rangle$ 90°

This is the axis the experiment will be performed along. The frequency is the expected frequency for the birefringence and is in line with the analytic prediction, as expected.

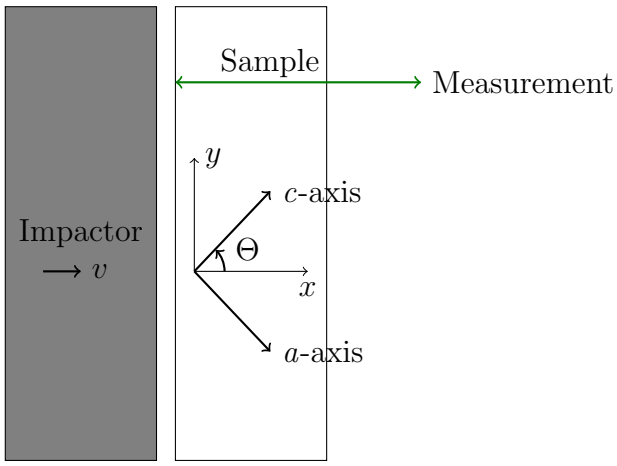


Figure 3.8: The physical impact geometry remains the same, with the impact occurring planar and along the x axis. The sample's crystallographic optical axis (c-axis) is rotated an angle Θ from the x axis.

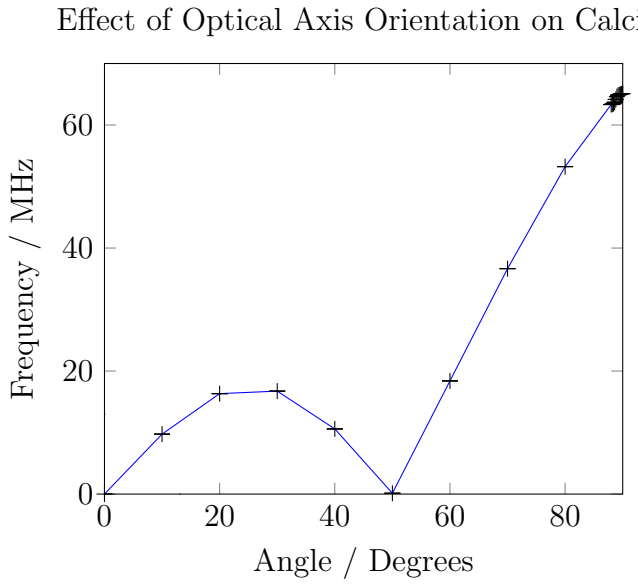


Figure 3.9: The effect of a 90° rotation of the optical axis (c-axis) of calcite with respect to the shock direction. The zero polarisation oscillation frequency at 50° to the optical axis and occurs as the reduction in path length caused by sample compression perfectly cancels the increase in path length from the increased birefringence. Data points are calculated using the model described in this section, the photoelastic tensor from Nelson *et al.* [53] and the elastic tensor from Dandekar [12]. As small tilt errors around the c-axis are of interest in experiments in chapter 7, 20 additional simulations were run in the 85° – 90° range. Error bars are too small to be seen on this scale.

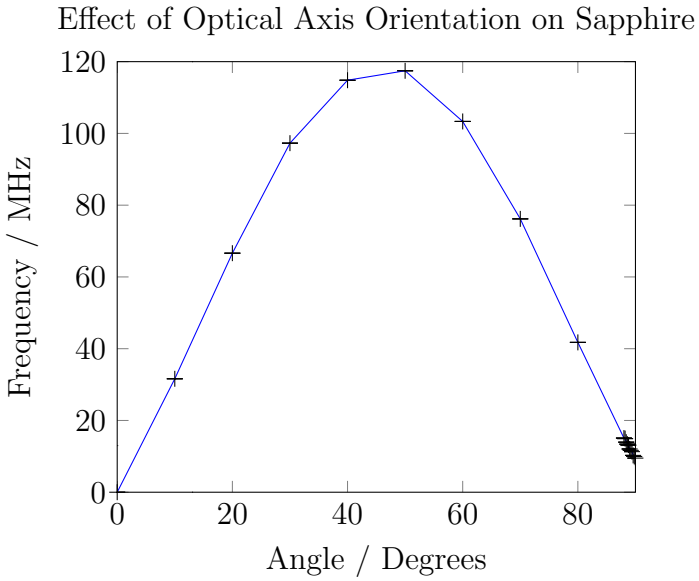


Figure 3.10: The effect of a 90° rotation of the optical axis (c-axis) of sapphire with respect to the shock direction. As sapphire's birefringence decreases with compression, a large increase in frequency is seen around 43°, the same crystallographic plane as calcite's zero birefringence in figure 3.9. Data points are calculated using the model described in this section, the photoelastic tensor from Reintjes and Schulz [70] and the elastic tensor from Tarumi *et al.* [40]. As with figure 3.9, small tilt errors around the c-axis are of interest in experiments in chapter 7, 20 additional simulations were run in the 85° – 90° range. Error bars are too small to be seen on this scale.

***c*-axis** $\langle 0\,0\,0\,1 \rangle$ **0°**

This direction is the optical axis, and hence shows no birefringence for calcite or sapphire, as expected. The material remains uniaxial behind the shock front.

***b*-axis** $\langle 0\,1\,1\,0 \rangle$ **90°**

This direction is optically identical to the a-axis, however there is a slight mechanical difference because of the three fold rotational symmetry rather than being transversely isotropic. The small change in observed frequency which might be expected is too small to discern however.

cleavage $\langle 1\,0\,\bar{1}\,1 \rangle$ **72°**

This is the cleavage direction for calcite and also the s-cut direction for sapphire. It shows birefringence.

3.4.2 Impact Tilt

The effect of impact tilt was simulated, and found to have a negligible effect on the measured birefringence for a 10 mrad tilt. The effect was beyond the precision of the calculation, which was much greater than the experimental precision. Beyond 10 mrad of impact tilt the light would not be collected by the polarimeter, so this was not simulated.

3.5 Chapter Conclusions

Given the variation in experimental predictions based on different sapphire literature, a error propagation method was implemented that used Monte Carlo methods to calculated expected errors. It was necessary to generate physically consistent variations of the elastic and photoelastic tensors, and this was achieved with PCA. The error analysis of sapphire literature values found that, although there were large discrepancies, the difference was

within three standard deviations based on the experimental error quoted in the literature data. This is a significant result as it shows that in the dynamic regime, small variations in tensor values lead to large changes in dynamic response.

The modelling of expected data sets has allowed an estimation of measurement error likely to be introduced by impact tilt. It is found that impact tilt is likely to be negligible when compared to experimental uncertainties inherent in a high speed measurement. This gives confidence to the findings of any experimental results. The development of the model and the results presented in this thesis are published in [3].

Furthermore, the development of Monte Carlo simulation of errors for anisotropic tensors will allow meaningful comparison of static experimental data with dynamic experimental data. This has not been achieved for the measurement of birefringence before.

Chapter 4

Measuring Calcite Birefringence with the 12.7 mm Bore Light Gas Gun

A series of experiments were conducted to measure the birefringence of calcite on the ISP's small 12.7 mm bore gas gun. Initial experiments were conducted by the author under the guidance of Dr. David Chapman, whilst experiment three was conducted by the author. Due to the small bore size the area of sample inertially confined to one dimensional strain is small (around 8 mm) which presents a challenge when fielding multiple optical diagnostics (PDV and polarimetry). The kinematic mounts and turning mirrors needed to align the polarimeter and PDV probe are larger than 10 mm, physically making it difficult to align both independently. The solution was to make the rear surface PDV probe co-linear with the polarimeter beam. These experiments on calcite showed that birefringence could be measured. It was necessary to improve the polarimeter accuracy using higher extinction ratio optics (10000:1 over 100:1) as well as using upshifted PDV (described in section 6.2) to increase precision in measurements of shock velocity and particle velocity to 0.5% in order to get accurate birefringence results.

Three experiments were conducted and the results are presented in this chapter. Shock

Shot	**Driver**	**Flyer**	l_0 **/ mm**	v **/ m s^{-1}**	u_p **/ m s^{-1}**	U_s **/ km s^{-1}**
P1	Copper	Copper	2.067±0.002	350±17	110±2	7.50±0.07
P2	None	PC	2.066±0.003	500±25	77±2	7.45±0.07
P3	Copper	Copper	2.078±0.004	250±13	115±2	7.50 ±0.07

Table 4.1: Summary of measured impact conditions for experiments one to three. The particle velocity, shock velocity values given here are for the first elastic precursor. sample thickness l_0 was measured with a micrometer before the experiment, and is used to calculate shock velocity.

Shot	σ_l **/GPa**	$\Delta n'$
P1	2.24±0.04	N/A
P2	1.51±0.04	-0.17210 ± 0.00005
P3	2.34±0.04	N/A

Table 4.2: Summary of calculated shock values for experiments one to three. Longitudinal stress is calculated using equation 2.1 using shock velocity and particle velocity data in table 4.1. The longitudinal stress values given here are for the first elastic precursor. birefringence is calculated using equation 2.25, in the case where a single wave structure was observed.

velocity and particle velocity are measured using PDV (the technique is described in detail in chapter 6) and a summary of experiments one to three is given in table 4.1. Longitudinal stress σ_l was calculated using equation 2.1, and birefringence using equation 2.25. The summary of these calculated values is given in table 4.2.

4.1 Facility Description

A full description of the facility is beyond the scope of this thesis so a brief outline will be given. For a full description see reference Eakins and Chapman [75]. The small bore light gas gun has a 12.7 mm bore barrel and is capable of firing at pressures up to 200 bar [75]. This gives an impact velocity of between 200 m s^{-1} and 800 m s^{-1} for a 6 g projectile (typical for a 2 mm thick copper flyer).

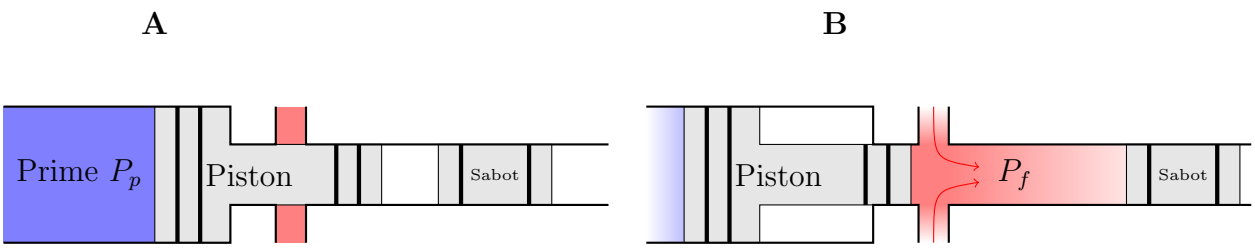


Figure 4.1: The piston is held in place by pressure behind the valve, whilst the firing gas is held in reservoirs either side. To fire, the rear chamber is dropped to vacuum, and the piston moves backwards. When the two side valves are open, the reservoirs empty behind the projectile, driving it forward.

4.1.1 Breech Design

The small bore gas gun had two configurable breeches, a reverse firing breech and a wrap around breech. Both of these breeches were used, as it was inconvenient to change them over and there was no experimental reason to choose one over the other for these experiments.

Reverse Firing

The reverse firing breech used a replaceable polycarbonate piston to act as a fast valve. An illustration is in figure 4.1. This design does not exert the sabot to excessive static pressure, and so allows a greater variety of sabot designs. Specifically hollow sabots can be used which are lighter and hence have a higher maximum impact velocity over solid sabots.

Wrap Around

For other concurrent experiments on the small bore gas gun, a new breech was designed which used the projectile itself as the valve. An illustration is shown in figure 4.2. This design allows a window to be placed in the rear of the breech so that an optical diagnostic such as PDV can be used on the rear of the sabot. Due to the sabot holding the full firing pressure, the sabots must not be crushed under this pressure. This restricts sabot design

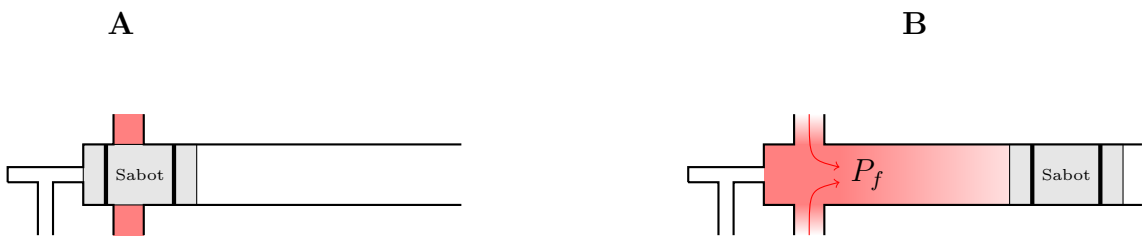


Figure 4.2: There is no piston, instead the sabot holds the pressure in the firing reservoirs back. To fire, the rear chamber is opened to a small chamber (pipe line) from the reservoirs and the projectile moves forward. When the two side vents are open, the reservoirs empty behind the projectile, driving it forward.

to solid sabots, increasing the minimum sabot weight, and hence reducing maximum velocity by around 100 m/s compared to the reverse firing breech.

4.1.2 Light Gates

Light gates were used on the 12.7 mm bore gas gun to trigger oscilloscopes and measure projectile velocity. The system uses two free space ThorLabs CPS635 laser diodes. directed at two bare fibre ends. The fibres collect light and this is detected outside the target chamber on two amplified photodiodes with a bandwidth of 100 MHz. The distance between the light gates is known, and two photodetectors record the time that the projectile blocks the light. Measuring the time between these events gives the projectile velocity and hence impact velocity at time of impact.

Errors

Estimating the distance between the light gates was achieved by using a micrometer, measuring the distance between the half signal points of the two gates. By this method the light gates were situated 11.5±0.5 mm apart, and taking the 50% signal level from the photodiodes as 'cut', then a temporal error of the order of 100 ns is introduced. Typical velocities are 300 m s^{-1} to 600 m s^{-1} so travel times are between 34.5 μs and 17.3 μs. Assuming errors are Gaussian then by this method by far the most dominant error source is the distance between the light gates which leads to an expected error on

velocity of about 5%.

Light gates do not detect if the projectile is still accelerating when it exits the muzzle, which can be a source of significant systematic error. Calibration shots using a PDV probe to measure projectile acceleration showed the projectile to have reached a constant velocity.

4.1.3 Test Targets

A number of test experiments were conducted to calibrate the gas gun's breech pressure to projectile velocity profile, as well as to test triggering and delay times. Aluminium plates and economy glass mirrors made suitable targets with impedances similar to calcite.

Sample	Thicknesses / mm			
	Flyer	*Driver*	*Sample*	*Glue*
P1	3.0±0.2	1.903±0.002	2.067±0.002	-0.005±0.004
P2	2.0±0.2	N/A	2.066±0.003	N/A
P3	3.0±0.2	1.905±0.004	2.078±0.004	0.07±0.09

Table 4.3: Dimensions of flyer and the layers in the target for all experiments. With a sample diameter of 12 mm a 0.004 mm variation in thickness corresponds to around 0.3 mrad of non-parallelism between the two faces. Glue layers are inferred by measuring sample and driver prior to glueing, and total thickness post-glueing. The negative glue layer thickness for sample P1 is due to the glue thickness being below the precision of this method.

4.2 Calcite Experiment One

A preliminary test experiment on an aluminium plate demonstrated that the triggering off the first light gate was effective, and a delay of 100 μs caught the impact event on the oscilloscopes, which had a 500 μs recording window. A 2 GHz bandwidth Tektronics 7254 sampling at 5 GS/s recorded both the PDV and the polarimeter data. The PDV channel used 100 mV/div at 50 Ohm impedance and the polarimeter used 2 mV/div on the vertical scale, also with 50 Ohm impedance. The target velocity was 300 m s^{-1}, which was measured with the light gate error of ±15 m s^{-1}.

4.2.1 Experimental Setup

The first experiment was performed with a copper driver on the calcite sample. Dimensions of the target are given in table 4.3. A copper flyer was used as the impactor and the impedance calculation is shown in figure 4.4.

Several challenges presented themselves when setting up for the experiment and a full layout is shown in figure 4.3. The height of the polarimeter components did not match the height of the barrel, so a longer optical path was needed to pitch the polarimeter beam down. Furthermore the target was aligned with the barrel laser, and then the diagnostics aligned to the target. Aligning the PDV probe required moving the dichroic mirror, which altered the polarimeter beam path. Iteratively an optimum was achieved,

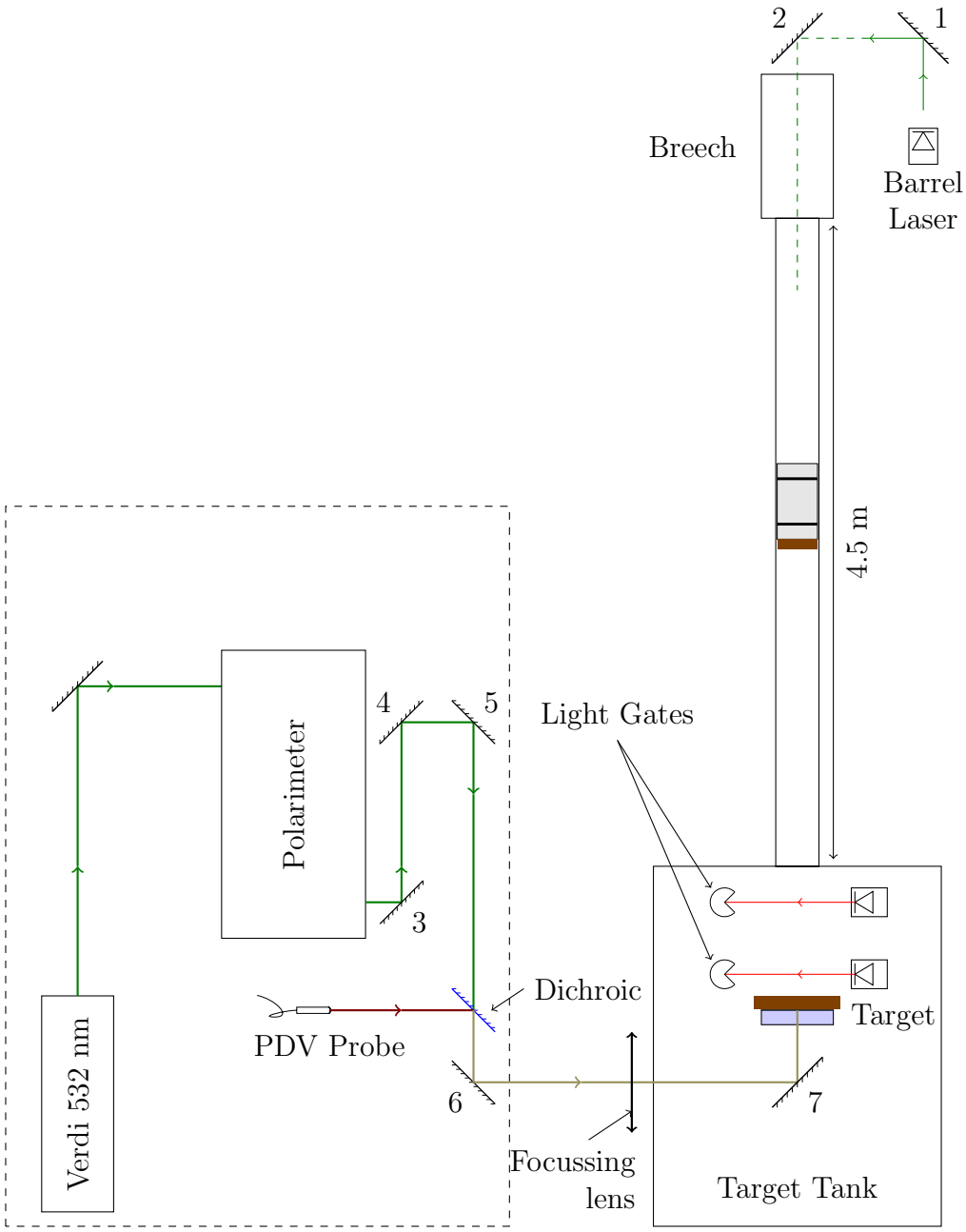


Figure 4.3: Setup of small gas gun room, not to scale. A barrel laser can be aligned down the barrel with mirrors 1 and 2, and is useful for aligning a mirrored target by aligning the target so that the reflected beam is also aligned down the barrel. Due to the optical height difference between the polarimeter and the barrel, an optical relay was needed to lower the beam (mirrors 3 – 5). The PDV was made co-linear at the dichroic mirror. A lens was introduced to improve collection efficiency, however the lens was optimised for 532 nm light, so the target was not at the focal point for the PDV probe. The lens was also mounted between the alignment mirrors 6 and 7, which were used to bring the light in normal to the target.

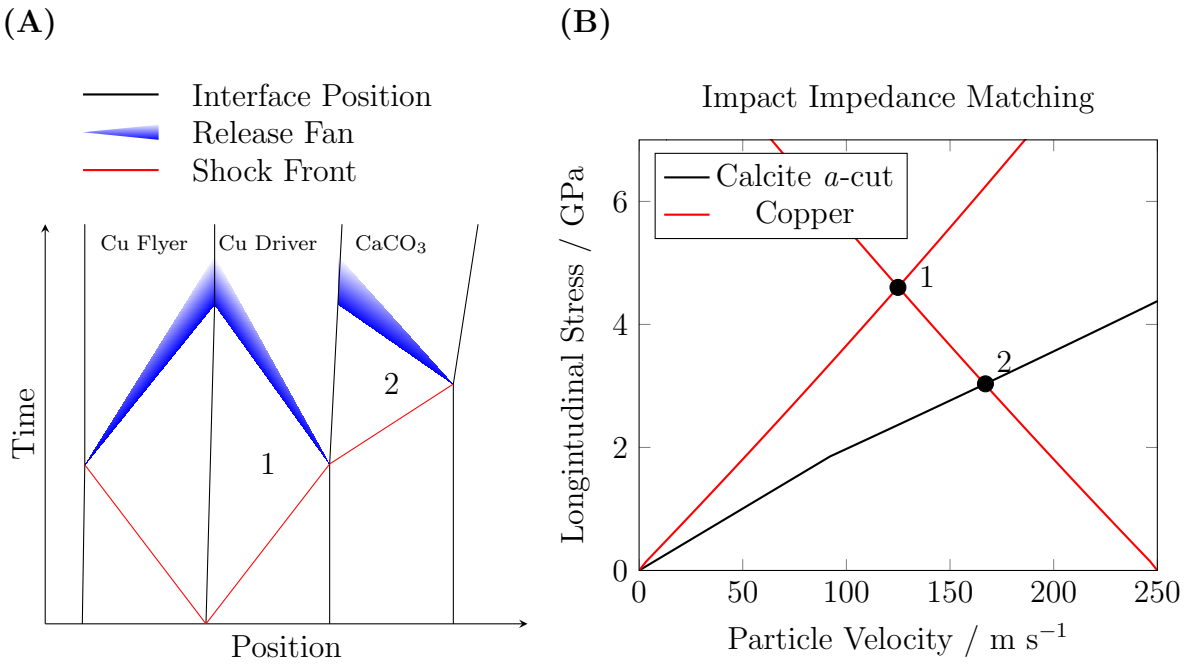


Figure 4.4: **A:** The x-t diagram for the impact in calcite experiment one. The initial shock creates a state (1) in the copper driver. When this shock reaches the calcite interface a release is reflected and a shock transmitted creating a state (2) in the calcite. **B:** The states 1 and 2 are determined using impedance matched Hugoniots, with Hugoniot data from Marsh [65] (see figure 2.2). For the two copper – copper impacts the first state is the copper – copper intersection, and then the copper releases to the calcite – copper intersection. The release curve is assumed to be the same as the Hugoniot as for low pressures, the annealed Oxygen Free High Conductivity (OFHC) copper Hugoniot closely matches the isentrope.

and signal was increased by using a convex lens to focus the polarimeter and PDV onto the target. The alignment procedure, with reference to figure 4.3 was as follows:

1. Align barrel laser to barrel using mirrors 1 and 2.
2. Insert target into target mount and align target such that barrel laser reflected back up the barrel.
3. Align polarimeter laser to target using mirrors 3 and 4.
4. Align PDV to rear surface using the probe mount and dichroic mirror.

Polarimeter

The polarimeter for this experiment was setup as in figure 4.5. Circular polarised light was launched into the target using a ThorLabs linear polariser LPVISB050-MP2 and a quartz multi-order quarter wave plate WPMQ10M-532. A Thorlabs polarising beam splitting cube PBS251 was used to detect $\pm 45^{o}$ polarised light. A Beam Intensity Monitor (BIM) was also added to detect the overall beam intensity. Thorlabs BS013 50:50 Beamsplitting cubes were used as they had a lower polarisation dependence than other beam splitting optics. Typical plate beamsplitters polarise transmitted and reflected light to an extinction ratio of 1:2. Cube beamsplitters polarise to an extinction ratio of 1:1.1, twenty times less polarised than plate beamsplitters.

4.2.2 Results

In the rear surface PDV shown in figure 4.6, a second wave travelling at 4.78 km s^{-1} was observed. An elastic precursor from the copper driver was also observed in the velocity profile from the impact surface. The final stress state was above the HEL and known calcite-II transition for this material.

The loss of polarimeter signal after 40 ns and the loss of PDV signal from the impact surface after 100 ns was thought to be due to impact tilt. Later work suggests this may be more likely due to a loss of transmission in calcite at higher pressures.

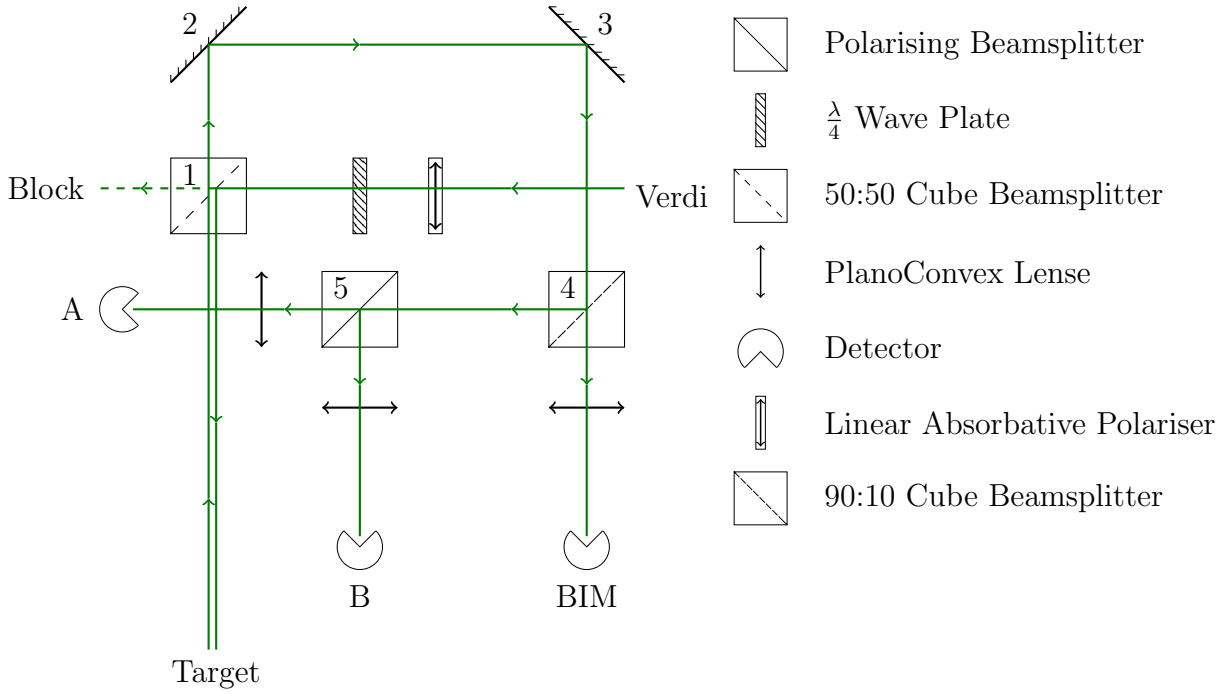


Figure 4.5: Design of the polarimeter used in the first experiment (not to scale). The input Verdi beam is converted to circular polarised light prior to reaching beam splitter 1. Half the light is reflected towards the target, and the other half is put into a beam dump. Light collected from the target passes back through beam splitter 1, and is reflected via mirrors 2 and 3. These were used to align the reflected beam onto beam splitter 4 and the BIM. 90% of the light is reflected from beam splitter 4 towards polarising beam splitter 5, where the S and P components are separated onto their respective detectors. Detectors used were Thorlabs Det10A detectors which are unamplified silicon photodiodes with a 1 GHz bandwidth.

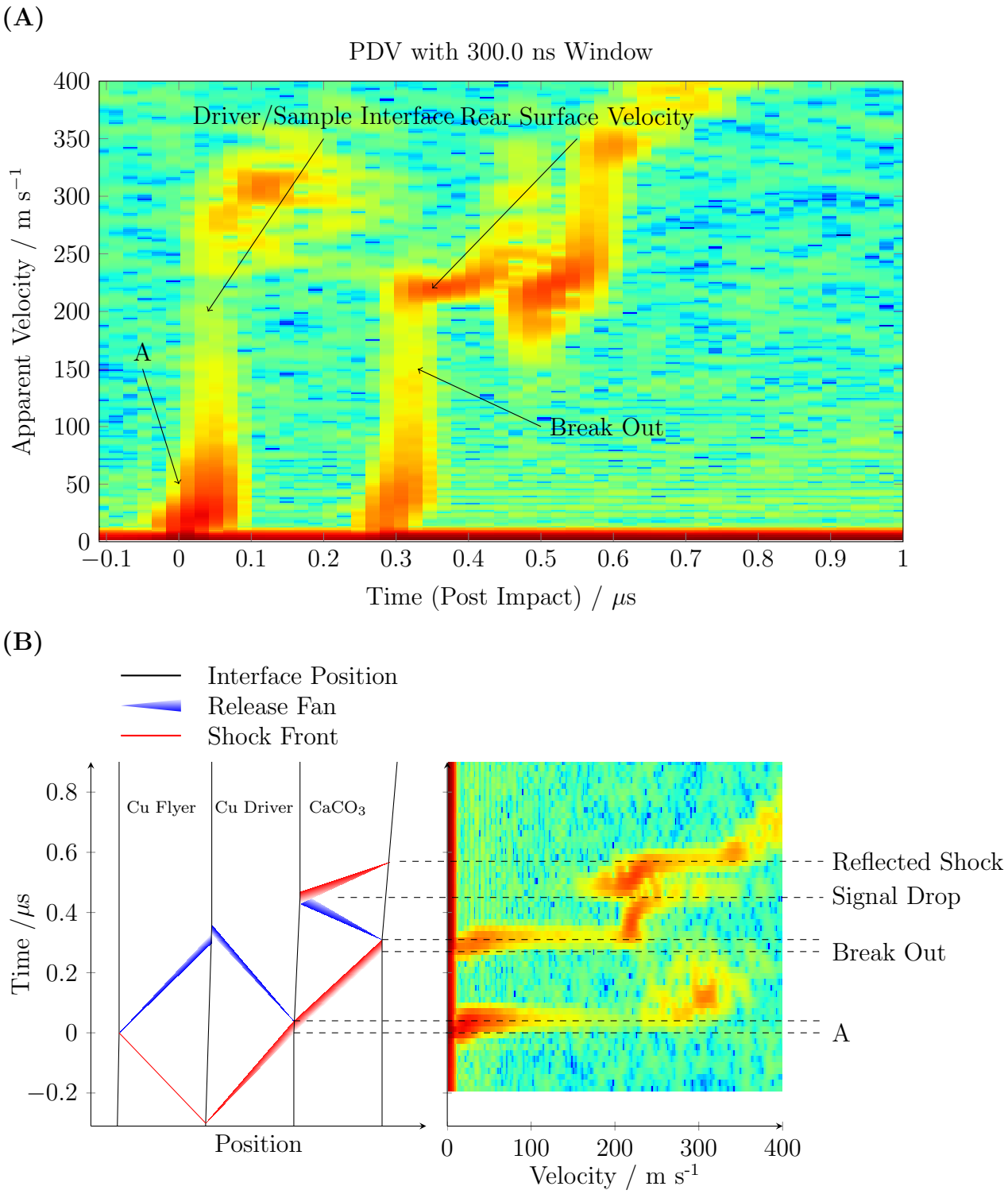


Figure 4.6: In this first experiment a copper driver was used. In the PDV spectrogram **(A)** a small ramp precursor is visible, labelled A and arriving around 100 ns before the main shock with an amplitude of approximately 15 m s^{-1}. This is most likely due to strength in the copper driver which, whilst low, is not negligible for these low pressure impacts. The signal from the impact surface is lost after 200 ns. This could be due to the material becoming opaque or could be increased scattering caused by cracking and failure. It is approximately coincident with the calcite release reaching the copper – calcite interface, as shown in **(B)**.

4.2.3 Summary

PDV data and polarimeter data were successfully recorded, demonstrating that the experimental technique worked. However, the elastic precursor from the copper driver as well as the calcite – calcite II transition caused a complex wave structure in the sample. This violates the single wave assumption necessary for the birefringence measurement, so although the polarimeter recorded data, it is not possible to convert this to a birefringence.

From a practical point of view, combining the PDV with the polarimeter beam made setting up this experiment extremely time consuming. A lens was added to focus the polarimeter and PDV onto the target, however chromatic aberration over the 532 nm to 1550 nm wavelength difference is significant, even with a standard achromatic lens, and the anti-reflective coating on the lens is not optimised for both 1550 nm and 532 nm. It is also not desirable to use a focussed polarimeter, as the birefringence measurement is a measure of the total birefringence along the optical path. If the beam is focussed then there is a greater variation in optical path length through the material (rays at the edge of the beam are focussed at an angle through the sample, increasing the path length).

4.3 Second Calcite Experiment

Using a polycarbonate flyer the final stress state in the calcite was reduced to below the HEL and calcite-II transition, and polarimetry data were recorded for 200 ns, shown in figure 4.9. It was found during the analysis that it was difficult to determine the polarisation state more generally as each detector did not act as a vector. This was due to the use of linear polarising filters. As these filters are absorptive filters, there is a loss of information at the filter, and in the system, particularly in the circular detector path, as well as the polarising beam splitting cube not splitting the polarisation states uniformly. This leads to an experimental error which varies with polarisation state, and is difficult to quantify.

4.3.1 Experimental Method

In order to reduce the time taken to setup the experiment the PDV relay was redesigned. Rather than a collimating probe, a 100 mm focussing probe was used and the focal point relayed using a large biconvex lens as in figure 4.7. This lens could be moved to adjust the focal point, and was before the dichroic mirror so it did not interfere with the polarimeter beam. A two mirror adjustment for the PDV was achieved with mirrors 1 and 2 in figure 4.7 and for the polarimeter two mirrors between the polarimeter and the PDV board gave independent alignment. Another pair of mirrors after the dichroic, mirror 3 in figure 4.7 and the final turning mirror before the target, allowed both beams to be aligned onto the target together.

Polarimeter

The polarimeter was extended to include a circular channel as shown in figure 4.8. This was achieved using a beam splitting cube followed by a waveplate and linear absorbing polariser with a 1000:1 extinction ratio. The BIM was kept but the overall path length was reduced as much as possible. This was to avoid the need for a lens to collect light

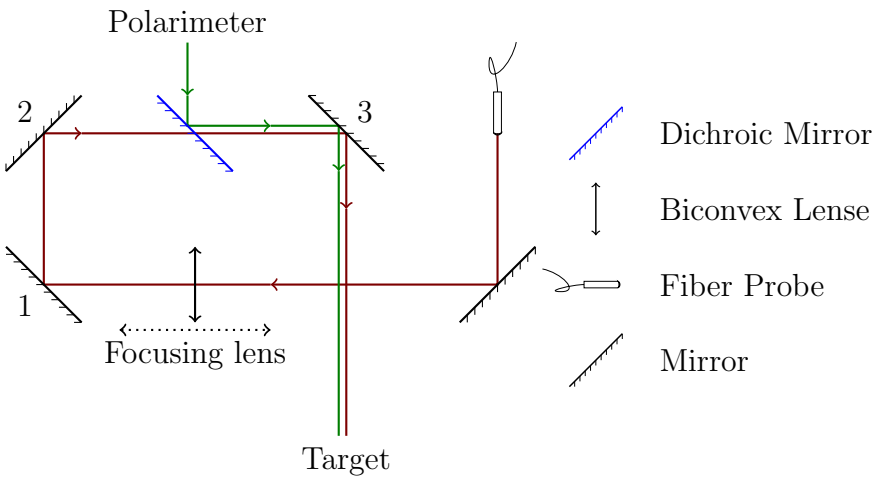


Figure 4.7: Method for making the polarimeter and PDV co-linear. A focussing PDV probe was used so a biconvex lens was used to relay the focus onto the target. The biconvex lens can be moved along the beam path to adjust the focus of the PDV. As the polarimeter is collimated, there are no lenses on the polarimeter beam path. A two mirror alignment with mirrors 1 and 2 after the lens allows the PDV alignment to be adjusted. Mirrors for aligning the polarimeter are placed before this breadboard.

from the sample.

4.3.2 Results

With the modifications from the experimental design of experiment one, the polarimeter recorded data for significantly longer, and the data is shown in figure 4.9. The linear 45° channel did not record any data. It is also noticeable that the BIM channel is polarisation sensitive, as it records an oscillating signal with the same frequency, but different phase, as the circular channel.

The rear surface PDV in figure 4.10 showed a single wave structure, indicating that the data can be used to measure the shocked birefringence.

4.3.3 Summary

When attempting to quantify errors on the polarimeter, it was found that using linear polarising absorptive filters on polarimeter channels made it difficult to accurately determine errors. This was due to a loss of information introduced by the absorption. It is

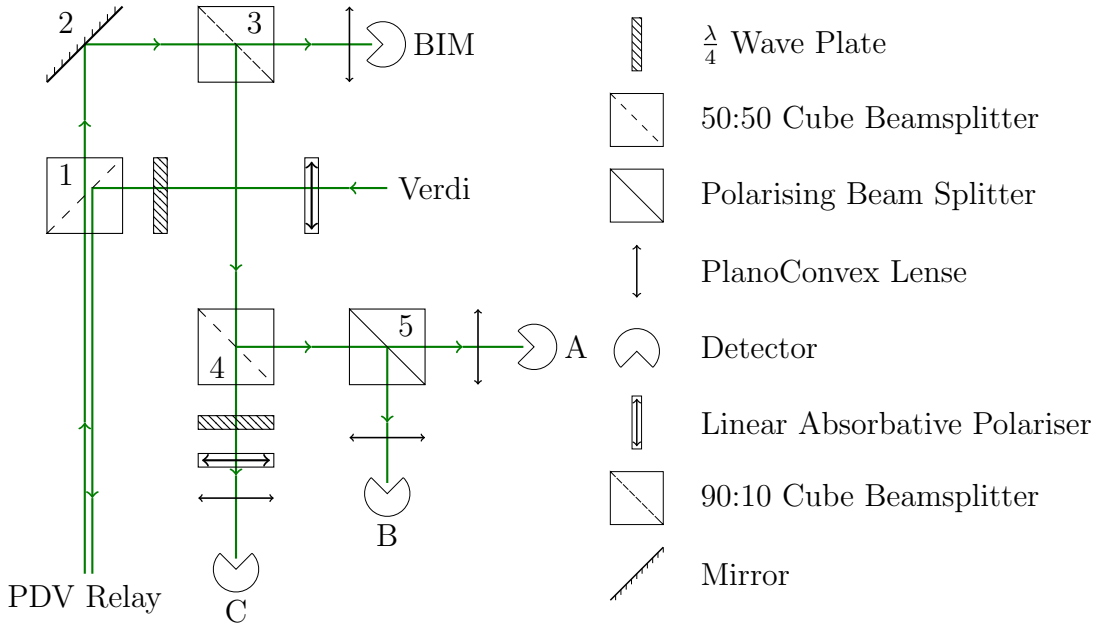


Figure 4.8: Design of the polarimeter used in preliminary experiment two. A new circular detector (detector C) was added that used a linear polarising filter and wave plate to measure the circular component.

impossible to tell the difference between a low intensity unpolarised beam and a higher intensity partially polarised beam. Because of this ambiguity, it was difficult to determine a degree of polarisation, hence unpolarised light may be recorded as polarised. The polarising beam splitting cube also had non-symmetric extinction ratios (10:1 for transmitted vs. 100:1 for reflected), and so the polarisation states detected were not strictly orthogonal.

During the alignment procedure it become apparent that a small amount of light from the polarimeter was leaking into the PDV probe through the dichroic mirror. This caused concerns as the PDV detectors are sensitive and easily damaged by more than 5 mW of incident light, and the polarimeter was using 2 W.

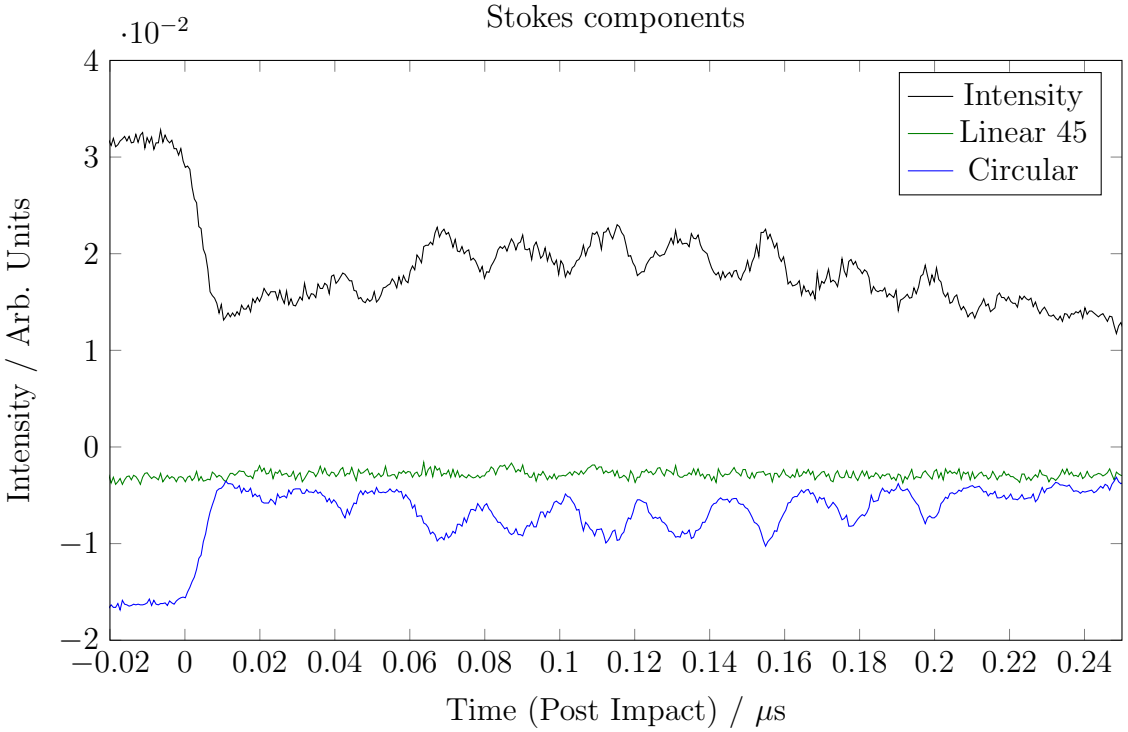


Figure 4.9: Polarimetry data for preliminary shot two. The signal was recorded for significantly longer than shot one and without a copper driver there was no observed preliminary ramp as in experiment P1. The oscillation in polarisation caused by varying birefringence and path length can have its frequency estimated by using a Fast Fourier Transform (FFT). The intensity component measured by the BIM in figure 4.8 has a polarisation dependence, as evident by its oscillation at the same frequency as the circular component. By comparing the detector channel directly, the phase of the oscillation is different, indicating it is a real polarisation effect rather than an oscillation in light intensity.

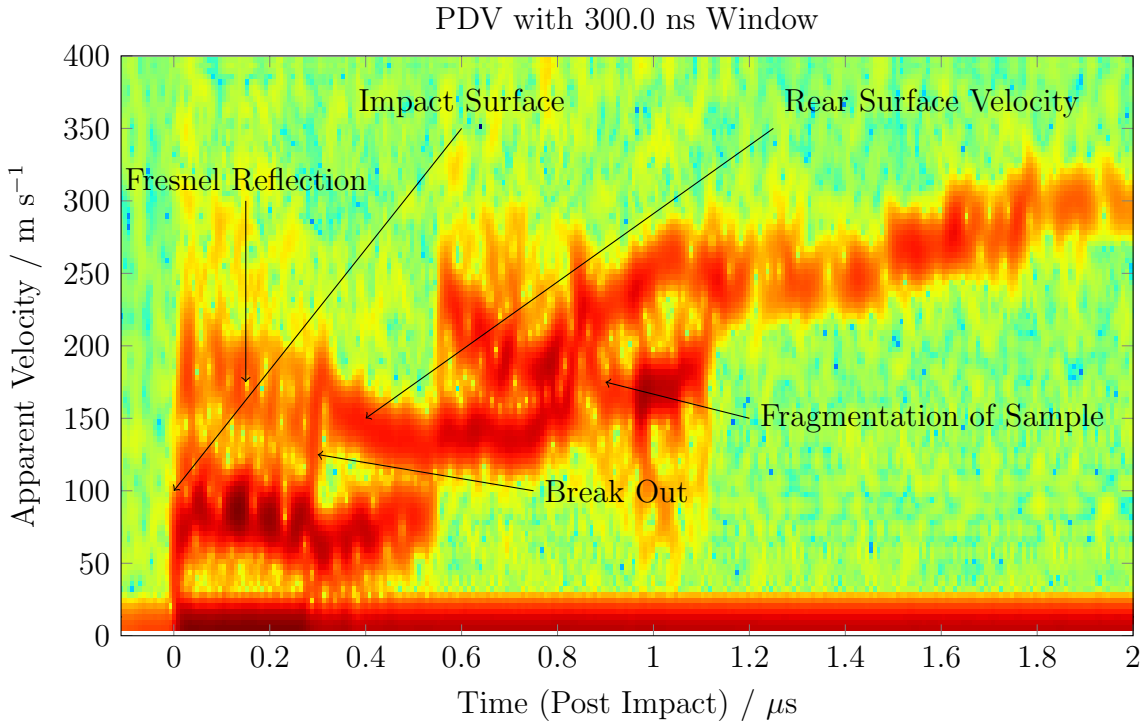


Figure 4.10: PDV spectrogram with short time window for preliminary experiment two. The single wave structure with no preceding ramp can be seen clearly at the impact surface. Strong Fresnel reflections inside the sample can be seen as velocity components which are of lower intensity and twice the velocity of the base velocity. The reflection from the impact surface marked feature A shows a beat in intensity. This is caused by the two refractive indices in calcite giving rise to two very close frequencies. The temporal velocity resolution of this PDV data set is not high enough to resolve the two frequencies. For this reason an upshifted configuration (see section 6.2) was used in later experiments.

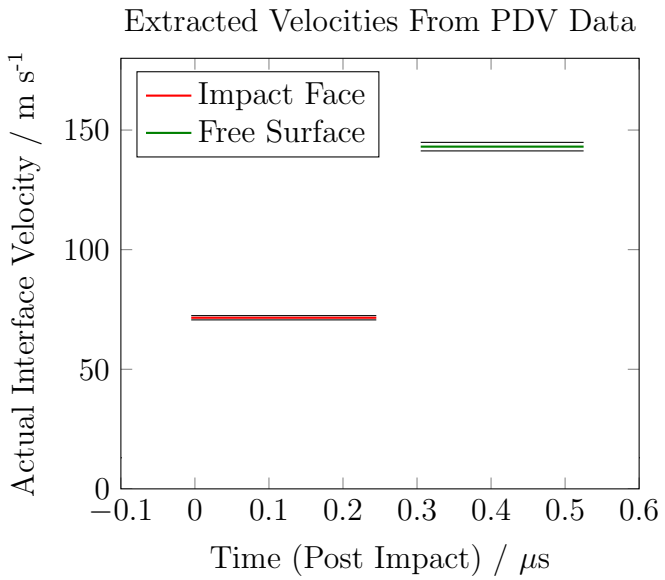


Figure 4.11: Fitted free surface velocity from spectrogram in figure 4.10 and calcite/driver interface velocity corrected for calcite's refractive index. The black lines represent one standard deviation. The velocity is the average spectrogram peak across the entire time of the fit.

4.4 Third Calcite Experiment

4.4.1 Experimental Method

The PDV board design was effective and so was kept identical apart from the addition of a 1550 nm laser line filter in front of the fibre probe. This was to protect the PDV detectors from any 532 nm light passing through the dichroic mirror. The line width of the filter was 5 nm.

The target had a copper driver, as several targets with copper drivers were prepared prior to experiment one. A copper flyer was used as in experiment one, to give a symmetric impact. A symmetric impact gives the most accurate shock state, as the particle velocity must be half the impact velocity by conservation of momentum. This required a low muzzle velocity, which was problematic. A low velocity requires a low firing pressure, and at low firing pressure the error on expected muzzle velocity is relatively high (around 10%).

Polarimeter

An updated polarimeter was built which used two Wollaston prisms to detect orthogonal polarisation states, and a wave plate so that one Wollaston prism probed left and right circular polarisation states. As all light into the system ended on a detector, there was no requirement to use a BIM. The Wollaston prism has identical extinction ratios of 10000:1 for each polarisation, an improvement of 10^2 over the polarising beam splitter.

4.4.2 Results

The PDV showed a large drop in signal immediately after impact and break out. It was suspected that a large impact tilt lead to the diagnostics going out of alignment. There was no data recorded on the polarimeter.

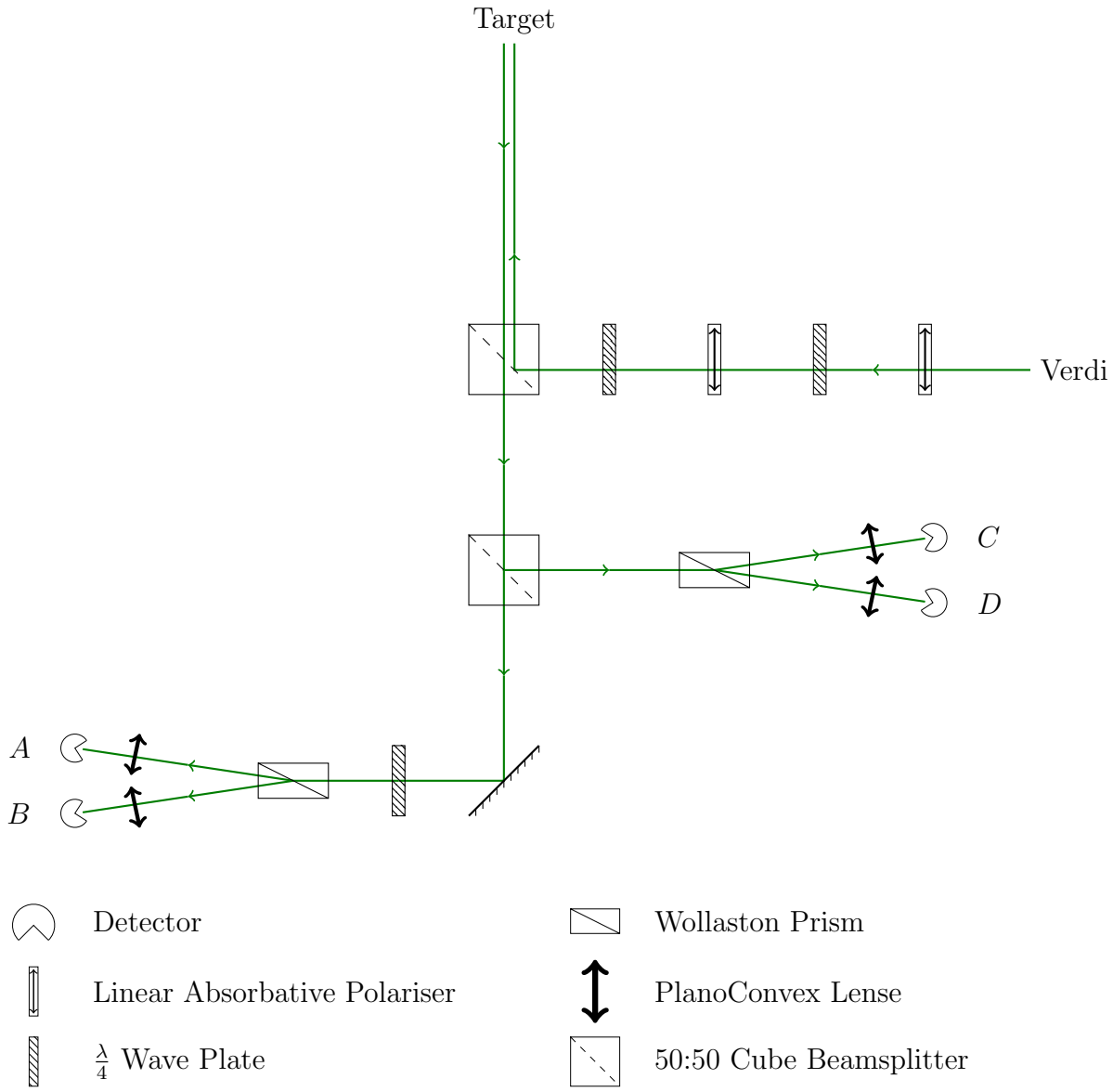


Figure 4.12: This setup of the polarimeter avoided the need for a BIM, whilst measuring more polarisation states. Channels C and D are linear polarised channels and are orthogonal to each other. As the sample is mounted with its optical axis at 45° to the Wollaston prisms, subtracting the intensity at C from the intensity at D gives the linear 45° stokes component. Channels A and B use a quarter wave plate before the Wollaston prism and so measure the left and right handed circular components. Subtracting A from B gives the circular stokes vector component. Summing all four detectors gives the total intensity, hence the first stokes vector component.

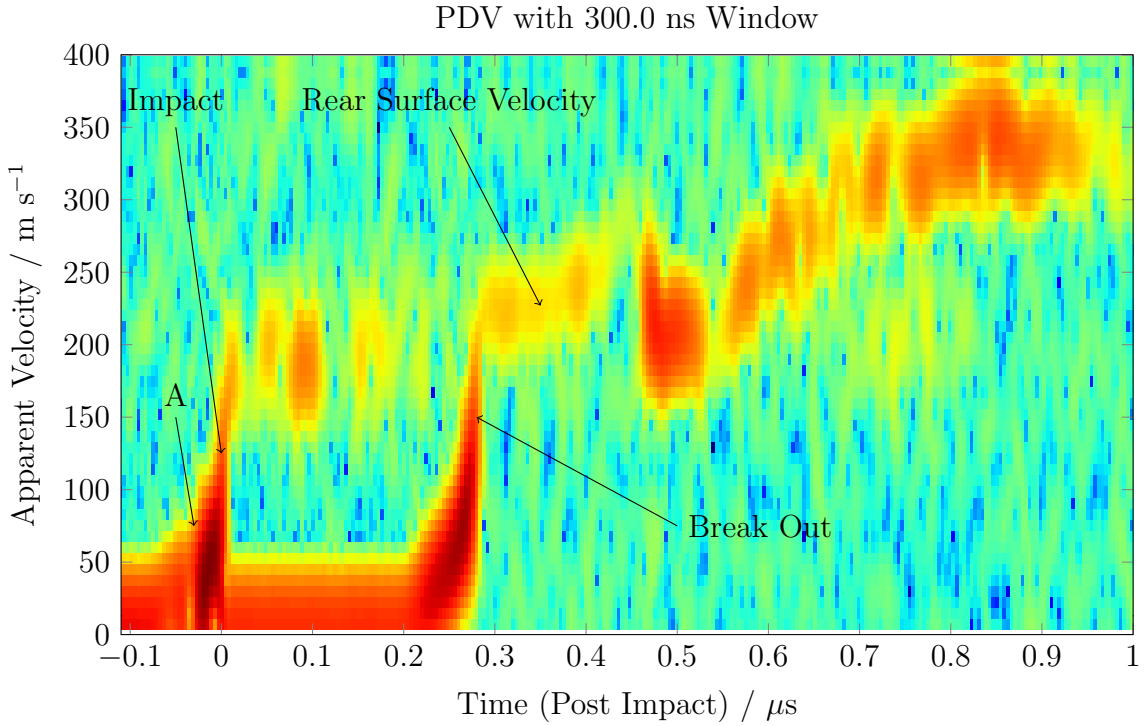


Figure 4.13: An generation three configuration (see section 6.2) was used for experiment three, improving resolution on the Short Time Fourier Transform (STFT). The signal detected from the moving impact surface and the moving rear surface is significantly lower than the stationary signal intensity. This result is consistent with a high impact tilt moving the reflected beam outside of the collection optics. Only diffuse reflections would have made it back into the PDV optics, and as both surfaces are strong specular reflectors, the diffuse component is very low. There is a signal drop out at 0.45 μs, the same time as in experiment one, indicating a real effect rather than laser speckle. This time point is consistent with lateral release waves reaching the centre of the target, ending the one dimensional state and accelerating the sample further, or it may be due to sample fracturing completely and the velocity measured is the final velocity of the sabot.

4.4.3 Summary

There was no signal detected on the polarimeter, and a very weak signal on the PDV. It was suspected that the impact tilt was unusually high, and the polarimeter was moved out of alignment, possibly due to the long flight time (around 100 μs) of the projectile. The flight time between the projectile leaving the muzzle and impact was high for two reasons, firstly the low velocity of the shot, and secondly the large distance (nearly twice the sabot length) needed for the light gates. This prompted the move to the large bore gas gun where tilt could be more easily measured, and the free flight distance of the sabot would be lower (in comparison to the length of the sabot).

4.5 Discussion

Experiment P2 showed a single shock wave and polarimetry was recorded on the circular channel. Using equation 5.6 the birefringence in the shocked region was calculated to be $\Delta n' = -0.17210 \pm 0.00005$. This represents a very low change in birefringence under shock compression for calcite, an unusual result. The prediction presented in chapter 3 predicts a birefringence value of $\Delta n' = -0.17262 \pm 0.00007$. This is a significant deviation from the prediction of -0.52$\pm$0.07$\times 10^{-3}$.

This series of experiments demonstrated that using birefringence very precise measurements of refractive index differences can be made. This is because the technique is inherently a difference measurement, directly measuring the difference between the two refractive indices, rather than individually measuring each and subtracting.

4.6 Conclusions and Further Work

In experiment one, a polarimeter signal consistent with birefringence was observed. With modifications to the setup from experiment one, experiment two demonstrated a much improved measurement method. However it was suspected that tilt on this gas gun was

Shot	**Driver**	**Flyer**	v / **m s^{-1}**	u_p / **m s^{-1}**	U_s / **km s^{-1}**	$\Delta n'$
P1	Copper	Copper	350 ± 17	110 ± 2	$7.5 - \pm 0.07$	N/A
P2	None	PC	500 ± 25	77 ± 2	7.45 ± 0.07	-0.17210 ± 0.00005
P3	Copper	Copper	250 ± 13	115 ± 2	7.50 ± 0.07	N/A

Table 4.4: Summary of results for preliminary experimental work.

an issue, and as the bore was too small to permit an accurate tilt measurement, further experiments would need to be conducted on a larger bore gas gun.

Birefringences have been calculated here in table 4.4 using a single step wave model outlined in section 2.6.1. As in experiment one the PDV indicated this single wave assumption was wrong, the above birefringences are subject to an unknown systematic error. The key improvements from these experiments were:

- Removing the copper driver and performing direct impact experiments. This was done as all experiments with copper drivers showed an initial precursor motion, so a single step wave shock was not a realistic model.

- Adding 2 circular channels to the polarimeter so that birefringence could be directly measured, regardless of sample orientation.

- An Anti-Reflective (AR) coating at 532 nm was added to the sample rear surface to reduce polarimeter back reflectance.

Tilt could not be measured in any of these experiments. Based on the results from experiment three tilt may be a serious issue and it would be beneficial to measure this in future experiments. A larger target would be needed, hence the large bore gas gun was used for future experiments.

Chapter 5

Final Configuration of High Speed Polarimeter for Shock Physics Applications

A polarimeter is an experimental instrument for measuring the polarisation state of a light beam. There are several distinct approaches to achieving this measurement. The simplest design is to use a rotating polarisation element and record the change in intensity on a detector. This is cost effective and also very accurate as long exposures drastically increase the precision of the measurement. However, these techniques are not suitable for high speed applications where the polarisation varies in time. Division of amplitude polarimeters are preferred for this as they record several states simultaneously. However they are not as precise as the rotating element polarimeters, as they only record intensity at a small number of polarisations, rather than sampling at many.

Many high speed polarimeters are designed for performing ellipsometry measurements. These measurements occur at an oblique angle of incidence with the sample. Because of this the input polarisation optics are separate to the polarimeter. However for birefringence measurements a normal incidence polarimeter is required, and the input polarisation must be separated from the output using a beam splitting cube. This introduces

unique challenges not encountered by other division of amplitude polarimeters as some input polarisation light will leak into the polarimeter, and this source of systematic error must be quantified. High speed polarimeters [34] are limited by detector technology. Typically at 532 nm the fastest photodetectors are silicon based photodiodes and operate at a bandwidth of 2 GHz.

The final setup of the polarimeter as used in the large bore gas gun experiments in chapter 7 is presented here. A series of static calibration measurements and dynamic demonstration experiments on the small 12.7 mm bore gas gun were performed prior to large gas gun shots.

Economy mirrors were used as demonstration targets because the shock impedance of glass is similar to calcite and they provide a similar sample geometry with an aluminium surface and optically transparent sample. The glass was soda-lime float glass. Mirrors were used to validate the final polarimeter setup prior to use on the large bore gas gun. The polarimeter was set up with a comparable path length to that used in large bore gas gun experiments (around 1 metre). By avoiding the light gates and placing the target as close as possible to the muzzle, a signal was recorded on the polarimeter, capturing release.

Many free space shock physics diagnostics use imaging to reduce the sensitivity of the instrument to sample tilt. A large low F-number lens close to the target collects as much light from as wide an angle as possible. This collected light is focused onto successive optical elements and finally the detectors. The polarimeter developed in chapter 5 specifically uses collimated light so that path length and angle of incidence effects on polarisation are negligible. Demonstrating that the polarimeter could record a signal in a dynamic experiment and that therefore small tilt was not a problem, was an important validation step for an instrument which did not image the light.

5.1 Experimental Configuration

As described in chapter 4, earlier implementations of the polarimeter had absorptive filters to detect the polarisation. As the absorptive system has different total light intensity falling on the polarised detectors for different polarisations, the signal to noise varies significantly with polarisation. For the rapidly oscillating polarisation that is produced in the experiments, the varying signal to noise leads to a large error in calculating the optical axis. The optical axis calculation is described in section 2.6.2. Using the same number of detectors a more accurate design, shown in figure 5.1 uses two pairs of detectors, with each operating in a pair detecting orthogonal polarisation states. This gives a constant signal to noise across the Stokes component detected by a given detector pair. Whilst the circular channels are sufficient for a birefringence measurement, the linear channels allow a determination of the angle of the optical axis.

The source for the dynamic experiments was a 2 W Coherent Verdi operating at 532 nm. The Verdi is linearly polarised, and is passed through an arbitrarily orientated periscope prior to entering the polarimeter. This means the polarisation is linear, however the orientation is not known. The first linear polariser, element 1, is used to fix the input polarisation into a known (vertical) orientation. The first waveplate, element 2, then gives circularly polarised light. This allows the orientation of polariser θ to be rotated without impacting the intensity of light, important for calibration measurements. In dynamic experiments, the elements 1 and 2 are removed and the input linear polariser LP1 is set to angle θ to give circular polarised light and this setup is shown in figure 5.2.

The marked back-reflections in figures 5.1 and 5.2 are important because they pass through a wave plate (WP1). This leads to a rotation of the polarisation state. In the static configuration (used to calibrate the polarimeter and the samples prior to dynamic experiments) as elements are rotated the effect on the input polarisation state is not linear because the interference generated by the marked back-reflection (the input light is coherent) creates components of the polarisation which rotate at higher frequency. As

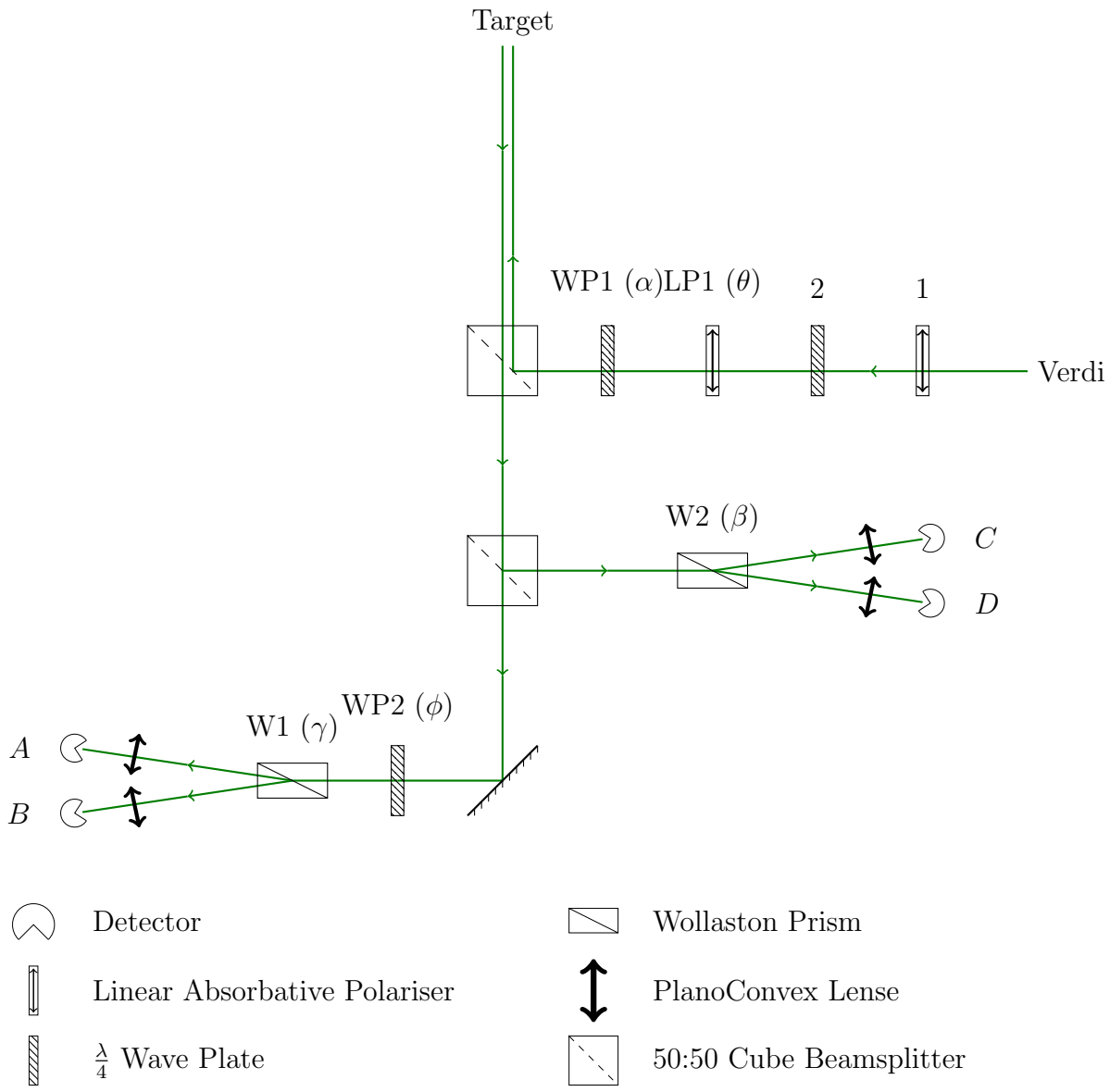


Figure 5.1: The setup of the polarimeter for static calibration of large gas gun experiments, with significant back reflections marked as dotted lines. Each detector pair, AB and CD, detect orthogonally polarised light. The detectors are ThorLabs DET10A silicon photodiodes with a 10 V reverse bias 0.8 mm^2 active area and 1 ns rise/fall time. The linear polariser LP1 and quarter waveplate (analyser) WP2 are in rotation mounts and have their angle set at angles θ and ϕ respectively prior to the experiment. The input quarter wave plate WP1 and two Wollaston prisms W1 and W2 are fixed and their relative angles (α, β and γ respectively) need to be determined. It is convenient to set $\beta = 0$ and quote all angles relative to β.

the wave plates were designed for 532 nm wavelength light at normal incidence, and the beam splitting cubes are only polarisation insensitive at normal surface incidence, tilting the optics so that back-reflections did not propagate in the system was not an option. All optical elements were AR coated to 0.5% at 532 nm. This gave an error in optical axis angle of around $\pm 4^{o}$.

5.2 Calibration

The polarimeter needs to be calibrated. Mathematically this is the process of determining the matrix $\underline{\mathbf{M}}$ in equation 5.1 which relates the optical intensity I detected at each detector to the Stokes vector S.

$$\underline{S} = \underline{\mathbf{M}}\ \underline{I} \tag{5.1}$$

For an ideal four channel polarimeter sensitive to circular and $\pm 45^{o}$ light, the matrix $\underline{\mathbf{M}}$ would be

$$\begin{pmatrix} 1 & 1 & 1 & 1 \\ 0 & 0 & 0 & 0 \\ 0 & 0 & 1 & -1 \\ 1 & -1 & 0 & 0 \end{pmatrix} \tag{5.2}$$

.

However for an arbitrary orientated linear detector on the polarimeter, equation 5.3 gives a better estimate of $\underline{\mathbf{M}}$.

$$\begin{pmatrix} 1 & 1 & 1 & 1 \\ 0 & 0 & \cos(\alpha-\beta) & -\cos(\alpha-\beta) \\ 0 & 0 & \sin(\alpha-\beta) & -\sin(\alpha-\beta) \\ 1 & -1 & 0 & 0 \end{pmatrix} \tag{5.3}$$

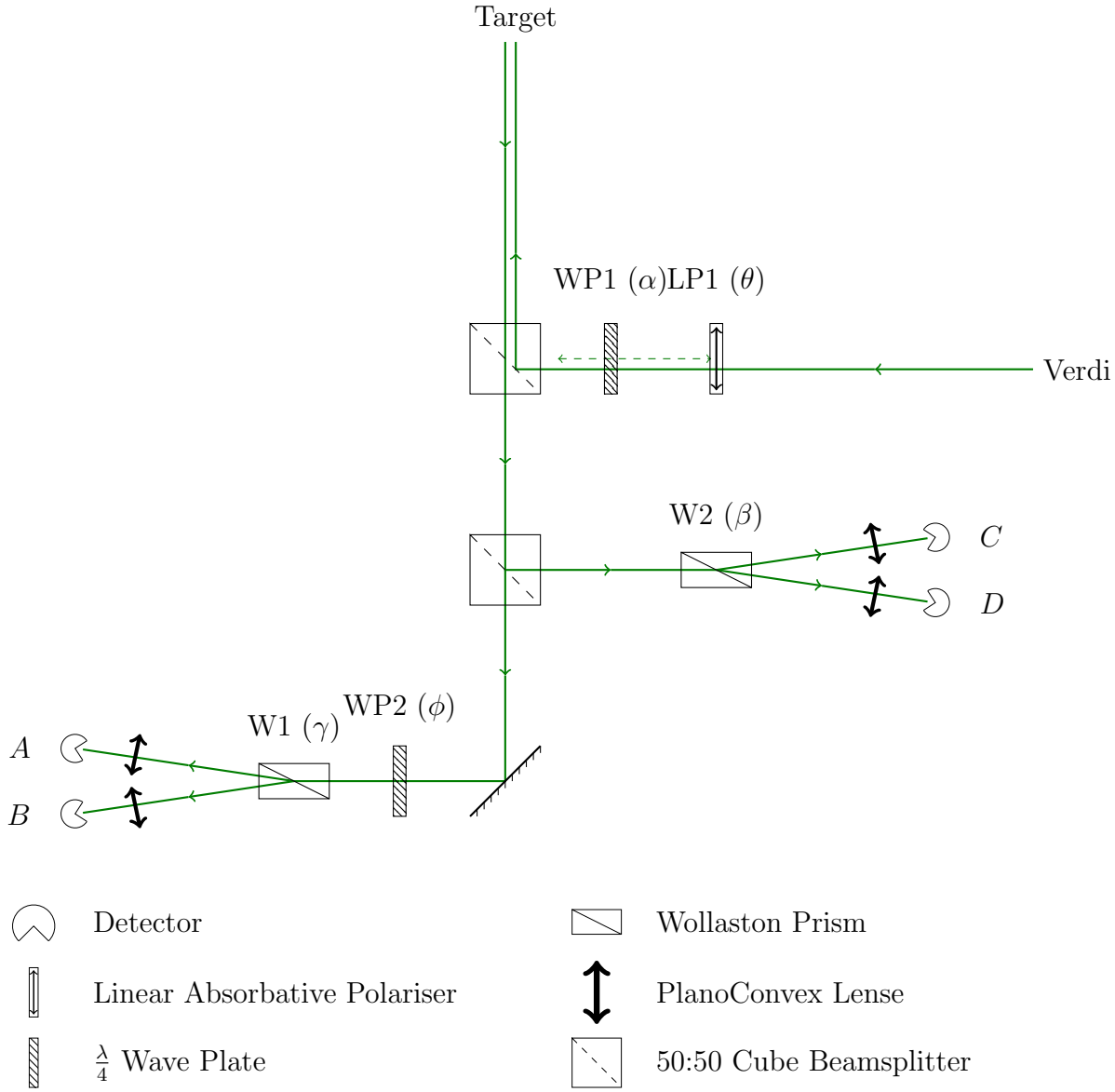


Figure 5.2: The setup of the polarimeter as used in the large gas gun experiments, with significant back reflections marked as dotted lines. Each detector pair, AB and CD, detect orthogonally polarised light. The linear polariser LP1 and quarter waveplate (analyser) WP2 are in rotation mounts and have their angle set at angles θ and ϕ respectively prior to the experiment. The input quarter wave plate WP1 and two Wollaston prisms W1 and W2 are fixed and their relative angles (α, β and γ respectively) need to be determined. It is convenient to set $\beta = 0$ and quote all angles relative to β.

The detectors were demonstrated to be linear up to 2 W (the light intensity range available). The damage threshold for the detectors was nominally 5 W, as stated by the manufacturer. The intensity variation was achieved by rotating a half wave plate at the laser output, and then passing the beam through a polarising beam splitting cube. The transmitted intensity then varied as the cosine squared of the half wave plate angle.

Within the polarimeter however, the beam splitting cubes are not necessarily perfectly 50:50 and the detectors do not necessarily have the same gain. To measure the relative gains of each polarimeter channel, the total intensity (derived from the half wave plate angle) vs. each individual detectors measured intensity I_n (normalised against the sum total of all detectors intensities $\frac{I_n}{I_A+I_B+I_C+I_D}$) is plotted in figure 5.3 and a least square fit performed. The gradient of the least squares fit gives the relative gains G_n. It is necessary to normalise each detector to the sum total of all detectors so that any polarisation dependence of the gains is negated. This gives the pre-factor with which to normalise the detector intensities in the polarimeter, which represents both the variation in gain of each detector and the variation in transmission and reflection of the beam splitting cube (labelled 4 in figure 5.1). This second matrix must have a determinant of one. This is now a complete model detector matrix for the polarimeter, given in equation 5.4.

$$\underline{\mathbf{M}} = \begin{pmatrix} 1 & 1 & 1 & 1 \\ 0 & 0 & \cos(\alpha-\beta) & -\cos(\alpha-\beta) \\ 0 & 0 & \sin(\alpha-\beta) & -\sin(\alpha-\beta) \\ 1 & -1 & 0 & 0 \end{pmatrix} \begin{pmatrix} G_A & 0 & 0 & 0 \\ 0 & G_B & 0 & 0 \\ 0 & 0 & G_C & 0 \\ 0 & 0 & 0 & G_D \end{pmatrix} \tag{5.4}$$

The error on each Stokes component is not equal. From equation 5.2 the linear component is not measured so a degree of polarisation is not known.

5.2.1 Calibrating the Polarimeter

The linear detector pair is used to define the zero axis from which all other angles are measured. The angles of different optical elements are labelled in figure 5.1. A summary

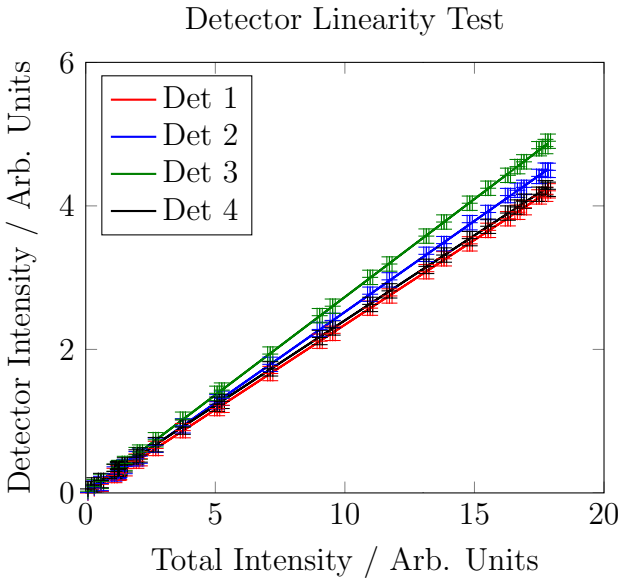


Figure 5.3: The normalised intensity measured by each detector vs. the intensity supplied to the polarimeter. The lines are linear fits to the data points, and the gradient is the relative gain of the channel G_n, including beamsplitting cubes and optical losses in the polarimeter. The lines do not intersect zero, and this represents the individual detectors dark current.

α	β	γ	θ_0	ϕ_0
-15 ± 4	0.0	2.27 ± 0.1	-31 ± 3	-10.9 ± 0.5
0.0+/-0	15 ± 4	17 ± 4	-16 ± 5	4 ± 4

Table 5.1: Calibration values for the polarimeter, all values are in degrees. The value of β is zero by definition on the upper line, which is our convention in calibration. These values can be re-expressed in terms of $\alpha = 0$ (second line), which is useful when determining the optical axis ζ of a sample.

of the values of each angle is given in table 5.1.

An optical element is rotated through 360° in 10° increments with a measurement taken at each increment. The measurement is the average of all the points in an oscilloscope reading. The oscilloscope used was a Tektronix 2024, 200 MHz bandwidth and 10 thousand points were sampled and averaged. This gave a mean and standard deviation for each measurement, with the error on the order of 0.1%. As the laser diode source is not perfectly stable (typical line width of 0.3 nm, RMS deviation in intensity of 20%), the sweep time needs to be kept fairly low (order of 10 μs). The extra linear polariser and waveplate on the input allow the intensity after the second linear polariser θ to be

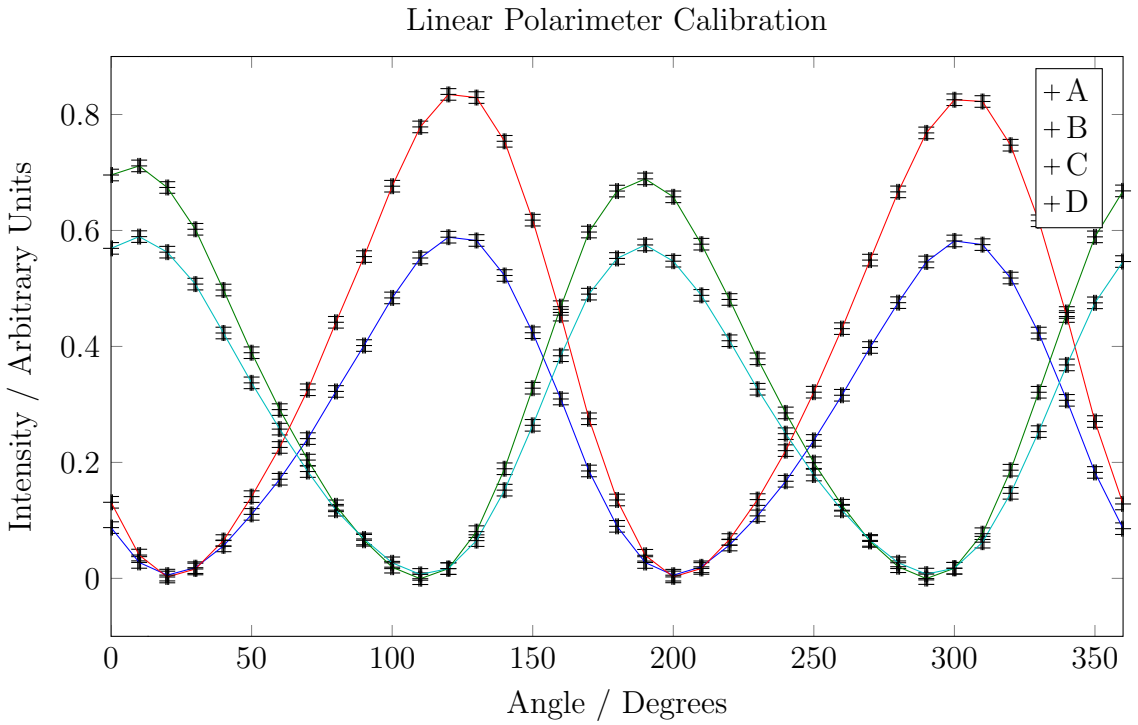


Figure 5.4: Intensity detected by each polarimeter detector for rotating linear input polariser LP1, without analyser WP2. Both pairs AB and CD should detect nominally linear polarised light. A shows the same phase as C, and B shows the same phase as D, however the peak of A and C does not coincide with the trough of B and D. This is due to higher order terms caused by back-reflections in the polarimeter.

fairly uniform.

Finding γ

By rotating θ without the waveplates α or ϕ present, the polarisation entering Wollaston prisms β and γ is the same, assuming that the 50:50 beam splitters split the polarisation evenly. This gives an output such as that in figure 5.4. The phase difference between the AB detector pairs and CD detector pairs is the angle $\beta - \gamma$. As can be seen from figure 5.4 there is a second component to the polarisation which rotates at twice the frequency as would be expected for a rotating linear polariser. This is likely a back-reflection through an input waveplate, marked by dotted lines in figure 5.1.

By analysing the FFT of the signal the phase of the primary polarisation can be extracted and the value of γ found. This also gives a value of θ_0 the zero value of the θ

polariser.

Finding ϕ_0

The zero angle of the analyser is found by rotating the analyser with a constant circular input. Using a FFT approach the phase of the first harmonic is found, and this is the phase offset between ϕ and γ, hence $\phi_0 = \gamma + \phi_m$ where ϕ_m is the measured offset. This gives the ϕ_0 offset in relation to β.

Finding α

It is necessary to rotate the input polarisation θ and the analyser ϕ. Eliminating unwanted back-reflectance by filtering the data with a FFT allowed the α value to be found. The final detector matrix using the values in table 5.1 is

$$\underline{\mathbf{M}} = \begin{pmatrix} 0.945 & 1.01 & 1.09 & 0.948 \\ 0 & 0 & -0.71 & 0.616 \\ 0 & 0 & -0.83 & 0.72 \\ 0.945 & -1.01 & 0 & 0 \end{pmatrix} . \tag{5.5}$$

Error on this matrix is hard to quantify, as it is variable with input polarisation state. As the determinant is zero, indicating that the error for certain polarisations tends to infinity, it is more informative to consider angular errors on the specific polarisation states that the birefringent material will generate. This will be circular and close to linear 45°. The error for these polarisation states is 4° based on table 5.1.

5.3 Analysis of Sample Birefringence and Optical Axis

In order to calculate the birefringence and optical axis of the shocked material, the dynamic polarimetry data needs to be analysed. This section will discuss the analysis of

polarimetry data measured from dynamic shock compression experiments.

5.3.1 Birefringence

Equation 5.6 represents the shocked birefringence $\Delta n'$ as a function of shock velocity, particle velocity, the original birefringence and the oscillation frequency in the polarimeter. The full derivation is in section 2.6.1 in which it is assumed that the shock wave behaves as a single step function in the optical dielectric tensor.

$$\Delta n' = \frac{f\lambda + 2U_s\Delta n}{2(U_s - u_p)} \tag{5.6}$$

In order to find the frequency f of the polarisation oscillations a FFT was taken of the circular component of the stokes vector. The peak was fitted with a three point parabola on a log scale, equivalent to a Gaussian peak (see appendix A).

5.3.2 Optical Axis

In order to calibrate the initial optical axis orientation ζ, several amplitude calibration measurements are needed. The linear input of the polarimeter θ was rotated in increments of 10^o through 360^o with a sample mounted in the target beam path. Measurements of the returned polarisation state were taken using the same method as the static calibration (averaging all 10000 samples on a Tektonix 2024 oscilloscope, 10 μs sweep time).

Amplitude measurements for the linear components, and comparison with circular components, indicate a degree of rotation for the optical axis. Measurements prior to impact allow a comparison of the optical axis before and during compression by estimating ζ from the stokes vector

$$\underline{S} = \begin{pmatrix} {E_0}^2 \\ \sin^4(\zeta){E_0}^2(e^{2i\frac{l}{\lambda}\Delta n}) \\ \cos^4(\zeta){E_0}^2(e^{2i\frac{l}{\lambda}\Delta n}) \\ i{E_0}^2(e^{2i\frac{l}{\lambda}\Delta n}) \end{pmatrix}$$

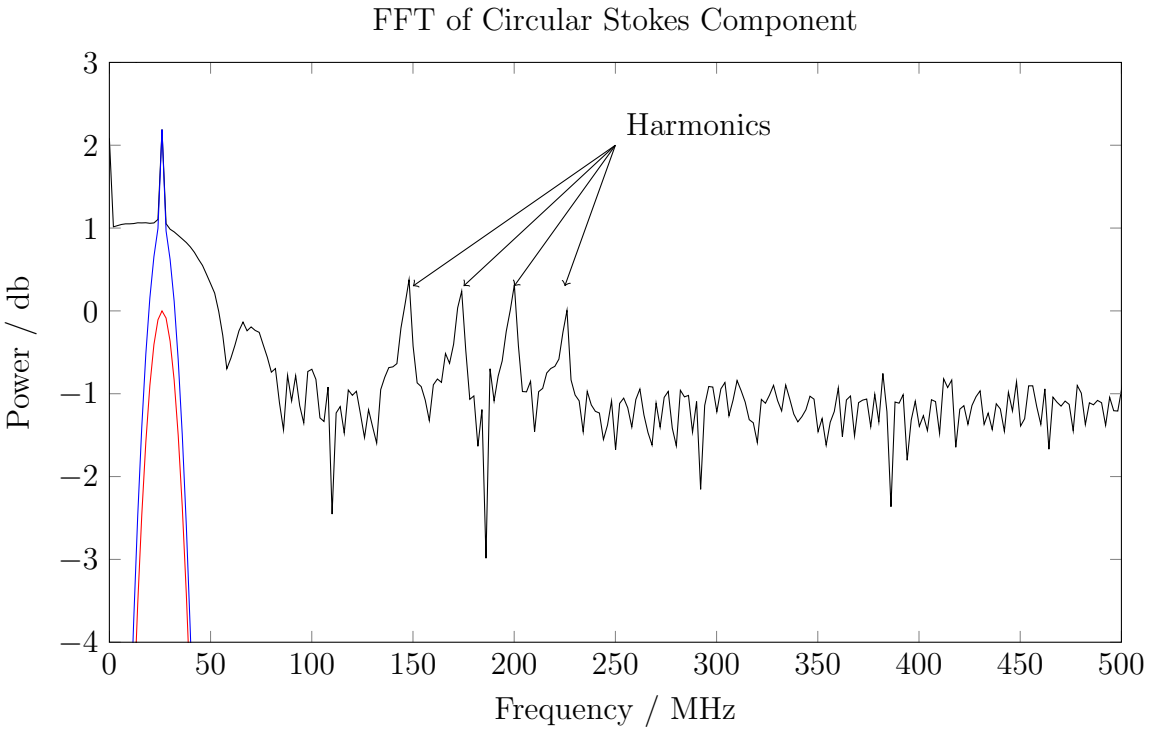


Figure 5.5: An example of peak fitting using a parabola, and windowing using an associated Gaussian for experiment C2. The raw FFT is in black, the fitted peak is shown in blue and the normalised Gaussian filter in red. The filtered signal is the multiplication of the filter with the original signal and only contains the frequency of interest. The higher harmonics are most likely caused by the super Gaussian window used for the raw FFT signal. They are integer multiples of the fundamental frequency, which has been selected using the red Gaussian filter.

from this the rotation of the optical axis is

$$\zeta \propto \arccos(\sqrt{\frac{S_3}{S_4}}). \tag{5.7}$$

The amplitude component of a given frequency can be extracted by windowing the FFT and discarding phase information. This is achieved by multiplying the FFT by a Gaussian centred around the oscillation frequency shown in figure 5.5, setting negative frequency components to zero and finding the magnitude of positive components. The inverse Fourier transform gives the amplitude of this frequency component as a function of time.

For a parabolic fit in logarithm space of the form

$$y = Af^2 + Bf + C \ , \tag{5.8}$$

where A, B and C are constants to be fitted, the coefficients for the Gaussian fit

$$G(f|\mu,^2) = \exp \frac{(f-\mu)^2}{\sigma^2}$$

in normal space are

$$\mu = -\frac{B}{2A} \tag{5.9}$$

$$\sigma^2 = 2\frac{C}{B^2} \tag{5.10}$$

This is used to determine the parameters for the filter to use. For a full description of the fitting algorithm see appendix A.

The amplitude ratio between the S_3 and S_4 components of the stokes vector should remain constant during the course of the shock wave propagation through the sample. This can be verified by plotting $\frac{S_3}{S_4}$ as a function of time, and an error estimated using it.

5.4 Sources of Error

In the dynamic experiment back-reflectance can be ignored as all surfaces generating unwanted back-reflectance are stationary. If the surface is stationary, it contributes no oscillating components to the polarisation, so the frequency for birefringence measurements is not affected. In calibration back-reflections cause significant systematic errors that must be accounted for. The polarisation state does not rotate uniformly as optical elements are rotated.

The random error on frequency was conservatively taken as half the peak width, approximately 3 MHz. The error from crystallographic tilt was predicted to be 1 MHz

in section 3.4, and so crystallographic tilt was assumed to be negligible.

For the amplitude analysis the fractional random errors are larger. The random error due to thermal noise is higher for amplitude measurements than frequency measurements, as the noise is Gaussian and uncorrelated. The analysis method introduced a maximum time resolution which is of the order of the frequency of the oscillations (around 20 ns for experiments in chapter 4). The error introduced in calibration puts the maximum precision on an initial optical axis measurement of $\pm 4^{o}$.

5.5 Chapter Conclusions

This design for a high speed polarimeter has key advantages over other designs in the literature. By using a circular input polarisation state and measuring the circular output component, the polarimeter is sensitive to birefringence for arbitrary rotations of a sample. Whilst less accurate than a 6 detector polarimeter for specific linear polarisations, and hence unable to accurately determine the degree of polarisation, the 4 detector polarimeter is simpler to align and retains the necessary accuracy for circular polarisations. The design presented in this chapter will also allow the measurement of the optical axis in the shocked region, a measurement which has not been attempted before in the shock compression field.

Chapter 6

Experimental Methods for Large Gas Gun Experiments

Based on the conclusions of chapter 4, a new series of experiments was planned on the ISP 100 mm bore single stage gas gun. This would permit a measurement of impact tilt to be made due to the larger bore compared to the 13 mm gun. The method of measuring tilt is discussed in section 6.2.2. A second recommendation, to study a second material, was also implemented and sapphire was chosen as the target material. It was desired to load each sample in its elastic regime, with the final longitudinal stress to be below the material's HEL. In order to achieve this literature Hugoniot's from Marsh [65], [24] and [13] were used to produce impedance matched impacts shown in figure 6.1.

The selected flyer materials and impact velocities are given in table 6.1 and the predicted Hugoniot states shown in figure 6.1. Impact velocities were selected to provide even spacing in longitudinal stress along the elastic part of the target's Hugoniot. After the 800 m s^{-1} sapphire experiment S1 described in chapter 7 it was found that the a-cut sapphire had plastically yielded. This meant the single wave assumption was not valid, and so experiment S4 was conducted at 660 m s^{-1}.

The 100 mm bore gas gun has an 8 channel PDV system (described further in section 6.2.1) for measuring velocities, of which 6 channels were utilised. Four channels

Shot	Target	Flyer	v / m s^{-1}	u_p / m s^{-1}	σ_l / GPa
S1	Sapphire	Copper 1001	800.0	382	17
S2	Sapphire	Copper 1001	400.0	185	8.2
S3	Sapphire	Copper 1001	600.0	281	13
S4	Sapphire	Copper 1001	660.0	310	14
C1	Calcite	Magnesium AZ31B	200.0	58.8	1.2
C2	Calcite	PMMA	250.0	36.2	0.73
C3	Calcite	Magnesium AZ31B	250.0	73.9	1.5

Table 6.1: Selected impact flyers and velocities for large gas gun experiments, based on the impedance matched Hugoniot's in figure 6.1 and the aim of having evenly spaced shock states in longitudinal stress. After experiment S1 it was discovered that the yield stress was lower than the expected yield stress based on Jones *et al.* [24], so experiment S4 was performed.

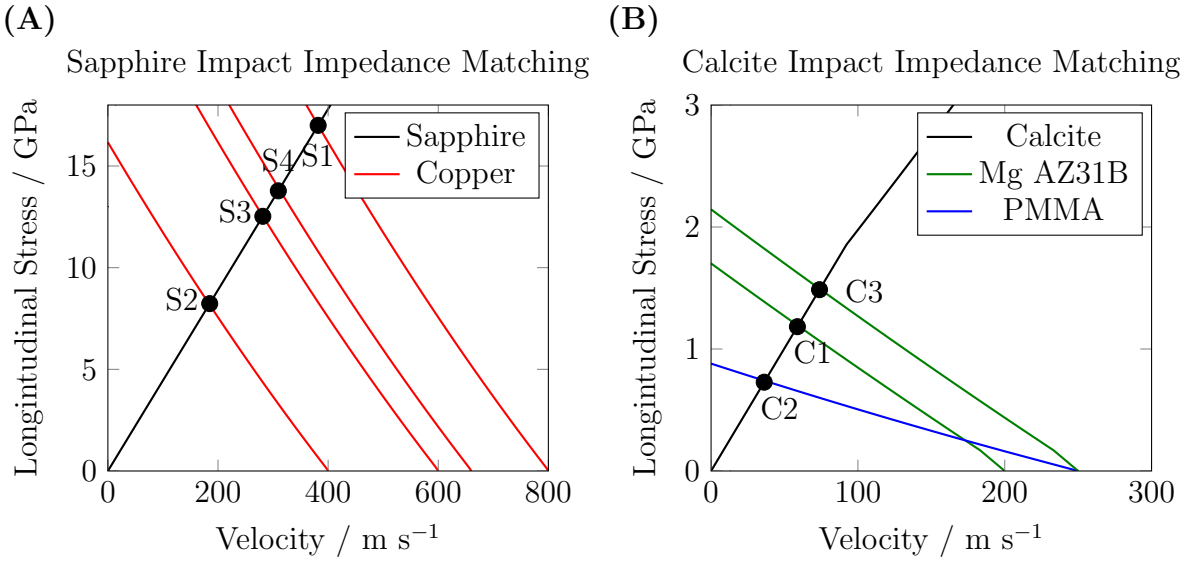


Figure 6.1: The Hugoniots of each target material are shown, sapphire (*left*) is taken from Jones *et al.* [24] and calcite (*right*) is taken from Ahrens and Gregson [13], Dandekar [12]. Each impact configuration (impact velocity, flyer material) is shown for each target. Where the Hugoniots intersect shows the predicted longitudinal stress and particle velocity for that experiment. Impact configurations were chosen to provide even longitudinal stress spacing along the targets elastic Hugoniot. All flyer Hugoniots are taken from Marsh [65], and the analytical fit in longitudinal stress particle velocity space is plotted.

were used to make the Time of Arrival (ToA) measurements necessary for the impact tilt calculation, one channel for rear surface velocity and one channel for projectile velocity. The PDV probe for projectile velocity was required as there is no light gate system on the 100 mm bore gas gun. In the 13 mm bore gas gun experiments light gates were used to trigger the oscilloscopes, hence a different triggering system was needed on the 100 mm bore gun. A system using contact shorting pins, described in section 6.1.2, was used. As the polarimeter was a unique development for this series of experiments, it is discussed separately in chapter 5.

6.1 Description of 100 mm Bore Gas Gun

Light gas guns have been used for decades in shock physics as a means of accurate and repeatable loading of samples. The large 100 mm bore gas gun uses helium gas because of its high sound speed and low safety hazards compared to hydrogen. The achievable velocity range is 200 m s^{-1} – 1400 m s^{-1} and typical projectile weights can vary from 500 g to 4 kg. The location of the target from the barrel end can be varied, but typically it is one sabot length, approximately 300 mm. A photo of the Imperial College large bore gas gun is in figure 6.2.

The breech on the 100 mm bore gun uses a double diaphragm which allows the highest firing pressures to be used. Two breeches of 30 litres and 100 litres can be interchanged and an illustration in figure 6.3 shows the firing mechanism. Aluminium diaphragms are used for pressures up to 150 bar, and for higher pressures brass diaphragms are used. The target chamber can be reduced to a vacuum of around 50 mTorr, and a mylar diaphragm separates the target chamber from the expansion tank, which is at a rough vacuum. The expansion tank also holds a large steel tube filled with rags, which is used to slow and stop the projectile and target after impact.

Feed throughs for diagnostics consist of eight BNC feed throughs, a fibre feed through capable of feeding at least twelve fibres, and optical window ports on either side of the

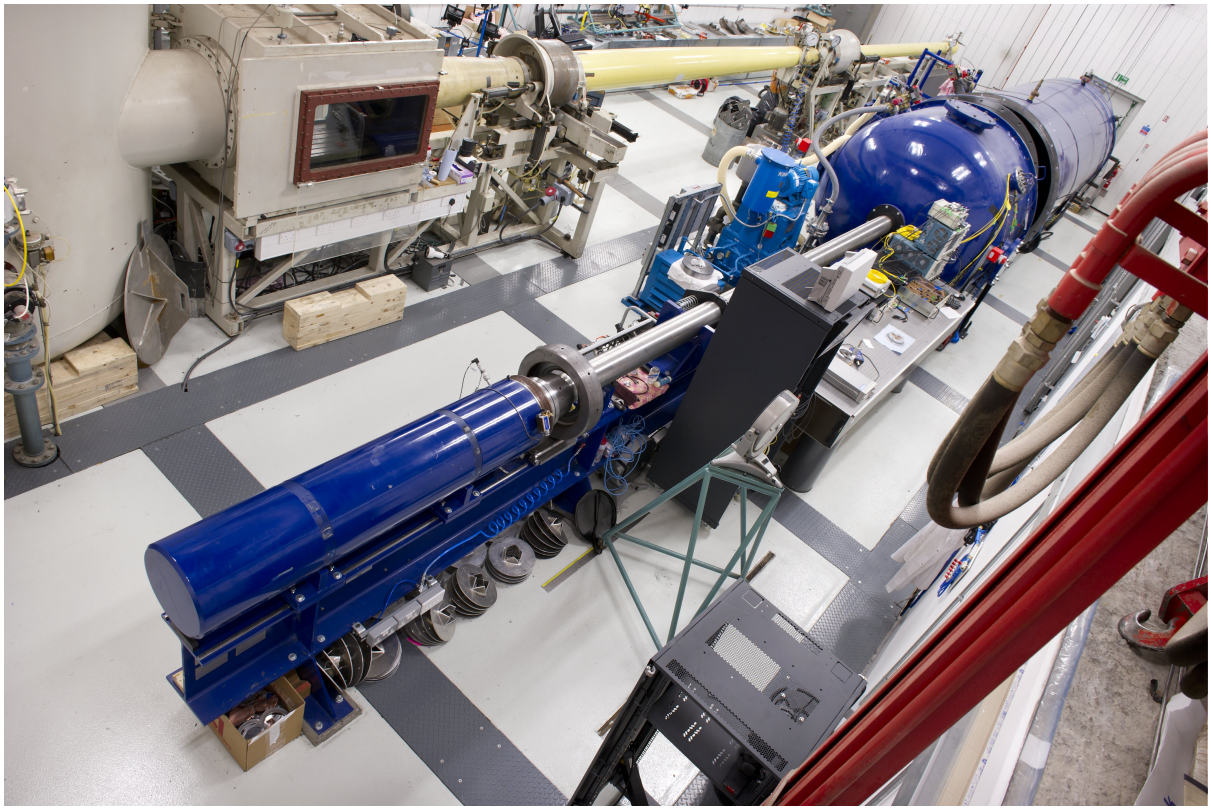


Figure 6.2: Photograph of the 100 mm bore large gas gun at Imperial College London. The breech end is closest to the camera.

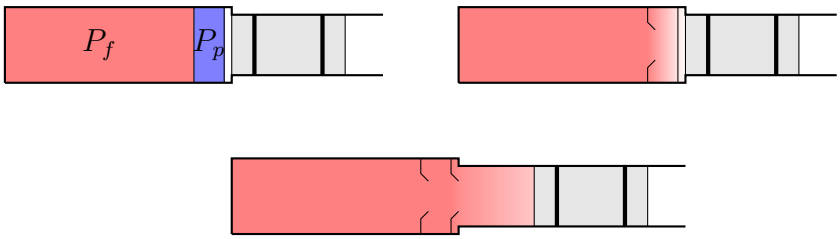


Figure 6.3: The breech on the large bore gas gun uses two diaphragms which burst at a pressure P such that $P_p < P < P_f$. The gun is fired by dropping the intermediate pressure P_p to vacuum. This exposes the first diaphragm to the full pressure P_f, causing it to burst. The second diaphragm is then exposed to the full pressure and also bursts rapidly.

target chamber. The optical window for the free space polarimeter was AR coated for 532 nm light. Two BNC ports were used for triggering the diagnostics, and six fibres were put through the fibre feed through on each experiment presented in this work.

Alignment of the target is carried out by using a barrel plug which is known to have a flat surface perpendicular to the axis of the barrel. A reference flat with a micrometer is then placed on the target mount location, and the distance from target mount to barrel plug is measured at various angles. To adjust the distance so that the two planes are parallel, three differential bolts can be turned. Each full turn moves the target plate approximately 50 μm. By rotating around the target mount, the target mount can be adjusted until its is perpendicular to the barrel with an accuracy of ± 15 μm. This equates to an angular uncertainty of ± 0.3 mrad over 100 mm diameter of the target mount.

Each target is attached to a target ring which is flat and parallel to at least 1 mrad. These are attached using nylon bolts to the target mount in the target chamber, and are sacrificial for each shot. The aim being that the target ring comes away from the target mount without deforming the flat reference surface in the target tank that is used for alignment.

6.1.1 Shot Characterisation

An important aspect of any experiment is knowing the conditions under which it was performed, hence it is necessary to accurately measure and characterise each gas gun

shot to ensure accuracy and precision in any final results. The primary requirements are to measure the impact velocity, and to confirm that the impact was planar to 1 mrad as this was thought to be a limiting factor in chapter 4.

Impact velocity

It is necessary to know that the projectile has reached a steady velocity when it impacts the target, and to know precisely what velocity this is. A OZ optics collimated -60 dB back reflectance PDV probe (described in section 6.2) was used on each large gas gun experiment to measure the impact velocity of the projectile on the large gas gun. As the PDV technique measures a velocity history, it is possible to confirm that the projectile had reached a steady velocity prior to impact.

Knowing projectile velocity is crucial as this determines the shock state. The exact impact velocities can be used with the predictions shown in figure 6.1 to give the expected longitudinal stress and particle velocity of the impact surface. The accuracy of literature Hugoniot's limits the accuracy of this technique to around 3% percent in both particle velocity and longitudinal stress. As the experiments will measure shock velocity and particle velocity, allowing a direct calculation of the sample Hugoniot, the impedance matching method can be compared to the sample Hugoniot for consistency with literature and with the experimental method.

Plate Impact (One Dimensional Loading)

The impact of the flyer with the target needs to be flat and parallel. Deviations from this ideal are called impact tilt. Impact tilt launches a shock into the target material at an angle which is greatly exaggerated over the initial impact tilt. This is because the flyer impacts the target at around (for example in calcite) 200 m s^{-1}whilst the shock wave is launched into the target at 7.4 km s^{-1}. This leads to a difference in angle of $\frac{7.4}{0.2} = 35$ fold increase in tilt angle (valid for small angles).

Tilt can be measured by recording ToA at a given interface at different angles and

radii, then computing the required tilt to generate such a time delay. There are two sources of error, the precision in ToA measurements and the precision in radii measurements. The larger the radii the smaller the fractional error, hence small bore gas guns are very difficult to perform precise tilt measurements on. For a radii greater than 10 mm, precision in ToA measurements is the most significant source of error. Generation zero PDV probes were used as these give the greatest accuracy for a ToA measurement, and are also cost effective.

6.1.2 Timing and Triggering

It is crucial that the diagnostics trigger when the projectile impacts the target. Delay generators are used to trigger the diagnostics at the correct time. The trigger event depends on constraints of the particular target and target chamber setup. Shorting pins were used for triggering on the 100 mm bore gun. A timing diagram, an example of which is in figure 6.4, is useful to visualise triggering events and delays. A schematic of the oscilloscope setup for a large gas gun shot is shown in figure 6.5

The triggering system used two shorting pins, running into a logic trigger on the Tektronix 4054 oscilloscope. If either pin shorted, the Tektronix 4054 would trigger the rest of the oscilloscopes. From the sabot shorting the pins, it is necessary to estimate the time until the impact event which we wish to record. Time of flight of the projectile is determined by the distance travelled, measured before the experiment, and the velocity of the projectile. As the projectile velocity is only estimated before the shot and is not known, there has to be an appreciable recording time window to ensure the event is captured. Due to this uncertainty in the firing velocity of the gas gun, the trigger to target distance needed to be minimised. The shorting pins were therefore placed on the target frame, approximately 30 mm from the impact surface.

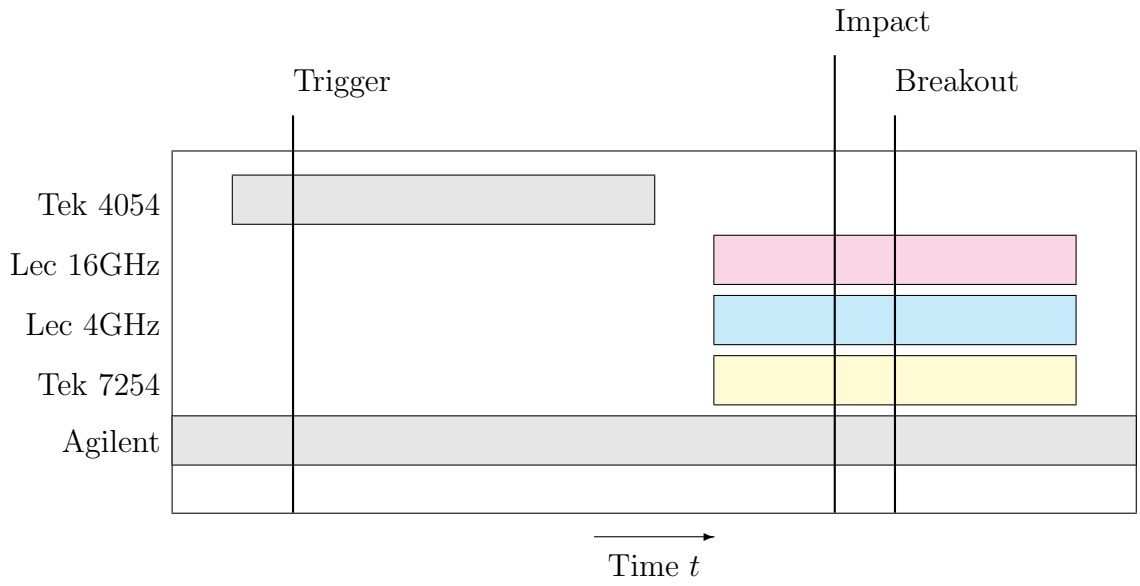


Figure 6.4: An example timing diagram for large bore gas gun shots. These are useful for visualising the temporal layout of an experiment, and the recording windows of each diagnostic. In these experiments a Tektronix 4054 oscilloscope was used to record the shorting pins and trigger the other oscilloscopes. The LeCroy (lec) 16 GHz bandwidth was used for the upshift PDV channels, and the LeCroy 4 GHz bandwidth used for the tilt PDV probes. The Tektronix 7254 oscilloscope was used to record the polarimeter and the Agilent was used to record exact event timing, such as the triggers for each oscilloscope. As these experiments are relatively straightforward, the timing diagram is not complex, the primary concern is ensuring that the correct delay is set from the trigger event (30 mm shorting pins). As the projectile velocities are generally low a small error in velocity can lead to a large uncertainty in the impact time. Reducing the distance from the trigger pins to the impact surface reduces the absolute uncertainty in projectile flight time (from which the delay is determined). For this reason triggering pins were mounted on the target to reduce the distance to around 30 mm.

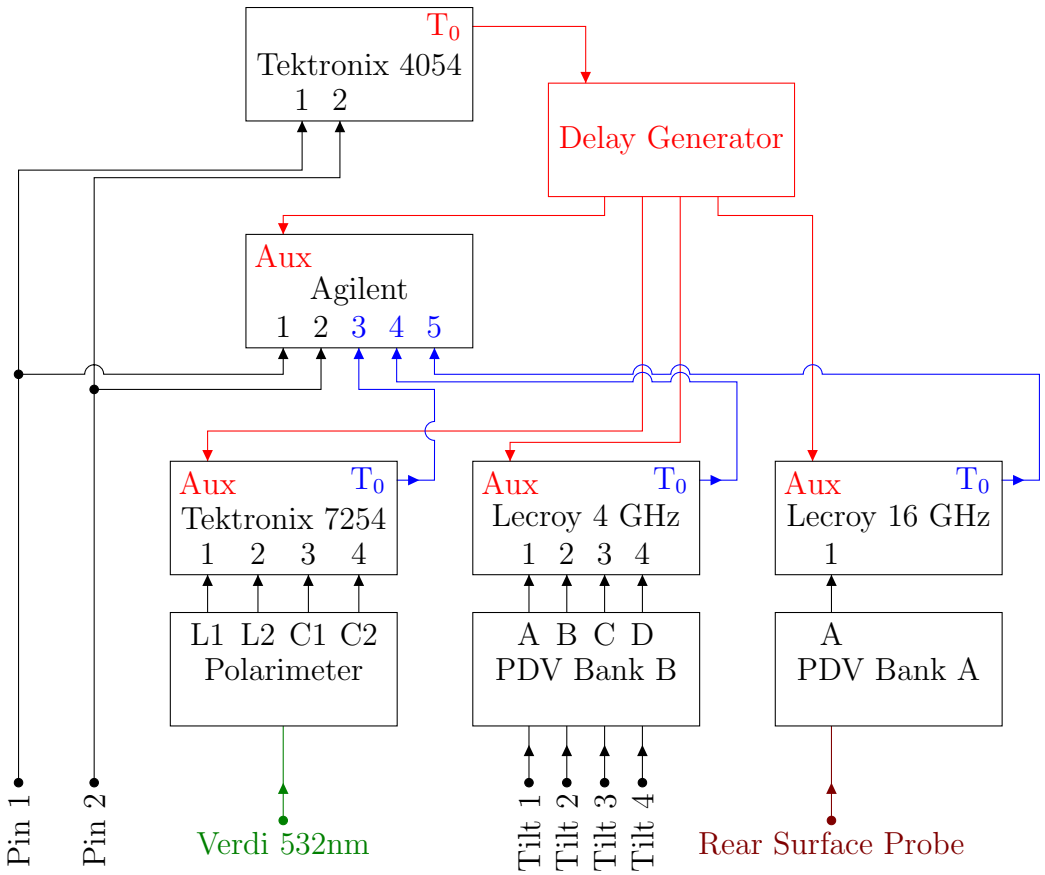


Figure 6.5: Triggering schematic, showing the system of triggering for every oscilloscope used in the large gas gun experiments. When the projectile shorts pin one or pin two, the Tek 4054 triggers the delay generator. The delay time is set per experiment based on pin to target distance and intended impact velocity. The delay generator triggers all data recording oscilloscopes. By recording round trip times between a test trigger and an oscilloscope, a delay for each leg of the triggering system, including internal oscilloscope and coaxial cable lengths, can be measured. Equipment list:

- Tektronix 4054, bandwidth 400 MHz
- Lecroy 16 GHz, bandwidth 16 GHz, 50 GS/s, 100 μs record time
- Lecroy 4 GHz, bandwidth 4 GHz, 20 GS/s, 100 μs record time
- Tektronix 7254, bandwidth 2 GHz, 5 GS/s, 100 μs record time
- Agilent, bandwidth 1 GHz, 1 GS/s, 1 ms record time. Records trigger events from other oscilloscopes to aid timings.
- Delay Generator, Quantum Composer

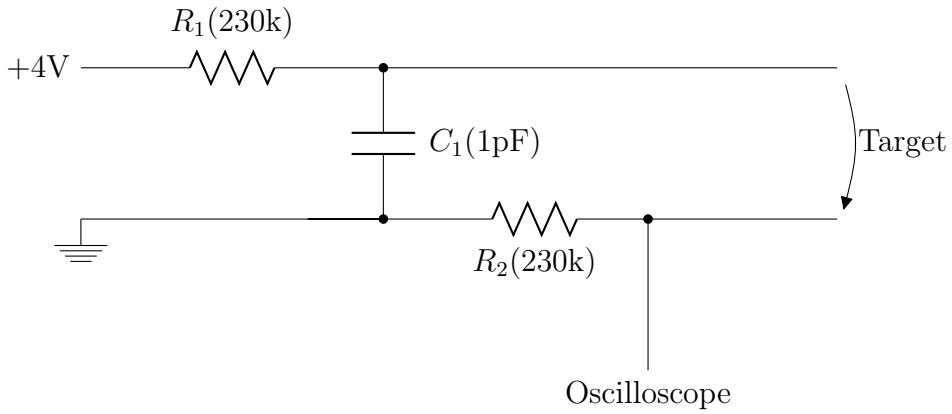


Figure 6.6: Electronic setup of shorting pins, when a short is made across the target pair by a metallic projectile, the capacitor discharges through resistor R_2 to ground, creating a 4 volt spike on the oscilloscope. The RC constant of the circuit is 2.3×10^{-7} s, the measured 80% fall time on the oscilloscope was 4×10^{-7} s, likely caused by a higher capacitance, either due to the capacitor itself being higher than quoted or the layout of the circuit board creating additional capacitance.

Shorting Pins

Shorting pins are made from two aluminium wires which when shorted by impact with a metallic object, generate a signal which is recorded on an oscilloscope. The flyer needed to be a conducting material, so for the PMMA flyers a 10 mm aluminium ring was put around the edge of the flyer. The system charges a capacitor across the pair of aluminium wires, and when the pair is shorted by direct conduction through a metallic projectile a sharp rise time (4×10^{-7} s to reach 80% of height) peak is seen in the oscilloscope trace. An illustration of the electronic setup is shown in figure 6.6.

6.2 Photonic Doppler Velocimetry (PDV)

PDV is a technique originally developed by Strand *et al.* [26]. Whilst the PDV setup varied from shot to shot in chapter 4, on the large bore gas gun the setup was more consistent. The different forms of PDV fielded on experiments in chapter 7 are discussed below, though the basic principle is the same. Light is reflected from a moving surface and interfered with a local oscillator, which may be back reflectance from the probe,

the original laser on a different fibre, or a second entirely separate laser. The system effectively acts as a Michelson interferometer, but as the arms are not path length matched there is the requirement for a very stable laser (or laser pair). Typically the lasers will have a coherence length of several kilometres. PDV was used to measure projectile velocity, impact tilt, impact time, breakout time and rear surface velocity. This effectively characterises the entire shot, as discussed in section 6.1.1.

6.2.1 Experimental Configuration

The 8 channel PDV system, built by Dr. David Chapman, uses an NKT seed and NKT Boostik laser. These tunable 1550 nm lasers allow accurate selection of reference and probe frequencies to use in the PDV system. Three distinct setups are used, with the primary difference being the source of the local oscillator. The entire system is fibre optic based using circulators and splitters to build the interferometer. An illustration of the basic system is given in figures 6.7-6.11. Imperial College has a number of lasers available from IPG and NKT, all with a typical stability of 0.85% optical power Root Mean Square (RMS) deviation over 1 hour and a line width of 0.01 nm:

- NKT Adjustik 1550 nm tunable laser. Used as reference.
- NKT Adjustik and Boostik 1550 nm tunable laser 2 W optical power. Used for probes and reference.
- IPG ELR-2-1550-LP-SF 1550 nm fixed wavelength, 2 W optical power output.

Generation Zero

This configuration uses back reflectance from the probe as the local oscillator as shown in figure 6.7. Imperial College's bank B was configured in this setup for measuring time of impact, and a schematic of the setup is shown in figure 6.8. This setup has the advantage of being able to use bare fibre ends which are very cost effective. The reflection from the probe end interferes with the signal from the moving surface resulting in a temporal

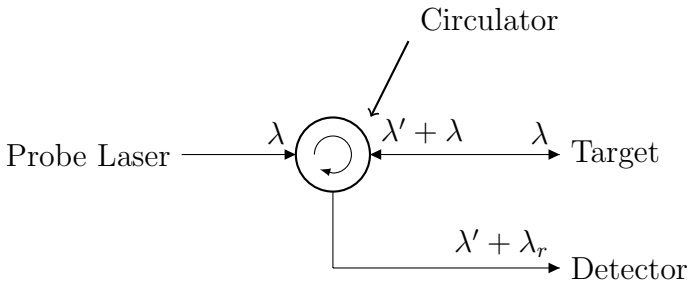


Figure 6.7: Illustration of a generation zero PDV system. The reference λ_r is the original probe laser wavelength λ, reflected from the probe.

fringe pattern. The fringe spacing is related to the velocity of the moving surface (each fringe occurs for half a wavelength of motion). The generation zero system was used for precise ToA measurements at the impact plane which allowed a measurement of tilt.

Generation One

This configuration uses a low back reflectance probe, typically less than -40 dB achieved using an AR coating, and splits the laser source into the probe arm and a reference arm as shown in figure 6.9. This design has the advantage over generation zero of being able to set the power of the reference independently of the signal from the target, allowing one to optimise the signal to noise ratio. The main disadvantage is the increased cost of the fibre probes.

A generation one PDV channel was used to measure projectile velocity as this allowed separate reference / probe powers to be set. As there is no reflection prior to the projectile being seen by the probe, it is necessary to know the zero velocity frequency, which is zero on a generation one channel. As the probe records the velocity history, any acceleration is detected, and using a long FFT window allows a precision of around 0.5 m s^{-1}.

Generation Three - Upshifted

Using low back reflectance probes a second laser at a slightly different frequency is used as the local oscillator, shown in figure 6.11. This setup allows for an apparent velocity to be set, and changes to the apparent velocity measured. The main advantage is in

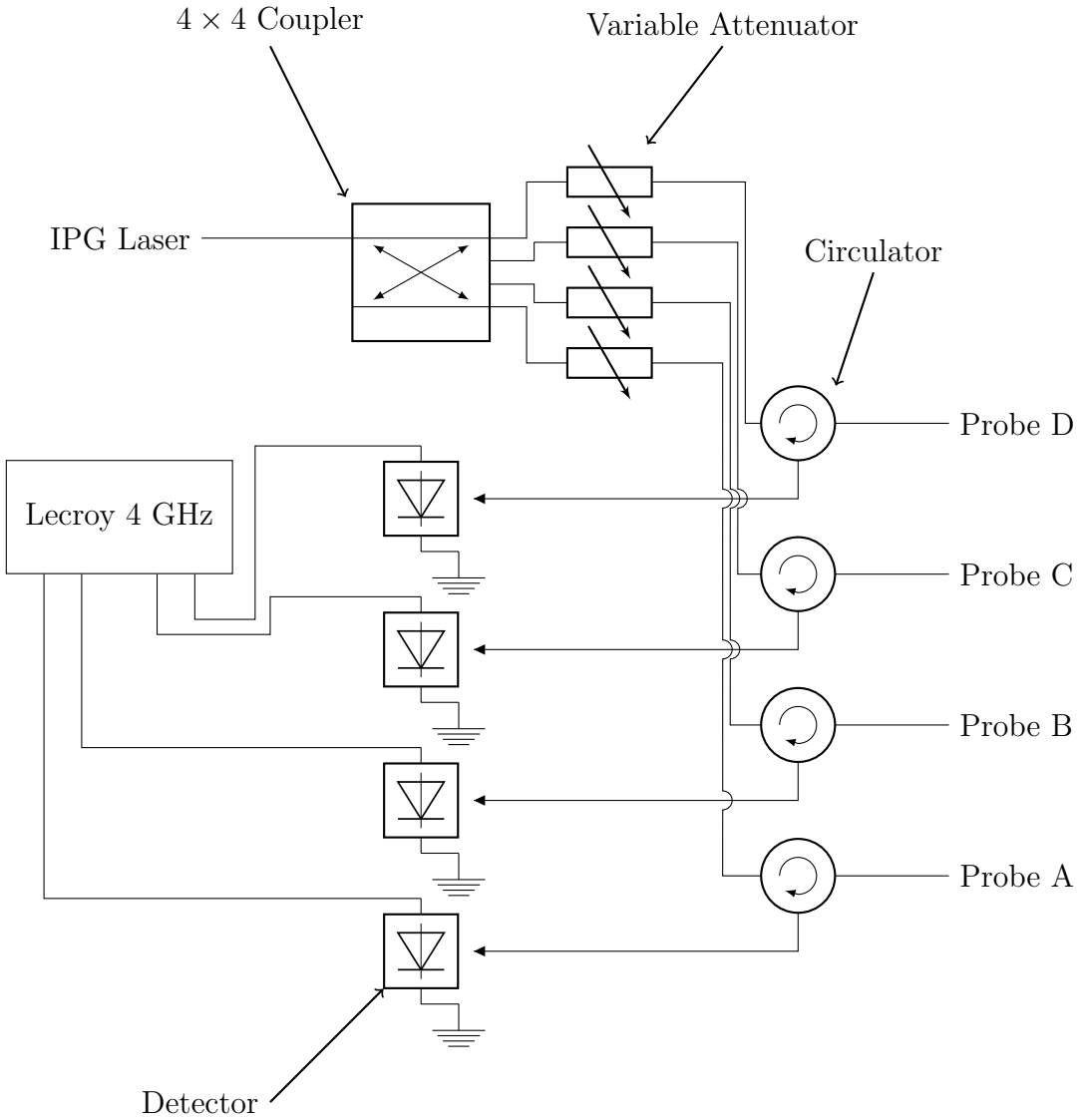


Figure 6.8: Configuration of PDV bank B on the large bore gas gun for tilt measurements. Each channel is on generation zero configuration with no dedicated reference. Bare fibre probes are used which give appreciable back reflectance, providing the reference. Power levels on probes can be individually set, however as the reference is reflected from the probe end, there is no way to set the reference power separately. Because of this signal to noise is fixed. Mitek 12 GHz bandwidth InGaAs photodetectors are used.

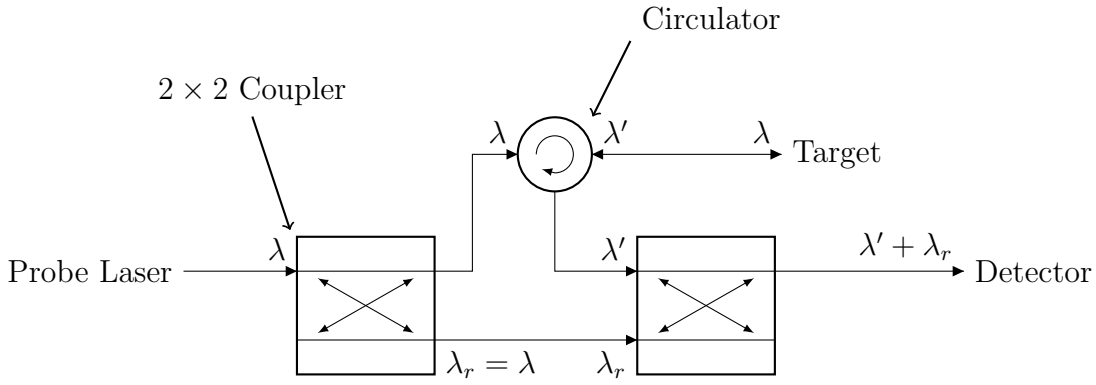


Figure 6.9: A generation one PDV system. The reference λ_r is again the original probe laser wavelength λ, but this time it follows a separate path, and is not reflected from the probe. Reference and probe power levels can be adjusted independently.

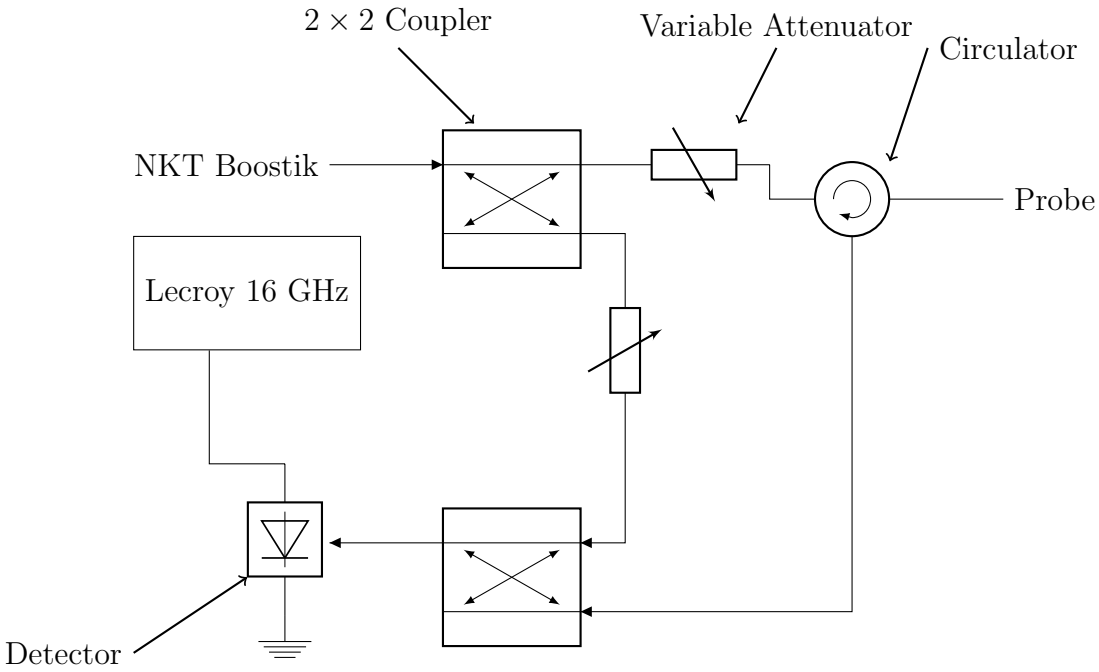


Figure 6.10: Schematic of the projectile velocity PDV system. A single channel is used in generation one, and connected to channel 2 on the LeCroy 16 GHz oscilloscope. 50 GS/s sampling rate is used, and a low (-40 dB) backreflectance probe used.

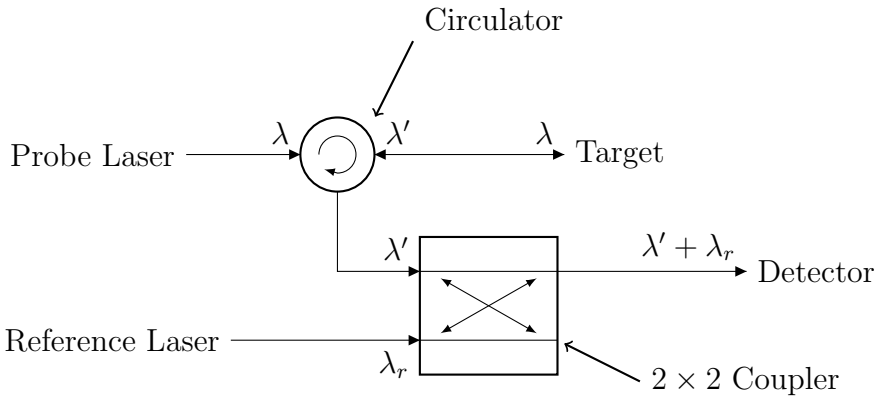


Figure 6.11: Upshifted generation three PDV system using a close but slightly different reference wavelength λ_r. This causes an apparent initial doppler shift, improving temporal and velocity resolution.

accuracy for short time events (less than 10 ns) such as elastic precursors where high velocity resolution and high temporal resolution are desired. Generation zero and one cannot provide the same simultaneous velocity and temporal resolution and the reason for this is explained in section 6.2.2. The main disadvantage is that, without knowing the apparent velocity beforehand, the actual velocity cannot be calculated, which makes it ineffectual in measurements such as projectile velocity, where there is no stationary measurement.

The increased temporal/velocity resolution of the upshifted configuration is needed for the rear surface velocity measurement. This is because the experiments performed in this thesis are at relatively low velocity, and simultaneously require temporal accuracy to determine shock velocity. The Imperial College bank A PDV was setup in an upshifted configuration, however only one channel was used. The schematic of the system is shown in figure 6.12. A higher bandwidth oscilloscope is required as the initial beat frequency was set to 5 GHz, and a 16 GHz LeCroy was used sampling at 50 GS/s.

6.2.2 Analysis of PDV for Impact and Rear Surface Velocimetery

The analysis of the PDV data was dependant on the physical quantity sought.

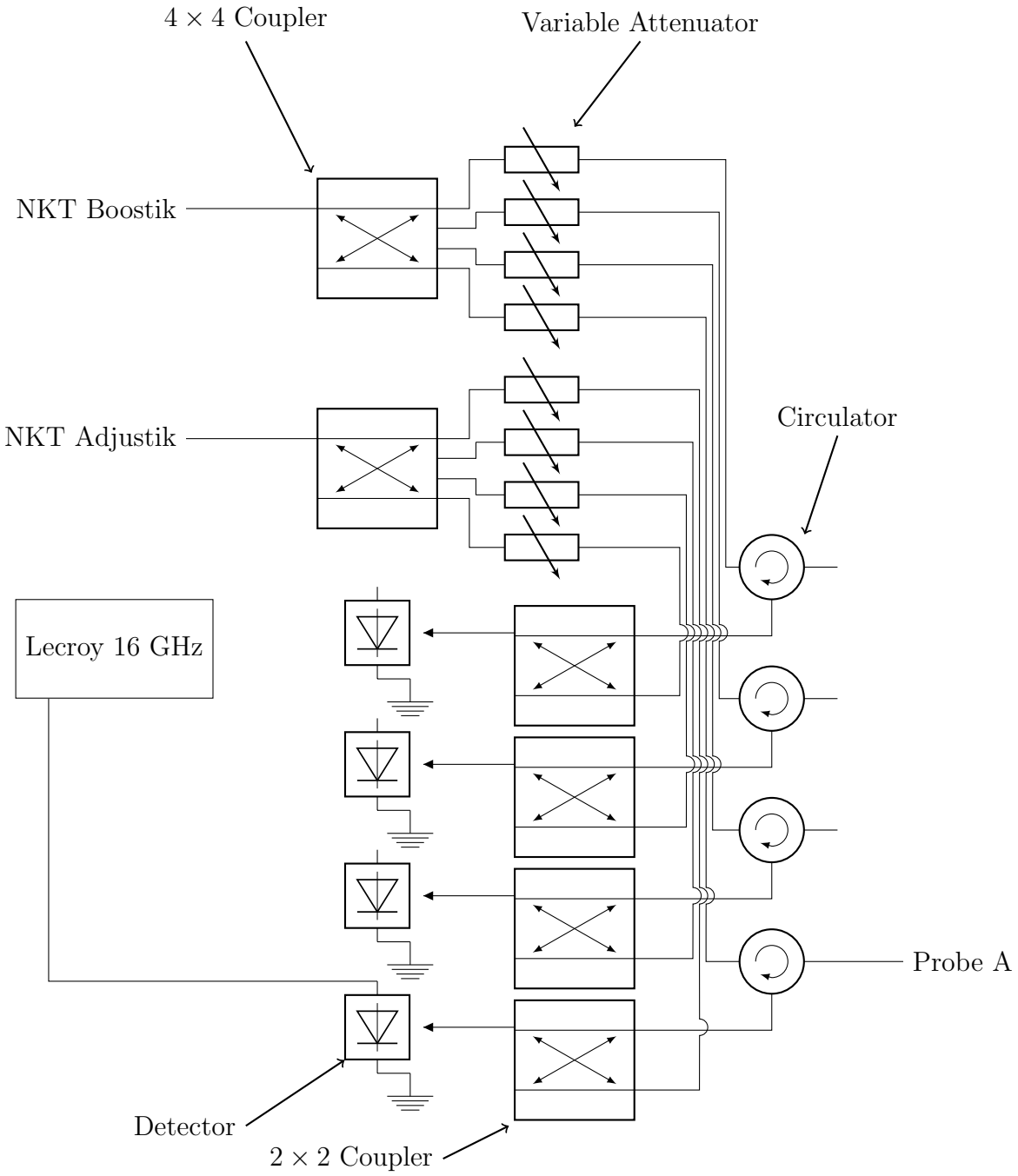


Figure 6.12: Upshifted generation three PDV system used on the large bore gas gun, configured for rear surface velocity measurement. Only one channel is used, although the bank contains four separate channels. Each reference and probe power level can be set individually. Mitek 12 GHz bandwidth photodetectors are used, and the sampling rate on the oscilloscope is 50 GS/s.

Generation Zero (Tilt ToA Measurements)

In order to accurately characterise the error of ToA from non-upshifted PDV data, the reduced chi squared parameter is useful. This is a goodness of fit measure, and can be used to identify when a data set no longer conforms to a model, within the noise level. The parameter is defined in equation 6.1 and is a function of the observed data O the expected value from the model E and the variance of the data due to noise V. The noise must be Gaussian for this to be a good parameter.

$$\chi_r{}^2 = \frac{1}{\nu} \sum \frac{(O-E)^2}{V} \tag{6.1}$$

The value ν is the degrees of freedom, which is defined as

$$\nu = N - n - 1$$

where N is the number of data points and n is the number of fitting parameters in the model.

There are two ways to measure ToA on a generation zero PDV oscilloscope signal. The noise can be estimated directly prior to impact by taking a mean and standard deviation of the pre impact data, and a flat line fitted to this. When the signal deviates from the estimated noise by a significant amount (usually $\chi_r{}^2 > 2.0$) then the surface is assumed to have started moving. The second approach finds the frequency, phase and amplitude of the signal and fits a sinusoidal wave post-impact. The fit is then compared to the noise level, estimated pre impact, and when a significant deviation is observed, the ToA is set. Figure 6.13 shows an example of the sinusoid fitting technique.

Whilst the flat line approach is far more reliable and simpler to implement, as fitting a sinusoid through least squares fitting is notoriously difficult, the final results are quite different. The flat line approach reliably detects impact surface motion 10 ns prior to the impact as determined by fitting the sinusoid. This is likely due to gas in front of the

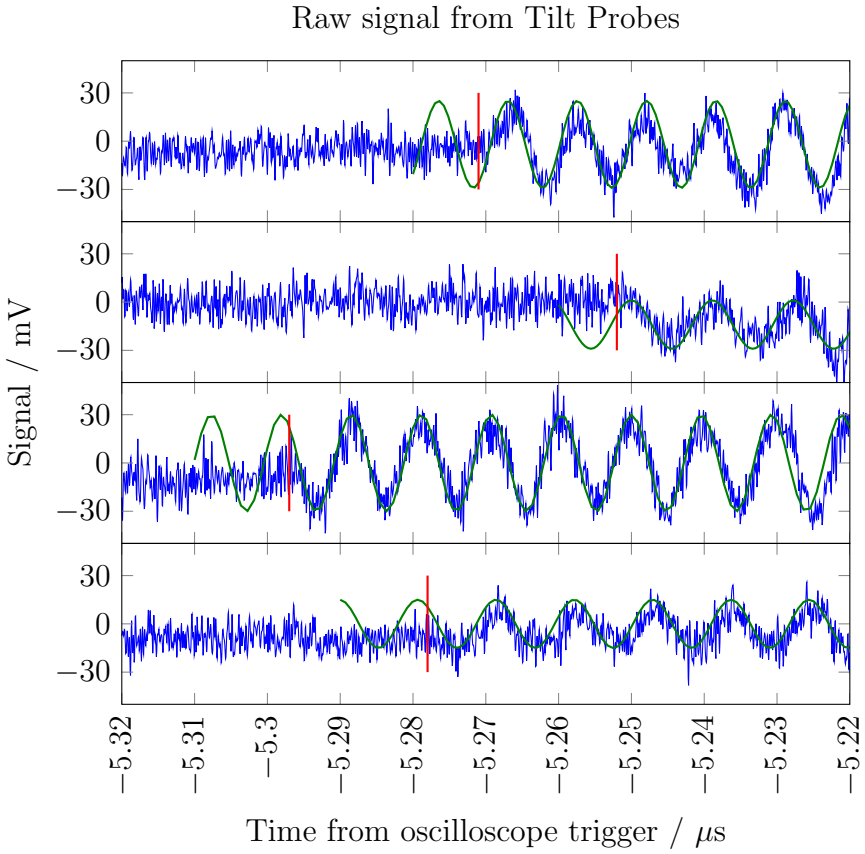


Figure 6.13: Example oscilloscope signal (*blue*) from a bare fibre generation zero PDV channel. A sinusoid (*green*) fitted to the signal after the jump point is extrapolated to before the jump point (left). The position where the signal deviates from the noise floor is determined using a reduced chi squared analysis and the position is marked with a red line. These points are used in figure 6.14 to determine the tilt, and error is estimated using the signal noise visible in this figure.

projectile being shocked up as the vacuum base pressure is around 50 mTorr. The total motion of the impact surface prior to the high frequency sinusoid appearing is around 100 nm over 10 ns for a total average velocity of around 10 m s^{-1}. The arrival of the projectile at the impact surface is therefore when the sinusoid begins. The arrival time determined by fitting to the sinusoid is more accurate for the measurement of ToA than by fitting to the flat pre-impact signal.

Once the ToA measurements for different angular positions have been found, the tilt is calculated by fitting a sinusoid to the time angle points. The set of points at the same radii r are fitted for phase, amplitude and mean against their angular location. The frequency is assumed to be unity. Figure 6.14 shows an example fit and error analysis.

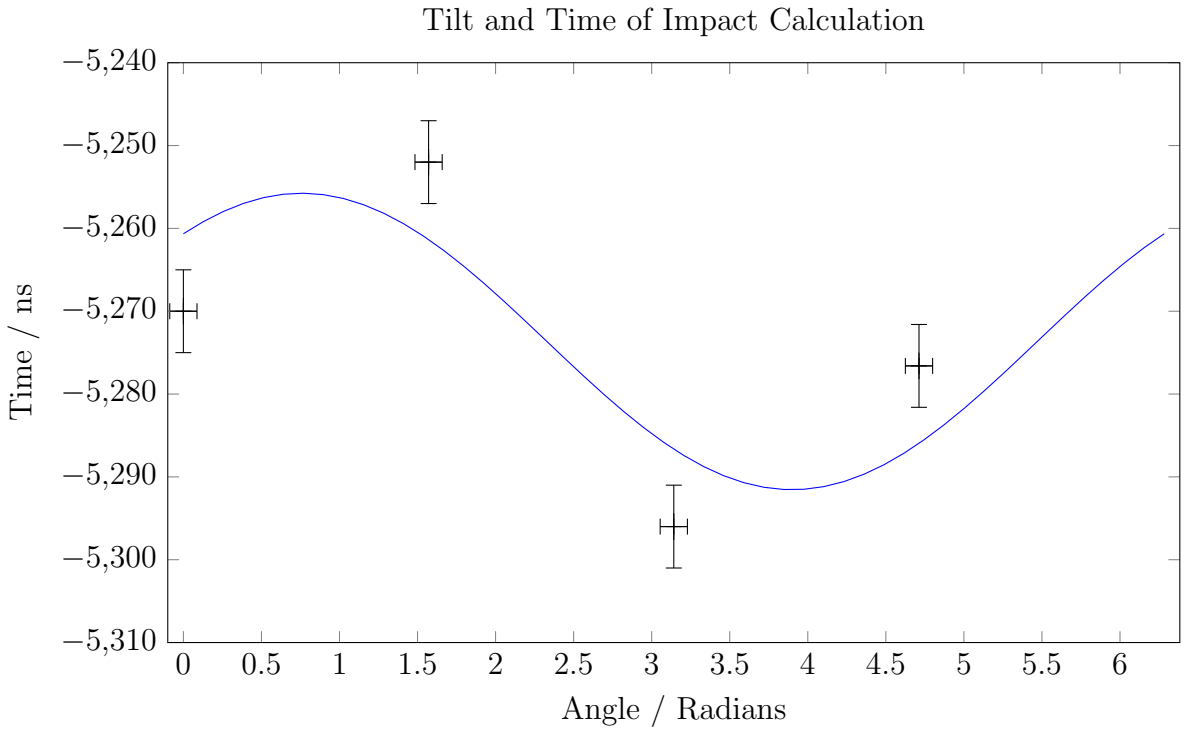


Figure 6.14: After each ToA measurement is made, the angle vs. time difference is plotted and a 1 Hz sinusoid fitted. Whilst counter intuitive given the above data, the 1 Hz frequency restriction is due to the assumption that both surfaces are flat, so any variation in impact time is caused purely from angular tilt. The amplitude of the sinusoid gives the tilt value, and the angle is determined by its phase. The disagreement between the 1 Hz fitted sinusoid and the data points is most likely caused by residual roughness on the surface of the impactor and projectile, causing the impact to not reside on a flat plane.

The average is taken as the time of impact, and the tilt is calculated through equation 6.2 where t_a is the temporal amplitude of the sinusoid.

$$\theta_i = v\frac{t_a}{r} \tag{6.2}$$

Generation One (Impact Velocity Measurement)

The impact event is found, and a FFT taken prior to the impact time event. The peak corresponds to projectile velocity. The line width can be taken as a conservative estimate of error [76], typically yielding ± 0.5 m s^{-1}. Acceleration can be checked for qualitatively by performing a Short Time Fourier Transform (STFT) on the pre-impact signal. This

will show any changes in velocity over the preceding 50 μs or so, indicating acceleration during impact.

Generation Three (Rear Surface Velocity Profile)

Analysis of the rear surface velocity profile uses techniques from the field of signal processing. Whilst there are several approaches to the analysis of PDV data, the most common, and that which is followed in this thesis, is to use a STFT. Dolan [77] provides an in-depth discussion of accuracy and precision effects in PDV. The STFT gives a velocity spectrogram, and by varying window width, the temporal vs. velocity resolution can be selected. Various signal processing techniques are used to enhance the accuracy and precision of the data.

An apparent velocity u is calculated from the doppler equation where f_b is the beat frequency, or heterodyne frequency, defined as $|f_r - f'|$, shown in equation 6.3. The wavelength of the laser light λ_r is needed and the factor of 2 is due to the reflective surface acting as both a receiver and emitter, so the doppler shift is doubled.

$$u = \frac{1}{2} f_b \lambda \tag{6.3}$$

The choice of the sliding FFT width determines a trade off in temporal and velocity resolution, as the velocity is related to frequency. Using the definition of the Fourier transform it can be shown that the frequency precision is inversely proportional to the temporal precision in equation 6.4.

$$\begin{aligned} g'(\tau, \omega) &= \int g(t) w(t - \tau) e^{-i\omega t} \, dt \\ v &= \frac{1}{2} f_b \lambda \\ g'(\tau, \omega) &= g'(\tau, \frac{2v}{\lambda}) \end{aligned}$$

For a time feature of Gaussian uncertainty δt then $g(t)$ has the form

$$g(t) = e^{-\frac{t^2}{2\delta t^2}}$$

The Fourier transform of this is

$$g'(\omega) = 2\delta t^2 e^{-2\delta t^2 \omega^2}$$

Hence the relation between width of the Gaussian uncertainty in frequency and temporal space is

$$\frac{\delta t^2}{\delta \omega^2} = \text{const}$$

converting to velocity gives

$$\frac{u\delta t^2}{f\delta v^2} = \text{const} \tag{6.4}$$

In order to find the frequency peak a three point parabolic fit is done is figure 6.15. The maximum value is used as the centre and the two points either side are used for the fit. If the parabolic fit is done on a log scale, then this is equivalent to a Gaussian (see appendix A). This makes the peak estimate algorithm much faster than a Gaussian fitting algorithm.

$$f = At^2 + Bt + C \tag{6.5}$$

The location of the peak can be found by solving the differential of equation 6.5 and setting to zero, see appendix A.

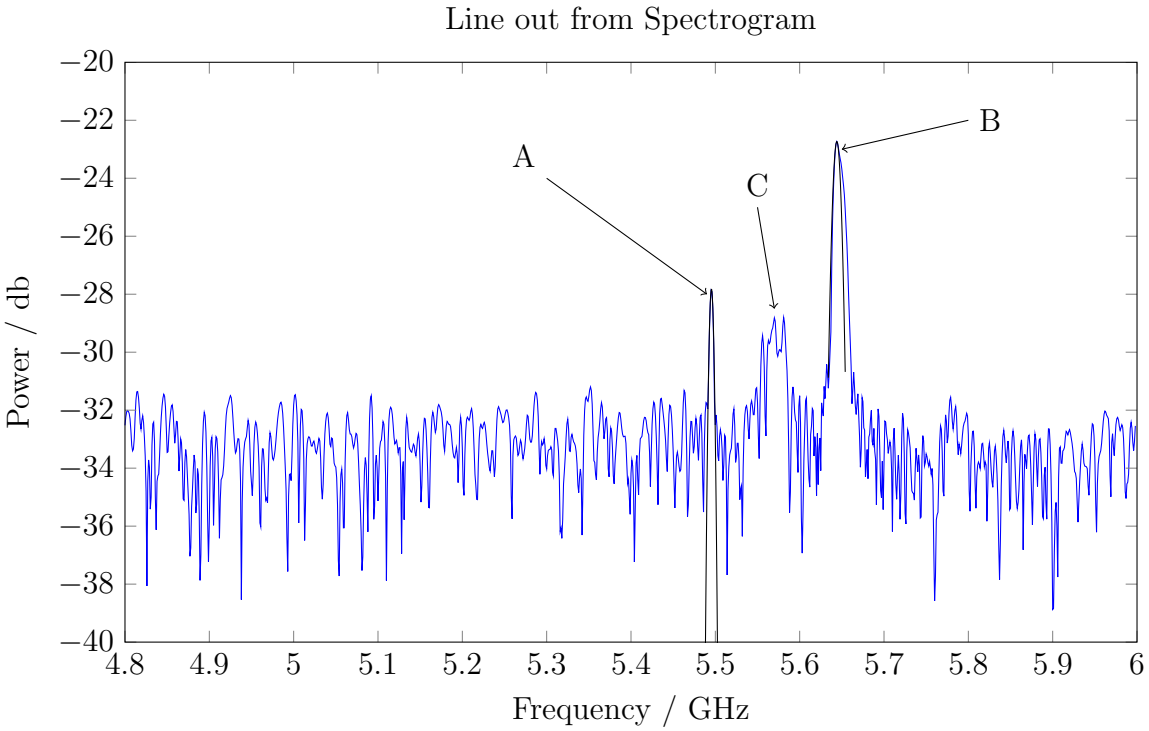


Figure 6.15: A frequency line out from a PDV spectrogram, with the peaks fitted using a parabolic fit. Peak A is the zero velocity reflection from the probe end, and stationary back reflectance in the system. Peak B is the reflection from the rear surface interfering with the reference laser. The feature at C is the reflection from the impact surface, which does not have a well defined peak as this lineout is taken from the short time window spectrogram, which does not have the frequency resolution to identify the two distinct frequencies present.

6.2.3 Sources of Error

Random error due to noise is easy to characterise. Consider an area of the spectrogram with no signal, and fit a Gaussian profile to the noise. Any signal can then be given a signal to noise ratio based on this noise model. Systematic errors are few, the primary error being the wavelength of the light used. A small error in laser wavelength (± 0.01 nm) is generally insignificant by comparison to the temporal vs. velocity resolution limit discussed in the previous section and measured by Dolan [76]. Taking half the line width of the peak as the random error in velocity is a conservative estimate, however it is precise enough for the purposes of this thesis as the dominant error in birefringence calculations is the error on the frequency measured by the polarimeter.

PDV measures the velocity component in the direction of the probe, so an angular misalignment of a probe will introduce a systematic error. The component is

$$v_m = v \cos\theta \tag{6.6}$$

.

However the value of $\cos\theta$ is 0.9988 for a θ of 0.05 radians so this correction is negligible by comparison to signal noise as all probes were aligned to better than 0.05 radians (2^o). Signal was lost on probes misaligned by more than 2^o as reflections were specular off a mirrored surface, requiring precise alignment.

6.3 Chapter Conclusions

The methods presented here are used to characterise and measure the shock compression behaviour of *a*-cut sapphire and calcite. Sapphire has previously been measured with VISAR and a wealth of Hugoniot information exists for it [24, 28, 39, 22]. There are fewer PDV measurements for *a*-cut sapphire, and no optical window correction exists for *a*-cut sapphire at 1550 nm, although there is data at 514.5 nm to compare with by

Jones *et al.* [24]. *a*-cut calcite has not been studied since Ahrens and Gregson [13] so using modern PDV techniques will improve the precision of Hugoniot measurements for *a*-cut calcite. Grady [48] studied *c*-cut calcite with VISAR, so precise *c*-cut and *a*-cut measurements can be compared for the first time. The development of the polarimeter contributes a new measurement technique to shock compression of dielectric materials and so is presented in chapter 5.

Chapter 7

Large Gas Gun Results

For the large bore gas gun work, several individuals contributed. Steve Johnson and David Pitman provided technical support, manufacturing sabots and the target back plate, as well as loading, firing and cleaning the gun. Dr. David Chapman built the eight channel PDV system and setup the PDV lasers for each shot, as well as inputting his experience into the design of the triggering and timing system. Jack Patten and Jasmina Music offered assistance with the setup of each shot.

Following the recommendations presented in chapter 4, a larger 100 mm bore gas gun was used for a second series of experiments. The larger bore allows a larger area of one dimensional strain, and so the one dimensional shock state can be maintained for a longer duration. This will give a more accurate measure of birefringence as the polarisation oscillation frequency can be measured to a greater accuracy. The large bore also allows an array of PDV probes to be mounted to measure impact tilt, and the larger radius reduces the fractional error on the measurement. As the birefringence result of experiment P2 did not agree with the expectation in chapter 3, experiments were also performed on sapphire. Previous experimental work by other groups [24] showed sapphire to behave as expected. The polarimeter as described in chapter 5 was used.

A summary of the experimental measurements can be found in table 7.1, which can be compared to the planned experimental work in chapter 6. The derived Hugoniot

Shot	Target	Flyer	l_0 / mm	v / m s^{-1}	u_p / m s^{-1}
S1	Sapphire	Copper 1001	8.003 ± 0.002	800 ± 0.5	354 ± 2
S2	Sapphire	Copper 1001	7.993 ± 0.006	414 ± 0.5	190 ± 2
S3	Sapphire	Copper 1001	7.92 ± 0.006	600 ± 0.5	278 ± 2
S4	Sapphire	Copper 1001	7.916 ± 0.003	657 ± 0.5	306 ± 2
C1	Calcite	Magnesium AZ31B	8.05 ± 0.002	206 ± 0.5	61 ± 2
C2	Calcite	PMMA	7.958 ± 0.002	262 ± 0.5	40 ± 2
C3	Calcite	Magnesium AZ31B	8.059 ± 0.014	255 ± 0.5	74 ± 2

Table 7.1: Summary of experiments performed in this chapter. The measured values for sample thickness l_0 were measured with a micrometer prior to the experiment. The impact velocity and particle velocity measurements were extracted from the relevant PDV data.

Shot	U_s / m s^{-1}	σ_l / GPa	Δn
S1	11.64 ± 0.05	16.4 ± 0.1	$-0.00649 \pm 1e-05$
S2	11.38 ± 0.05	8.59 ± 0.09	$-0.007431 \pm 8e-06$
S3	11.6 ± 0.05	12.81 ± 0.1	$-0.007082 \pm 8e-06$
S4	11.63 ± 0.05	14.18 ± 0.1	$-0.006954 \pm 9e-06$
C1	7.42 ± 0.05	1.79 ± 0.06	$-0.17204 \pm 5e-05$
C2	7.39 ± 0.05	1.19 ± 0.06	$-0.172 \pm 5e-05$
C3	7.42 ± 0.05	2.19 ± 0.06	$-0.17198 \pm 5e-05$

Table 7.2: Summary of calculated experimental results performed in this chapter. shock velocity U_s is calculated from shock transit time and sample thickness. longitudinal stress σ_l is calculated using equation 2.1. birefringence Δn is calculated using equation 2.25.

condition and birefringence values are in table 7.2.

7.1 Experimental Setup

Whilst the experimental concept is similar to the concept in chapter 4 the larger scale of the 100 mm bore gas gun, for example the considerably larger target chamber and capture tank, lead to different design constraints. It is not possible to mount the PDV board outside of the tank as the path length between the target and the tank window is greater than 1 m. This makes a suitable lens relay between fibre probe and target at least 2 m in length, impractical with the space constraints around the perimeter of the large gun. The PDV relay was therefore not used, and a dichroic mirror and a fibre probe were mounted directly behind the target as illustrated in figure 7.1.

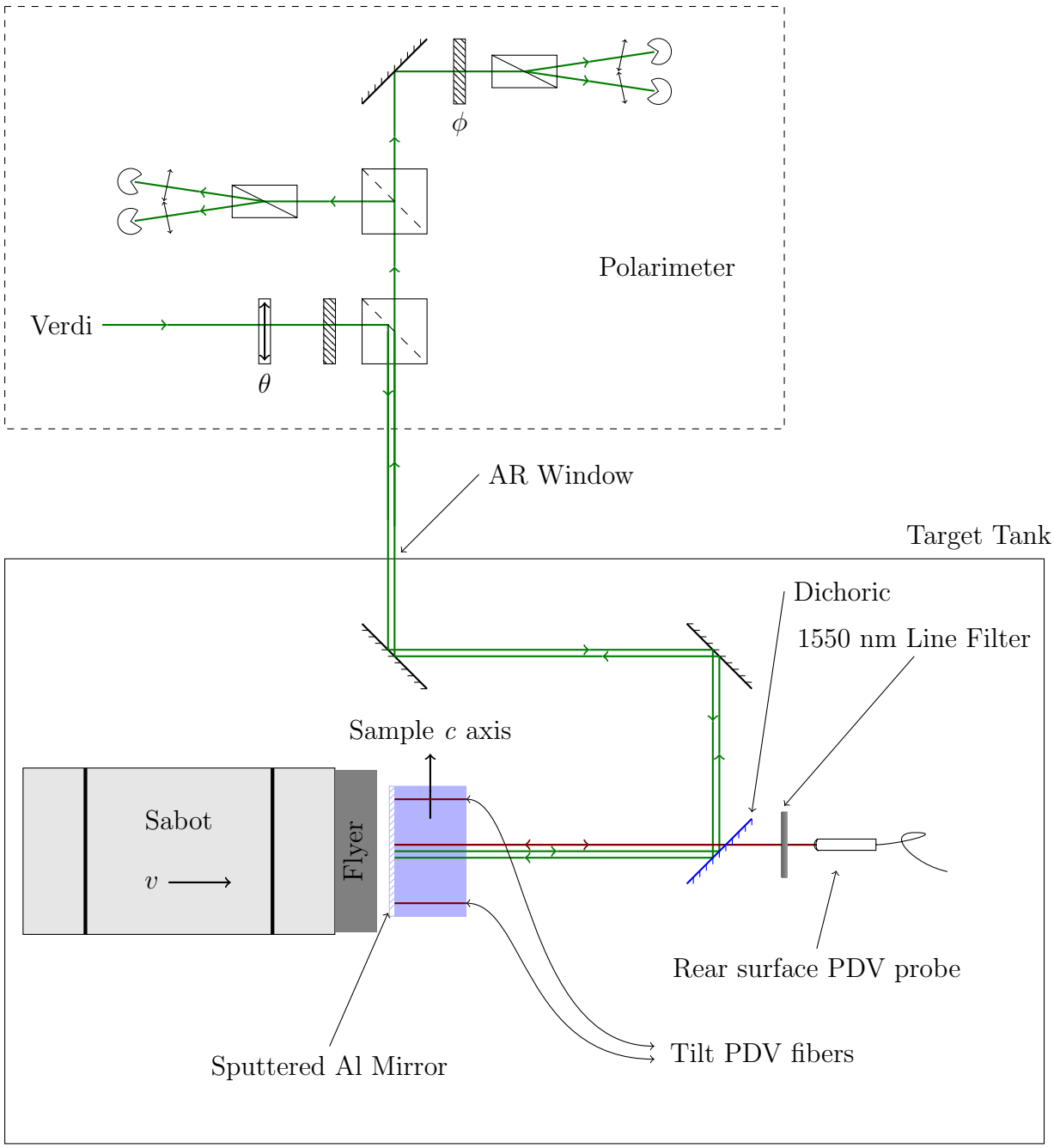


Figure 7.1: Illustration of the experimental geometry (not to scale). The flyer thickness was nominally 8 mm and the rear surface probe stand off 140 mm. Dichroic mirrors from Knight Optical were used to separate the polarimeter beam from the PDV probe. An aluminium back plate (not shown) was used to mount the sample, PDV probes and dichroic mirror to the target ring.

Each target was assembled by the author in house, with the individual parts being machined or manufactured separately. The target back plates (see figure 7.2) were machined in the Imperial College Physics Instrumentation Workshop by Mr. David Pitman. The impact face was lapped flat to nominally 3 light bands by the author. ThorLabs optical posts and kinematics were used to hold the optical assembly to the rear of the target, shown in figure 7.3. Superglue was used to attach the dichroic to the kinematic, and 5 minute two part epoxy was used to attach the rear surface PDV probe to the kinematic. The rear plate was attached to the target ring using M5 nylon bolts with the intention of failing post impact, to reduce the stress on the target frame. Isometric projections of the target assembly are shown in figure 7.5, and a photo of target C2 is shown in figure 7.6, aligned in the large bore gas gun target chamber.

The samples were 25×25 mm square and nominally 8 mm thick. Careful measurements of sample thickness with a micrometer are required to accurately determine shock velocity and these measurements are given in table 7.3. The sample was attached to the centre of the target back plate by directly placing the target on the surface, and using styrene glue at each corner to hold it in place. This ensured that the impact surface was parallel to the rear surface plate to within 1 mrad (based on tolerances of the samples, and measurements of the back plate's flatness).

The path length from the polarimeter to the target is approximately 1.5 m, including two turning mirrors inside the target tank. These two sacrificial turning mirrors inside the tank allowed the polarimeter to be aligned onto the target inside the target tank, requiring only the author to align. Fine adjustment prior to sealing the tank required a second person to check signal levels on the polarimeter, which was situated outside of the tank next to the tank window.

The first polarimeter turning mirror was shielded somewhat, however the second mirror needed replacing after each shot as dust embedded in the mirror greatly reduced its reflectivity. As a dichroic mirror was sacrificed each experiment simple cold mirrors from knight optical (part 700FCQ4040) were used. These mirrors offered around 90%

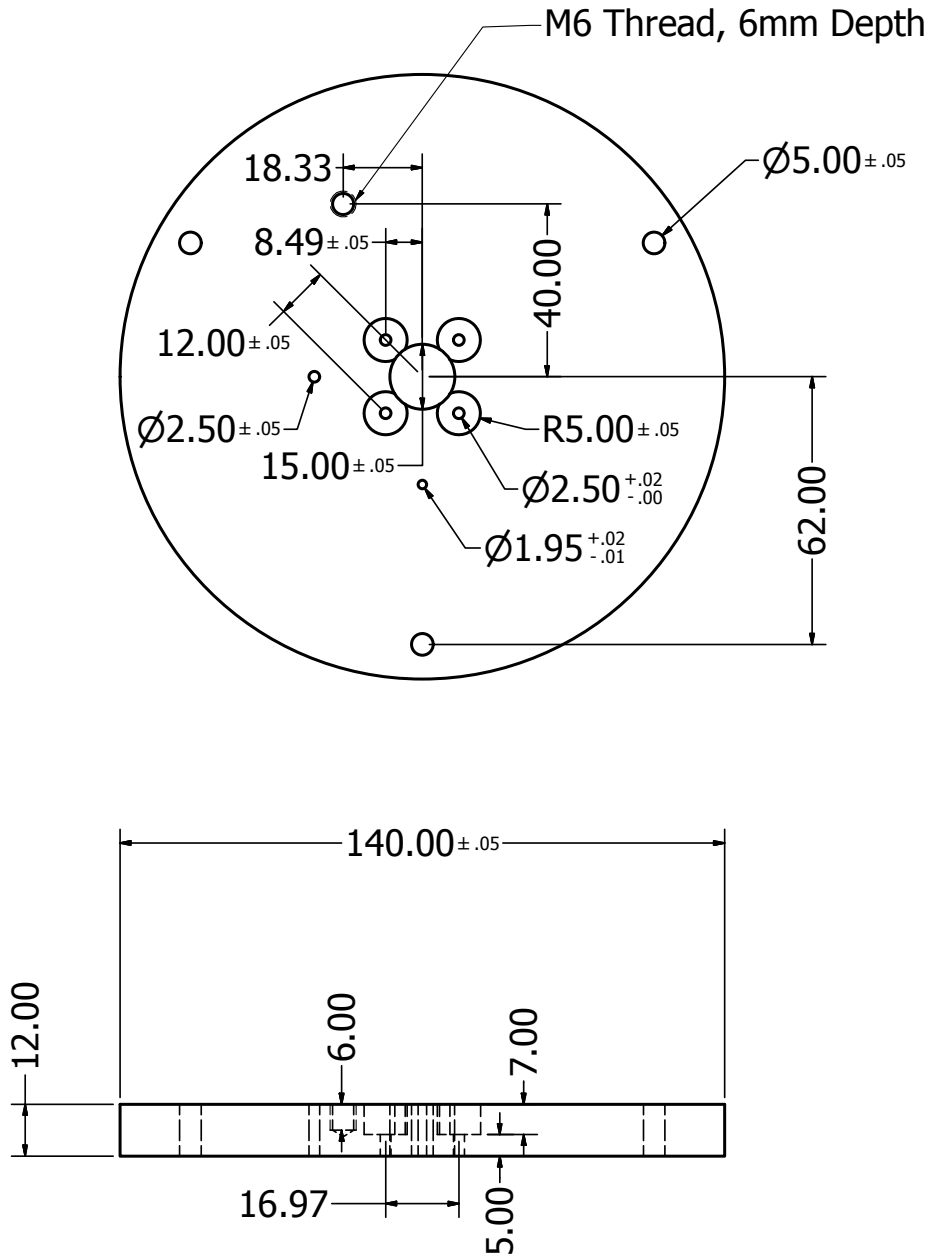


Figure 7.2: Back plate of target machined in house at Imperial College Physics Workshop by Mr. David Pitman. The impact surface was lapped. A 20 mm diameter hole in the centre allows optical diagnostics to be fielded onto the target sample. Tilt PDV probes (2 m FC fibre patch cables) are directly mounted into the aluminium back plate, as well as the velocity probe (Oz Optics collimated -60 dB back reflectance), and all held with 5 minute epoxy.

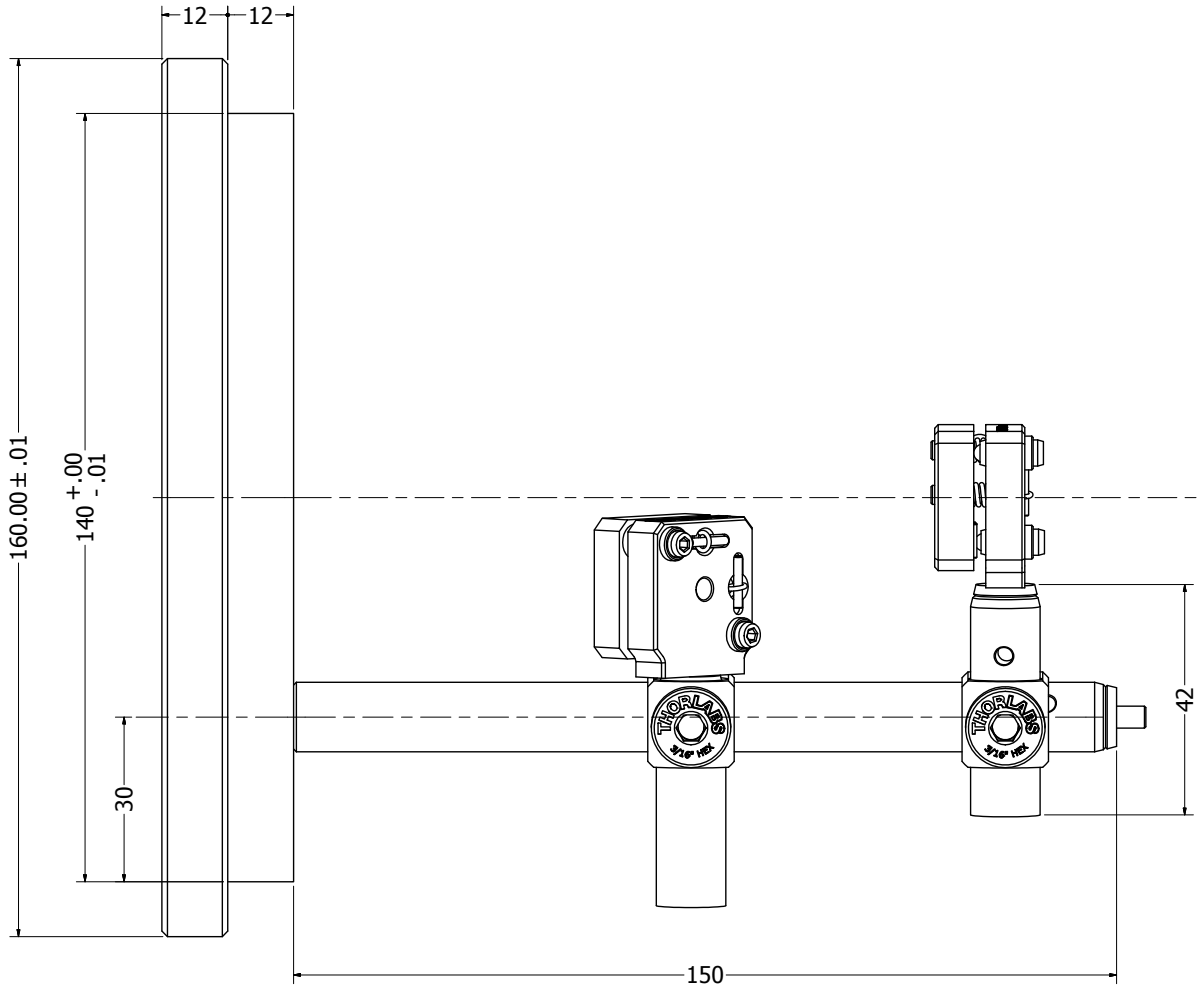


Figure 7.3: Side profile of target. ThorLabs optical posts (150 mm, 40 mm) and compact kinematic mounts (KMSS/M) were used to attach optics to rear surface. The rear surface PDV probe was a collimated probe from Oz Optics, held using 5 minute epoxy into the rear kinematic. Superglue was used to bond the dichroic to the central kinematic.

Sample	**Thickness / mm**	**Parallelism / mrad**
S1	8.003 ± 0.003	0.47 ± 0.14
S2	7.993 ± 0.006	1.07 ± 0.14
S3	7.920 ± 0.006	1.07 ± 0.14
S4	7.916 ± 0.002	0.40 ± 0.14
C1	8.050 ± 0.002	0.00 ± 0.14
C2	7.958 ± 0.002	0.07 ± 0.14
C3	8.059 ± 0.014	2.1 ± 0.14

Table 7.3: Sample thicknesses for each shot and calculated parallelism of each sample. The parallelism is calculated by measuring the difference between minimum and maximum values for thickness measurements, and dividing this by the radius of the measurement (15 ± 1 mm). Sample thicknesses are measured at each corner using a micrometer.

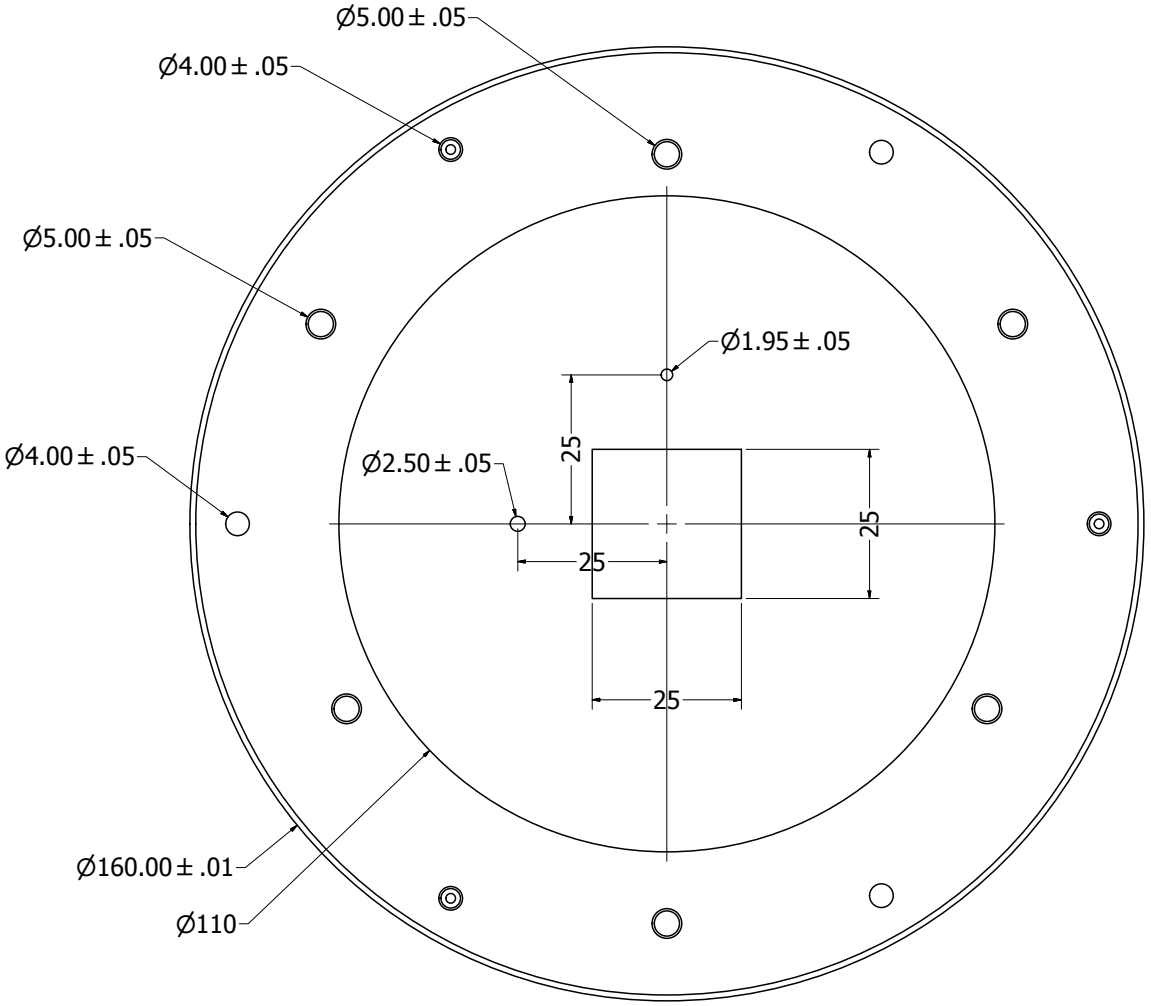


Figure 7.4: Impact surface of target with calcite or sapphire sample in the centre. The sample was placed directly onto the back plate, and bonded using styrene around the sample edges. The outer ring is attached to the back plate using M5 nylon bolts.

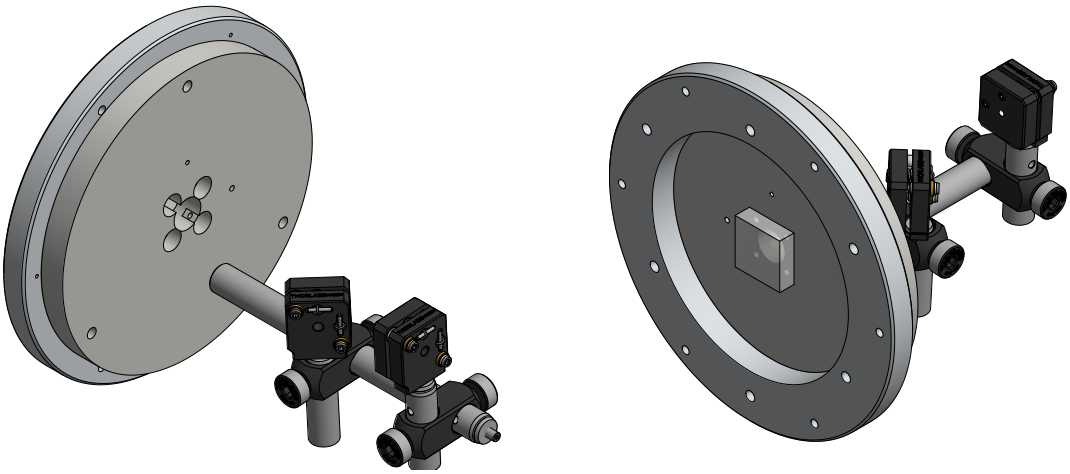


Figure 7.5: Isometric projections of large bore gas gun target. The entire assembly is destroyed each experiment.

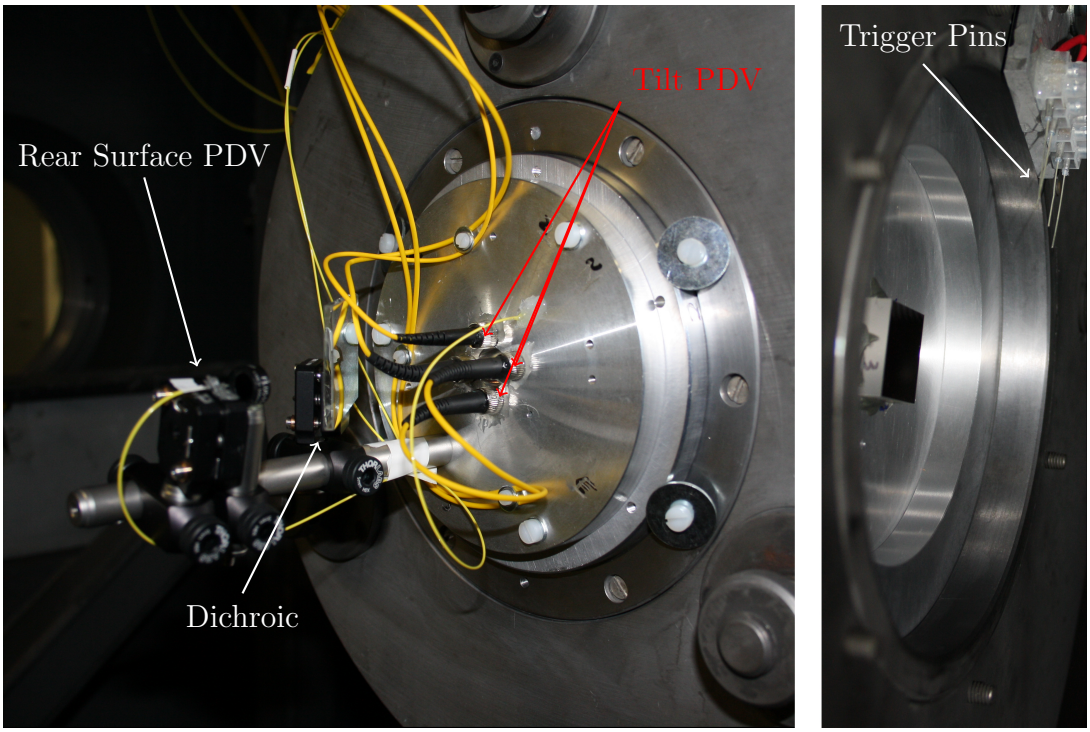


Figure 7.6: *Left:* Photograph of the rear of calcite target C2 assembled and aligned in the target tank of the 100 mm bore gas gun. The aluminium back plate and optics can be seen. *Right:* Calcite sample C3 on reverse of aluminium plate. The trigger pins, which short when in contact with the sabot, triggering the oscilloscopes to record the experiment, can be seen in the top right.

transmission above wavelengths of 1200 nm and 95% reflection at wavelengths below 700 nm. This meant that some polarimeter light was transmitted to the PDV probe, necessitating a 1550 nm line filter with a 5 nm transmission band width. The silicon ThorLabs DET10A detectors on the polarimeter were not sensitive to 1550 nm light, and the 1550 nm light leaving the fibre probe was less than 1 mW in power, so no filters were added to the polarimeter as it was assumed the small amount of 1550 nm light reaching the polarimeter would have a negligible effect on any measurements. As the polarimeter used collimated light, the wavefront error at the dichroic is significant. If the wavefront is distorted too much, the signal returned to the polarimeter is reduced substantially. This is because the specular reflection becomes diverging, and with no image relay some of the light is lost. The dichroic and turning mirrors had a $\lambda/10$ wavefront error, which was sufficient.

An important improvement over the experimental setup in chapter 4 is that, due to the larger diameter bore, impact tilt can be measured. This is achieved with four generation zero PDV probes mounted on the sample. Each PDV probe records the time at which the interface starts moving and the impact tilt can be calculated using methods described in chapter 6.

7.2 Sapphire

Four experiments were performed with a summary presented in table 7.4. The range of experiments was initially chosen to be under the expected longitudinal stress HEL of 18 GPa for *a*-cut sapphire, based on Jones *et al.* [24]. After the first experiment it was determined that the HEL for the *a*-cut sapphire in this study was closer to 14 GPa in line with other orientations of sapphire [39], and so the experimental parameters were adjusted accordingly.

As discussed in chapter 1, sapphire has been studied extensively in the shock physics community. It has a high yield stress of around 12 GPa, and has been used as an optical

Shot	Flyer	l_0 / mm	v / m s^{-1}	u_p / m s^{-1}	σ_l / GPa
S2	OFHC copper	7.993 ± 0.006	414 ± 0.5	190 ± 2	8.59 ± 0.09
S3	OFHC copper	7.92 ± 0.006	600 ± 0.5	278 ± 2	12.81 ± 0.1
S4	OFHC copper	7.916 ± 0.003	657 ± 0.5	306 ± 2	14.18 ± 0.1
S1	OFHC copper	8.003 ± 0.002	800 ± 0.5	354 ± 2	16.4 ± 0.1

Table 7.4: Summary of sapphire large gas gun experiments. Impact velocity v, particle velocity u_p and sample thickness l_0 are directly measured. Longitudinal stress σ_l is calculated through the Hugoniot momentum conservation jump equation 2.1.

window material by many groups. This has lead to an extensive body of optical and mechanical measurements on several orientations of sapphire under shock compression. Any further measurement can therefore be compared to an extensive body of literature making sapphire an excellent standard with which to compare experimental methods.

For the sapphire experiments the PDV used a downshifted configuration, with a reference frequency higher than the initial probe frequency. This increased the range of detectable velocities, as it was expected that the shock front would have a significant reflectivity. A reference wavelength of 1549.336 nm was used, set and measured internally on the NKT Adjustik.

7.2.1 PDV Analysis

The rear surface PDV data were analysed using the method described in section 6.2 to extract shock velocity and particle velocity values for each impact. The base frequency was found by computing the FFT of the signal prior to shock arrival t_0, and this was set as the zero velocity frequency. Short time windows of 80 ns were used in the STFT for measuring shock velocity and long time windows of 300 ns were used for particle velocity. The short window STFT for experiment S2 is given in figure 7.7.

As described in section 6.2.2 the apparent velocity is calculated using equation 7.1 taking the laser wavelength of the reference laser, measured internally on the NKT Adjustik. The apparent velocity in figure 7.8 is the actual velocity of the rear surface, however the impact surface requires a window correction as the optical path length is altered by the refractive index of the sapphire. The window correction can be measured by comparing

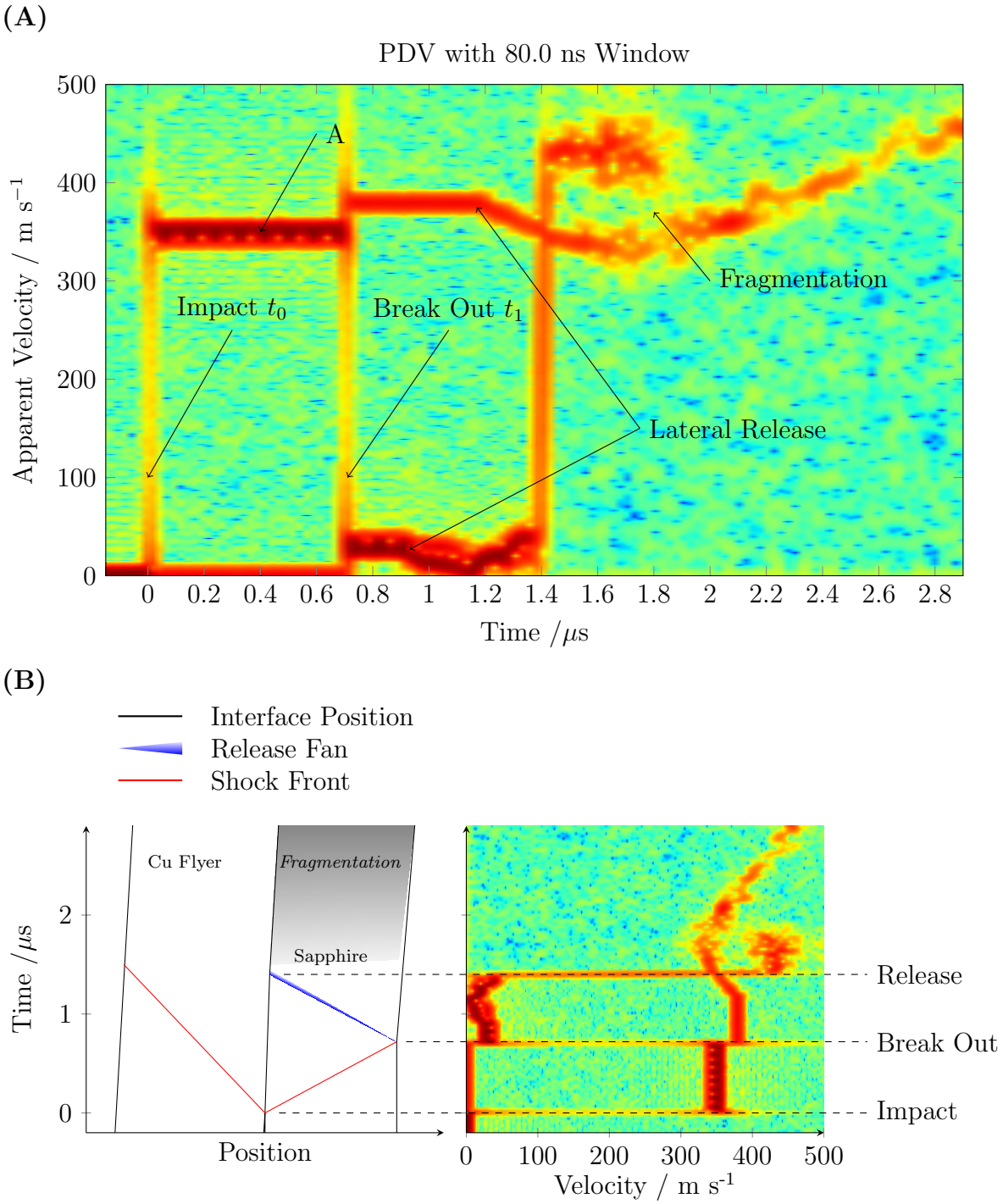


Figure 7.7: **(A)** PDV data from the sapphire experiment S2, with the apparent velocity axis corrected for downshifting. The reflection from the impact surface (marked A) shows a beat intensity due to two very close frequencies. These cannot be distinguished with the short time window used here, but are clear in figure 7.8. After lateral release, the impact surface and rear surface begin to slow, followed by fragmentation of the sample. The fragmentation leads to a wide spread of particles moving at different speeds, evident from the band of velocities present after the lateral release. **(B)** $x-t$ diagram of impact, with key features marked.

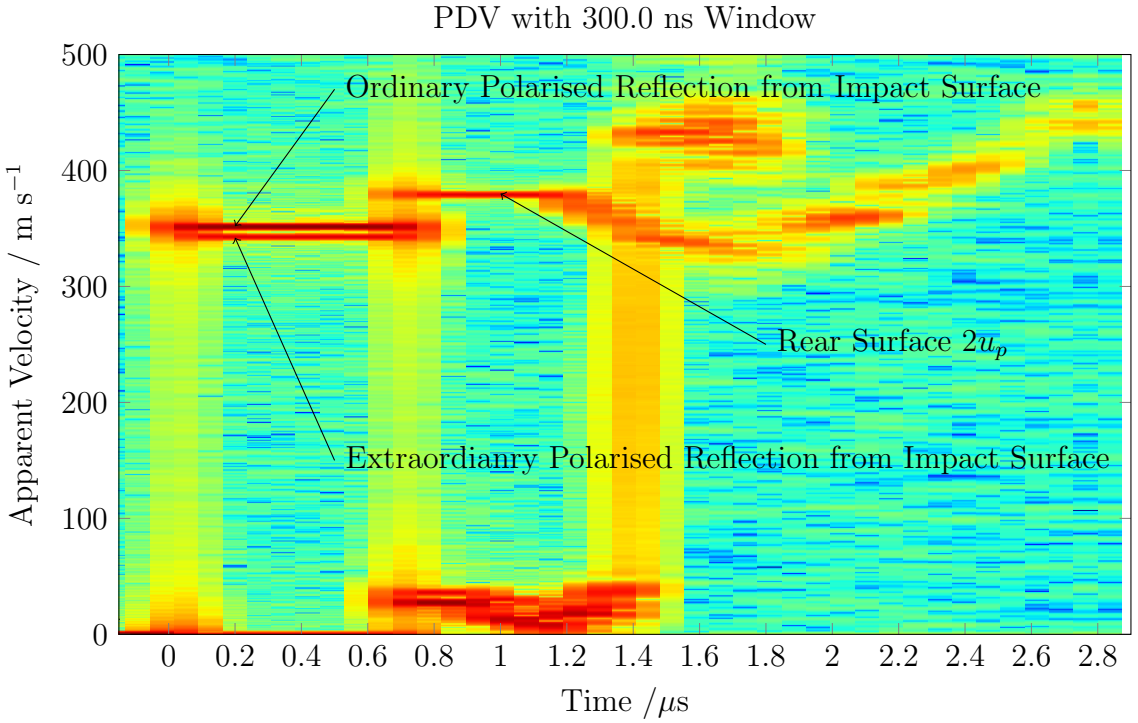


Figure 7.8: PDV data from the sapphire experiment S2 (same raw data as figure 7.7, longer STFT window), with the apparent velocity axis corrected for downshifting. The long time window allows a precise measurement of the free surface velocity. It is also possible to resolve the two frequencies present in the reflection from the impact surface, caused by the birefringence of the sample. These two frequencies are used in section 7.2.3 to calculate the birefringence at 1550 nm.

the free surface velocity and the apparent velocity at the impact surface, and further analysis of this result is in section 7.2.3. The corrected velocities are shown in figure 7.9, where the velocity is taken as the average plateau velocity across the time indicated by the line.

$$u = \frac{1}{2} f_b \lambda \tag{7.1}$$

The experimental longitudinal stress can be calculated using the jump equation 2.1 and the calculated values are given in table 7.5.

Longitudinal stress and particle velocity are conserved at the impact plane, and both the impact velocity and the flyer Hugoniot's are known [65], so an expected particle velocity can be found for each shot. The impact velocity can be measured to 0.5 m s^{-1}and

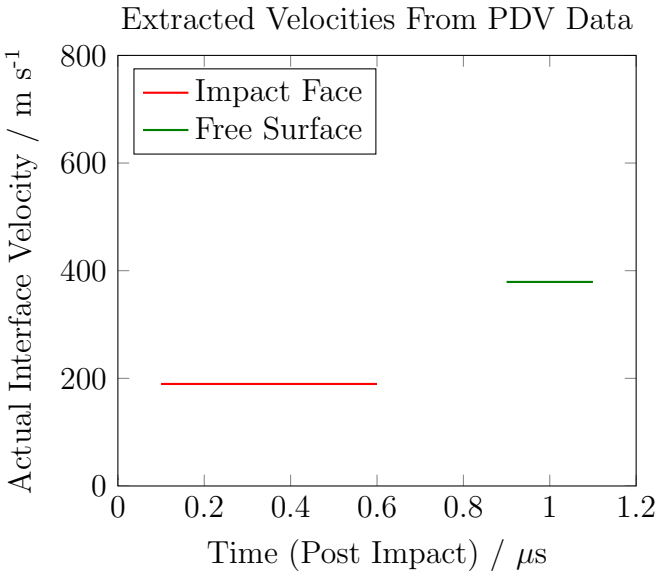


Figure 7.9: Velocities extracted from PDV data in figure 7.8, with the impact surface velocity corrected for index of refraction effects. It is travelling at half the free surface velocity and this is used to calculate a window correction for both the ordinary and extraordinary polarisations. The velocity is calculated as the average peak over the length of the line and the error is the width of the line.

Shot	U_s **/ km s^{-1}**	u_p **/ km s^{-1}**	σ_l **/ GPa**	ρ **/ g cm^{-3}**	ε **/ %**
S2	11.38 ± 0.01	0.19 ± 0.002	8.59 ± 0.09	4.047 ± 0.01	1.666 ± 0.018
S3	11.6 ± 0.01	0.278 ± 0.002	12.81 ± 0.1	4.078 ± 0.01	2.392 ± 0.017
S4	11.63 ± 0.01	0.306 ± 0.002	14.18 ± 0.1	4.088 ± 0.01	2.635 ± 0.017
S1	11.64 ± 0.01	0.354 ± 0.002	16.4 ± 0.1	4.105 ± 0.01	3.042 ± 0.017

Table 7.5: Measured velocities and calculated Hugoniot state variables for sapphire experiments.

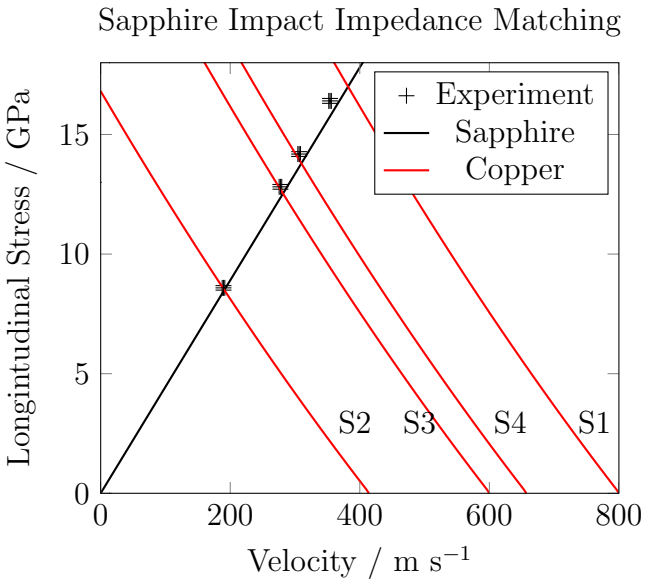


Figure 7.10: Predicted sapphire Hugoniot compared with measured values found using the relationship $\sigma_l = \rho_0 U_s u_p$. The copper flyer Hugoniots for each impact are plotted, and the corresponding measured Hugoniot state for each experiment. It is expected that each point should fall on the copper – sapphire intersection, within experimental error.

the longitudinal stress particle velocity Hugoniot is known to within a percent for the copper flyer at these pressures. The expected particle velocity can then be compared with the measured particle velocity from the PDV data. Figure 7.10 plots the flyer Hugoniots against the sapphire Hugoniot at the measured impact velocities from table 7.4. This gives an expected longitudinal stress and particle velocity in the first shock state, which is in agreement with the measured longitudinal stress and particle velocity state from table 7.5.

7.2.2 Polarimetry

The raw data from the oscilloscope, which recorded the intensity measured by each polarimeter detector, was analysed as in section 5.3, generating a set of Stokes vectors for each time point. The circular stokes component was analysed using a FFT to find the frequency of the polarisation oscillation. The centre of the frequency peak was found with a three point parabolic fit and the error on the frequency was conservatively taken as half the line width. The PDV data were analysed for each shot to obtain shock velocity and

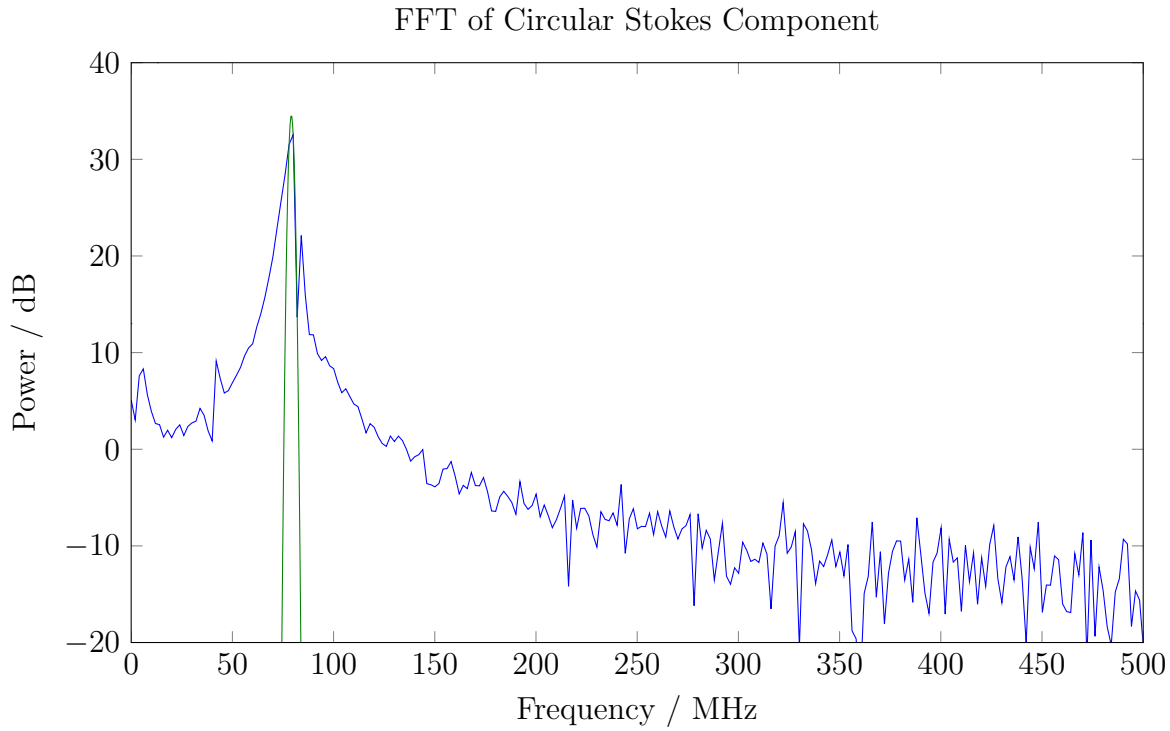


Figure 7.11: Sapphire experiment S1 polarimetry. FFT of circular Stokes component from the polarimeter data. The peak has been fitted with a three point parabolic fit (*green*).

particle velocity for each experiment. Using equation 7.2 (first derived in section 2.6.1) the measured shock birefringence can be found for each shot and these results are presented in figure 7.12. We can see from figure 7.12 that the experimental results agree with literature values by Jones *et al.* [24] for the photoelastic behaviour of sapphire, with the exception of the yield point.

$$\Delta n' = \frac{f\lambda + 2U_s\Delta n}{2(U_s - u_p)} \tag{7.2}$$

7.2.3 Window correction for PDV and Direct PDV Birefringence Measurement

As the PDV measurement reveals two refractive indices, a window correction can be calculated for each refractive index using the method in section 2.6.3. The key equation

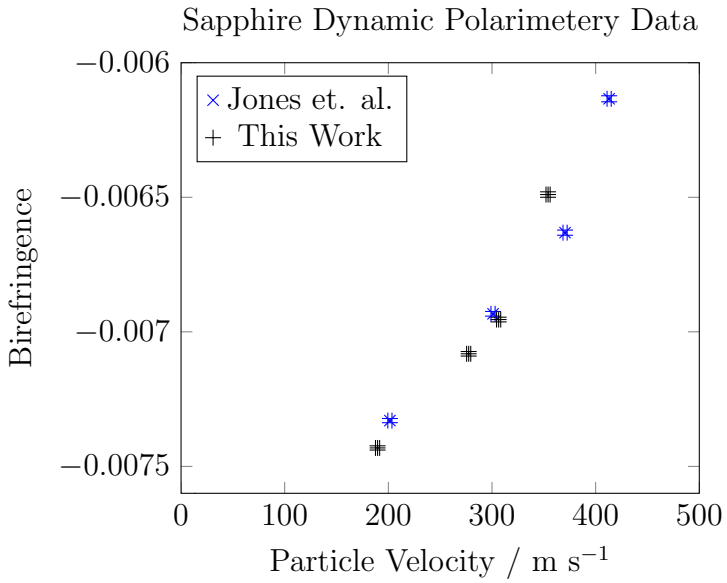


Figure 7.12: Calculated shocked birefringence $\Delta n'$ from polarimeter data for sapphire. Data from Jones *et al.* [24] has been added for comparison. As the wavelength of light used is different between this work (532 nm) and Jones *et al.* [24] (514.5 nm), as well as the sapphire source being different, there is a slight offset in the two data sets caused by optical dispersion and batch variation. The chromatic dispersion in birefringence is -0.0001 at room temperature and pressure [78].

(equation 2.30) is reproduced below

$$n' = \frac{\frac{1}{2}\omega - n_0 u_p}{u_p - U_s} \ . \tag{7.3}$$

By calculating the difference between the shocked ordinary and shocked extraordinary refractive indices, a birefringence measurement can be made at 1550 nm. The long time window PDV data in figure 7.8 allows accurate determination of the two refractive indices. The 1550 nm birefringence was found to be in close agreement with polarimetry data, however the errors on the birefringence measurements with PDV are higher than with the polarimetry results. The two measurements can be compared in figure 7.13, and are in agreement within error.

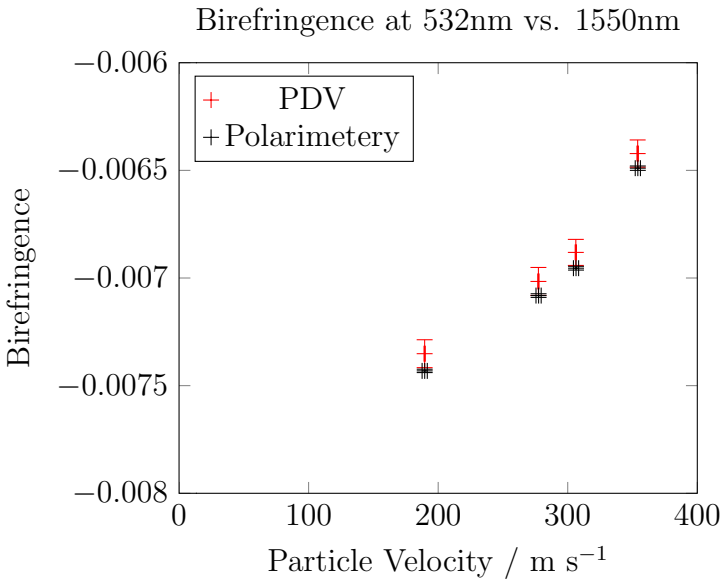


Figure 7.13: Comparison of polarimetry vs. PDV birefringence measurements in sapphire. The effect of optical dispersion (1550 nm vs. 532 nm) can be seen as a slight zero offset between the two data sets. The 532 nm data intersects at $\Delta n = -0.0081$, and the 1550 nm intersects at $\Delta n = -0.0078$ which is consistent with optical dispersion in synthetic sapphire measured by Malitson [78].

Shot	**Flyer**	l_0 **/ mm**	v **/ m s^{-1}**	u_p **/ m s^{-1}**	σ_l **/ GPa**
C2	PMMA	7.958 ± 0.002	262 ± 0.5	40 ± 2	0.81 ± 0.04
C1	Magnesium AZ31B	8.05 ± 0.002	206 ± 0.5	61 ± 2	1.22 ± 0.04
C3	Magnesium AZ31B	8.059 ± 0.014	255 ± 0.5	74 ± 2	1.49 ± 0.04

Table 7.6: Summary of calcite experiments performed on the large bore gas gun.

7.3 Calcite

Three experiments were performed with calcite with final longitudinal stress states ranging from 0.8 GPa to 1.5 GPa. This is below the longitudinal stress calcite HEL and calcite – calcite II phase transition of 1.8 GPa. Because of this the wave structure in the calcite should be approximated well by a single step wave shock. A summary of the experiments is outlined in table 7.6.

7.3.1 PDV Results

As for sapphire, the base reference frequency was found, and set as the zero velocity. For shock speed the times of arrival needed to be measured accurately so a short FFT

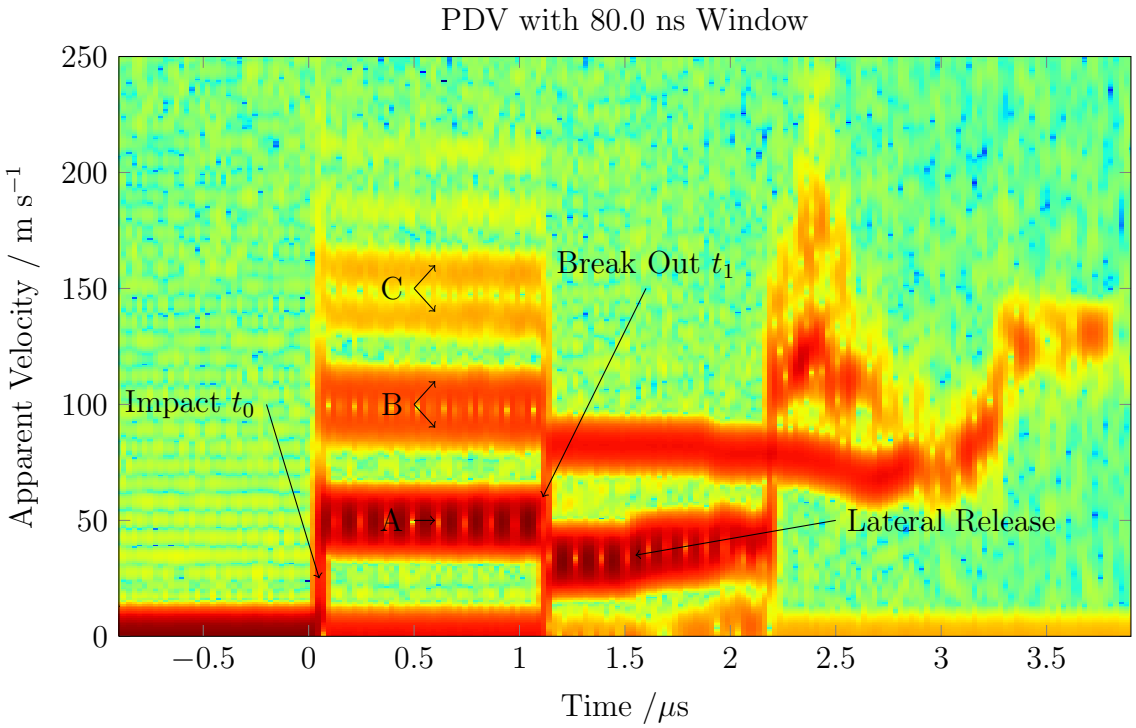


Figure 7.14: Short window PDV spectrogram for calcite experiment C2, the short window is used to give greater time accuracy. This allows accurate determination of the shock velocity. The AR coating on the calcite was optimised for 532 nm, so strong reflections at the free surface were present for 1550 nm, which the PDV operates at. These reflections return to the moving surface and are doppler shifted by the same degree again. This leads to higher velocity features (B and C) from the impact surface that are integer multiples of this first peak (marked A), with reducing power. The beating in the impact surface reflection is due to the low frequency (velocity) resolution, and the two frequencies (visible in figure 7.15) cause an amplitude oscillation known as beating. After lateral release the material is no longer in uniaxial strain, and fracture begins to occur. The lateral release changes to velocity of the surfaces, and fracture causes the spread in velocities to be observed.

window length of 80 ns was used in figure 7.14, whilst for particle velocity the free surface velocity needed to be measured accurately so a long window length of 300 ns was used in figure 7.14. The extracted velocities, corrected for index of refraction effects are shown in figure 7.16.

Once particle velocity and shock velocity are extracted from the PDV probe, the longitudinal stress state and other variables can be calculated from the jump equations. Table 7.7 presents the shocked state calculated from shock velocity and particle velocity data. The longitudinal stress is then compared with expected longitudinal stress particle

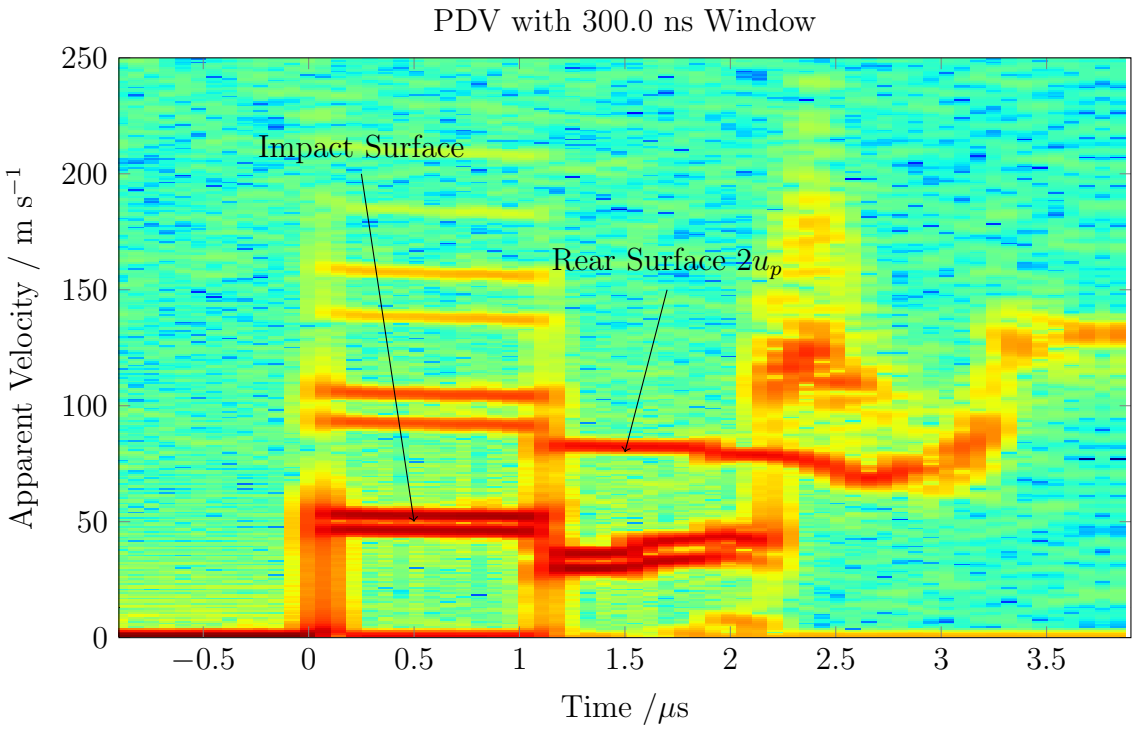


Figure 7.15: Long window PDV spectrogram for calcite experiment C2 used for greater velocity accuracy over figure 7.14. Multiple doppler shifted features are visible again. The beating observed in figure 7.14 is resolved into two distinct frequencies due to the higher velocity resolution.

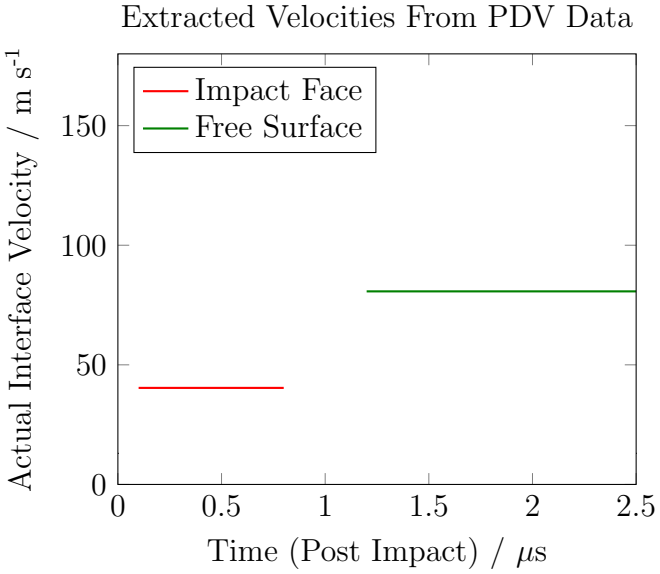


Figure 7.16: Velocities from PDV data in figure 7.15 with the impact interface corrected for index of refraction effects. The impact interface travels at half the free surface velocity, allowing a calculation of the window correction for both the ordinary and extraordinary refractive indices of calcite. The velocity is calculated as an average of the time frame of the line, and the error is the width of the line.

Shot	U_s / **km s^{-1}**	u_p / **km s^{-1}**	σ_l / **GPa**	ρ / **g cm^{-3}**	ε / **%**
C2	7.389 ± 0.01	0.04 ± 0.002	0.81 ± 0.04	2.725 ± 0.01	0.55 ± 0.03
C1	7.419 ± 0.01	0.061 ± 0.002	1.22 ± 0.04	2.732 ± 0.01	0.82 ± 0.03
C3	7.418 ± 0.01	0.074 ± 0.002	1.49 ± 0.04	2.737 ± 0.01	1 ± 0.03

Table 7.7: Measured velocities and calculated Hugoniot state variables for calcite experiments.

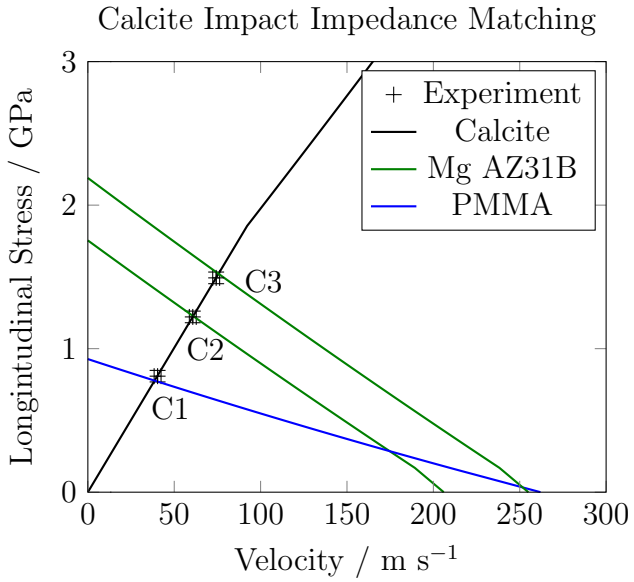


Figure 7.17: Predicted calcite elastic Hugoniot from Ahrens and Gregson [13] and measured values for all experiments (data points). Flyer Hugoniots are from Marsh [65] and an elastic perfectly plastic strength model has been applied to the flyer materials. Experimental points are within error of the intersects, which give the expected Hugoniot state.

velocity state from the impact velocity and flyer Hugoniot and presented in figure 7.17.

Hugoniot Measurements

As both shock velocity and particle velocity are measured on the same experiment, it is possible to check the literature Hugoniot measurements of calcite. This is done in figure 7.18, in principle the shock velocity should be constant with particle velocity as the wave is elastic. In practice a small increase in elastic shock velocity with particle velocity is usually found, as is the case in the results presented here. The shock velocity measured in these experiments is higher than that measured by Ahrens and Gregson [13], however the results here are in agreement with longitudinal sound speed measurements

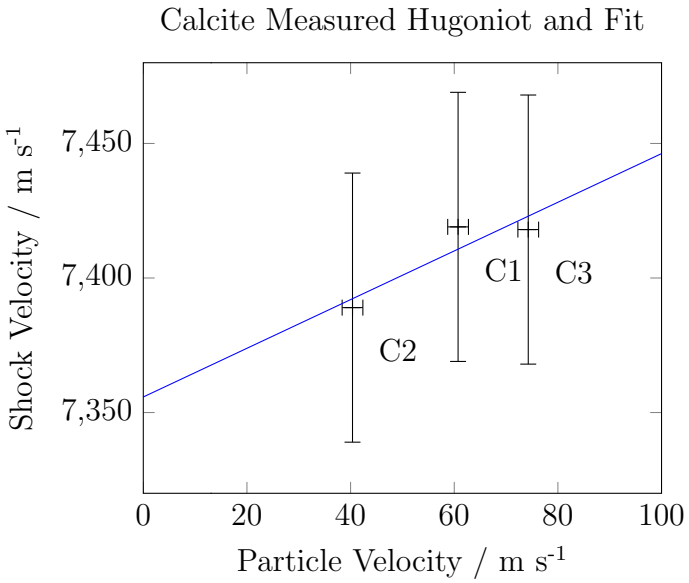


Figure 7.18: The Hugoniot plotted in the shock velocity particle velocity plane. The blue line is a linear fit to the three calcite experimental data points, shots C1 – C3.

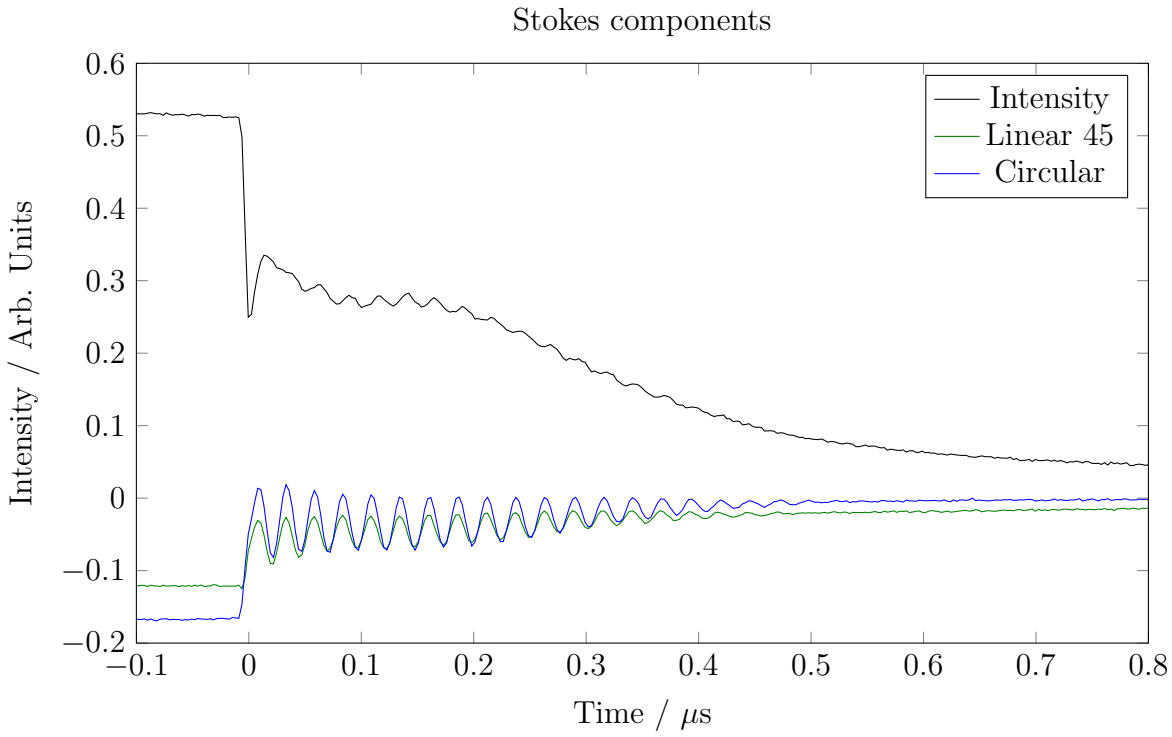
by Dandekar [12]. It is likely that the higher velocity impacts in Ahrens and Gregson [13] work are the cause of the lower observed elastic longitudinal wave velocity. As the trend at low pressures (this work) is for increasing longitudinal sound speed with particle velocity, it should be expected that Ahrens and Gregson [13] would observe a higher elastic precursor velocity, however they observe a lower velocity. This is likely caused by the higher pressure experiments in Ahrens and Gregson [13] causing a phase change in the calcite, allowing the material to relax, slowing the elastic precursors.

7.3.2 Polarimeter Results

The polarimetry data were analysed with the same method as that used for sapphire. The stokes vector components and the FFT of the circular stokes component are shown in figure 7.19.

Once a frequency is calculated, this is combined with shock velocity and particle velocity data from PDV to calculate a shocked birefringence. As shown in figure 7.20, it was found that there was no change in birefringence in the shocked region for calcite.

(A)



(B)

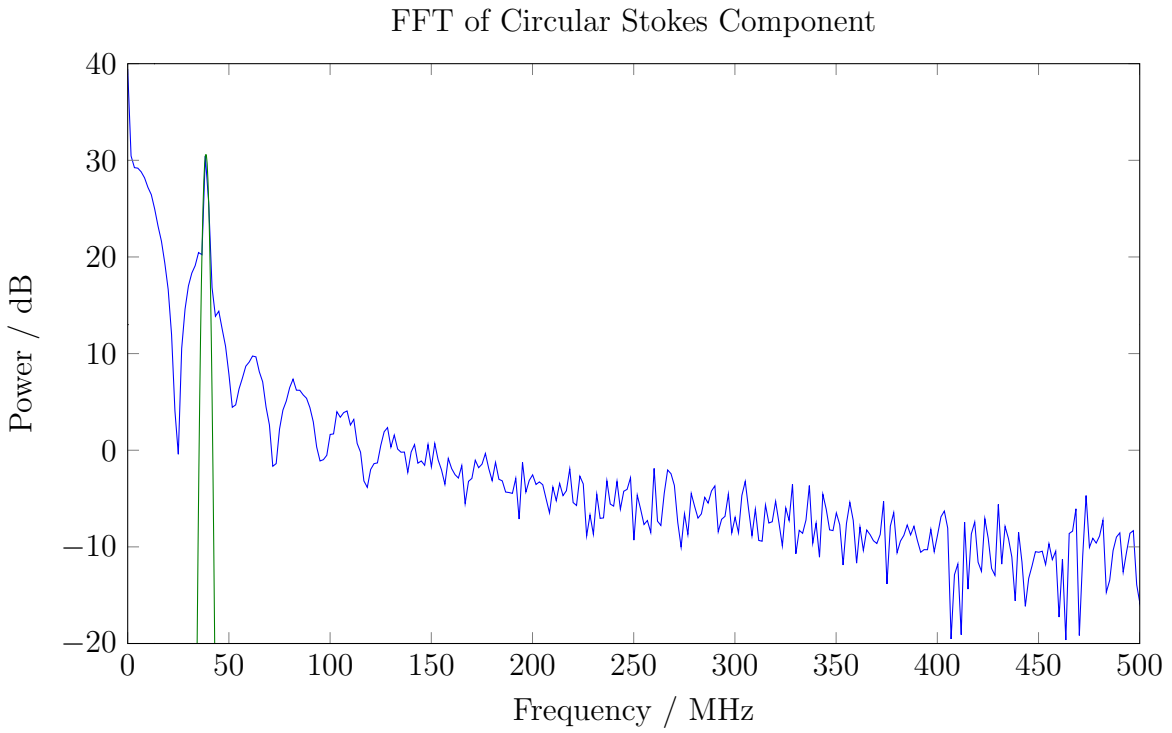


Figure 7.19: Polarimeter data from calcite experiment C1. The individual stokes components as a function of time are shown in figure **A**. In figure **B** the circular stokes component is processed using a FFT to find the frequency and a three point parabolic fit is made to the peak data point, and each either side. Side lobes on the FFT can be seen and are caused by the super Gaussian window used in the FFT analysis.

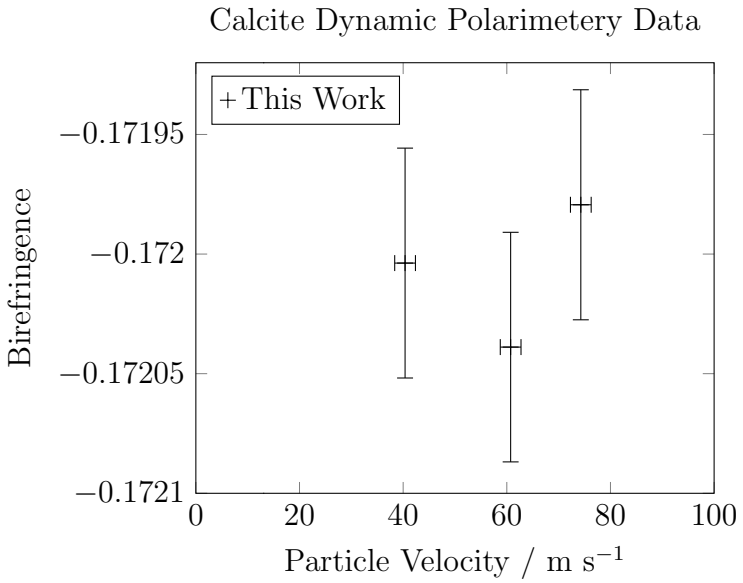


Figure 7.20: Calculated shocked birefringence $\Delta n'$ from polarimeter data for calcite. The original birefringence of -0.172 means this result is entirely consistent with no change in birefringence under shock compression.

7.3.3 Window correction for PDV and Direct PDV Birefringence Measurement

Using the PDV window correction method outlined for sapphire in section 7.2.3, a birefringence at 1550 nm was calculated for calcite. Again, the PDV method was found to be consistent with polarimetry data, showing no change in birefringence. There is a stronger dispersion effect than with sapphire, and as shown in figure 7.21, the PDV and polarimetry data sit further apart.

7.4 Measurements of Optical Axis

In chapter 3 it was predicted that the optical axis of the shock compressed region would be rotated with respect to the unshocked material. This is due to a non-zero value in the photoelastic $\underline{\mathbf{p}}_{14}$ component. An analysis of the amplitude of linear and circular components measured by the polarimeter, as discussed in chapter 5, provides a measure of the optical axis in the shocked region.

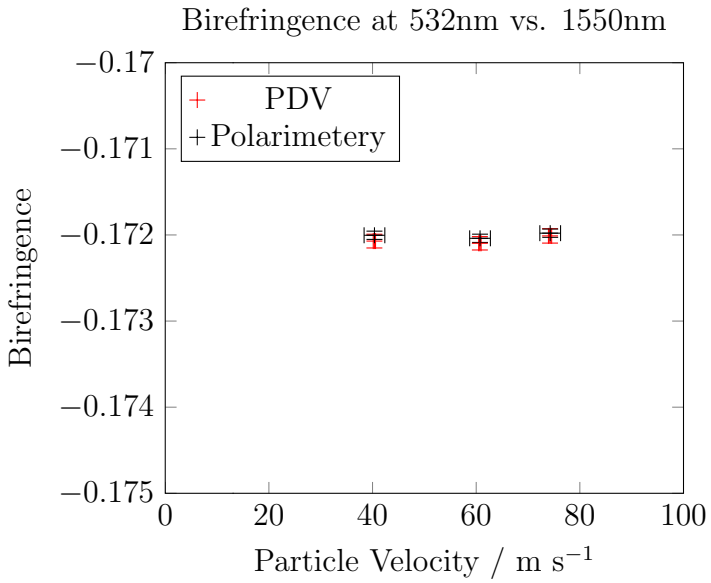


Figure 7.21: Comparison of polarimetry vs. PDV birefringence measurements in calcite. They are in agreement, with a slight constant offset consistent with optical dispersion between 1550 nm and 532 nm [79].

Post-processing of the FFT data was carried out to calculate the relative amplitudes of the polarimeter to get an estimate of the optical axis angle. This included spectral filtering to remove back-reflections which had different frequencies to the reflection from the impact surface.

The rotation of the optical axis was estimated by comparing pre-shot calibration data with filtered shock data. The optical axis angles are given in table 7.8 and the change plotted as a function of particle velocity for each material in figure 7.22. The error bars are quite large, and therefore it is difficult to draw firm conclusions from this data.

7.5 Chapter Conclusions

In this series of experiments, several literature results (Kanel *et al.* [39], Ahrens and Gregson [13]) have been confirmed. Furthermore the use of PDV to record velocity history has improved the precision of these previous literature results. In addition, there are several new measurements made, not previously in the literature.

The *a*-cut calcite Hugoniot measured by Ahrens and Gregson [13] has been confirmed

Sample	Angle / Degrees		
	Unshocked	**Shocked**	**Absolute Difference**
C1	45±4	53±4	8±4
C2	46±4	54±4	8±4
C3	46±4	27±4 *	19±4
S1	43±4	51±4	7±4
S2	45±4	64±4	19±4
S3	44±4	49±4	5±4
S4	45±4	72±4	27±4

Table 7.8: The optical axis before and during each experiment as measured from the polarimeter. *Experiment C3 shows a decrease in shocked angle. This could be due to the calcite sample being reversed (orientated at 180°) to the other two. As the optical axis looks identical in both directions it is impossible to distinguish the reversed crystal. It is therefore the change in angle which should be considered.

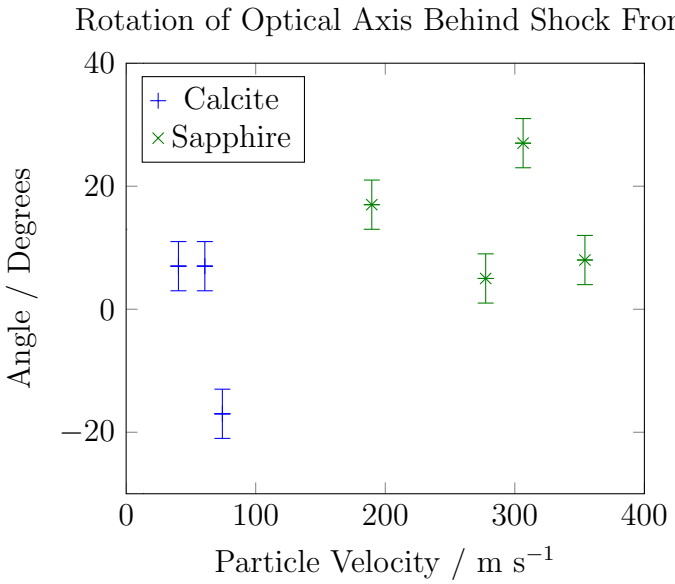


Figure 7.22: Rotation of optical axis for sapphire and calcite under shock compression. Due to the presence of anomalous points, both for calcite and sapphire, no firm conclusions have been drawn. There does appear to be a trend for increasing optical axis rotation with increasing particle velocity (as expected), which warrants further investigation.

at low velocities, up to 100 m s^{-1} particle velocity. The longitudinal elastic shock velocity has been found to be consistent with ultrasound data by Dandekar [12] for these impact velocities. This is in contradiction to Ahrens and Gregson [13] work which found a lower longitudinal elastic shock velocity, however the lowest peak shock pressure in Ahrens and Gregson [13] work was around 5 GPa higher than here, above both the Calcite – Calcite-II and Calcite-II – Calcite-III phase transitions.

Birefringence and polarimetry measured in this work for *a*-cut sapphire has been found to be in agreement with Jones *et al.* [24], with the exception of a small offset consistent with dispersion [78]. Taking this 1% dispersion in birefringence into account, the birefringence particle velocity relationships agree to within experimental error. The shock velocity particle velocity Hugoniot for sapphire has been measured, and also found to agree with Jones *et al.* [24], well within experimental error. The HEL for *a*-cut sapphire has been measured as between 14 GPa and 16 GPa. This value is lower than that found by Jones *et al.* [24] (who give 18 GPa), however it is consistent with other measurements by Kanel *et al.* [39]. This is most likely due to the larger sample thicknesses in this work than and Kanel *et al.* [39] than in Jones *et al.* [24].

New results around the window correction for *a*-cut sapphire at 1550 nm show minimal dispersion and are consistent with 514.5 nm window correction [78]. Window corrections for *a*-cut calcite have not previously been measured at any wavelength. Birefringence has not been quantitatively measured in *a*-cut calcite before. Here results at 532 nm and 1550 nm are consistent and show a zero change in birefringence, and the dispersion is consistent with Ghosh [79]. These birefringence measurements are published in Tear and Proud [3].

Chapter 8

Discussion

The use of normal incidence polarimetry in chapter 7 was successfully used to measure birefringence in the shocked region of a homogeneous *a*-cut trigonal crystal of sapphire and calcite. Birefringence measurements were performed to a precision of 1 part in 10000. Measurements were confined to the elastic regime of calcite (1.2 GPa longitudinal stress, 100 m s^{-1} particle velocity) and sapphire (14 GPa longitudinal stress, 660 m s^{-1} particle velocity). A discussion of the use of polarimetry as a technique followed by the experimental results for sapphire and calcite will be presented in this chapter.

8.1 Improvements in the Polarimetry System

The polarimeter used in this thesis makes use of Wollaston prisms to split light into orthogonal linear polarisations. Wollaston prisms were found to be a necessary improvement over polarising beam splitting cubes as the Wollaston prisms had symmetric extinction ratios of 10000:1 for both polarisations. Polarising beam splitting cubes had extinction ratios which were different for S (1:100) and P (1:10) polarisations, so the error on each polarisation was different.

Calibration methods were developed to filter out back-reflectance from optics such as beamsplitting cubes, which passed multiple times through waveplates. This source

of error is a significant problem for normal incidence polarimetry where the light beam needs to be separated with a beam splitting cube. As the incidence and return path to the target are the same there is no way to completely remove back reflectance. Using polarising optics at an angle is not advised, particularly with wave plates and beam splitters, as an unknown systematic error is introduced in the polarisation state. This is due to S and P polarisations not having equal reflection and transmission coefficients for non-normal incidence.

The measurement of an oscillation frequency in the polarisation of light returned from a birefringent sample has allowed a direct measurement of the shocked birefringence. Using a ThorLabs DET10A 1 GHz bandwidth detector and a 2 GHz bandwidth oscilloscope, the polarisation oscillation of between 10 MHz and 200 MHz was successfully measured with a typical error of 2 MHz.

The measurement of the shocked optical axis has been less successful, with errors being too large to effectively determine whether the optical axis rotated by the 7° that was predicted in chapter 2. The main source of error is in the initial orientation of the crystal, which was limited to ±4°. Due to back-reflectance in the polarimeter it is significantly harder to determine the static optical axis with the method described in chapter 5. Rotating the analyser to determine the optical axis of the dielectric prior to shock compression would improve the error on the initial value for the optical axis orientation ζ. This may bring the error to below the expected rotation of around 7° [24].

8.1.1 Further Developments

The polarimeter can be extended to look at spatially resolved features. Wollaston prisms have a high acceptance angle, so images can be relayed through them effectively, and imaged onto a streak camera. Another option is to use a similar type of polarising prism which displaces the two orthogonal polarisations rather than refracting them. For example the ThorLabs BD40 creates a spatial separation of 4 mm whilst keeping both polarisation propagating in parallel, allowing both images to be focused onto the same

camera. Both of these methods would allow a spatially resolved line of two orthogonal polarisations to be imaged, and a line birefringence measurement as a function of time could be achieved. This would probe sample homogeneity and planar loading, and potentially open the possibility of investigating inhomogeneous birefringent materials.

Furthermore, the measurement of the birefringence has allowed a polarimeter frequency particle velocity relationship to be developed. This allows direct measurement of the shocked state in a *a*-cut window without the need for expensive VISAR or PDV systems. It is likely that this could be achieved without a coherent source and a monochromatic light source would be sufficient if it is intense enough. This system would require a few polarising optics and a single detector of lower bandwidth than usually required for PDV. Without the interferometry system in VISAR the source does not need to be coherent, and so a cheaper light source could be used.

8.2 Sapphire

8.2.1 Hugoniot Literature Comparison

The Hugoniot measurements are in agreement up to 16 GPa longitudinal stress with a linear elastic model and yield at 14±1 GPa longitudinal stress. Whilst this HEL is in disagreement with Jones *et al.* [24], who quote an 18±1 GPa longitudinal stress HEL, the result is in general agreement with other studies such as Kanel *et al.* [39], who use similar sample thicknesses to samples in this thesis. Given Jones *et al.* [24] used thinner 2.5 mm samples than the 8 mm samples used in this thesis, the discrepancy is most likely due to the elastic precursor decay in sapphire, a process causing the yield stress to reduce with reducing strain rate. For sapphire the elastic precursor does not become stable and continues to decay until at least 20 mm [39].

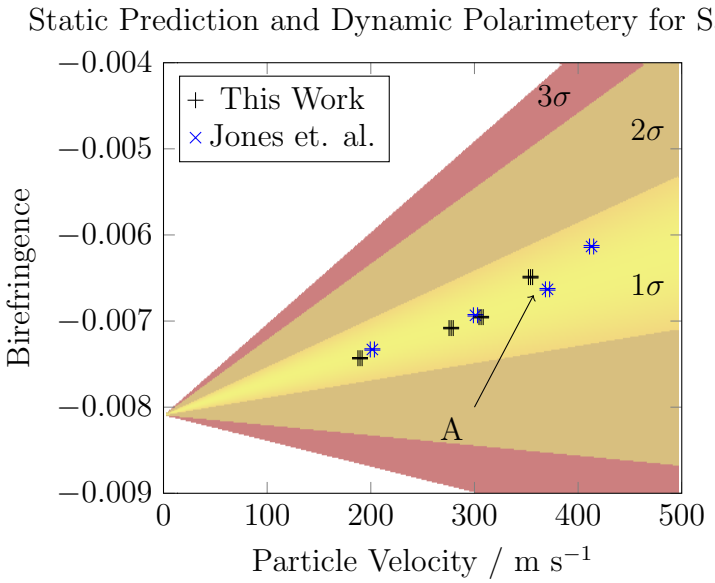


Figure 8.1: Calculated shocked birefringence $\Delta n'$ from polarimeter data for sapphire. Data from Jones *et al.* [24] has been added for comparison. Both show an upward trend above 300 m s^{-1} particle velocity, which is due to the material yielding. As the samples in Jones *et al.* [24] were thinner than in this work, yield occurs at a lower longitudinal stress, and so the upward trend begins earlier in this work than in Jones *et al.* [24]. This is particularly evident from the discrepancy at point A. The photoelastic prediction using data from Reintjes and Schulz [70] in chapter 3 has been added with 1σ, 2σ, and 3σ bands shown.

8.2.2 Birefringence Prediction Comparison

From figure 8.1 the measured result from this work agrees both with the measurements of Jones *et al.* [24], and with the photoelastic constants put forward by Jones *et al.* [24], Reintjes and Schulz [70]. Taking into account a 5% error on the photoelastic matrix it is clear that the result falls well inside the 1σ confidence interval. The birefringence reduces sharply post-yield, a further experiment significantly above yield would be beneficial in identifying whether the birefringence drops to zero, indicating an isotropic material state has been reached.

It is plausible that sapphire, not being strongly anisotropic, is comparatively well described by an isotropic mechanical model. Its optical behaviour, however, does require an anisotropic model in the elastic regime. The window correction for a-cut sapphire is 1.8963±0.0002, as identified by Jones *et al.* [24], whilst c-cut is 1.7864±0.0002, measured

by Setchell [37]. This difference cannot be explained by an isotropic optical model, however the application of static anisotropic photoelastic data does predict the birefringence measured, strongly supporting a linear anisotropic model.

8.2.3 Further Investigations

Their are two main directions for further investigating the sapphire results in this thesis and both are outlined in this section. The first, related to the work of Jones *et al.* [24], is to combine static photoelastic measurements with dynamic measurements using Bayesian inference to inform and improve the photoelastic estimate. The second is to investigate the yield of sapphire optically, investigating the behaviour of the birefringence close to yield and post yield to inform the degree of anisotropy present in the yielded material.

Bayesian Inference

Bayesian inference is used to improve model parameter estimates based on new experimental data. This initially requires an understanding of the uncertainty on the model parameters and how this affects predictions made using the model. With the Monte Carlo simulation of errors in the photoelastic model, developed in chapter 3, the uncertainty in the photoelastic model has been quantified.

Using Bayesian inference, the new experimental results presented in this work to correctly adjust the maximum likelihood estimators on the original photoelastic tensor, however a better estimate of p_{14} which is particularly difficult to measure statically [72, 70, 57] could be achieved.

This could be extended further confidence bounds could be narrowed on the original photoelastic constants using the experimental results in chapter 7.

Post-Yield Birefringence

The transmission of the sample reduces at higher longitudinal stress, however as a reduction in birefringence has been detected post yield it would be interesting to investigate the

longitudinal stress limit of birefringence measurements in sapphire. Sapphire has been observed to lose strength after yielding by Reinhart *et al.* [80]. If sapphire has entered a strengthless fluid like phase after yield, then it is unlikely to show birefringence as it is likely to be isotropic. Birefringence measurements would be a semi-quantitative measure of the degree of anisotropy remaining in a sample.

8.3 Calcite

8.3.1 Hugoniot and Sound speed Comparison

Comparison with Ahrens and Gregson [13] reveals a disagreement with the elastic precursor velocity. Ahrens and Gregson [13] measured an elastic precursor velocity of 7.2±0.1 km s^{-1} for *a*-cut calcite however, as noted in their paper, this did not agree with Peselnick and Robie [51] and neither does it agree with a later measurement by Dandekar [12]. Measurements in chapter 7 of the elastic shock velocity (without a plastic shock) measure 7.41±0.02 km s^{-1} which is in agreement with sound speed velocities measured by Peselnick and Robie [51], Dandekar [12]. Elastic shock velocity data from chapter 4 in the instances where an elastic precursor and plastic shock were recorded also measure 7.41±0.03 km s^{-1}, which is again not in agreement with Ahrens and Gregson [13]. The significantly higher peak pressures in Ahrens and Gregson [13] may be responsible, as the sample thicknesses were comparable in both the work by Ahrens and Gregson [13] and this thesis ruling out precursor decay, such as that observed for sapphire, as a possible cause.

8.3.2 Birefringence Prediction Comparison

It is clear from figure 8.2 that the calcite experimental data from the new work described here is more than 3σ from the simulated Monte Carlo error bands for a 5% photoelastic matrix error and 1% elastic matrix error.

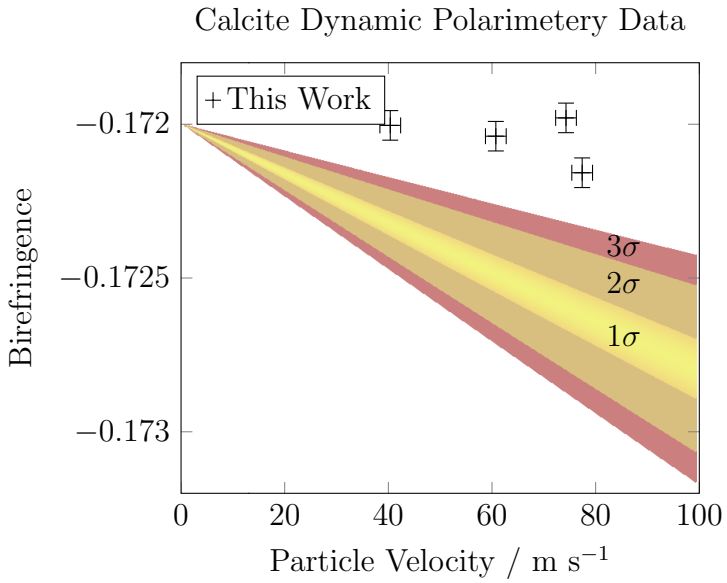


Figure 8.2: Calculated shocked birefringence $\Delta n'$ from polarimeter data for calcite. The photoelastic prediction using data from Nelson *et al.* [53] in chapter 3 has been added with 1σ, 2σ, and 3σ bands shown, demonstrating significant disagreement between dynamic and static photoelastic behaviour.

The unusual birefringence result contributes another example of calcite's unusual properties under dynamic conditions. Ahrens and Gregson [13] noted several phase changes, corroborated by Grady [48] and consistent with static measurements by Bridgman [45]. Evidence of a time dependent nature to the calcite I – calcite II phase transition was supplied by Stapleton [49], and Grady [48] observed but could not explain a release wave profile which was inconsistent with general phase transformation mechanisms described in Duvall and Graham [81].

It is likely that the observations in calcite which do not fit with currently understood models of shock propagation are manifestations of the same underlying unusual material property. Specific possibilities are outlined below, and discussed in the rest of this section.

1. The photoelastic constants were measured incorrectly in the original work.

2. The assumptions of a single shock wave in the material is incorrect.

3. The material is elastically highly non-linear.

4. The material is optically highly non-linear.

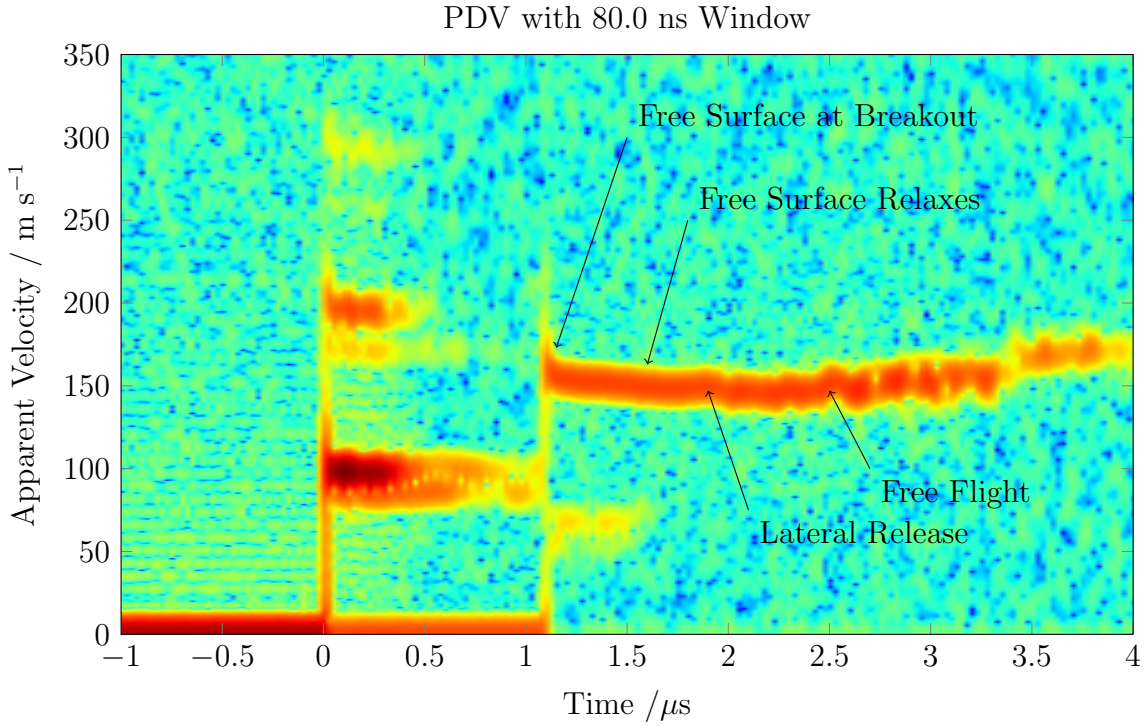


Figure 8.3: Calcite experiment C3. The free surface reflection shows a drop in velocity shortly after breakout, around 10 m s^{-1} in magnitude. After 1.9 μs lateral release waves reach the centre of the sample, ending the one dimensional strain state. This causes variations in velocity followed by free flight of the sample, evident as a weaker velocity signal present at later time. As there is a single velocity peak it is unlikely that the sample has fragmented at this point, and the rear surface holds its integrity.

5. Calcite I - calcite II phase transition.

The first point will be dealt with swiftly, the authors in Nelson *et al.* [53] measured many materials and their other measurements have been subsequently corroborated. It therefore seems fair to assume that, as the same technique was applied to calcite, the calcite work is reliable and no systematic error is present. Changing the value of the photoelastic tensor also would not explain the unusual mechanical properties observed, and so is insufficient on its own.

Single Wave Assumption

At first observation the calcite rear surface profiles indicate a single wave structure in the material. However, careful inspection of rear surface profiles for calcite, particularly

at higher longitudinal stress shot C3 in figure 8.3, shows a drop in particle velocity post breakout. This is consistently observed in every experiment. Whilst the shock wave may be a single front, there is structure in the state behind the shock front, and some stress relaxation occurs immediately behind the shock front, leading to a 10 m s^{-1} drop in free surface velocity (an 8% drop for experiment C3).

Stapleton [49] observed a difference in initial longitudinal stress state for *c*-cut calcite at impact time, compared with a small time later. This relaxation happened over 50 – 100 ns, however this was only observed for material shocked to above the calcite I – calcite II transition point. The observed 2.1% density compression required to cause the phase transition has not been reached in any of the experiments in this work (see table 7.7).

Elastic non-linearity

The observed discrepancy may be due to elastic non-linearity. Stapleton [49] included up to third order non-linear elastic constants in their model of *c*-cut calcite. Elastic non-linearity has two effects, firstly the longitudinal stress particle velocity Hugoniot for impedance matching predictions is too shallow if only first order terms are used. This is unlikely to be sufficient in explaining results, as the Hugoniot was measured directly for each experiment, and the Hugoniot prediction was not used in deriving the birefringence measurement. Secondly, linearity is responsible for ensuring that the wave input into the material propagates in a steady manner, and the wave shape does not evolve with time. In a non-linear elastic system the shock wave may change shape over time, and the step wave model may no longer be appropriate.

Elastic non-linearity is particularly difficult to include with the non-linear photoelastic model, as the photoelastic tensor is found using the elastic constants. If the elastic behaviour is non-linear then this affects the original calculation of the photoelastic constants. In calculating the photoelastic model the effect of including non-linear elasticity is to vary the strain with a given particle velocity. This is because the elastic behaviour gives the shock velocity at a given particle velocity, and the strain used in the model

is given by $\frac{u_p}{U_s}$. Elastic constants for calcite have been measured up to third order and the material is known to be somewhat non-linear in this regard with 3$^{\text{rd}}$ order terms representing 2% of the stress at 1% strain. To bring the experimental results into line with the photoelastic prediction in figure 8.2, the required absolute deviation in strain is around 0.01, and given the absolute strain in the shocked region is about 0.01 this is a doubling of the strain. Elastic non-linearity, only introduced in the calculation of the Hugoniot, is insufficient to explain the observed deviations.

Optical non-linearity

If the photoelastic constants are not linear, a second order term may be needed. Calcite, as an ionic material with a wide band gap, is expected to be fairly linear however. There are no absorption edges near the wavelengths of operation, calcite has $> 99\%$ transmission over the wavelength range 2000 nm – 200 nm at room temperature and pressure. The power received by the photodiodes did drop rapidly at higher velocity impacts, however this may easily indicate scattering rather than absorption. For many materials the photoelastic constants are applicable at strains above yield. This is due to the fact that optical properties are determined by the electron configuration and in an ionic material the electrons are bound tightly to the ions. The optical properties are therefore most dependent on the location of ionic sites in the lattice, and providing the crystal structure is maintained during yield, the assumptions that go into the photoelastic model hold.

Scattering of light implies the material is yielding or failing in some way, however the rear surface velocity profile in figure 8.3 does not indicate failure. The rear surface remains intact as evident by a single velocity peak, and there is no rear surface behaviour such as a velocity drop which would indict tensile failure (spall).

Phase Change

The calcite I – calcite II phase transition has been observed at 1.8 GPa longitudinal stress. All experiments in chapter 7 are below this phase transition stress, however

partial phase transformation may be occurring. In Wang [54] it was postulated that partial phase transformation may be responsible for the observed reduction in elastic wave speed, and so an in depth investigation into the mechanics of a partial calcite I – calcite II transformation was carried out. The postulated method was found to be inconsistent with experimental results, particularly by Aidun [50], and so it seems unlikely that this is the primary cause of the inconsistency at such low pressures.

8.3.3 Further Investigations

The unusual behaviour of calcite would be best explained by elastic non-linearity, caused by being close to the phase transition stress. Merrill and Bassett [46] suggested that the calcite II transition is caused by a phonon instability, an oscillation of the lattice which, at higher longitudinal stress no longer returns to the original lattice position. It is possible that in *a*-cut calcite this phonon mode has its propagation direction close to that of the shock propagation direction, and over a short time the initial delta function like pulse of the impact evolves into a set of phonon modes, one of which is responsible for the calcite – calcite II transition.

In order to investigate this it would be necessary to construct a non-linear elastic model which, making use of higher elastic tensor terms, predicts elastic wave propagation. Combining this with a consistent photoelastic model would be necessary if optical validation was to be used. This would require the consistency of photoelastic results with a non-linear elastic model to be considered. It may be necessary to consider the effect of a nonlinear elastic model on the Brillouin scattering used to determine the photoelastic tensor in work by Nelson *et al.* [53].

Given that Nelson *et al.* [53] present their original results, it would be possible to calculate a new photoelastic tensor that is consistent with a non-linear elastic model. Given that Nelson *et al.* [53] use a linear elastic model to calculate strain when estimating the photoelastic tensor, it may be that a linear photoelastic model is sufficient, providing the systematic error introduced to the strain by elastic non-linearity is corrected.

Chapter 9

Conclusions

It has been demonstrated that a time resolved polarimeter can be used to measure shock birefringence in compressed homogeneous dielectrics. Agreement between polarimeter, PDV and VISAR analysis for sapphire has been demonstrated to the level of 1%, well within experimental error. Furthermore the birefringence values obtained through experimental measurement of dynamic compression are in agreement with static literature data for sapphire, to within 5% of the static photoelastic matrix.

Experimental PDV results for a-cut calcite are in agreement with previous literature at the 1% level (typical error on PDV and VISAR systems). Direct measurements of the Hugoniot compared with impedance matching predictions are in agreement to within 1% and within the error of the PDV measurements. The birefringence results are not however consistent with a prediction based on a linear anisotropic photoelastic model. With a 5% error on the photoelastic model, the measured results are well outside 3σ from the expectation, and deviate fractionally by 0.5%.

In order to bring together some conclusions a short review of previous work followed by a review of the work presented in this document will be given. The aims laid out in section 1.5.1 will then be addressed and successes and shortcomings identified.

9.1 Previous Work

Previously there has been extensive work on single crystals of sapphire and some work on single crystal calcite under shock compression. This thesis has focussed on identifying yield points, phase transitions, and characterising the variation with crystal axis. Few studies have been performed in the purely elastic regime, and often Hugoniots for different orientations are presented with little comment on the relationship. Furthermore due to elastic precursor decay there exists a variation in the HEL of sapphire for a specific orientation and varying sample thickness which is greater than the observed variation of the HEL with a specific sample thickness and varying orientation.

Optical measurements of sapphire have shown it to be optically anisotropic under shock compression as expected. Despite this an isotropic modified Gladstone-Dale model is the only optical model for shock compressed sapphire currently available, with specific fitted constants for different orientations. No similar optical measurements have ever been obtained for single crystal calcite.

9.2 This Work

By studying a-cut sapphire verification of the linear photoelastic model can be made, and agreement was found with other independent research group findings. Studying a-cut calcite extends the study of this highly anisotropic material into orientations beyond the c-axis with modern diagnostics. Hugoniot agreement was found with Ahrens and Gregson [13], however wave profiles generated by using modern velocimetry techniques allow more shock wave structure to be observed for shock propagation along the a-axis.

The estimation of anisotropic errors from static literature data for comparison with dynamic data allows the significance of discrepancies to be addressed. With sapphire, discrepancies in static data and dynamic data have been taken into account when studying anisotropic effects. The Monte Carlo approach employed in chapter 3 supports the view that mechanical differences in sapphire orientation are no greater than the experimental

error. Mechanically, for all intents and purposes, sapphire can be treated as isotropic.

Optically sapphire maintains its anisotropy up to the yield point. The use of birefringence to verify the optical behaviour of the materials showed sapphire to behave as predicted in chapter 3 and is also in line with findings by Jones *et al.* [24]. This study revealed calcite to behave in an unexpected way at much lower particle velocities than previously expected.

9.2.1 Linear Photoelastic Predictions

Linear elastic theory and linear photoelastic theory have been combined to produce optical predictions for anisotropic dielectrics under shock compression. These predictions are presented in chapter 2, and it was discovered that small variations in key components of the photoelastic tensor could significantly alter the predicted birefringence particle velocity relationship. To investigate this further a Monte Carlo method for correlated errors on tensor components was developed in chapter 3. It was found that the various literature photoelastic tensors for sapphire agreed at the 3σ confidence level.

9.2.2 Develop and Verify Birefringence Technique

Birefringence was selected as a method of experimentally verifying photoelastic predictions. A series of simulations were performed in chapter 3 to show that expected sources of error such as impact tilt and crystallographic tilt were not likely to render the measurement insensitive to birefringence. A polarimeter was designed to perform birefringence measurements as well as estimate the optical axis of the shocked material and the analysis for a single step wave shock was presented in chapter 5. Experimental work on sapphire showed agreement with Jones *et al.* [24] and with PDV measurements. Polarimetry showed improved precision over PDV as birefringence is a direct difference measurement, rather than direct refractive index measurement. It was challenging to estimate the shocked optical axis, and errors on the measurement value were of the same

order as the measurement value itself.

9.2.3 Experimental Work

Sapphire was used to demonstrate the validity of the birefringence technique, repeating results from other groups who used different techniques to measure the same effect. The photoelastic results by Jones *et al.* [24] are in complete agreement with the results of this thesis, with an absolute deviation of 0.00002 (fractional 0.3%), less than the error on this work or Jones *et al.* [24]. The HEL for sapphire was observed to be 14 GPa in the results of chapter 7, which is in agreement with Kanel *et al.* [39]. Jones *et al.* [24] observed a 18 GPa HEL, however this is consistent with the long elastic precursor decay observed in sapphire.

Calcite has been investigated using the same technique however there was no agreement between dynamic calcite birefringence and static photoelastic data. Chapter 8 has put forward a number of possible causes, based on quantitative and semi quantitative data obtained from computational modelling and experimental results.

It is suggested that the most likely cause is elastic non-linearity being high in calcite due to the presence of a phase transition to calcite II occurring at 1.8 GPa longitudinal stress. This non-linearity could potentially cause a non-uniform strain behind the shock front. A velocity reduction of around 10 m s^{-1} in the free surface velocity of calcite was observed, consistent with a reduction in strain behind the shock front.

Introducing a non-linear elastic model in order to predict wave behaviour has been put forward by Stapleton [49], however making this model consistent with photoelastic models is a challenge. The measurement methods used to find the photoelastic tensor use a linear elastic model, and so a re-analysis of Nelson *et al.* [53] would be necessary using a non-linear elastic model to make the photoelastic tensor consistent.

9.3 Further Work

Whilst there are several possible directions to extend the work described in sections 8.2.3 and 8.3.3, one key direction for the work as a whole is to investigate the effect of pressure shear. Only one dimensional strain loading states have been considered, and a key purpose of this work was to demonstrate that a linear photoelastic model describes anisotropic window materials shocked in different directions. Extending this into strain states which contain a shear component and are no longer one dimensional will make available anisotropic windows for more complex loading geometries such as wave reflections at bi-crystal interfaces.

Bibliography

[1] G. R. Tear, D. E. Eakins, D. J. Chapman and W. G. Proud. Technique to measure change in birefringence under shock compression. In M. Furlanetto, W. J. Evans and W. T. Buttler, editors, *Shock Compression Condens. Matter*, volume 500, page 2020. Journal of Physics: Conference Series, Seattle, 2014. doi:10.1088/1742-6596/500/19/192020

[2] G. R. Tear, D. J. Chapman, D. E. Eakins and W. G. Proud. Birefringence Measurements in Single Crystal Sapphire and Calcite Shocked Along the *a* Axis. In *Shock Compression Condens. Matter*. Tampa, FL, 2015 (accepted)

[3] G. R. Tear and W. G. Proud. Predicting the Optical Behaviour of Shock Compressed Dielectrics. In *Shock Compression Condens. Matter*. Tampa, FL, 2015 (accepted)

[4] R. Courant and K. O. Friedrichs. *Supersonic Flow and Shock Waves*. John Wiley & Sons, New York, fifth edition, 1967

[5] C. H. Lu, B. a. B. Remington, B. R. Maddox, B. Kad, H. S. Park, S. T. Prisbrey and M. a. M. Meyers. Laser compression of monocrystalline tantalum. *Acta Mater.*, 60(19):6601–6620, 2012. doi:10.1016/j.actamat.2012.08.026

[6] F. Cao, I. J. Beyerlein, F. L. Addessio, B. H. Sencer, C. P. Trujillo, E. K. Cerreta and G. T. Gray III. Orientation dependence of shock-induced twinning and substructures in a copper bicrystal. *Acta Mater.*, 58(2):549–559, 2010. doi:10.1016/j.actamat.2009.09.033

[7] M. S. Schneider, B. Kad, D. H. Kalantar, B. a. Remington, E. Kenik, H. Jarmakani and M. a. Meyers. Laser shock compression of copper and copperaluminum alloys. *Int. J. Impact Eng.*, 32(1-4):473–507, 2005. doi:10.1016/j.ijimpeng.2005.05.010

[8] M. Budzevich, V. Zhakhovsky, C. White and I. Oleynik. Evolution of Shock-Induced Orientation-Dependent Metastable States in Crystalline Aluminum. *Phys. Rev. Lett.*, 109(12):1–5, 2012. doi:10.1103/PhysRevLett.109.125505

[9] J. M. McNaney, L. M. Hsuing, N. R. Barton and M. Kumar. Shock driven twinning in tantalum single crystals. *AIP Conf. Proc.*, 1195(2009):1127–1130, 2009. doi:10.1063/1.3295000

[10] H. Jarmakani, J. McNaney, B. Kad, D. Orlikowski, J. Nguyen and M. Meyers. Dynamic response of single crystalline copper subjected to quasi-isentropic, gas-gun driven loading. *Mater. Sci. Eng. A*, 463(1-2):249–262, 2007. doi:10.1016/j.msea.2006.09.118

[11] E. Loomis. Modeling of Elastic Waves in Dynamically Loaded NiAl Bicrystals. *J. Eng. Mater. Technol.*, 129(4):513, 2007. doi:10.1115/1.2772328

[12] D. P. Dandekar. Elastic Constants of Calcite. *J. Appl. Phys.*, 39(6):2971, 1968. doi:10.1063/1.1656709

[13] T. J. Ahrens and V. G. Gregson. Shock compression of crustal rocks: Data for quartz, calcite, and plagioclase rocks. *J. Geophys. Res.*, 69(22):4839–4874, 1964

[14] G. R. Johnson and W. H. Cook. A constitutive model and data for metals subjected to large strains high strain rates and high temperatures. *... 7th Int. Symp. ...*, 1983

[15] F. J. Zerilli and R. W. Armstrong. Dislocation-mechanics-based constitutive relations for material dynamics calculations. *J. Appl. Phys.*, 61(5):1816–1825, 1987. doi:10.1063/1.338024

[16] M. A. Shehadeh, H. M. Zbib, T. Diaz De La Rubia, M. A. Shehadeh, H. M. Zbib and T. Diaz De La Rubia. Modelling the dynamic deformation and patterning in fcc single crystals at high strain rates: dislocation dynamics plasticity analysis. *Philos. Mag.*, 85(15):1667–1685, 2005. doi:10.1080/14786430500036470

[17] J. D. Clayton. Analysis of shock compression of strong single crystals with logarithmic thermoelastic-plastic theory. *Int. J. Eng. Sci.*, 79:1–20, 2014. doi:10.1016/j.ijengsci.2014.02.016

[18] J. T. Lloyd, J. D. Clayton, R. H. Becker and D. L. McDowell. Simulation of shock wave propagation in single crystal and polycrystalline aluminum. *Int. J. Plast.*, 60:118–144, 2014. doi:10.1016/j.ijplas.2014.04.012

[19] J. D. Clayton. Nonlinear Eulerian thermoelasticity for anisotropic crystals. *J. Mech. Phys. Solids*, 61(10):1983–2014, 2013. doi:10.1016/j.jmps.2013.05.009

[20] M. D. Furnish, T. J. Vogler, C. S. Alexander, W. D. Reinhart, W. M. Trott and L. C. Chhabildas. Statistics of the Hugoniot elastic limit from line VISAR. In M. Elert, M. D. Furnish, R. Chau, N. Holmes and J. Nguyen, editors, *Shock Compression Condens. Matter*, volume 955, pages 521–524. AIP Conference Proceedings, Waikoloa, 2007. doi:10.1063/1.2833129

[21] S. Case and Y. Horie. Modelling the shock response of polycrystals at the mesoscale. *Shock Compression Condens. Matter*, 307(2006), 2005. doi:10.1063/1.2263323

[22] L. M. Barker and R. E. Hollenbach. Shock-Wave Studies of PMMA, Fused Silica, and Sapphire. *J. Appl. Phys.*, 41(10):4208, 1970. doi:10.1063/1.1658439

[23] T. J. Vogler and L. C. Chhabildas. Strength behavior of materials at high pressures. *Int. J. Impact Eng.*, 33:812–825, 2006. doi:10.1016/j.ijimpeng.2006.09.069

[24] S. C. Jones, B. A. M. Vaughan and Y. M. Gupta. Refractive indices of sapphire under

elastic, uniaxial strain compression along the a axis. *J. Appl. Phys.*, 90(10):4990, 2001. doi:10.1063/1.1409576

[25] S. C. Jones and Y. M. Gupta. Refractive index and elastic properties of z-cut quartz shocked to 60 kbar. *J. Appl. Phys.*, 88(10):5671, 2000. doi:10.1063/1.1319329

[26] O. T. Strand, D. R. Goosman, C. Martinez, T. L. Whitworth and W. W. Kuhlow. Compact system for high-speed velocimetry using heterodyne techniques. *Rev. Sci. Instrum.*, 77(8):083108, 2006. doi:10.1063/1.2336749

[27] L. M. Barker and R. E. Hollenbach. Laser interferometer for measuring high velocities of any reflecting surface. *J. Appl. Phys.*, 43(11):4669–4675, 1972. doi:10.1063/1.1660986

[28] S. C. Jones, M. C. Robinson and Y. M. Gupta. Ordinary refractive index of sapphire in uniaxial tension and compression along the c axis. *J. Appl. Phys.*, 93(2):1023, 2003. doi:10.1063/1.1530716

[29] B. M. LaLone, O. V. Fat'yanov, J. R. Asay and Y. M. Gupta. Velocity correction and refractive index changes for [100] lithium fluoride optical windows under shock compression, recompression, and unloading. *J. Appl. Phys.*, 103(9):093505, 2008. doi:10.1063/1.2912500

[30] B. J. Jensen, D. B. Holtkamp, P. a. Rigg and D. H. Dolan. Accuracy limits and window corrections for photon Doppler velocimetry. *J. Appl. Phys.*, 101(1):013523, 2007. doi:10.1063/1.2407290

[31] D. J. Chapman, D. E. Eakins, D. M. Williamson and W. G. Proud. Index of refraction measurements and window corrections for PMMA under shock compression. In M. L. Elert, W. T. Buttler, J. P. Borg, J. L. Jordan and T. J. Vogler, editors, *Shock Compression Condens. Matter*, volume 442, pages 442–445. AIP Conf. Proc., Chicago, 2012. doi:10.1063/1.3686313

[32] A. Seifter and D. C. Swift. A new sub-nanosecond spectral ellipsometer for shock physics applications. *Phys. Status Solidi Curr. Top. Solid State Phys.*, 5(5):1073–1076, 2008. doi:10.1002/pssc.200777833

[33] C. a. Bolme, S. D. McGrane, D. S. Moore and D. J. Funk. Single shot measurements of laser driven shock waves using ultrafast dynamic ellipsometry. *J. Appl. Phys.*, 102(3), 2007. doi:10.1063/1.2767376

[34] L. Bakshi, S. Eliezer, G. Appelbaum, N. Nissim, L. Perelmutter and M. Mond. A full Stokes vector ellipsometry measurement system for in situ diagnostics in dynamic experiments. *Rev. Sci. Instrum.*, 83(5), 2012. doi:10.1063/1.4717675

[35] J. H. Nguyen and N. C. Holmes. Shock-Induced Birefringence in Lithium Fluoride. In M. D. Furnish, N. N. Thadhani and Y. Horie, editors, *Shock Compression Condens. Matter*, volume 620, pages 1251 – 1254. Atlanta, 2002. doi:10.1063/1.1483766

[36] J. E. Field, S. M. Walley, W. G. Proud, H. T. Goldrein and C. R. Siviour. *Review of experimental techniques for high rate deformation and shock studies*, volume 30, 2004. doi:10.1016/j.ijimpeng.2004.03.005

[37] R. E. Setchell. Refractive index of sapphire at 532 nm under shock compression and release. *J. Appl. Phys.*, 91(5):2833, 2002. doi:10.1063/1.1446219

[38] T. C. T. Ting. *Anisotropic Elasticity: Theory and Applications*. Oxford University Press, New York, 1st edition, 1996

[39] G. I. Kanel, W. J. Nellis, a. S. Savinykh, S. V. Razorenov and a. M. Rajendran. Response of seven crystallographic orientations of sapphire crystals to shock stresses of 1686 GPa. *J. Appl. Phys.*, 106(4):043524, 2009. doi:10.1063/1.3204940

[40] R. Tarumi, H. Ledbetter, H. Ogi and M. Hirao. Low-temperature elastic constants of monocrystal corundum (α-Al 2 O 3). *Philos. Mag.*, 93(36):4532–4543, 2013. doi:10.1080/14786435.2013.837225

[41] J. R. Gladden, J. H. So, J. D. Maynard, P. W. Saxe and Y. Le Page. Reconciliation of ab initio theory and experimental elastic properties of Al2O3. *Appl. Phys. Lett.*, 85(3):392, 2004. doi:10.1063/1.1773924

[42] R. A. Graham and W. P. Brooks. Shock-wave compression of sapphire from 15 to 420 kbar. The effects of large anisotropic compressions. *J. Phys. Chem. Solids*, 32:2311–2330, 1971

[43] Y. M. Gupta, G. E. Duvall and G. R. Fowles. Dislocation mechanisms for stress relaxation in shocked LiF. *J. Appl. Phys.*, 46(2):532–546, 1975. doi:10.1063/1.321678

[44] T. Mashimo, H. Yasuharu and K. Nagayama. Elastoplastic properties under shock compression of Al2O3 single crystal and polycrystal. *J. Appl. Phys.*, 63(2):327–336, 1988. doi:10.1063/1.340298

[45] P. W. Bridgman. The high pressure behavior of miscellaneous minerals. *Am. J. Sci.*, 237(1):7–18, 1938. doi:10.2475/ajs.237.1.7

[46] L. Merrill and W. A. Bassett. The crystal structure of CaCO3 (II), a high-pressure metastable phase of calcium carbonate. *Acta Cryst.*, B31:343, 1975

[47] J. R. Smyth and T. J. Ahrens. The crystal structure of calcite III. *Geophys. Res. Lett.*, 24(13):1595–1598, 1997

[48] D. E. Grady. High-Pressure Release-Wave Measurements and Phase Transformation in CaCO3. In Y. Gupta, editor, *Shock Waves Condens. Matter*, pages 589–593. Springer US, Spokane, WA, 1986. doi:10.1007/978-1-4613-2207-8_84

[49] B. S. Stapleton. *Response of single crystal calcite shocked to 40 kbar along the c-axis.* Ph.D. thesis, 1990

[50] J. B. Aidun. *Study of shear and compression waves in shocked calcium carbonate.* Ph.D. thesis, Washington State University, 1989

[51] L. Peselnick and R. A. Robie. Elastic Constants of Calcite. *J. Appl. Phys.*, 33(9):2889, 1962. doi:10.1063/1.1702572

[52] H. Kaga. Third-Order Elastic Constants of Calcite*. *Phys. Rev.*, 172(3):900 – 919, 1968

[53] D. F. Nelson, P. D. Lazay and M. Lax. Brillouin Scattering in Anisotropic Media: Calcite. *Phys. Rev. B*, 6(8):3109 – 3120, 1972

[54] C. Wang. Velocity of compressional waves in limestones, marbles, and a single crystal of calcite to 20 kilobars. *J. Geophys. Res.*, 71:3543–3547, 1966

[55] C. Biellmann, F. Guyot, P. Gillet and B. Reynard. High-pressure stability of carbonates: quenching of calcite-II, high-pressure polymorph of CaCO3. *Eur. J. Miner. Sci.*, 5:503–510, 1993

[56] A. Van Valkenburg. High Pressue Optics. *Appl. Opt.*, 9(1):1–4, 1970

[57] I. L. Chistyi, V. F. Kitaeva, N. N. Sobolev and V. P. Bakhar. Investigation of the Molecular Scattering of Light in a Sapphire Single Crystal. *Sov. Phys. JETP*, 36(4):783 – 788, 1973

[58] N. M. Balzaretti, J. P. Denis and J. a. H. da Jornada. Variation of the refractive index and polarizability of sapphire under high pressures. *J. Appl. Phys.*, 73(3):1426, 1993. doi:10.1063/1.353240

[59] T. a. Davis and K. Vedam. Photoelastic properties of sapphire (α-Al2O3). *J. Appl. Phys.*, 38(11):4555–4556, 1967. doi:10.1063/1.1709181

[60] R. E. Setchell. Index of refraction of shock-compressed fused silica and sapphire. *J. Appl. Phys.*, 50(12):8186, 1979. doi:10.1063/1.325959

[61] X. Cao, J. J. Li, J. J. Li, X. Li, L. Xu, Y. Wang, W. Zhu, C. Meng and X. Zhou. Refractive index of r-cut sapphire under shock pressure range 5 to 65GPa. *J. Appl. Phys.*, 116(9):093516, 2014. doi:10.1063/1.4894854

[62] D. B. Hayes, C. a. Hall, J. R. Asay and M. D. Knudson. Continuous index of refraction measurements to 20 GPa in Z-cut sapphire. *J. Appl. Phys.*, 94(4):2331, 2003. doi:10.1063/1.1595710

[63] T. A. Davis and K. Vedam. Variation of the Refractive Indices of Calcite with Pressure to 7 kbar. *Phys. status solidi*, 26:285 – 290, 1968

[64] L. Davison and M. Shahinpoor, editors. *High-Pressure Shock Compression of Solids III*. Springer US, New York, first edition, 1998

[65] S. P. Marsh, editor. *LASL Shock Hugoniot Data*. University of California Press, Los Angeles, 1st edition, 1980

[66] C. a. Bolme and K. J. Ramos. The elastic tensor of single crystal RDX determined by Brillouin spectroscopy. *J. Appl. Phys.*, 116(18):183503, 2014. doi:10.1063/1.4901461

[67] A. Yariv and P. Yeh. *Optical Waves in Crystals*. John Wiley & Sons, New York, 1st edition, 1984

[68] P. A. Rigg, M. D. Knudson, R. J. Scharff and R. S. Hixson. Determining the refractive index of shocked [100] lithium fluoride to the limit of transmissibility. *J. Appl. Phys.*, 116, 2014. doi:10.1063/1.4890714

[69] D. R. Goosman. Analysis of the laser velocity interferometer. *J. Appl. Phys.*, 46(8):3516, 1975. doi:10.1063/1.322079

[70] J. Reintjes and M. B. Schulz. Photoelastic Constants of Selected Ultrasonic Delay-Line Crystals. *J. Appl. Phys.*, 5254(1968), 1968. doi:10.1063/1.1655948

[71] M. H. Manghnani. Elastic Constants of Single-Crystal Rutile. *J. Geophys. Res.*, 74(17):4317 – 4328, 1969

[72] R. Waxler and E. Farabaugh. Photoelastic constants of ruby. *J. Res. Natl. Bur. Stand. Sect. A Phys. Chem.*, 74A(2):215, 1970. doi:10.6028/jres.074A.016

[73] G. W. Stewart. *Matrix perturbation theory.* Academic, Boston, 1990

[74] S. C. McClain, L. W. Hillman and R. A. Chipman. Polarization ray tracing in anisotropic optically active media. I. Algorithms. *JOSA A*, 10(11):2371–2382, 1993

[75] D. E. Eakins and D. J. Chapman. X-ray imaging of subsurface dynamics in high-Z materials at the Diamond Light Source. *Rev. Sci. Instrum.*, 85(123708), 2014. doi:10.1063/1.4904275

[76] D. H. Dolan. Foundations of VISAR analysis. Technical Report April, Sandia National Laboratories, Albuquerque, 2006

[77] D. H. Dolan. Accuracy and precision in photonic Doppler velocimetry. *Rev. Sci. Instrum.*, 81(5):053905, 2010. doi:10.1063/1.3429257

[78] I. H. Malitson. Refraction and Dispersion of Synthetic Sapphire. *J. Opt. Soc. Am.*, 52(12):1377, 1962. doi:10.1364/JOSA.52.001377

[79] G. Ghosh. Dispersion-equation coefficients for the refractive index and birefringence of calcite and quartz crystals. *Opt. Commun.*, 163(1):95–102, 1999. doi:10.1016/S0030-4018(99)00091-7

[80] W. D. Reinhart, L. C. Chhabildas and T. J. Vogler. Investigating phase transitions and strength in single-crystal sapphire using shockreshock loading techniques. *Int. J. Impact Eng.*, 33(1-12):655–669, 2006. doi:10.1016/j.ijimpeng.2006.09.083

[81] G. Duvall and R. A. Graham. Phase transitions under shock-wave loading. *Rev. Mod. Phys.*, 49(3):523–579, 1977. doi:10.1103/RevModPhys.49.523

Appendix A

Equations

Several of the mathematical expressions for computational work are written out long hand here. These are the actual forms of equations used.

To solve

$$f = At^2 + Bt + C \tag{A.1}$$

analytically over 3 points (t_i, f_i)

$$\begin{aligned}
A &= \frac{t_3(f_2 - f_1) + t_2(f_1 - f_3) + t_1(f_3 - f_2)}{(t_1 - t_2)(t_1 - t_3)(t_2 - t_3)} \\
B &= \frac{{t_3}^2(f_1 - f_2) + {t_2}^2(f_3 - f_1) + {t_1}^2(f_2 - f_3)}{(t_1 - t_2)(t_1 - t_3)(t_2 - t_3)} \\
C &= \frac{t_3 t_2(t_2 - t_3)f_1 + t_3 t_1(t_3 - t_1)f_2 + t_1 t_2(t_1 - t_2)f_3}{(t_1 - t_2)(t_1 - t_3)(t_2 - t_3)}
\end{aligned}$$

And the location of the maximum is given by

$$\begin{aligned}
\frac{d}{dt}f &= 2At + B \\
0 &= 2At + B \\
t &= -\frac{B}{2A}
\end{aligned}$$

This is equivalent to a Gaussian on a log scale

$$\begin{aligned} y &= \exp \frac{(x-\mu)^2}{\sigma^2} \\ \ln y &= \frac{(x-\mu)^2}{\sigma^2} \\ &= \frac{1}{\sigma^2}x^2 - \frac{2\mu}{\sigma^2}x + \frac{\mu^2}{\sigma^2} \end{aligned}$$

so the mean and standard deviation of the Gaussian are

$$\begin{aligned} \mu &= -\frac{B}{2A} \\ \sigma &= \frac{1}{\sqrt{A}} \end{aligned}$$

Appendix B

Extended Results

This is the full results of all experiments conducted in this thesis. The rear surface velocity profiles for each shot are shown, both using short time windows and long time windows in the STFT analysis. Polarimetry data is shown as the stokes components, and the FFT of the circular component is shown for each shot. The Polarimetry FFT also shows the fitted peak indicating the frequency used for the birefringence analysis.

B.1 Preliminary Calcite Experiments

These experiments were conducted on the 12.7 mm gas gun with 2 mm thick samples. The polarimeter was in a state of development, and so some polarimetry data is missing (experiment P3), and not all stokes components are available (experiment P1).

Shot	**Driver**	**Flyer**	l_0 **/ mm**	v **/ m s^{-1}**	u_p **/ m s^{-1}**	U_s **/ km s^{-1}**
P1	Copper	Copper	2.067±0.002	350±17	110±2	7.50±0.07
P2	None	PC	2.066±0.003	500±25	77±2	7.45±0.07
P3	Copper	Copper	2.078±0.004	250±13	115±2	7.50 ±0.07

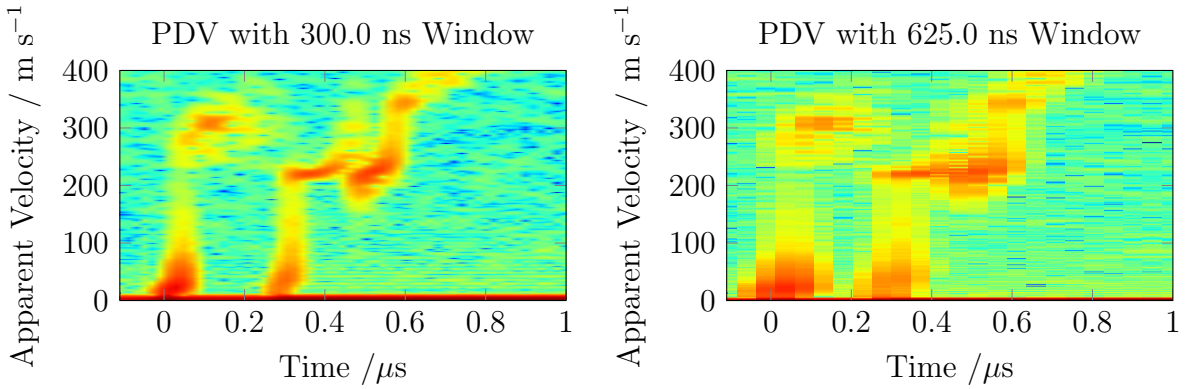


Figure B.1: PDV data for experiment P1. A generation one PDV system was used for this experiment. There is a precursor ramp before the main shock caused by the copper driver.

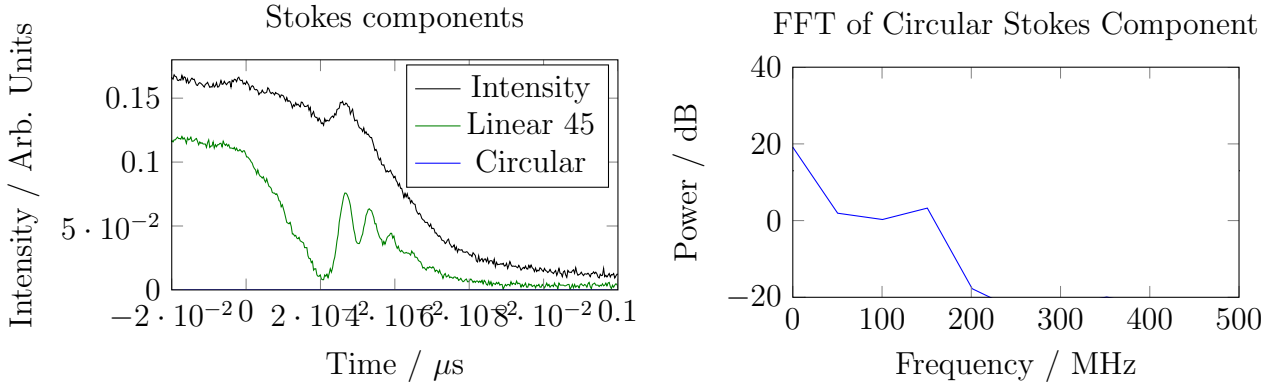


Figure B.2: Polarimetry data for experiment P1. Only the linear 45° component was used in this experiment.

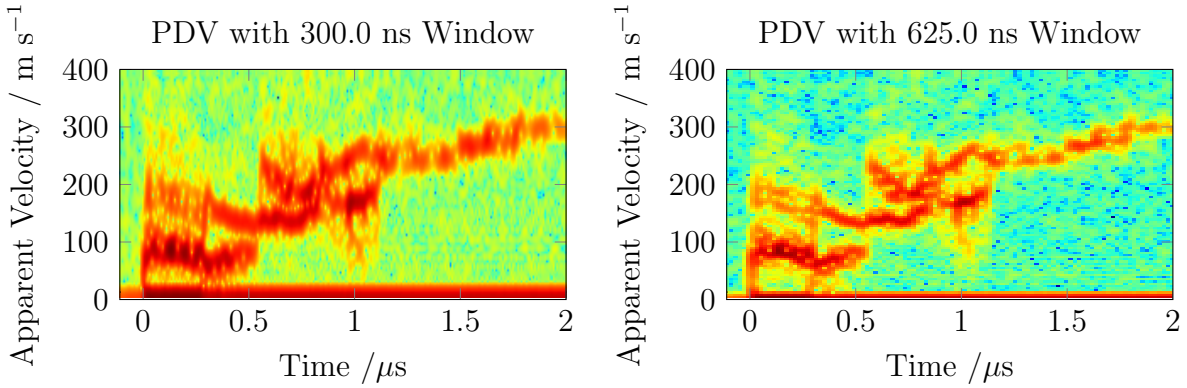


Figure B.3: PDV data for experiment P2, a generation one PDV system was used, with no AR coating on the calcite.

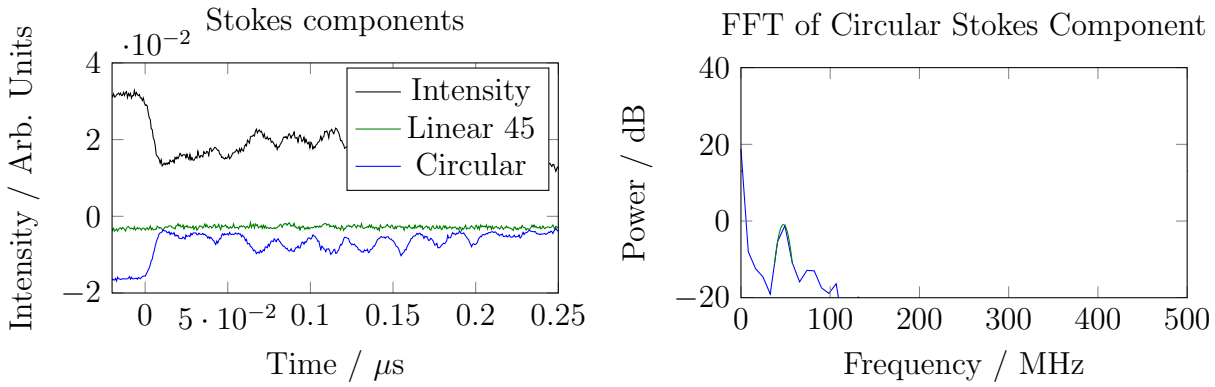


Figure B.4: Polarimetry data for experiment P2. No signal was detected on the linear polarisation detector.

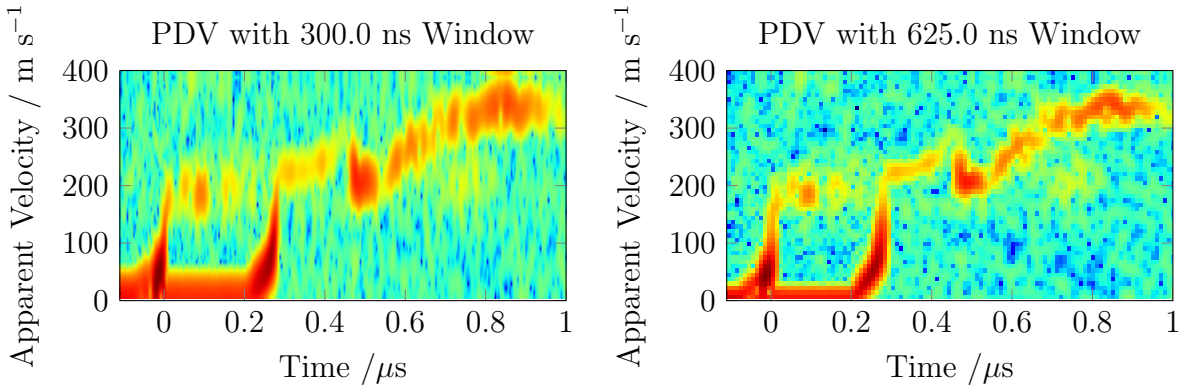


Figure B.5: PDV data for experiment P3. An upshifted generation three PDV system was used. Excessive impact tilt lead to misalignment of the target post impact, drastically reducing signal from both the impact plane and the rear surface.

B.2 Calcite Large Bore Gas Gun Experiments

The large bore gas gun series of experiments on calcite is presented here.

Shot	**Flyer**	l_0 / **mm**	v / **m s^{-1}**	u_p / **m s^{-1}**	σ_l / **GPa**
C2	PMMA	7.958 ± 0.002	262 ± 0.5	40 ± 2	0.81 ± 0.04
C1	Magnesium AZ31B	8.05 ± 0.002	206 ± 0.5	61 ± 2	1.22 ± 0.04
C3	Magnesium AZ31B	8.059 ± 0.014	255 ± 0.5	74 ± 2	1.49 ± 0.04

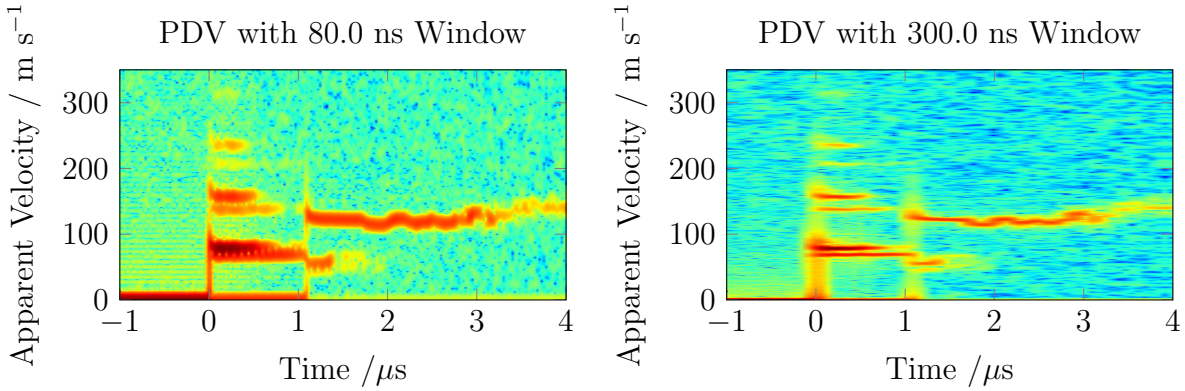


Figure B.6: PDV data for experiment C1

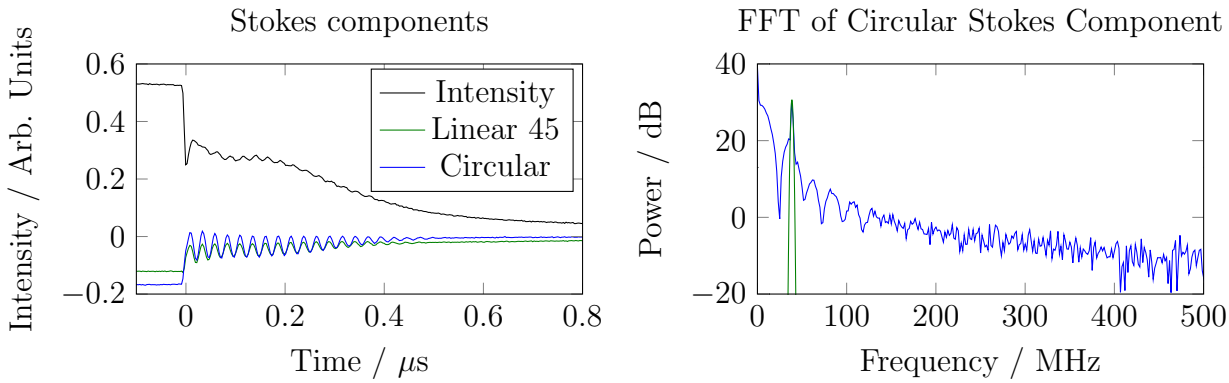


Figure B.7: Polarimetry data for experiment C1

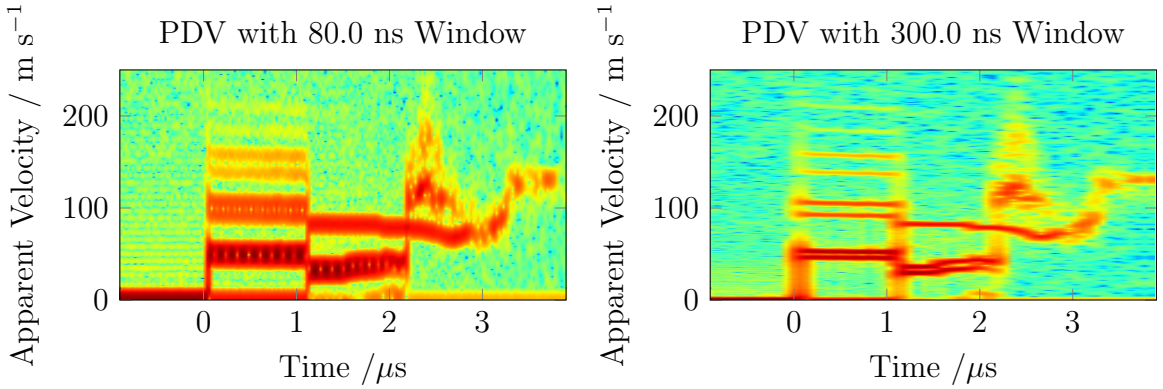


Figure B.8: PDV data for experiment C2

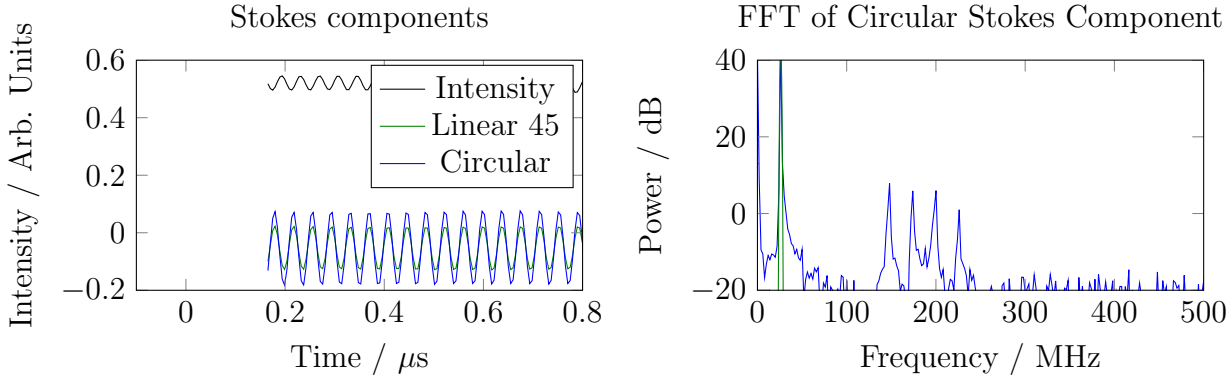


Figure B.9: Polarimetry data for experiment C2

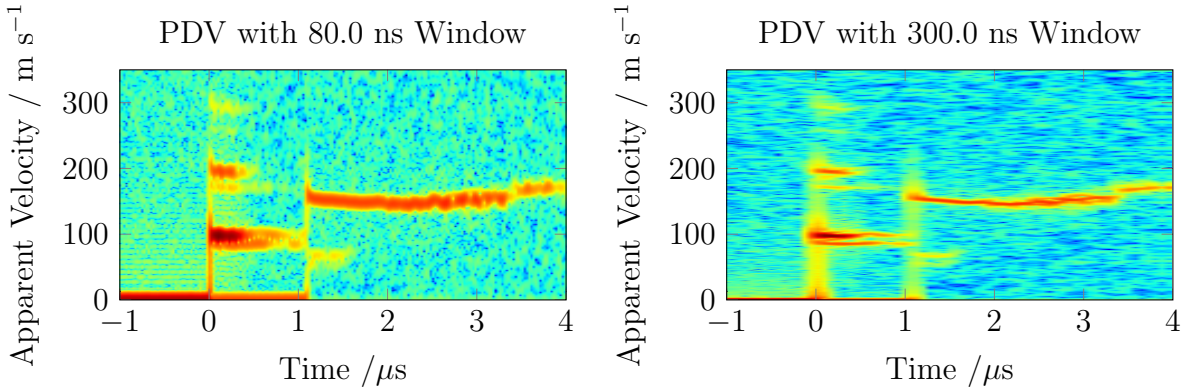


Figure B.10: PDV data for experiment C3

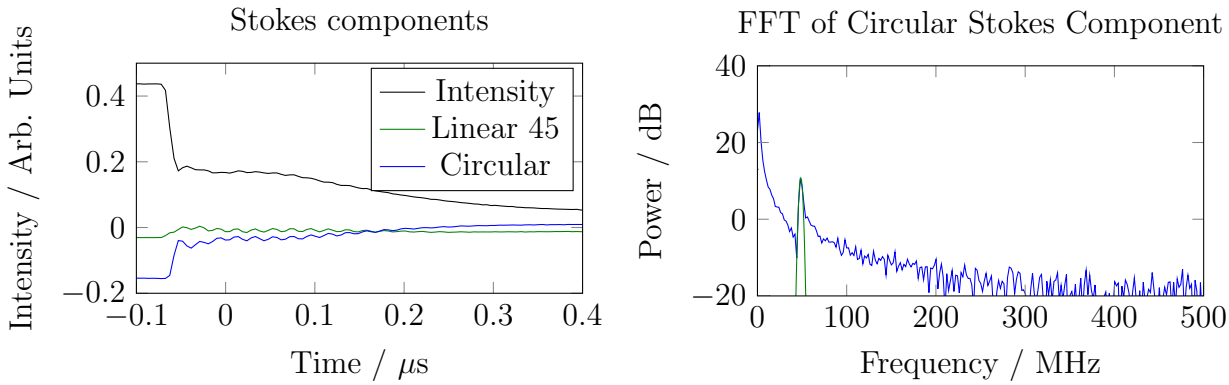


Figure B.11: Polarimetry data for experiment C3

B.3 Sapphire Large Bore Gas Gun Results

The sapphire series of experiments is presented here.

Shot	**Flyer**	l_0 / **mm**	v / **m s^{-1}**	u_p / **m s^{-1}**	σ_l / **GPa**
S2	OFHC copper	7.993 ± 0.006	414 ± 0.5	190 ± 2	8.59 ± 0.09
S3	OFHC copper	7.92 ± 0.006	600 ± 0.5	278 ± 2	12.81 ± 0.1
S4	OFHC copper	7.916 ± 0.003	657 ± 0.5	306 ± 2	14.18 ± 0.1
S1	OFHC copper	8.003 ± 0.002	800 ± 0.5	354 ± 2	16.4 ± 0.1

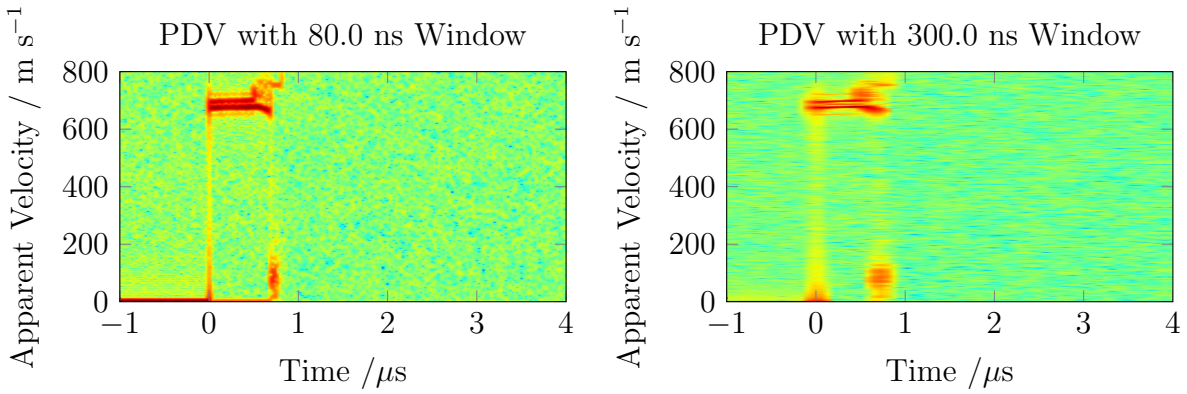


Figure B.12: PDV data for experiment S1

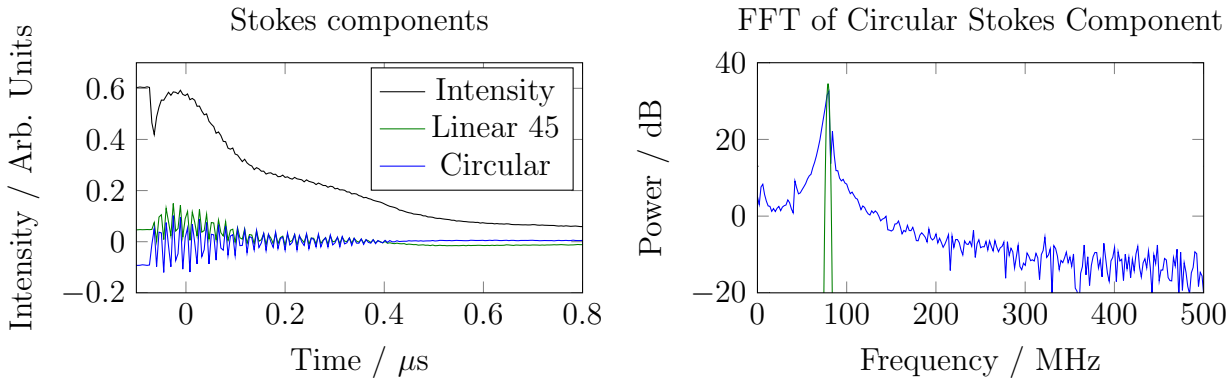


Figure B.13: Polarimetry data for experiment S1

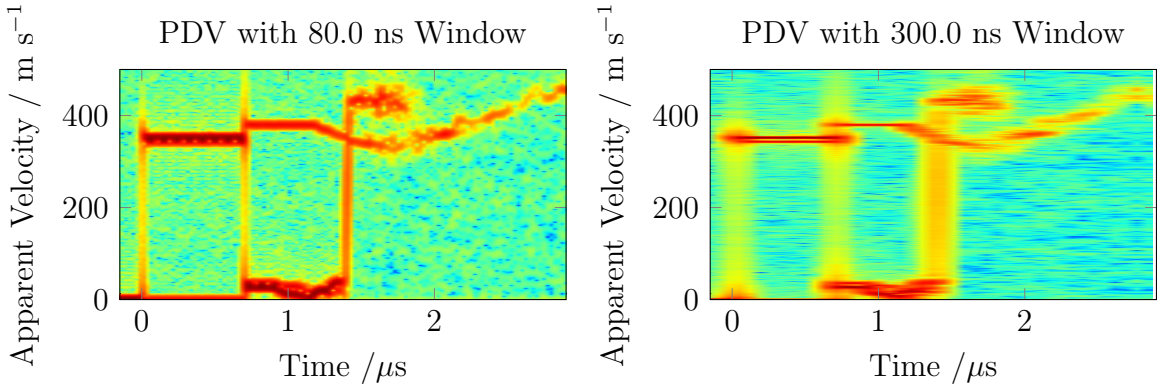


Figure B.14: PDV data for experiment S2

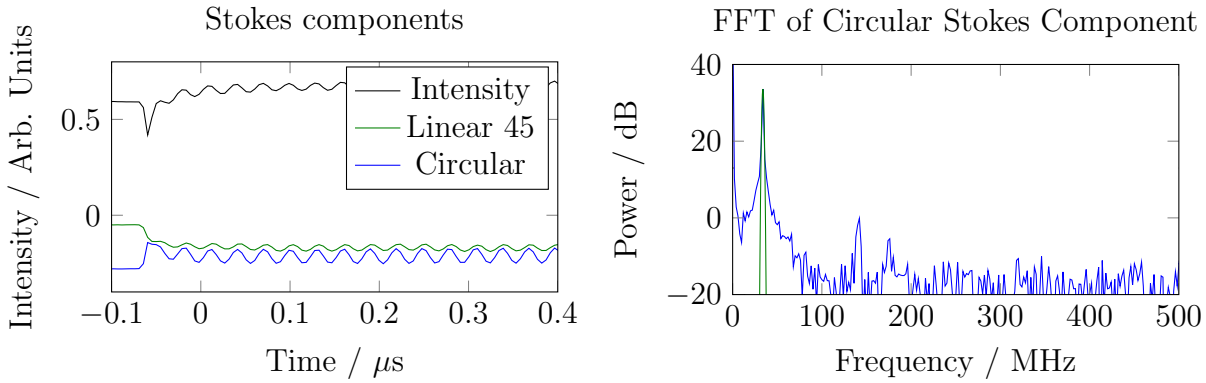


Figure B.15: Polarimetry data for experiment S2

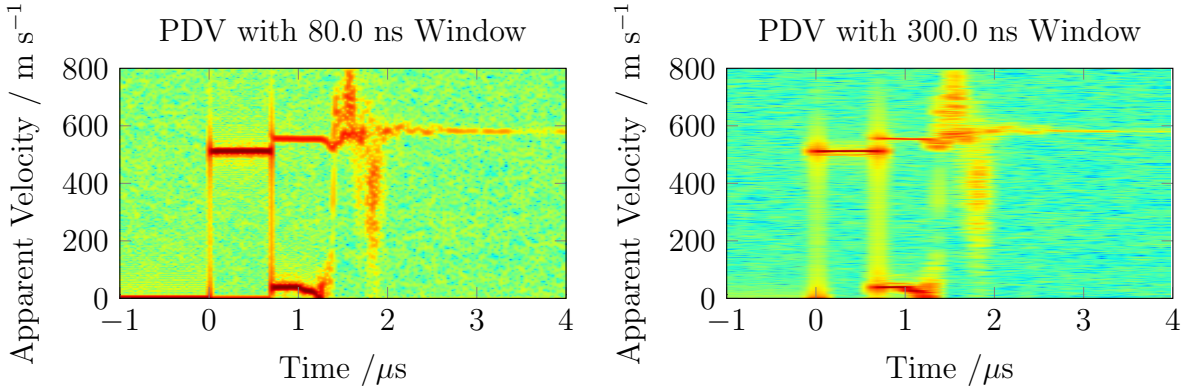


Figure B.16: PDV data for experiment S3

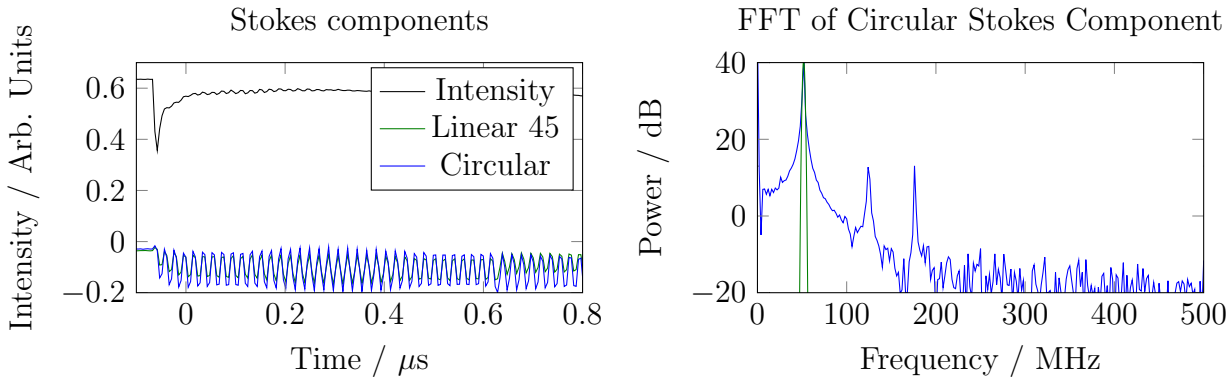


Figure B.17: Polarimetry data for experiment S3

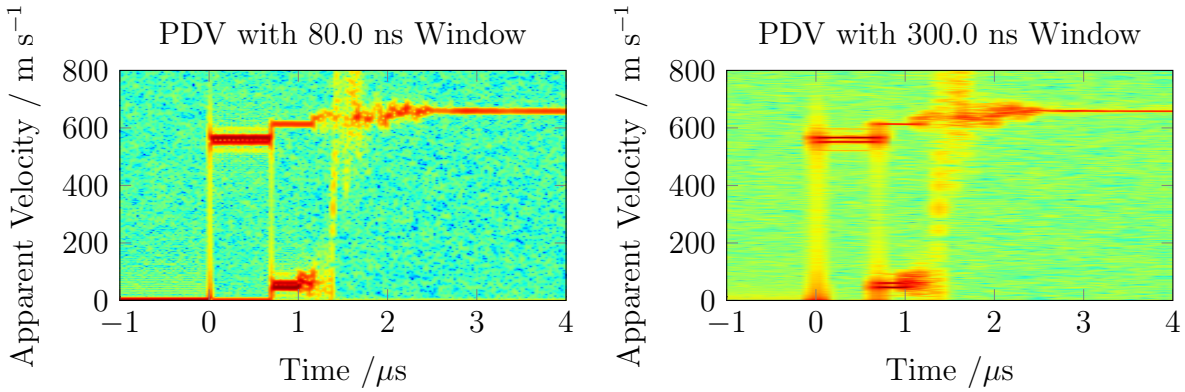


Figure B.18: PDV data for experiment S4

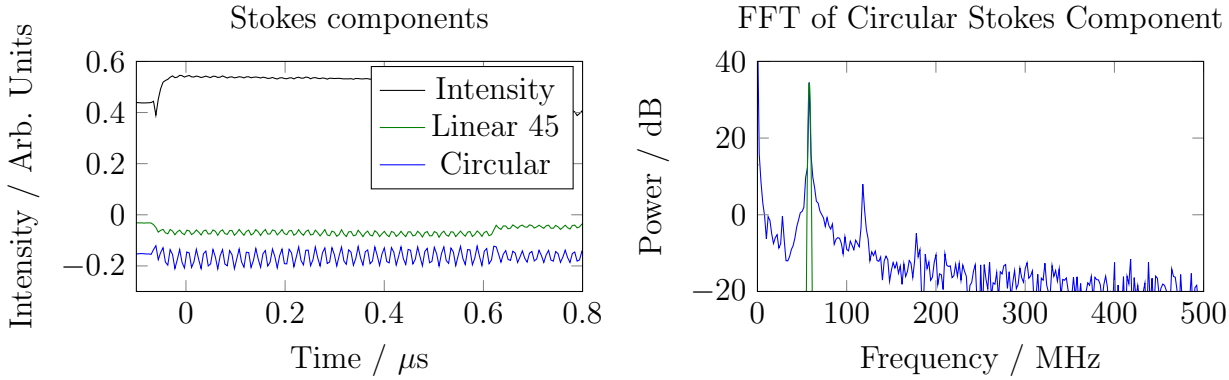


Figure B.19: Polarimetry data for experiment S4

Appendix C

Material Model Constants

C.1 Copper

Constant	Value	Unit	Reference
ρ_0	8.924 ± 0.01	g cm^{-3}	
ν	0.3424 ± 0.002		Marsh [65]
C_b	3.927 ± 0.014	km s^{-1}	Marsh [65]
C_l	4.76 ± 0.01	km s^{-1}	Marsh [65]
C_t	2.33 ± 0.01	km s^{-1}	Marsh [65]
σ_Y	70 ± 1	MPa	
s	1.51 ± 0.01		Marsh [65]

C.2 Magnesium AZ31B

Constant	Value	Unit	Reference
ρ_0	1.776 ± 0.001	g cm^{-3}	
ν	0.299 ± 0.002		Marsh [65]
C_b	4.482 ± 0.016	km s^{-1}	Marsh [65]
C_l	5.7 ± 0.01	km s^{-1}	Marsh [65]
C_t	3.05 ± 0.01	km s^{-1}	Marsh [65]
σ_Y	0.097 ± 0.001	GPa	
s	1.21 ± 0.01		Marsh [65]

C.3 PMMA

Constant	Value	Unit	Reference
ρ_0	1.186 ± 0.001	g cm^{-3}	Marsh [65]
ν	0.333 ± 0.004		Marsh [65]
C_b	2.221 ± 0.015	km s^{-1}	Marsh [65]
C_l	2.72 ± 0.01	km s^{-1}	Marsh [65]
C_t	1.36 ± 0.01	km s^{-1}	Marsh [65]
σ_Y	0.08 ± 0.08	GPa	
n_0	1.481 ± 0.001		Chapman *et al.* [31]
s	1.33 ± 0.01		Marsh [65]

C.4 Aluminium 6061

Constant	Value	Unit	Reference
ρ_0	2.703 ± 0.01	g cm^{-3}	
ν	0.3402 ± 0.0015		Marsh [65]
C_b	5.266 ± 0.015	km s^{-1}	Marsh [65]
C_l	6.4 ± 0.01	km s^{-1}	Marsh [65]
C_t	3.15 ± 0.01	km s^{-1}	Marsh [65]
σ_Y	0.11 ± 0.01	GPa	
s	1.34 ± 0.01		Marsh [65]

C.5 Sapphire Reintjes

Constant	Value	Unit	Reference
ρ_0	3.985 ± 0.001	g cm^{-3}	
$\underline{\mathbf{C}}$	$\begin{pmatrix} 497 & 502 & 115 & 22.4 & 0 & 0 \\ 502 & 497 & 115 & -22.4 & 0 & 0 \\ 115 & 115 & 502 & 0 & 0 & 0 \\ 22.4 & -22.4 & 0 & 147 & 0 & 0 \\ 0 & 0 & 0 & 0 & 147 & 22.4 \\ 0 & 0 & 0 & 0 & 22.4 & -2.65 \end{pmatrix}$	GPa	Tarumi *et al.* [40]
$\underline{\eta}$	$\begin{pmatrix} 0.319 \\ 0.319 \\ 0.322 \\ 0 \\ 0 \\ 0 \end{pmatrix}$		Malitson [78]
$\underline{\mathbf{p}}$	$\begin{pmatrix} 0.25 & 0.038 & 0.005 & 0.02 & 0 & 0 \\ 0.038 & 0.25 & 0.005 & -0.02 & 0 & 0 \\ 0.032 & 0.032 & 0.23 & 0 & 0 & 0 \\ 0.01 & -0.01 & 0 & 0.1 & 0 & 0 \\ 0 & 0 & 0 & 0.002 & 0.1 & 0 \\ 0 & 0 & 0 & 0 & 0.01 & 0.106 \end{pmatrix}$		Reintjes and Schulz [70]

C.6 Sapphire Waxler

Constant	Value	Unit	Reference
ρ_0	3.985 ± 0.001	g cm^{-3}	
$\underline{\mathbf{C}}$	$\begin{pmatrix} 497 & 502 & 115 & 22.4 & 0 & 0 \\ 502 & 497 & 115 & -22.4 & 0 & 0 \\ 115 & 115 & 502 & 0 & 0 & 0 \\ 22.4 & -22.4 & 0 & 147 & 0 & 0 \\ 0 & 0 & 0 & 0 & 147 & 22.4 \\ 0 & 0 & 0 & 0 & 22.4 & -2.65 \end{pmatrix}$	GPa	Tarumi *et al.* [40]
$\underline{\eta}$	$\begin{pmatrix} 0.319 \\ 0.319 \\ 0.322 \\ 0 \\ 0 \\ 0 \end{pmatrix}$		Malitson [78]
$\underline{\mathbf{p}}$	$\begin{pmatrix} 0.23 & 0.03 & -0.02 & 0 & 0 & 0 \\ 0.03 & 0.23 & -0.02 & 0 & 0 & 0 \\ 0.04 & 0.04 & 0.2 & 0 & 0 & 0 \\ -0.01 & 0.01 & 0 & 0.1 & 0 & 0 \\ 0 & 0 & 0 & 0 & 0.1 & -0.01 \\ 0 & 0 & 0 & 0 & 0 & 0.1 \end{pmatrix}$		Waxler and Farabaugh [72]

C.7 Sapphire Jones

Constant	Value	Unit	Reference
ρ_0	3.985 ± 0.001	g cm^{-3}	
$\underline{\mathbf{C}}$	$\begin{pmatrix} 497 & 502 & 115 & 22.4 & 0 & 0 \\ 502 & 497 & 115 & -22.4 & 0 & 0 \\ 115 & 115 & 502 & 0 & 0 & 0 \\ 22.4 & -22.4 & 0 & 147 & 0 & 0 \\ 0 & 0 & 0 & 0 & 147 & 22.4 \\ 0 & 0 & 0 & 0 & 22.4 & -2.65 \end{pmatrix}$	GPa	Tarumi *et al.* [40]
$\underline{\eta}$	$\begin{pmatrix} 0.319 \\ 0.319 \\ 0.322 \\ 0 \\ 0 \\ 0 \end{pmatrix}$		Malitson [78]
$\underline{\mathbf{p}}$	$\begin{pmatrix} 0.23 & 0.043 & -0.02 & 0 & 0 & 0 \\ 0.043 & 0.23 & -0.02 & 0 & 0 & 0 \\ 0.028 & 0.028 & 0.2 & 0 & 0 & 0 \\ 0.01 & -0.01 & 0 & 0.1 & 0 & 0 \\ 0 & 0 & 0 & 0 & 0.1 & 0.01 \\ 0 & 0 & 0 & 0 & 0 & 0.1 \end{pmatrix}$		Jones *et al.* [24]

C.8 Calcite ¡10-10¿

Constant	Value	Unit	Reference
ρ_0	2.712 ± 0.001	g cm^{-3}	
$\underline{\mathbf{C}}$	$\begin{pmatrix} 148 & 55.4 & 54.5 & -20.8 & 0 & 0 \\ 55.4 & 148 & 54.5 & 20.8 & 0 & 0 \\ 54.5 & 54.5 & 85.7 & 0 & 0 & 0 \\ -20.8 & 20.8 & 0 & 32.7 & 0 & 0 \\ 0 & 0 & 0 & 0 & 32.7 & -20.8 \\ 0 & 0 & 0 & 0 & -20.8 & 46.3 \end{pmatrix}$	GPa	Dandekar [12]
$\underline{\eta}$	$\begin{pmatrix} 0.364 \\ 0.364 \\ 0.453 \\ 0 \\ 0 \\ 0 \end{pmatrix}$		Ghosh [79]
$\underline{\mathbf{p}}$	$\begin{pmatrix} 0.062 & 0.147 & 0.186 & -0.011 & 0 & 0 \\ 0.147 & 0.062 & 0.186 & 0.011 & 0 & 0 \\ 0.241 & 0.241 & 0.139 & 0 & 0 & 0 \\ -0.036 & 0.036 & 0 & -0.058 & 0 & 0 \\ 0 & 0 & 0 & 0 & -0.058 & -0.036 \\ 0 & 0 & 0 & 0 & -0.011 & 0 \end{pmatrix}$		Nelson *et al.* [53]

Appendix D

List of Symbols

Accoustic tensor	The acoustic or Kristoffel-Green tensor is defined as $$C_{ijkl}x_j x_l$$ where C_{ijkl} is the elastic tensor and x_i is the direction of wave propagation. The eigen solutions to this rank two tensor give wave velocities and polarisations.	Q
Angular Frequency	The frequency of an oscillation in radians per second rad s^{-1} equal to frequency as $$\omega = 2\pi f \quad \text{(D.1)}$$	ω
Birefringence	Difference in ordinary and extraordinary refractive indices. Can be defined as $$\Delta n = n_e - n_o$$ or as $$\Delta n = \frac{1}{\sqrt{\eta_2}} - \frac{1}{\sqrt{\eta_3}}$$	Δn

Chi Square Distribution	The distribution of a sum of independent random gaussian variables. Useful in tests for significance when noise is known to be Gaussian.	χ^2
Density	Mass per unit volume	ρ
Dielectric constant	Dielectric constant, relates the applied electric field to the residual electric field expressed as a tensor ϵ_{ij}	ϵ
Elastic tensor or matrix	Bulk material property relating stress to strain, either expressed as a tensor C_{ijkl} if a basis independant quantity is wanted or often as a 6 X 6 matrix $\underline{\mathbf{C}}$ in experimental work.	C
Electric field	Electric field, usually expressed as a vector $\mathbf{E}$ with components (E_x, E_y, E_z).	E
Frequency	Frequency of oscillations.	f
Gruneisen Gamma	A measure of variation of the Hugoniot with pressure. A key material parameter in the Mei-Gruneisen equation of state.	Γ
Impact Tilt	The degree to which the flyer and target planes are not co-planer.	θ_i
Impact velocity	Projectile velocity prior at the moment of impact. It is necessary for the projectile to be travelling at a constant speed prior to impact to get an accurate measure of this value and to ensure that the flyer is in as equilibrium state as possible.	v

Longitudinal Stress	The stress experienced in the shock propagation direction.	σ_l
Optical Axis Orientation	The angle between the optical axis and the $\pm 45^{o}$ polarisation frame of reference, usually determined by a polarimeter.	ζ
Optical impermeability	Related to speed of propagation of electromagnetic waves in a material	η
Optical Intensity	The intensity of the optical wave, defined as $< A^2 >$	I
Optical Phase	The phase of the optical wave.	ϕ
Particle velocity	Velocity of the material in a shock wave.	u_p
Permeability	Permeability of free space is equal to $4\pi \times 10^{-7}$ N A^{-2}	μ
Photoelastic tensor or matrix	Usually expressed as a matrix, this bulk material property relates strain to changes in the optical impermeability in Voigt notation.	p
Polarisation State	A state of polarisation of an optical wave. Can be represented in several forms including a Jones vector, a Stokes vector and a Poynting sphere.	S
Pressure	Pressure	P
Reduced Chi-Squared	A normality test of a distribution, normalised to the number of free parameters. If the value is unity, then the data set is exactly normally distributed, deviations from unity indicate the degree to which the data set is normally distributed.	${\chi_r}^2$

Sample Thickness	The original sample thickness prior to impact. Necessary for determining the shock velocity.	l_0
Shock Tilt	The degree to which the shock front and ideal impact plane are not co-planer.	θ_s
Shock velocity	Velocity of the interface between material with two different particle velocities.	U_s
Strain	Deformation of a material, as a proportion of it's original length. Can be expressed in tensor form or Vogit notation.	ε
Wave vector	The wavevector $\mathbf{k}$ of a wave with its magnitude defined as $\frac{2\pi}{\lambda}$	k
Wavelength	The peak to peak distance.	λ

Appendix E

Acronyms

AR Anti-Reflective

BCC Body Centred Cubic

BIM Beam Intensity Monitor

DHPC Diamond High Pressure Cell

DoF Degrees of Freedom

EBSD Electron Back-Scatter Diffraction

EoS Equation of State

FCC Face Centred Cubic

FEM Finite Element Method

FFT Fast Fourier Transform

HEL Hugoniot Elastic Limit

ISP Institute of Shock Physics

OFHC Oxygen Free High Conductivity

PCA Principle Coordinate Analysis

PDV Photonic Doppler Velocimetry

PETER Pressure Energy Temperature and Extreme Rates

SCCM Shock Compression of Condensed Matter

STFT Short Time Fourier Transform

ToA Time of Arrival

VISAR Velocity Interferometry System for Any Reflector

Appendix F

Glossary

Birefringence Material property arising from anisotropy in the materials electronic structure. This gives *two* refractive indices in perpendicular directions.

Cauchy Tensor A stress or strain tensor, obeying the tensor transformation rules for a change in coordinates.

Expectation The expected mean of a random variable. If a set of values are taken from a random variable, and the mean of these values is calculated, then as the number of values taken increases, the mean should converge on the expectation.

Gladstone-Dale An optical model for isotropic materials giving a linear refractive index to density relation.

HEL The Hugoniot Elastic Limit (HEL) is the elastic limit of the material under shock compression.

Hugoniot A material dependant equation relating two of the variables in the jump equations, usually shock velocity and particle velocity. It is only valid at a specific pressure and density, and requires a EoS to calculate if the material is shocked more than once.

Monte Carlo Monte Carlo methods employ randomly generating many perturbed values in a known distribution, computing these, and then analysing the resulting distribution to find the expected error.

Optical Axis Direction in a birefringent material in which the propagating light ray is unaffected.

Optical Window An optical window is a material which is placed on the back of a sample so that optical diagnostics can measure the sample window interface. This allows experiments to be performed in which the sample is not released whilst it is being measured. Such experiments are ring up and release curve measurements where off Hugoniot states are measured. The material must be optically transparent and well characterised under shock compression.

Shock Impedance Shock impedance in a material is defined as $U_s\rho_0$ and effectively relates the transmission and reflection of a shock wave at an interface.

Voigt Notation Notation for stress and strain described in [38]. It uses material specific coordinates and is related to the Cauchy tensor.